Bio-inspired computing leveraging the synchronization of magnetic nano-oscillators

Philippe Talatchian

NNT : 2019SACLS008

Thèse de doctorat

Bio-inspired computing leveraging the synchronization of magnetic nano-oscillators

Thèse de doctorat de l'Université Paris-Saclay
préparée à l'Université Paris-Sud

Ecole doctorale n°564 Physique en Ile-de-France (EDPIF)
Spécialité de doctorat : Physique

Thèse présentée et soutenue à Palaiseau, le 9 Janvier 2019, par

PHILIPPE TALATCHIAN

Composition du Jury :

Ian O'CONNOR Professeur, École Centrale de Lyon	Rapporteur
Liliana BUDA-PREJBEANU Enseignante-chercheuse, CEA-SPINTEC	Rapporteur
Myriam PANNETIER-LECOEUR Directrice de Recherche, CEA-Service de Physique de l'État Condensé	Examinatrice et présidente
Julie GROLLIER Directrice de Recherche, Unité Mixte de Physique CNRS-Thales	Directrice de thèse
Damien QUERLIOZ Directeur de Recherche, Centre de Nanosciences et de Nanotechnologies	Invité
Paolo BORTOLOTTI Chercheur, Thales	Invité

Thèse préparée au sein de l'Unité Mixte de Physique CNRS-Thales

1 Avenue Augustin Fresnel
91767 Palaiseau Cedex,
France

REMERCIEMENTS

Cette thèse est le fruit de trois belles années passées à l'Unité Mixte de Physique CNRS-Thales. Je veux en premier lieu remercier Julie Grollier de m'avoir accueilli à l'UMR et de m'avoir donné cette opportunité de travailler sur un superbe sujet de thèse. Travailler avec toi a été un grand plaisir et j'espère avoir beaucoup appris pendant ces quelques années à tes côtés. Si aujourd'hui je m'oriente vers la recherche c'est sans doute en grande partie dû à ta bienveillance et à la passion que tu as pu me communiquer.

Je tenais à remercier les membres de mon jury. Notamment Myriam Pannetier-Lecoeur pour avoir présidé mon jury de thèse. Merci à Ian O'Connor et Liliana Buda-Prejbeanu pour avoir accepté de la rapporter, merci également à Paolo Bortolotti pour avoir participé à ma soutenance et pour son soutien scientifique et humain.

Ce travail ne serait pas ce qu'il a été sans l'immense contribution de Miguel Romera qui m'a tant appris expérimentalement dès mes premiers jours de thèse. Tu as été pour moi un incroyable soutien tout au long de cette longue aventure tant du point de vue scientifique qu'humain. J'espère qu'on se reverra d'ici là !

Un grand merci à tous ces gens formidables qui ont pu contribuer et aider à ce travail interdisciplinaire. Parmi cela Flavio Abreu Araujo qui m'a initié sur bien des plans. Que ce soit sur les simulations micromagnétiques ou sur les soirées "bibine" tu as été un éclaireur de tous les instants ! Merci à Vincent Cros, Paolo Bortolotti, Jacob Torrejon et leurs riches discussions qu'on a pu partager avec Steffen Wittrock et Samh Menshawy sur les oscillateurs à base de vortex magnétique qui n'ont pas encore délivré tous leurs secrets. Je voulais aussi remercier la direction du labo, Frédéric Petroff et Frédéric Nguyen Van Dau pour contribuer à un cadre à la fois chaleureux et d'excellence. Merci aussi à tous les autres permanents avec qui j'ai pu discuter de temps en temps. Merci en particulier à Nicolas Reyren pour ta bonne humeur et tes conseils sur la câbleuse et le wedge, ainsi que pour ton aide pour organiser la soutenance.

Merci aussi à ceux qui ont fabriqué les échantillons que j'ai pu étudier pendant ma thèse, notamment ceux de l'équipe du Pr. Yuasa parmi lesquels il faut souligner l'expertise de Sumito Tsunegi. Je remercie également les équipes d'Ursula Ebels de Spintec et de l'INL au Portugal pour les premiers échantillons que j'ai pu mesurer au début de ma thèse.

Un très grand merci à tous ces gens incroyables du C2N. Je remercie Damien Querlioz pour son aide et sa contribution importante à ce travail ainsi que pour ses conseils et expériences du Japon. Je garderai un très beau souvenir de tous les temples que j'ai pu visiter de façon infatigable avec toi à Kyoto ainsi que des délicieux restaus de Ramens. Un grand grand merci également à Nicolas Locatelli, Damir Vodenicarevic, Tifenn Hirtzlin et Maxence Ernoult qui ont contribué à ce travail et de qui j'ai pu recevoir dans la bonne humeur des conseils instructifs et des visions éclairantes.

Un gros merci à mon frère de thèse Mathieu avec qui j'ai partagé des moments inoubliables. Que ce soit pendant nos escapades nocturnes, entre Bruxelles et la Nouvelle-Orléans ou que ce soit dans l'adversité de l'écriture du manuscrit, tu as été un soutien indéfectible à tous les niveaux. Je veux également remercier un autre frère qui est Xavier qui comme Mathieu est un grand Mousquetaire. Ta perspicacité et tes blagues décalées m'ont permis de tenir dans ce bureau de fou qu'on a partagé avec Victor pendant ces trois ans. Néanmoins, Victor tu me manqueras énormément aussi. Tes chansons inspirées des Schtroumpfs ainsi que ta bonne humeur du vendredi soir resteront inoubliables. Merci à Ralph et Laura pour leurs attentions et pour avoir apporté un semblant de calme dans les moments les plus compliqués du bureau. Un grand merci à l'humour de mon co-conf William avec qui j'ai partagé la majorité de mes confs : "amazing french culture". Merci à Samh pour tous les moments qu'on a pu passer ensemble et les discussions sur l'expulsion ou la résonance du coeur de vortex. Je n'oublierai pas notre sortie dans ta belle berline. Merci à Juan et Alice pour vos conseils précieux sur la vie outre atlantique. J'éspère te revoir Alice, tu me manqueras! Merci à Steffen avec qui j'ai pas mal appris sur le bruit qu'il soit thermique ou autre et merci à certaines soirées qui rendaient bien bruités mes lendemains de monitorat. A ce propos, un grand merci pour l'accueil et le soutien de l'équipe pédagogique du département informatique de l'IUT d'Orsay notamment Jean-Claude Martin, Anne

Vilnat, Véronique Moriceau et bien d'autres pour m'avoir accueilli et fait confiance. Cette expérience d'enseignement restera pour moi très riche humainement. Merci à Madjid aussi pour ces quelques mois à travailler sur la magnéto-optique à Polytech. Merci à tous les thésards et post-docs du labo qui ont contribué à une ambiance des plus chaleureuses. En particulier merci à Mafalda, James, Salvatore, Maxence et Sophie pour leur chaleur humaine et leurs gourmandises dans le bureau ! Merci également à Marine avec qui la coupe du monde et les pique-niques avaient une ambiance euphorisante. Merci Florian pour tes histoires et blagues ! Merci à David, Martin et Seiha qui ne sont plus du labo ! Bon courage à Bogdan ! Merci aussi à Hugo, Lucile et Quentin à qui je souhaite du courage ! Merci Eliana pour ta bonne humeur et tes blagues de couloir ! Merci Danijela pour tes conseils en matière d'organisation de soutenance et pour le template! Merci à Anastasia et Nathan avec qui c'était un plaisir de travailler ! Je vous souhaite plein de futurs résultats excitants !

Merci à toutes les autres personnes extérieures au labo que j'ai pu rencontrer en conf ou ailleurs. Merci notamment à Anatoly Belanovsky et Alexei Khvalkovsiy pour m'avoir fait un peu découvrir le monde des MRAMs. Merci à Aurianne, Thanh Quy, et à tous les anciens de DQ. Merci à Kévin, Hicham, Aurélie et tous les autres de l'EIDD. Merci à Natacha pour ton soutien et ton regard alternatif sur la vie. Merci à Louise pour m'avoir fait découvrir Glasgow et les magnifiques environs verdoyantes. Tu m'as décidément donné envie d'avoir un petit chaton! Merci à Baptiste pour ta bonne humeur et les joggings matinaux au bois de Vincennes ainsi que les superbes concerts d'orchestre que tu as pu donner avec Clara que je n'oublie pas de remercier ! Je remercie également David et Béatrice qui m'ont toujours soutenu depuis que je suis petit ! Merci aussi à toutes les personnes à qui je pense souvent et qui ont peut-être été omises, je m'en excuse par avance. Merci à mon prof de Physique qui a cru un peu en moi pendant les années de prépa. Un grand merci à Léa et Zhicheng qui ont toujours été là pour moi que ce soit sur Skype ou ailleurs ! Je remercie l'immense soutien de mon père et de ma mère à qui je dois sans doute mon goût initial pour les maths et la physique. Merci également à ma grand-mère pour les appels du dimanche. Enfin merci également à ma petite soeur à qui je souhaite du bonheur et de la réussite très prochainement !

CONTENTS

LIST OF FIGURES

LIST OF TABLES

1

INTRODUCTION

In recent years artificial intelligence demonstrates impressive progress allowing to achieve cognitive tasks such as image or speech recognition which were initially too complex to be done by computers. Henceforth, beyond the execution of precise instructions, computation becomes more and more synonymous of systems able to learn from data and adapt their response as a function of their environment. This breakthrough was led by the development of innovative brain-inspired algorithms since the 50's. First observations of biological brain by neuroscientists gave rise to the development of one the most popular of such kind of algorithms, called artificial neural networks. Despite lack of understanding how the biological brain fully works, these algorithms were able to outperform humans in several particular tasks. A striking example of the power of these brain-inspired algorithms was highlighted through recent defeats of masters at the game of Go [16][17]. Even if this is a major feat in artificial intelligence AI community, it should not mask an important failure in the way these computation successes were achieved. Indeed, the energy consumption of computers running AI algorithms is much larger than the one of the biological brain, and it should continue to increase with the increase of the numbers of parameters required to be tuned for more and more complex tasks. One reason why running brain-inspired computing consumes more energy than the brain comes from fundamental architecture differences between the biological brain and nowadays computers where memory and processing are spatially separated causing an important back and forth transport of data and as a consequence a large energy dissipation. On the contrary, the brain is a massively parallel architecture where neurons and synapses holding processing and memory are entangled and close to each other. For this reason, conventional computers are not optimized for running brain-inspired algorithms. These observations motivate developing alternative approaches taking inspiration from biology, called bio-inspired computing approaches, and build alternative physical systems which combine high computing

performances for cognitive tasks and low energy consumption. In order to develop these brain-inspired systems, it is important to be able to emulate the behavior of biological neurons [18][19][20].

These computational units of the brain can be seen as small nonlinear oscillators connected to each other through tunable connection called synapses. Physicists and neuroscientists have developed different computing models based on assemblies of nonlinear oscillators [21][22]. For instance, leveraged dynamical phenomena occurring in the brain, such as synchronization, to compute. Such models are more powerful at pattern recognition when the number of oscillators is large (there are 10^{11} neurons and 10^{15} synapses in the brain). Implementing these models in hardware therefore necessitates assembling huge number of nonlinear oscillators. In order to avoid enormous circuit sizes, the physical devices emulating neurons and synapses should be sufficiently small. For this reason, nanodevices that can emulate the functionalities of neurons and synapses are required for building brain-inspired physical hardware. In particular, nano-oscillators are very promising to emulate biological neurons. Despite numerous theoretical attempts to achieve brain-inspired operations using assemblies of nano-oscillators, no physical demonstration was reported. This was mainly due to the high sensitivity of devices to noise at the nanoscale and the difficulty to tune the properties of such nano-oscillators. However, recently, by leveraging the exceptional properties of magnetic nano-oscillators, a first demonstration of brain-inspired computing was achieved using a single spin-torque nano-oscillator [23] for spoken digit recognition. However, to achieve more complex cognitive tasks, it is necessary to assemble together several oscillators, and to demonstrate a very important property of a neural network: learning. An iterative process through which a neural network can be trained using an initial fraction of the inputs and then adjusting internal parameters to improve its recognition or classification performance. One difficulty is that training assemblies of nano-oscillators requires tuning the coupling between them.

This thesis presents a first experimental demonstration of brain-inspired computing with a physical assembly of coupled nano-oscillators. This demonstration leverages the synchronization of spin-torque nano-oscillators for pattern classification illustrated through the demon-

stration of vowel recognition task. Importantly, through the high frequency tunability of spin-torque nano-oscillators, the learning ability of coupled nano-oscillators is demonstrated for the first time [24].

The first chapter of the thesis presents the main motivation of brain-inspired computing and focuses on the way oscillations observed in biological neurons can be leveraged to build computational models that can be implemented with assemblies of nano-oscillators. Different nano-oscillator technologies promising to achieve this goal are presented.

The second chapter introduces spin-torque nano-oscillators. The physical phenomena and principle leading to oscillations are described. A particular focus is given to the nonlinear dynamics and the synchronization ability of spin-torque nano-oscillators which will highlight their potential for brain-inspired computing.

The third chapter introduces briefly the particular class of magnetic vortex- spin-torque nano-oscillators studied in this thesis. The particular dynamics and synchronization ability of these oscillators is presented both theoretically and experimentally. I will show that the phase-locking properties of a spin-torque nano-oscillator to an external microwave source can be modified though the coupling to another oscillator.

The fourth chapter presents the main experimental brain-inspired computing results. I will show that four coupled spin-torque nano-oscillators can classify spoken vowels by synchronizing to external stimuli. The experimental learning procedure leads to a recognition rate of 88%.

The fifth chapter presents simulation studies performed in order to understand the origin of the recognition performances observed experimentally. The simulations show that the frequency tunability and mutual coupling between oscillators are crucial to obtain high recognition rates.

The sixth chapter presents a simulation approach for building larger

arrays of spin-torque nano-oscillators. I will present an analytical model that allows to optimize the operating points and the physical properties of the oscillators for brain-inspired computing. I show that array size of about 300 spin-torque nano-oscillators can be achieved taking into account the physics of the oscillators and manufacturing constraints.

Finally, I will present the main conclusions of both experimental and simulation approaches developed in this thesis. Several perspectives of this work will be briefly discussed.

2

OSCILLATIONS FOR COMPUTING

In this chapter, I will present the main motivation of taking inspiration from the brain and in particular from its oscillatory features to realize energy efficient computing devices. This will allow to introduce the brain-inspired computing approach developed in this thesis. In the first part of this chapter, a particular focus will be given to brain architecture and to biological neurons that can be seen as nonlinear oscillators. Then, brain-inspired computing approaches both in terms of algorithms and hardware will be briefly introduced, and the main brain-inspired approaches based on coupled oscillators, in particular those where synchronization phenomena is leveraged, will be described. Finally, a brief overview of nano-oscillator technologies available for building brain-inspired computing systems will be briefly introduced in the last section of this chapter.

2.1 OSCILLATIONS IN THE BRAIN

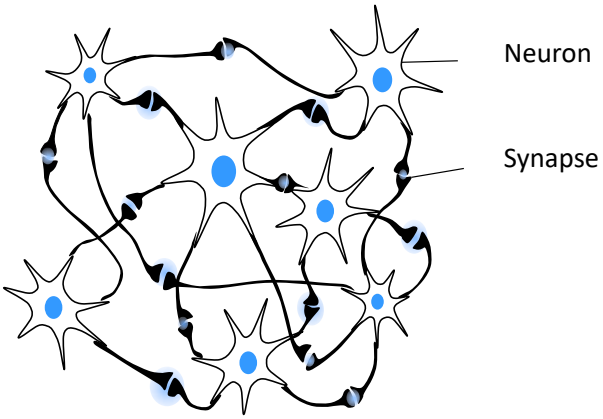

Figure 1: Schematic of a parallel network of neurons and synapses

Despite impressive progress since last century in the development of computing algorithms and hardware, for many cognitive tasks such as

speech or visual recognition, the brain is still much more energy efficient than classical computers. To have an idea, its power consumption is relatively low, of the order of 20 W [25]. From the computing point of view, this observation motivates to understand the way biological brain computes.

At the end of 19s and beginning of 20s century, first descriptions of the architecture of the brain were initiated by the work of Golgy and Ramon y Cajal, where the cellular texture was identified. Biological brain is composed by an astronomic number of interconnected nervous cells, called neurons which are estimated to be of the order 10^{11} in the human brain (see Fig. 1). These cells are connected to each other through tunable connections called synapses, which are estimated to be of the order of 10^{15}. The plasticity of the brain, allowing learning are due to this tunability of synapses. Synaptic mechanisms behind these processes are still not well understood. In this thesis, the main focus on the brain will concern biological neurons which are often seen as the "computation" unit of the brain.

2.1.1 *Description of biological neurons*

Biological neurons emit electrical signals which have a spiky shape if one draws the temporal evolution of the signal. Those spikes are emitted when neurons experience an external stimulus. They receive incoming trains of spikes from their dendrites (see Fig.2.b)). Thus, a very important process which occurs is the integration of these temporal stimuli in the cell body (as an electrical capacitor). Indeed, those electrical stimuli charge the membrane potential of the cell body (see Fig.2.c)). This integration occurs with a certain leakage. Then, when a certain threshold is reached for the membrane potential, the neuron fires an electrical spike (voltage) in the axon part (see Fig.2.d)) called as action potential.
Different models were proposed to describe the integration process of biological neurons [26], and a first detailed model describing the mechanisms behind the firing of the action potential was proposed in 50's by Hodgkin and Huxley [27]. In this model, the ion flows through the chemical permeable behavior of the membrane are described [28]. The model can be described as follows: the outside of the neuron

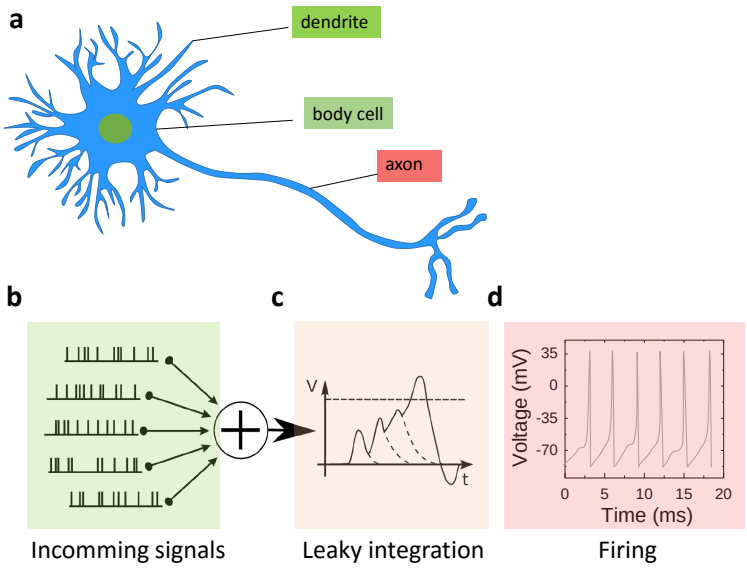

Figure 2: a) Schematic of a neuron composed of three main parts: cell body, dendrites and axon. b) Incoming signals from the dendrite. c) Leaky integration in the cell body. d) Firing of action potential in the axon.

is filled in majority by Sodium ions Na+, while the inside is filled in majority by Potassium ions K+. Two chemical gradients try to lead to a situation where the concentration of both ions are equal inside and outside of the membrane. It should be noticed that the membrane of the neuron (yellow in Fig.3.a)) has pores which allow ionic exchanges between the inside and outside of the membrane. In addition, ion pumps (represented in orange in Fig.3.a)) try to expels K+ ions and bring back Na+ ions inside of the membrane. Due to chemical mechanisms, there are more positive charges outside than inside the neuron. Thus, the membrane has a negative potential which is evaluated to -70 mV.

When it increases in the presence of external stimuli, the membrane potential reaches a first step at -55 mV. At this potential, the ion gated channels for Na+ (represented in clear green) open, and Na+ ions enter massively inside of the membrane causing an increase of the membrane potential. This phase is called as the "depolarization" phase. When the membrane potential reach a second threshold at

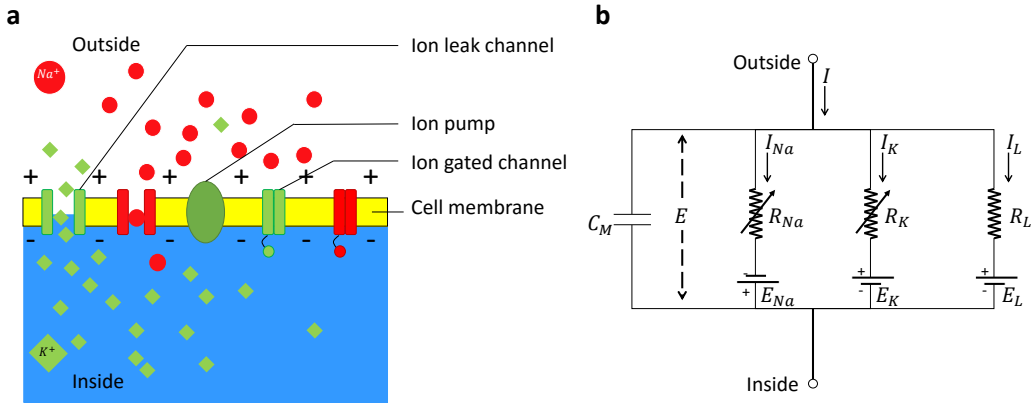

Figure 3: a) Schematic of the axon membrane: the inside of the neuron cell is in majority filled with potassium ions (K+) while the outside medium is in majority filled with sodium ions (Na+). The ions migrate through leak and gated channels, while an ion pump maintains the higher potassium concentration inside the neuron. b) Hodgkin-Huxley model: a capacitance models the membrane, the ion leak channels are modeled by a resistance and a generator, each gated channel for potassium and sodium ions is modeled by a gated resistance and a generator.

+35 mV, the Na+ gated channels close and K+ gated channels open. At this moment, K+ ions are massively expelled from the cell which causes a decrease of the membrane potential. This phase is called "repolarization". After this phase, both ion gated channels remain close and the ion pumps bring back the K+ and Na+ concentrations to the initial levels. This last phase is called "refractory" phase, and during it the membrane potential comes back to its initial level of -70 mV.

This spiking phenomena can be described by an equivalent electrical circuit presented in Fig.3.b). The capacitance C_M corresponds to the membrane, the generator E_L and resistance R_L corresponds to the ion pump and ion leak channels. The generator and gated resistance (E_K, R_K) and (E_N, R_N) represent the gated channels respectively for K+ and Na+ ions. External stimulus is represented by the current I.

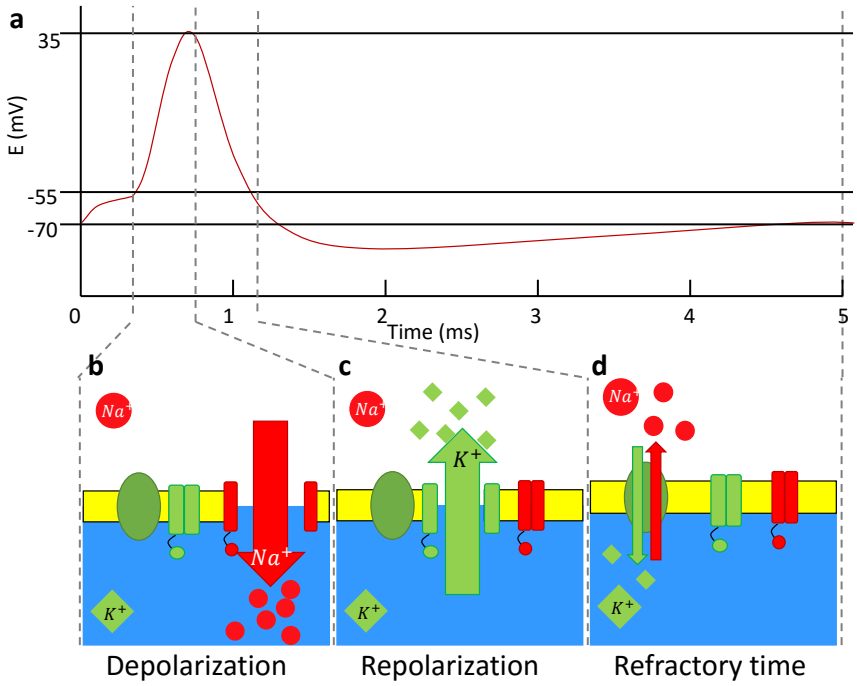

Figure 4: a) Schematic of the membrane potential evolution in time during the firing of an action potential. b) Depolarization phase: the sodium (Na+) gated channels opens c) Repolarization phase: the sodium gated channel close and the potassium (K+) gated channels open. d) Refractory time: both gated channels for potassium and sodium are closed. The ion pump brings the membrane potential back to it initial level.

It should be noticed that this model can be simplified by considering that once the membrane potential reaches a threshold (-55 mV), it spikes. Thus, one can consider that when neurons receive external stimuli, it integrates the signal with a leakage, then when a certain threshold is reached for the membrane potential, a spike occurs which is sent to the axon. The LIF model is called Leaky-Integrate and Fire model (LIF) [26]. This simpler model doesn't describe the biological refractory phase or the origin of the spike, however it constitutes a easier approach for computation. The equivalent electrical circuit of this model corresponds to the circuit presented in Fig.3.b) but without the two central branches containing the tunable resistances. In this model, the membrane potential leaks with a certain time constant

$\tau_M = RLC_M$ and the temporal evolution of the spike can be assimilated to a Dirac function.

2.1.2 *Why can neurons be modelled as nonlinear oscillators?*

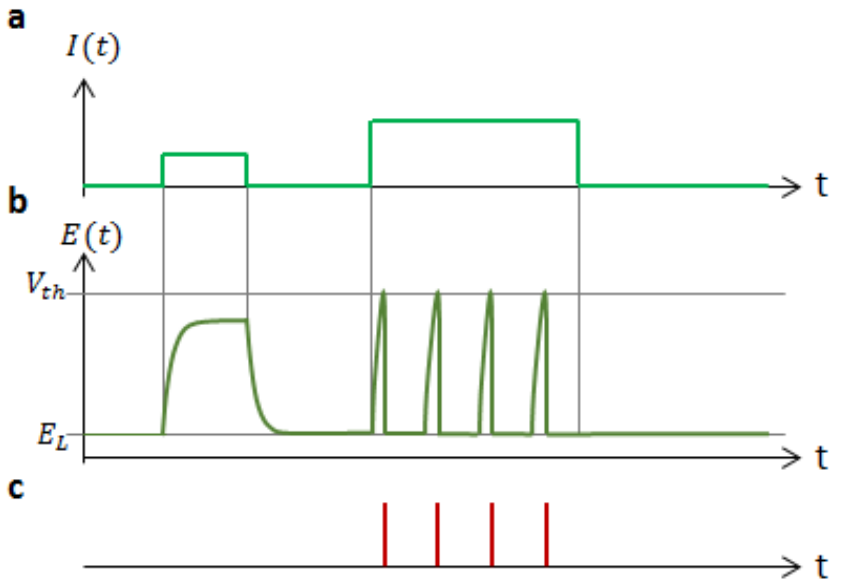

Figure 5: a) Temporal evolution of the input stimulus sent to a neuron following the LIF model. b) Temporal evolution of the membrane potential of LIF neuron. c) Output spike train.

Fig.5 shows how a neuron following the LIF model will react to two constant stimuli. For the first input step stimulus having a smaller amplitude, the potential membrane of the neuron doesn't reach the spiking threshold. Thus after the input step, the neuron leaks and comes back to its initial membrane potential. For the second input step having a higher amplitude, the membrane potential reaches the spiking threshold, thus the neuron spikes. This phenomena occurs periodically as long as the constant amplitude of the input stimulus is higher than a certain threshold value. One can even calculate the frequency of these emitted spikes (in the LIF model), called firing rate.

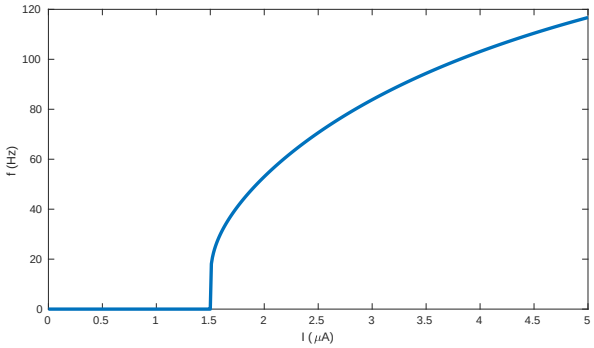

Figure 6: Evolution of the frequency of the firing rate of a neuron following the LIF model as a function of the input current (schematic).

The firing rate is plotted in Fig.6 as a function of the amplitude of the input current stimulus. Thus, using the LIF model, one can see from the evolution of the spiking frequency that the neuron is a nonlinear oscillator. Here, the nonlinear behavior comes from the fact that under a certain amplitude input stimuli, the neuron does not fire (is not oscillating) but once this threshold is reached it starts to oscillate with a frequency which depends nonlinearly on the amplitude of the stimulus.

From this important observation obtained using a simple spiking model for the neuron, and which can be also obtained with more elaborate models [29], the brain itself can be seen an assembly of small nonlinear oscillators (neurons), that are interconnected to each other through tunable connections (synapses). This approach is also consistent with various nonlinear phenomena observed in the brain and which characteristic of nonlinear dynamical systems, namely synchronization [21], complex transients [30], or chaos[31]. Even if the way the brain computes is not fully understood today [22], the previous observations motivated theoretical models to compute with assemblies of nonlinear oscillators [32][33] (presented in the next section) in order to build brain-inspired computing systems that can carry interesting features of the brain such as its low energy consumption. Following this line of thinking, in this thesis, we will focus on the implementation of brain-inspired computing systems made of assemblies of nonlinear oscillators. In particular their synchronization ability will be leveraged.

2.2 BRAIN-INSPIRED COMPUTING

In this section, the general context of brain-inspired computing both in terms of brain-inspired algorithms and dedicated brain-inspired hardware used for computing will be presented. At the end, a particular focus on brain-inspired approaches leveraging the oscillatory behavior of neurons (seen in the previous section) will be emphasized.

2.2.1 *Artificial neural networks*

Despite the lack of a complete understanding on how the biological brain fully works, first observations in neuroscience gave rise to a series of brain-inspired algorithms called as artificial neural networks. Those algorithms which are the first example of brain-inspired or neuromorphic computing approaches are today one of the most famous and widely used algorithms for solving complex problems in the field of "machine learning". For many problems, where it is very difficult or even impossible to implement an explicit rule for solving them, machine learning methods are able to learn an implicit rule. Machine learning algorithms find such implicit rules, by tuning their inner parameters. This tuning depends on the structure of the data on which those algorithms are applied. Different classes of learning can be identified such as: supervised learning, unsupervised learning and also reinforcement learning.

Nowadays, the most famous and widely used class of learning is the supervised learning class, popularized through the development of deep-learning in the last decades [34]. In this learning framework, two distinct phases should be distinguished: training and inference. During the training phase, the input data used for the learning process are initially labeled, meaning the algorithm a priori has an access to the class of the incoming input data. For instance, in the case of image classification problems, the image data are labeled by the name of the concept they represents (cat or dog for example). During this training phase, the inner parameters of the algorithms are modified. Once the algorithm has been trained successfully on this labeled data, those parameters become fixed. Then, the algorithm is then used to realize the inference phase. During this phase, new unlabeled data which

were not presented during the training procedure are sent as input and the algorithm applies what it learned during the training phase.

As opposite to supervised learning, unsupervised learning corresponds to algorithms for which the incoming data used for learning are not explicitly labeled, the unsupervised algorithm itself detect some regularities or structure in the input data without having any access to additional information. One famous example of unsupervised learning is K-clustering techniques [35]. This class of learning algorithms is typically used for problems where labeled input data are not available. Finally, reinforcement learning is a other distinct class of learning algorithms for which one should consider a framework problem where an agent takes action in an environment which should be explored. As a consequence of the action of that agent in this environment, its state variable is modified (for instance its position) and in addition it receives a cumulative reward as long as it acts in the environment.

The learning technique used in this thesis for the demonstration of neuromorphic operations with the magnetic nano-oscillators (introduced in next sections), will belong to supervised learning class. For this reason, we focus in the following on supervised learning methods, which are the most powerful today. First supervised learning algorithms appeared in the 50s through the development of perceptron algorithms allowing to find the linear combination parameters to fit data. After facing few disinterest periods refereed as "AI's winter", supervised learning encountered new success in 80s and 90s, partly due to the progressive increase of computational power. Many famous machine learning approaches were developed in the framework of supervised learning, namely support vector machine (SVM), kernel methods, and in particular artificial neural network. This last approach will be leveraged in the context of this thesis in order to realize neuromorphic computing.

Artificial neural network algorithms are constituted of a network of nonlinear units, called artificial neurons. Those artificial neurons are interconnected to each other through tunable connections called as synapses. Initially, most artificial neurons were spiking neurons,

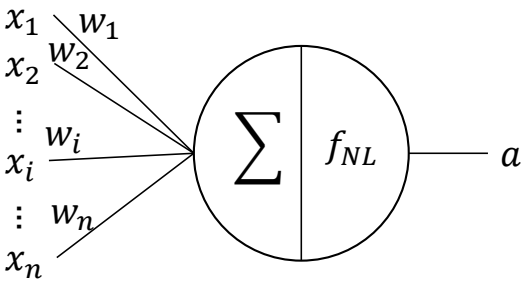

Figure 7: Schematic of a formal neuron.

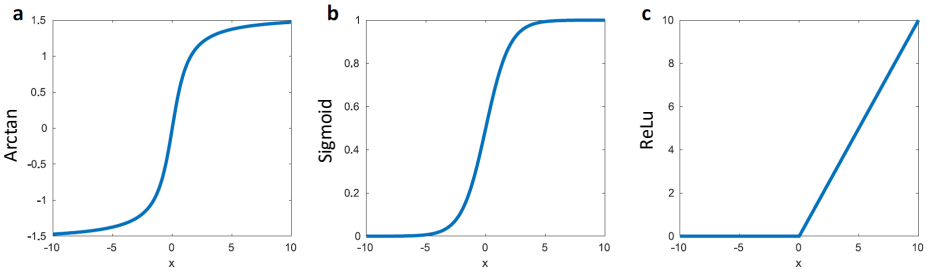

Figure 8: Most common activation functions used in artificial neural networks: a) Arc tangente function. b) Sigmoid function. c) Rectified Linear Unit function (ReLu).

however nowadays the most commonly used neurons are formal neurons which have a continuous response and as a consequence are much simpler than biological neurons presented in the previous section, see Fig.7. Those formal neurons achieve simply two tasks: they sum the inputs they receive, and apply to the resulting sum a nonlinear function called as activation function. The result of the application of this nonlinear function corresponds to the output of the formal neurons. In terms of neuroscience analogy, the activation function of such formal neurons can be seen as the firing rate response of the neuron presented in the previous section, see Fig.6. The most widely used activation functions are arctan, sigmoid, or rectified linear units (ReLu) drawn in Fig.8.

In the framework of supervised learning, artificial neural networks achieve the crucial learning step, by adjusting the connections weights between formal neurons. These adjustments are realized during the

training phase. During the inference phase where the ability of the artificial neural network is tested, the weights are fixed. In this phase, the input data encounters a series of nonlinear transformations learned during the training phase. In the following, we will focus on two examples of artificial neural network architectures widely used for supervised learning: feed-forward and reccurent neural networks.

2.2.1.1 *Feed forward neural networks*

In the 2000's, feed-forward neural networks became famous due to their achievement in state-of-the-art image recognition and web advertising. Such networks consist of several layers of neurons which are connected to each other, one after the other (neurons of the same layer are not connected to each other). In order to train this kind of architecture, an algorithm introduced in 80's called backpropagation [36] is used. Two important examples of feed-forward neural networks are fully connected neural networks and convolutional neural networks. In the case of fully connected networks, each neuron of a given layer is connected to all the neurons of the next layer, see Fig.9. As a result the number of weight connections in such a network is very large, and scales as the square of the number of neurons in each layer. For this reason, when the number of neurons in layers is increased, training such network become relatively complex. This occurs for problems where data have already a large dimension, for instance this is the case for image recognition.

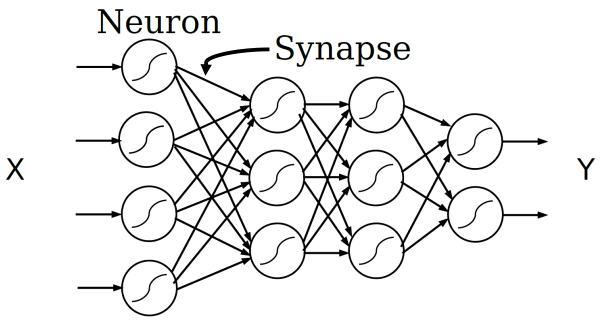

Figure 9: Schematic of a fully connected feed-forward neural network.

In order to solve image recognition problems, convolutional neural networks are used. Using them, the state-of-the-art in image recogni-

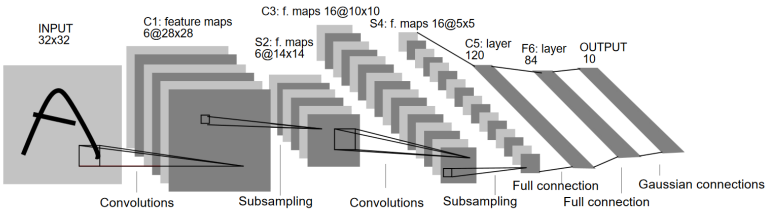

Figure 10: Schematic of the LeNet5, a convolutional neural network proposed by Y. LeCun for digit recognition.

tion is achieved [37]. In this kind of neural network, a filter forming a feature map (see Fig.10) realizes a convolution operation from one layer to the next. Here, only the parameters of the filter are tuned during the learning. As a consequence, the number of parameters to tune in convolutional neural network is much smaller than in fully connected neural networks. As for fully connected neural networks, learning is achieved using back-propagation algorithms. This kind of network shows very impressive results for image recognition tasks and is nowadays widely used in computer vision problems. As an example, inception network [38] was able to achieve, a recognition rate of 97%, which is better than human performance from the same task. However, it should be noticed that the training and inference of such feed-forward neural networks is computationally very costly. In the case of the inception network, 35 million parameters were adjusted to achieve training, and every inference requires 19 billions of operations [39]. In addition, feed-forward neural network can not be used to solve problems requiring to take into account sequential order in data, for instance problems such as time series prediction or speech recognition. For solving such problems recurrent neural networks are required.

2.2.1.2 *Recurrent neural networks*

Contrary to feed-forward neural networks, recurrent neural networks have a much larger connection possibility between neurons, and are not constrained to layer-to-layer connections. Those connections can form inner loops in the network and thus can cycle in different ways, see Fig.11. Due to architecture of such networks, the information cycles in the network can be seen as a memory, which is necessary to process sequential data as a sentence in speech recognition. Recurrent

neural networks were able to achieve state-of-the-art performances in speech recognition [40][41], in particular using two examples of such architecture namely bidirectional neural network (BRRN)[42], and long short term memory (LSTM) neural network [43]. In addition mixtures of convolutional neural network and LSTM neural networks were used to realize word transcription with human performance [44]. Later in this thesis, LSTM neural networks will be used to achieve a comparaison with the performances of the experimental oscillator-based neural network studied in chapter 5. Despite of numerous success of recurrent neural network, it is important to emphasize the fact that training such neural network is relatively difficult compared to feed-forward neural network, in particular, the algorithms may not converge to a solution even after an infinite number of training steps [45] [46]. In addition, the training algorithm used in such networks (LSTM and BRNN) called as back propagation through time [47] requires a large number of training operations and training steps. An alternative approach to train recurrent network is reservoir computing [48][49], where the internal connections of the recurrent network are not trained, and only connections required for the output read-out are trained. This particular approach will be discussed later in the oscillatory based architecure section where a first experimental demonstration using a spintronic nano-oscillator [23], was successfully achieved.

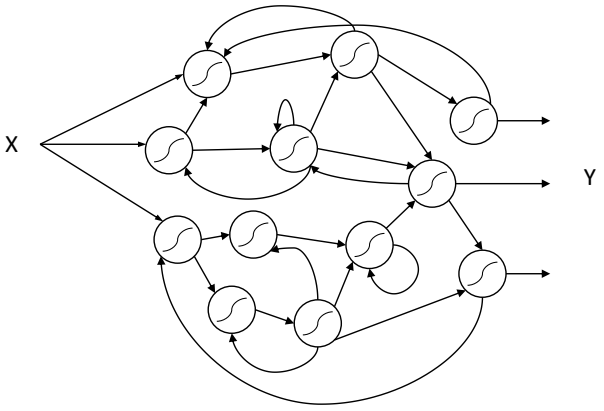

Figure 11: Schematic of a recurrent neural network.

2.2.2 *Limits of classical computers for running brain-inspired algorithms*

Nowadays, artificial neural networks became one of the most powerful computing algorithms used to solve tasks in the context of artificial intelligence. Indeed, as it was shown in the previous subsection, for tasks as image recognition or speech recognition, the performances overcome the human ones. Due to these high performances, they are currently used for big-data analytics such as financial trading and banking, on-line advertising, health care, medical diagnosis, autonomous driving cars, etc and will be an important development factor of the sector of the Internet of Things. However, it is important to emphasize that these brain-inspired algorithms require relatively large number of computational operations. For instance, few billions of operations [39] only for inference not considering the learning are required. Due to this large number of operations, running these brain-inspired algorithms on non brain-inspired hardware can be an important source of energy dissipation cost. Indeed, those algorithms are running on classical architecure computers were the foundation is refereed to as the Von-Neumann architecure. As can be seen in Fig. 12, in this architecture, the memory unit is spatially separated from the processing unit (CPU). In order to achieve a task, classical computers

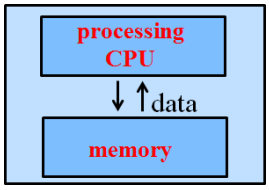

Figure 12: Schematic of the Von Neumann architecture.

follow a sequence of instructions: retrieve an information in the memory unit, send it to the processing unit to perform a computation, and finally store the result in the memory unit. Thus, data are processed and stored one by one in sequential manner. Due to this architecture, the bus is shared between memory and processing unit which is referred as "Von Neumann bottleneck" [50]. In this architecture, information needs to be retrieved in the memory which induces delays longer than the time required to do the computational operation.

Moreover, retrievement and storage of information is quite energy costly compared to the computation itself [51]. For these reasons, the Von Neumann bottleneck limits both the computational speed and is a problem in terms of energy consumption. On the contrary, neural network are massively parallel architecures, where a large number of parameters of the order of hundred millions [39] need to stored in the memory and retrieved. This corresponds to an important data flow between the memory and processing unit. For all of these reasons, the Von Neumann architecture is not well suited to run brain-inspired algorithms such as artificial neural networks.

Several hardware approaches were proposed to improve the computation efficiency of classical computers, for instance using multi-cores computing devices (corresponding to multiple Von Neumann architectures) and leverage graphical processing units (GPU) computing capability in order to accelerate computations to run neural networks used for example for image recognition [52]. Beyond the time delay for running these algorithms, some alternative approaches can also reduce the energy consumption with comparable results on few tasks, which is the case of the Field Programmable Gate Arrays (FPGA) [53]. Another solution is to use optical interconnects to reduce the bottleneck between logic and memory [54][55]. Recently, new hardware chip approaches specialized for machine-learning operations were proposed by the industrial sector. Some of the most famous example of those chips often called Application-Specific Integrated Circuits" (ASIC) are the Tensor Processing Units (TPU) developped by Google involved in recent alphaGo successes [16][17], A11 bionic neural engine (Apple), Holographic Processing Unit (Microsoft), NPUs (Nvidia).

In comparison with a single CPU unit, these approaches allow to gain orders of magnitude in term of energy consumption. Nevertheless, it still remains orders of magnitudes higher than the energy consumption of the biological brain, several tens to hundreds of kW compared to 20W [25]. Indeed, for all computing devices presented in this section, the Von Neumann bottleneck still remains an important energetic issue. The energy efficiency of the biological brain can be explained by its architecture where processing carried by neurons is spatially entangled with memory hold by synapses. As a result, the information

do not travel long round trips between memory and processing as in the Von Neumann architecture. This important observation motivates taking inspiration of the biological brain, not only for powerful brain-inspired algorithms developed in the last decades, but importantly for building physical hardware which can perform computation.

2.2.3 *Hardware for neuromorphic computing*

In the context of very large scale integration (VLSI), the term "neuromorphic" was introduced by Mead [56] at the end of the 80's. At that time, the first approach was to develop brain-inspired hardware using complementary metal oxide semiconductor (CMOS) technology. Thus, several implementation devices were realized emulating neurons following the Hodgkin-Huxley model [57], or the LIF model [58][59][60]. In order to look towards architectures with smaller area occupancy than those proposed in CMOS, some complementary approaches based on threshold switching materials were also developed. For instance, recently Pickett et al. proposed a scalable neuron implementation which resembles the Hodgkin-Huxley model using Mott insulators [61][20]. It should be noticed that in addition to trying to emulate neurons in hardware, a large effort is focused on leveraging tunable devices often refereed as memristors, in order to reproduce the behavior of synapses [62]. In this thesis, we will focus on another approach namely using oscillations and synchronization phenomena for computing. In this section, the main neuromorphic chips proposed for brain-inspired computing will be presented. Some of the implementations emulating individual neurons will be presented in the "nano-oscillators" section.

In the past decade, different neuromorphic chips were proposed to reproduce the behavior of large neural networks namely to emulate the way the brain works and also recently in order to build energy efficient computing devices. All of these neuromorphic chips were implemented with the classical CMOS technology and were developed both through academic (Human Brain Project, Brain in Silicon, ETH Zurich) and industrial (IBM and Intel) initiatives.

In 2012, as a part of the BrainScaleS project (part of the Human Brain Project), a neuromorphic chip called HICANN [63] [64] was

implemented. The main goal was to simulate large neural networks to understand the behavior of the brain. In this chip, the neurons are analog devices while synapses and the communications are digital. Each of these chips implements 128 000 synapses and 512 neurons where each neuron is modeled using the LIF model. The size of each neuron is close to $150 \times 10 \mu m^2$.

In the same approach, another neuromorphic chip called Neurogrid [65] developed in a different group (Brain in Silicon, Standford University) was used to run brain-inspired computational models. In this chip, the LIF model was used to emulate the behavior of the neurons. As for HICANN, the neurons are analog, while synapses are digital components, and the area occupied by each neuron was also comparable, of the order of $50 \times 50 \ \mu m^2$. However, an important difference compared to HICANN is that its transistors work in the sub-threshold conduction regime.

This sub-threshold regime of transistors was also used to implement analog neuron devices in neuromorphic chips proposed by Indiveri et al. [19] called Dynap-se. The area occupied by these neurons remains smaller than for Neurogrid, of the order of $20 \ \mu m^2$. In this chip, the synaptic connections remains digital. Those chips were used to achieve ECG signals classification [66].

A fully digital neuromorphic chip called SpinNNaker was also implemented to simulate brain-inspired neural networks (as a part of the Human Brain Project) [67]. In this case, all the neurons were simulated using classical micro-processors (ARM processors), see Fig. 13(left). Those chips were assembled in a large cluster platform made of 500k cores, see Fig. 13(right). If in terms size and power consumption, the SpiNNaker approach is still orders of magnitudes from the biological brain, it is a good example of a brain simulation implementation which consumes less energy than a classical supercomputer. Interestingly, with SpinNNaker, different kinds of neuron models can be used (LIF, Izkhevich model) which is important for the computational neuroscience community.

Another approach is the fully digital neuromorphic chip developped

Figure 13: Left: Circuit board of the SpiNNaker device composed of ARM processors. Righ: The 500 000 cores SpinNNaker Human Brain platform. Extracted from Hopkins et al. [1].

by IBM, called TrueNorth [2]. The chip emulates 1 million spiking neurons. The physical layout of this circuit is composed of 256 neurons which are used to simulate 4000 neurons by time-multiplexing. Each neuron emulates the LIF model. The size of each of these neurons is of the order of 100×10 μm^2, see Fig. 14. According to authors, this chip shows better energy consumption performances: consuming 769 times less than SpiNNaker and 176 000 times less than regular computing processors. This chip was able to realize real-time object detection tasks, however an important drawback is that it can not perform learning.

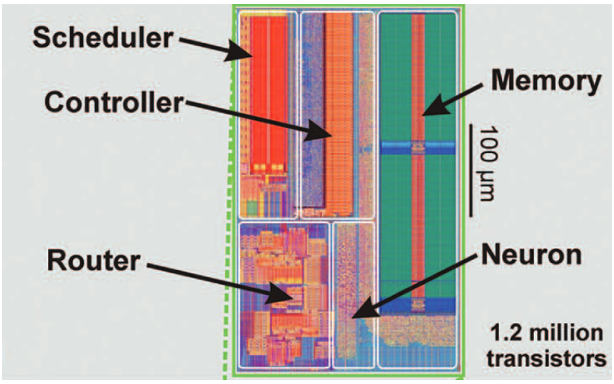

Figure 14: Physical lay-out of the TrueNorth chip, extracted from Merolla et al. [2].

More recently, in 2018, a similarly fully digital neuromorphic chip was proposed by Intel, called Loihi [68]. This chip can emulate 130 000 neurons, where each neuron is modeled using the LIF model. Contrary to the IBM chip, Loihi is able to perform learning, and it can solve tasks such as the LASSO optimization problem. As in all digital approaches, the size of its neurons is still quite large, of the order of tens of micrometer.

As a conclusion, mixed-analog-digital and fully digital neuromorphic chips where implemented using CMOS technology. In order to emulate large neural networks of spiking neurons, the energy consumption of these approaches is more efficient than the one of classical computers. However, it is still much larger than the one of biological brain. In addition, the hardware CMOS circuits used to emulate neurons in neuromorphic chips still have large lateral sizes (from few micrometers to few tens of micrometers [2][68]), which is detrimental to emulate large and dense on-chip neural networks. For these reasons, in order to emulate neurons and synapses, it is important to complement CMOS devices by alternative nanodevices which rich physics can emulate individually the nonlinear dynamics of the neurons observed in biology. Very promising nano-devices for this purpose are nano-oscillators, that will be presented later in this thesis.

2.2.4 *Computing using coupled oscillators*

In this subsection, we present briefly some computing approaches leveraging the dynamics of oscillators. Here, those are categorized in two classes: approaches which aim to solve a specific computing problem without necessarily leveraging a brain-inspired architecture, and those for which the oscillator dynamics is used to realize brain-inspired operations.

2.2.4.1 *Computing with coupled oscillators beyond the scope of brain-inspired approaches*

Since the 50's, oscillators were used to realize computing operations in binary computers called parametrons. Interestingly, in those initial approaches, the synchronization dynamics of oscillators was leveraged.

Two binary states were possible (bits of 0 or 1) depending on the phase difference of oscillators which in a synchronization situation can be 0 or π. Based on different coupling approaches between those oscillators, different logical gate operations were implemented in parametrons [69]. The oscillators used at that time were based on classical RLC circuits which were macroscale. However, in order to build more energy efficient computing devices, recently a new interest was found in parametron's model at the nanoscale, using super conducting nano-oscillators [70], relaxation nano-oscillators [71], or electromechanical nano-oscillators (NEMS)[72]. These different nano-oscillators technologies will be described in more details in section 2.3.

The dynamics of oscillators found also some interest in particular computing applications requiring heavy numbers of operations when using classical computers. In particular, a NP-hard problem called vertex coloring where an individual variable named "color" need to be attributed to each node of a graph in such a way that two neighboring connected nodes will have a distinguishable color, and this by minimizing the total number of different colors used in the all graph. In order to find this set of colors, one should choose accurately the coupling between oscillators in such a way that when they synchronize their phase repel (anti-phase)[73]. Using the idea, the vertex coloring problem was demonstrated to be solved using relaxation nano-oscillators (VO_2) [74], for different graph size and topologies.

Another problem requiring large number of operations is image segmentation which corresponds to merging together pixels belonging to a certain image region following a criteria which could be brightness of color. For this task, one can consider a 2D array of coupled oscillators, where every oscillator have a natural frequency corresponding to the input image. Due to the coupling in this array, and the resulting local synchronization, the frequency of oscillators converge to each other for some image regions having similar frequencies. This approach was studied in simulations using oscillator models that can be applied to neural, chemical, or electromechanical oscillators [75]. In particular, recently an interest was also found through simulations, to use coupled spin-torque nano-oscillators to achieve this task [76].

The dynamics of oscillators is also used to solve some degree-of- match problems which again are costly in terms of computation on classical computers. To evaluate the degree of match (for example between two images), it is necessary to calculate a distance between two vectors which can have relatively large dimensions requiring an increasing number of arithmetic operations as the dimension of the vectors grows. In the case of an assembly of coupled oscillators, the order parameter which can be seen as a measure of the synchronization of the assembly, is used to approximate the degree of match (DOM)[77]. Implementations using relaxation oscillators (VO_2) were proposed [78]. Based on the same idea, an implementation using four spin-torque nano-oscillators was proposed in simulations [76] to evaluate DOM. Similar approaches, including other kind of spintronic devices called spin-hall nano-oscillators were also recently proposed numerically [79]. It should be noticed that this degree of match evaluation is an important step to realize pattern classification task which will presented in the next subsections.

2.2.4.2 *Auto-associative memory using Hopfield networks*

Auto-associative memory is a type of memory process observed in biological brains where a specific memorized pattern can be retrieved from a noisy, incomplete or altered input information. For instance, using their auto-associative memory, many readers will be able to complete the following quote: "I came, I saw, ..." Without a huge effort, their brain will spontaneously find the complete sentence: "I came, I saw, I conquered." Auto-associative memories play an important role in auto-completion or error correction applications [80]. From the previous example, associative memory operations seem very easy and simple to realize in the brain, however they are very computationally costly if they are done on classical computers. To reduce the difficulty of achieving such operations, alternative approaches which try to take advantage of the physics of devices were proposed. In particular, in order to realize such auto-associative memory operations, Hopfield network [80] is an important example to mention. This network which belongs to the class of artificial recurrent neural networks is composed of a set of binary artificial neurons, which can have a value of 0 or 1. Inspired from condensed matter physics, these neurons can interact

with each other. By tuning the interaction between those neurons, the final state of the neurons matches the known pattern desired to be stored. This approach can be applied to dynamical systems, where the attractor of the system will correspond to the stored pattern. When a noisy or incomplete version of this pattern is presented to the network, the system is set according this input pattern and thus is away from attractor states. Because of the internal interactions in the network, the system dynamics leaves its initial state, and converge to the closest attractor, which coincides with the reconstruction of the complete corresponding pattern.

Based on first theoretical works on Hopfield networks [80][32], implementations leveraging the dynamics of coupled oscillators were proposed to realize auto-associative memories. Auto-associative memory for binary words was proposed using electromechanical oscillators (MEMS) [81][82], and some implementations using optical laser oscillators [83] were investigated. An approach using spin-torque nano-oscillators [76] was also imagined. However, it should be noticed that in such associative memories, the coupling between oscillators needs to be continuously tuned during operations. This tuning can be realized at the macro-scale for electrical van der Pol oscillators using arbitrary waveform signals [84][85] which is very difficult to achieve at the nano-scale. Another disadvantage of such architectures is that their scalability is limited. Indeed, for a network of N coupled oscillators, in order to achieve low error rate recognition theoretically $0.138N$ patterns can be stored, and this number is even lower in practical implementations [86].

2.2.4.3 *Hetero-associative memories and pattern classification*

Hetero-associative memories are an extension of auto-associative memory concept. Instead of associating an incomplete or altered input pattern to the same type of complete pattern, hetero-associative memories can associate for one input pattern type, a different pattern type. For instance, the biological brain can associate a certain smell to a a certain visual memory, in this case the type of pattern is completely different. According to some neuroscience investigations, this hetero-associative memory process is correlated with particular types

of oscillations in the brain [87]. This observation motivates the use of oscillators to implement computing architectures that can achieve hetero-associative memory operations. In a case where the associated pattern is a certain defined label, for instance "cat" or "dog" labels while the inputs are images of cats and dogs, the operation is similar to pattern classification. Here, the picture of the dog is associated to his name (and respectively for the cat). Thus, by recognizing a presented input pattern and associating it to a certain label, pattern classification is achieved. It should be emphasized that nowadays, in the context of machine learning, pattern classification is an important operation for various applications, for instance for medical diagnosis [88], or for image and object detection used by autonomous driving cars [89]. This use of pattern classification operations motivates the implementation of oscillator-based approaches which will be able through their dynamics to efficiently classify patterns. In the following approaches using oscillators in order to realize pattern classification will be presented.

One approach is to leverage the way assemblies of oscillators are able to efficiently evaluate the degree of match (see previous section) between stored patterns of a defined class and a new presented input. This evaluation of the matching pattern can be achieved in parallel using different assemblies of coupled oscillators in a circuit. In order to realize such kind of associative memories, several models were imagined with electromechanical oscillators (MEMS) [81], spin-torque nano-oscillators [90], or CMOS ring oscillators [91]. The architectures proposed in these works are interesting because they do not require an important tuning of coupling between oscillators (this is the case for instance in the architecture proposed by Holzel et al. [84]). However, as the number of stored pattern examples increases, a higher number of read-out circuits (often large in CMOS technology) for assemblies of oscillators are necessary. This is an important scalability problem for these architectures.

2.2.4.4 *Vassilieva's architecure*

Vassilieva et al. [3] proposed an alternative oscillator-based classification approach, where the number of oscillators is independent of

the number of stored examples. To achieve this goal, the associated labels of presented input examples correspond to the different synchronization read-outs that can be identified in an assembly of tunable coupled oscillators. Interestingly, this approach only requires to tune the natural frequencies of the oscillator assembly and to read-out the resulting synchronization states appearing in the network. These characteristics of the architecture make it very suitable for oscillator based hardware implementations at the nanoscale. Fig.15 shows the architecture and different synchronization states that can emerge as a function of the frequency of input oscillators. Interestingly, a learning approach where the natural frequency of oscillators is modified was proposed in order to realize pattern recognition. The architecture which was initially introduced in a theoretical context was adapted later by Vodenicarevic et al. [4] for physical implementations involving nanodevices. In particular, a detection scheme for the readout of synchronization states using counters was proposed [92].

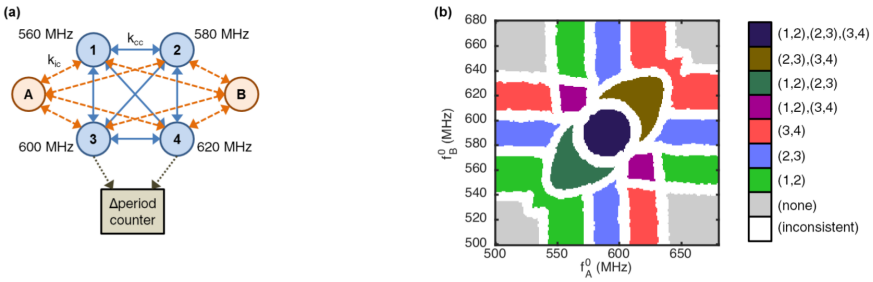

Figure 15: a) Diagram of the oscillator-based architecture proposed by Vassilieva et al. [3]. It is composed of two input oscillators A and B and four core oscillators labeled as 1,2,3 and 4. Blue arrows represent the coupling between core oscillators and orange arrows represent the coupling between core oscillator and one of the two input oscillators (A and B). b) Simulated output synchronization read-out map. Every colored area corresponds to a particular synchronization pair of core oscillators labeled in the colorbar. Figure extracted from Vodenicarevic et al. [4].

Due to presented advantages, this oscillator-based architecture and its learning approach will be adapted in chapter 4 to realize a first physical demonstration of pattern classification using spin-torque

nano-oscillators. Those oscillators, as it will be seen in following chapters, are particularly suitable to implement oscillatory networks such as the last one presented here. Nevertheless, other nano-oscillators are available and can be good candidates for similar implementations. Those will be presented in the next section.

2.3 NANO-OSCILLATORS

In this section, I present the main categories of nano-oscillators able to synchronize and that can be useful to build an oscillation-based computing system. It is important to note that other unmentioned valuable oscillator technologies can be found, but here we mainly select those which synchronization ability was demonstrated and that show a potential to be scaled down to the nanoscale. In this section, spin-torque nano-oscillators which are the central devices studied in this thesis are not included. They will be presented in details in the next chapter.

2.3.1 *Why do we need nano-oscillators?*

As it was presented in the beginning of this chapter, the brain has a tremendous number of interconnected neurons and synapses: 10^{11} neurons and 10^{15} synapses. Even in the case of brain-inspired algorithms such as alphaGo [93], one million of artificial neurons are required. From the observation of such large numbers, one can see that in order to build reasonable size physical brain-inspired computing system, the size of the physical devices emulating neurons and synapses need to be sufficiently small. From a simple numerical calculation, one can deduce that in order to implement a neuromorphic chip of 1 cm^2 surface area emulating more than 10^8 neurons, the lateral size of the physical neuron need to be smaller than 1 μm. This observation motivates brain-inspired implementations realized with nano-devices in order to emulate neurons and synapses. Thus, following this line of thinking and the oscillator-based computing approach described in the previous section, a particular focus is given to nanometric oscillators, called nano-oscillators.

2.3.2 *Nano-oscillators based on switching devices*

In general, these nano-oscillators are composed of a material able to switch between two or more internal states (physical or chemical). These switching materials are enclosed by two electrical electrodes through which an external voltage is applied. As shown in the previous chapter, such devices are very attractive to build neuristors that can emulate spiking neuron models such as the Hodgkin-Huxley or the LIF model [20]. But beyond this aspect, they also can be seen as auto-oscillators , called relaxation oscillators, that, for some of them are able to synchronize.

Their auto-oscillation property can be explained as follows. These devices leverage a large class of different materials that present an abrupt variation of their electrical property (resistance or voltage) due to a modification of their physical or chemical state. Importantly, those states themselves are also modified when the material experiences an applied voltage variation. That voltage variation is often due to the prior variation of the electrical material property. The combination of these two inter-dependent variations causes an oscillating electrical signal at the two terminals of the enclosed material. In terms of electrical transport measurement, this crucial property is often translated as a negative differential resistance. In order to deliver an applied voltage variation due to the prior variation of the electrical material property, a capacitive device connected in parallel or parasitic capacitance effects are required. Due to the voltage variations caused by the enclosed material, this capacitive device is periodically charged and discharged, see Fig. 16.

From an auto-oscillator point of view, the neuristor proposed by Pickett et al. [20] based on two Mott insulator Nb_2O_5 based memristors can be seen as a relaxation nano-oscillator that can emit spikes periodically when it is biased by a constant voltage. The lateral dimensions of the switching device (enclosed material) of such nano-oscillator can be nanometric, of the order of $100 \times 100\ nm^2$ [20] but according to predictions it can be scaled down to 10 nm [61]. In terms of energy consumption, data on power consumption are scarce. However, the energy for one switching event was evaluated to be smaller than 100

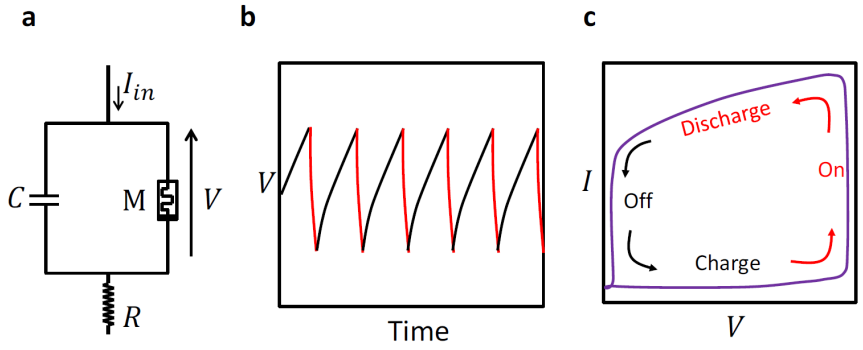

Figure 16: a) Auto-oscillator based on a memristive switching device: a capacitance C is in parallel of resistance switching device M. A load resistance R is connected in series. b) Schematic of the voltage vs time. c) Schematic of the current voltage curve for the resistance switching device M.

fJ [61]. The maximal spiking frequency of such devices can be of the order of 1 GHz (1 ns switching time)[20]. Still, the frequency tunability of such devices needs to be demonstrated experimentally, as well as their synchronization ability.

Another well studied example of such oscillators are those based on resistance switching materials experiencing a metal-insulating transition, such as VO_2, for which tunable oscillation frequencies between 90 and 300 kHz can be obtained [94][95]. Frequencies higher than tens of MHz can be reached [95]. Those oscillators show an endurance close to 250 millions cycles [96] which still needs to be improved. Their synchronization was demonstrated recently [97]. In these first works, the area that the switching device occupies (not considering capacitive elements), is close to the micrometer square ($3 \times 3\mu\ m^2$) [95] but according to author predictions they can be scaled down to 100 nm^2. Importantly, oscillators based on VO_2 attract researchers to demonstrate neuromorphic operations for image processing [98][99] or to find the degree of pattern matching [100]. Recently, such devices were also used to emulate neurons using the Hodgkin-Huxley model [101].

Other auto-oscillators based on TaO_x, TiO_x were proposed to realize

neuromorphic computing [102][103]. By including CMOS transistors, these oscillators show high frequency tunability comprised between 30 kHz and 300 MHz [102] and a frequency close to GHz was predicted [102]. Their synchronization was demonstrated [102] and first attempts to build an oscillatory neural network that can realize some associative memory operations [104][33] similar to the work of Hölzel et al. [85] are proposed. Finally, the area of the switching device is smaller than the micrometer, of the order of $700 \times 700\ nm^2$ (not considering the capacitive element) and authors predict that the device lateral size can be decreased down to 3 nm [102][105].

As a conclusion of this subsection, it should be noticed than in order to have auto-oscillations with switching devices, the presence of a capacitive element is crucial, thus the chip-integration of all the oscillator presented in this subsection should be mainly imposed by the size of the capacitor, which can be large. The other point is that, as it was discussed for neuristor devices, for many of those oscillators, an estimation of the number of operation cycles is still required. In addition, the existing estimations do not take into account the mean number of operation cycles of a large number of such devices which can be quite small considering the device to device variabilities.

2.3.3 *CMOS ring oscillators*

In order to build a fully CMOS based oscillator computing device, CMOS ring oscillators are quite attractive. Those oscillators consist of an odd number of "NOT" logic gates connected to each other and forming a ring scheme, see Fig. 17 [5]. Due to parasitic capacitive effects in such kinds of circuits, each of these logic gates switches with a certain delay time. As a result the signal propagating through this CMOS ring circuit is oscillating. Due to the fact that this type of oscillator is based on fully-digital CMOS technology, it is quite convenient in CMOS integrated circuit requiring an oscillating signal.

The frequency of these oscillators can be tuned by modifying the time delay of the switching which can be achieved by changing an additional current entering in each logic gate (I_{ctrl}, see Fig. 18).

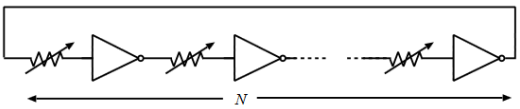

Figure 17: Schematic of a CMOS ring oscillator extracted from Retdian et al. [5].

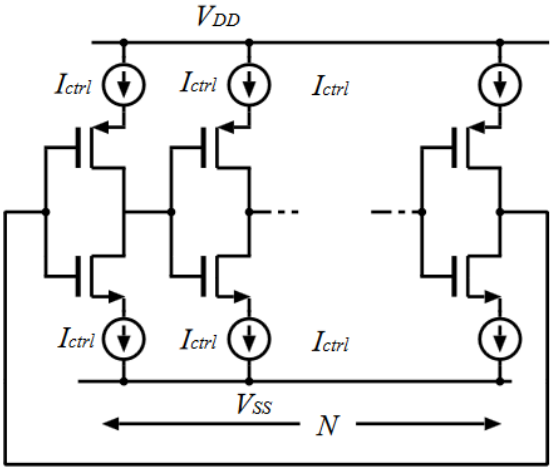

Figure 18: Schematic of the electrical circuit of a CMOS ring oscillator, for which the oscillation frequency can be tuned by modifying the current I_{ctrl}, extracted from Retdian et al. [5].

Through this technique, a single oscillator can have a large frequency tunability, as an example from 8 to 16 GHz [106]. In terms of energy efficiency some of them have relatively low power consumption of the order of 1.2 nW for a frequency of 1.49 GHz [107]. However they still occupy large areas (between $10^5 \mu m^2$ [106] and 40 μm^2). Synchronization of CMOS ring oscillators was demonstrated [106], and some models involving such kind of oscillators were proposed to build hetero-associative memory architectures [91], but still no physical implementation was reported.

2.3.4 *Electromechanical nano-oscillators*

Another important class of nano-scale oscillators are electromechanical oscillators used in nano-electromechanical systems (NEMS). These oscillators have a part that can oscillate mechanically in space. For read-out, mechanical oscillations are electrically measured through piezoelectric effects or electro-static interactions where a mechanical modification is converted into an electrical signal. Beyond the detection of an eventual oscillation, the read-out allows to actuate the mechanical motion of the NEMS cantilever. Without this feedback of the read-out, the cantilever behaves like a spring and thus cannot be seen as an auto-oscillator. For this reason this feed-back is essential to obtain auto-oscillations [108].

Fig. 19 shows the image of a NEMS cantilever with a co-integrated CMOS feedback circuitry, which implements an electromechancial auto-oscillator [6]. The read-out of the position of the cantilever is realized through the modification of the electrical capacitance between the cantilever and the electrode. The resulting electrical signal is amplified using a CMOS amplifier and then it actuates the cantilever through the electrostatic interaction. The presented NEMS device can reach mechanical frequency oscillations of the order of 8 MHz. The chip area occupied by the system was $50\times70\mu m^2$ which is still larger than the micrometer scale. Higher oscillation frequencies, as $f = 428$ MHz [7] with a high quality factor $Q = 2500$ were reported which make NEMS auto-oscillators quite attractive. The frequency of these oscillators can be tuned either by modifying dynamically the feed-back loop circuitry characteristics [109] or by modifying the stiffness of the moving part [110].

Several approaches propose to use NEMS for boolean computing, namely by implementing logic gates [111] or transistor switching devices [112] or by being implemented in memristive crossbar structures [113]. A hybrid NEMS-CMOS system was also proposed to emulate the LIF model of the neuron [114] (preliminary simulation work), for which a firing rate of 10 to 250 Hz was obtained. The energy consumption of such implementation was smaller than the one for a fully CMOS technology.

Interestingly, NEMS auto-oscillators are able to synchronize with each other using various coupling mechanisms, in particular through their mutual vibration corresponding to a mechanical coupling [115]. They can also synchronize through optical coupling [116]. In these cases, the coupling is a local mechanism involving neighboring NEMS oscillators. In addition, a global coupling solution based on electrical coupling [117], allows through an electrical circuitry to sum all the oscillating signals of the NEMS oscillators which are then sent back to each of them by actuating the mechanical oscillations. The nano-oscillators are attractive for computing, some preliminary simulation works propose hybrid CMOS-NEMS architectures to realize neuromorphic computing [114].

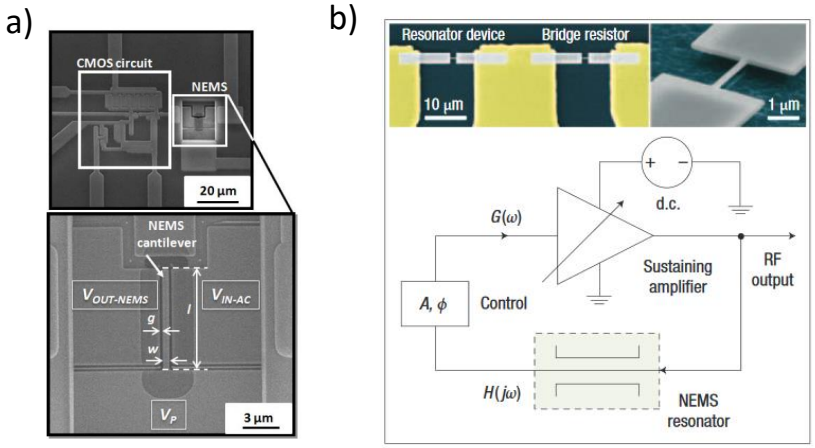

Figure 19: a) SEM image of the NEMS device and its CMOS circuit, extracted from Philippe et al. [6]. b) Image of the NEMS implementation including the feed-back loop, extracted from [7].

2.3.5 *Josephson junction nano-oscillators*

A Josephson junction is a junction made of two superconducting electrodes separated by a thin barrier which can be a thin insulating layer or a normal metal. When such a junction is voltage biased, an oscillating super-current is emitted. The frequency of this super-current

is defined as $f = \frac{V}{\phi_0}$ where $\phi_0 = 2.07mV/THz$ and V is the time averaged bias voltage across the Josephson junction [118]. By modifying the bias voltage, the frequency of this kind of nano-oscillator can be tuned from 100 kHz to 1 THz [119]. Interestingly, several Josephson junctions can electrically couple and synchronize to each other which allows to reduce considerably the frequency linewidth of the total emission of the array of Josephson junctions [120][121][122][123]. Since the observation of these synchonization phenomena, the nonlinear dynamics community became attracted to Josephson junctions [124] and applied the Kuramoto model to decribe its nonlinear dynamics. The size of such devices is often larger than the micrometer, however some studies shows that such Josephson junction based devices can scale down to the nanometer [125] which is attractive for circuit integration.

Recently, an experimental work [126] presents results where two Josephson junctions were used to emulate two coupled neurons. The energy per spike of such kind of Josephson neurons was evaluated to $10^{-17}J/spike$. Those results open interesting perspectives for neuronal computation and neuromorphic computing using Josephson junctions.

Despite of the presented advantages, unfortunately, Josephson junction nano-oscillators can not work at the room temperature. Even for high Tc superconductors with Tc=90K [127], a nitrogen based cooling system is still required. Nevertheless, they remain attractive for super-computing applications.

2.4 CONCLUSION

We have seen briefly in this chapter the main motivations of taking inspiration from the brain to realize computing devices. Nowadays, brain-inspired algorithms allow achieving complex cognitive tasks as pattern recognition. However, these powerful algorithms are still running on current sequential computers which have a very different architecture compared to the brain. In particular, the Von Neumann bottleneck is an important source of energy dissipation in these conventional computers. On the contrary, as we saw in the beginning of this chapter, the brain is a massively parallel architecture where

memory and processing are entangled in the form of neurons and synapses. This architecture difference can explain partly the relative low energy consumption of the brain compared to nowadays computers. For these reasons, brain-inspired computing is one the most promising approaches towards energy efficient computing. In this general context, one approach is to emulate the way neurons compute dynamically. For instance, these "computation" units of the brain can be seen as a nonlinear oscillators, and thus the brain as an assembly of nonlinear oscillators interconnected together by tunable connections. As a nonlinear dynamical system, the brain shows a large variety of nonlinear phenomena and in particular synchronization. This dynamical state which is believed to play an important role in memory processes of the brain, was leveraged by different computing models to realize various brain-inspired computing operations. Thus, the use of available oscillators able to synchronize to emulate neurons is an interesting approach. However, a major issue is the scalability of oscillator based architectures. Indeed, regarding the tremendous number of neurons and synapses in the brain, in order to build on-chip computing implementations, physical devices with a lateral size smaller than the micrometer are required to emulate those biological units. For this reason, nanometric oscillators called nano-oscillators are important for building such brain-inspired computing systems. For this purpose, several types of nano-oscillators available nowadays were presented at the end of this chapter. Despite of their suitable nanometric size for many applications, their low power consumption, the existing adapted computing models, and their demonstrated ability to synchronize, due to their high sensitivity to noise, no demonstration of neuromorphic computing at the nano-scale was reported with these nano-devices. In the next chapter, an exclusive focus will be given to magnetic nano-oscillators, more precisely to spin-torque nano-oscillators, through which first demonstrations of neuromorphic computing were established.

3

SPIN-TORQUE NANO-OSCILLATORS

In this chapter, I will present the theoretical and experimental state of the art of spin-torque nano-oscillators. The main physical phenomena behind spin-torque nano-oscillators, namely magnetoresistance and spin-transfer, will be presented. Those will allow to introduce the general concept of spin-torque nano-oscillator. Then, I will mainly focus on the dynamical response of these oscillators in presence of external stimuli, leading to the synchronization phenomenon which will be crucial in the neuromorphic approach presented in this thesis. Finally, the main potential application of spin-torque oscillators will be considered.

3.1 PHYSICAL PHENOMENA

Spin-torque nano-oscillators are spintronic devices. Spintronics, also called spin electronics, studies the influence of a quantum property of electrons, called spin, on transport properties in materials. To see this influence, ferromagnetic materials were intensively studied since Mott (1936)[128]. These materials provide the core foundation of spintronic devices. In order to understand the physical principle of spin-torque nano-oscillators, two important phenomena should be highlighted: magnetoresistance and spin-transfer. To understand how ferromagnetic materials give rise to these two phenomena, the electronic transport in ferromagnets is presented in the following.

3.1.1 *Electronic transport in ferromagnets*

In ferromagnetic materials, electrons contributing to the local magnetization, are separated in two categories of population, according to their spin state: a majority of spin states having a magnetic momentum parallel to the local magnetization of the ferromagnet, called majority spins, and a minority spin states having a magnetic mo-

mentum antiparallel to this magnetization, called minority spins. By convention these two populations will be respectively referred to as spins ↑ and ↓. At room temperature, two main classes of materials present ferromagnetic behavior: 3d transition metals and 4f rare earths. Due to the high electrical resistance and presence of localized conduction electrons, 4f rare earths are less used in spintronic devices and are mainly found in permanent magnets [129].

Importantly, 3d transition metals and their alloys, such as Co, Ni or Fe, combine excellent transport property and ferromagnetic behavior at room temperature, enabling their wide use for spintronic devices. At the Fermi level, 3d-transition metals possess an electronic structure with two kinds of conduction band-shells: 4s and 3d. Fig. 20-a corresponds to the electronic band structure of these materials having a high magnetization, such as Nickel or Cobalt. The 4s electrons are mainly non localized in the material and they have a band structure close to the one of classical metals. The electrical conduction in this material is mainly due to the 4s electrons while the ferromagnetism comes from the electrons of the 3d band.

In these materials, the exchange interaction encourages electrons to have the same spin direction as their neighbors. Therefore, the energy of an electron having its spin aligned with the local spin, will be smaller than the one which will be opposite to it. This induces an energy splitting of the 3d conduction shell into two energetically shifted sub-shells 3d↑ and 3d↓ (see Fig. 20-a). An asymmetry of the number of electrons of spin ↑ and ↓ is thus observed leading to different density of states at the Fermi level: $D_{\uparrow}(E_F) \neq D_{\downarrow}(E_F)$.

In the corresponding electronic band structure, one can see an overlap of 3d and 4s bands. Due to this overlap, when 4s electron charge carriers pass through the metal, they are scattered by the 3d localized states having the same energy and spin orientation. The difference of the density of state at the Fermi level implies a different scattering probability depending on the spin orientation. As an example in Fig. 20-a , the Fermi level is higher in terms of energy than the 3d↑ sub-shell. Therefore, in absence of localized d-band electrons, the 4s↑ conduction electrons are not scattered. While, on the contrary 4s↓ con-

duction electrons are scattered because 3d↓ electrons are still present at the Fermi level. At the end, considering these scattering processes, the resistivity of electrons ↓ is higher than electrons ↑: $r_\downarrow > r_\uparrow$. Therefore, the conductivity of the ferromagnetic material is spin dependent and can be described as two separate parallel conductive channels with different resistance ↑ and ↓ (see Fig. 20-b). This circuit model is often called the "two-currents" model used by Fert and Campbell [130]. In this case, the total resistivity r of the ferromagnetic material can be expressed as follows:

$$r = \frac{r_\uparrow r_\downarrow}{r_\uparrow + r_\downarrow} \tag{1}$$

However thermal fluctuations and defects in the metal can induce spin-flips, and therefore an additional term $r_{\uparrow\downarrow}$ should be taken into account.

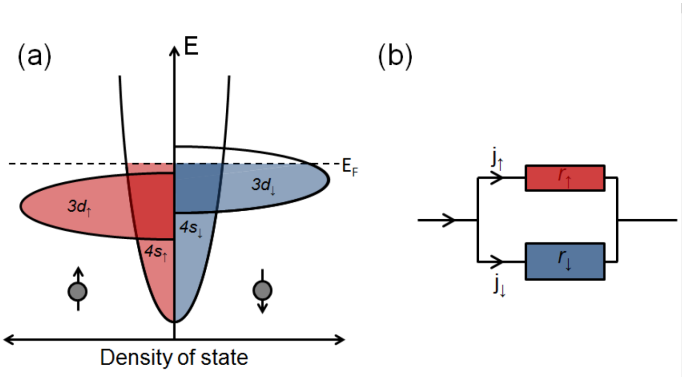

Figure 20: Figure extracted from [8]. a) Illustration of the electronic band structure of a 3d transition metal as Co or Ni. b) Equivalent conduction circuit representing the "two-currents" model.

To summarize, the resistivity of ferromagnetic materials based on 3d transition metals depends on the spin orientation of 4s conduction electrons. This leads to the "two-currents" model presenting two different resistivity channels for majority ↑ and minority spins ↓.

3.1.2 *Magnetoresistance effect*

One important consequence of the the spin dependent transport in ferromagnetic materials, presented in the previous subsection, is

the magnetoresistance effect. This effect was observed and studied in spin-valves having the following kind of stack structure: Ferromagnetic FM1/Non-magnetic/Ferromagnetic FM2 multi-layers.

If the non-magnetic layer is conductive, the structure is often called a metallic spin-valve, while if it is an insulating one, the structure is called a magnetic tunnel junction (MTJ). Depending on the direction of the injected current, with respect to the plane of layers in these structures, two different types of transport can be distinguished: current in the plane (CIP) or current perpendicular to the plane (CPP). In this thesis, the studied spin-torque nano-oscillators used for the neuromorphic operations will all have a magnetic tunnel junction MTJ structure and the current will be injected perpendicularly to the plane (CPP).

3.1.2.1 *Physical insight of Giant Magnetoresistance*

In magnetic multi-layers, the magnetoresistance effect was first explored in metallic spin-valves. This led to the discovery of the Giant magnetoresistance GMR effect by Fert and Grunberg [131][132].

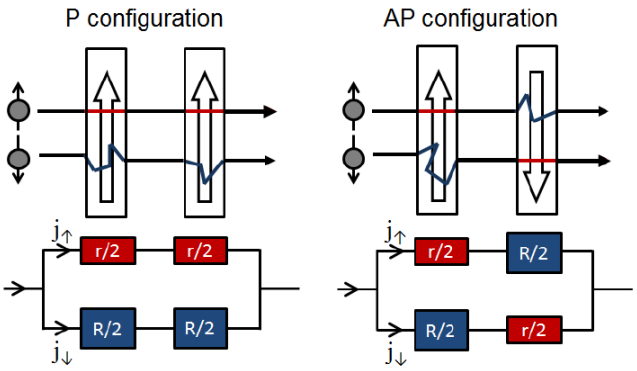

Figure 21: Figure extracted from [8]. Illustration of the "two-currents" model applied to a spin-valve.

Fig. 21 shows the equivalent resistance circuit depicting scattering of electrons in a spin-valve composed of two ferromagnetic layers separated by a metallic spacer. In order to simplify the transport description, one can neglect the scattering of electrons in the metallic

spacer, and assume that electrons stay half of their trajectory inside of one of the two ferromagnetic layers. Therefore, the two currents model presented in the previous subsection can be applied to this magnetoresistive device. Here we define the resistance of majority spin channel as $\frac{R}{2}$ and the resistance of of minority spin channel as $\frac{r}{2}$. As seen in the previous subsection, the resistance of the majority spin channel will be larger than the one for minority spins: $R > r$.

In the parallel P configuration $\uparrow\uparrow$, the magnetizations of the two magnetic layers are pointing in the same direction. Electrons passing through the multi-layer have the same spin (majority or minority) in the two ferromagnets. Therefore, one conduction electron has either a majority spin or either a minority spin in both ferromagnets. The total resistance of the multi-layer can be expressed as follows:

$$R_p = \frac{Rr}{R+r} \tag{2}$$

In the antiparallel AP configuration $\uparrow\downarrow$, the magnetization of the two layers are pointing in opposite directions. Electrons passing through the multi-layer do not have the same spin (majority or minority) in the two ferromagnets. Therefore, one conduction electron has a majority spin in one ferromagnet and has a minority spin in the other ferromagnet. The total resistance of the multi-layer can be expressed as follows:

$$R_{ap} = \frac{R+r}{4}. \tag{3}$$

The difference of resistance between the parallel and antiparallel configurations corresponds to the giant magnetoresistance GMR effect characterized by the following ratio:

$$GMR = \frac{R_{ap} - R_p}{R_p} = \frac{(R-r)^2}{4Rr} \tag{4}$$

In a more general case (intermediate configuration between AP and P configuration), where the magnetizations of the two ferromagnetic layers are noncollinear, the resistance of the magnetoresistive device

will depend on the relative angle between the two magnetizations θ [133][134]:

$$R = R_p[1 + \frac{GMR}{2}(1 - cos\theta)] \tag{5}$$

The "two-currents" model applied to a spin valve gives a physical insight in the magnetoresistive effect, but in order to take into account the effect of temperature and materials defects, one should consider the Valet-Fert [135] model, including spin diffusion and accumulation effects at the interfaces of the magnetic layers.

3.1.2.2 *Magnetoresistance in magnetic tunnel junction: tunnel magnetoresistance*

In magnetic tunnel junctions, where the non magnetic spacer is an insulating material, electrons are tunnel from one ferromagnetic layer to the other one. As for the classical electron conduction, described in the previous subsection, this tunneling process is spin dependent. As for metallic spin valves, the "two-currents" model can give a physical insight, but is not satisfactory to describe the magnetoresistance effects in magnetic tunnel junctions. In 1975, Jullière proposed a model [136], which assumes that the spin is conserved during the tunneling process, and that the tunneling probability of the electron is proportional to the product of the density of states at the Fermi level of either sides of the tunneling barrier (Fermi golden rule). Therefore, tunneling is achieved through two different spin-dependent channels. Fig. 22 illustrates these two tunneling channels in parallel and antiparallel configurations. The red and blue horizontal segments represent the density of states at the Fermi level respectively for majority $D_{\uparrow}(E_F)$ and minority $D_{\downarrow}(E_F)$ spins. The relative size of these segments helps to see that the density of states of majority and minority spins are not the same due to the energy shift of the two sub-shells. In the parallel configuration, majority spins tunnel to majority spin states and respectively for minority spins. Therefore, the conductance in this situation can be expressed as follows:

$$G_P \propto \ D^1_{\uparrow}(E_F)D^2_{\uparrow}(E_F) + D^1_{\downarrow}(E_F)D^2_{\downarrow}(E_F) \tag{6}$$

On the contrary, in the antiparallel configuration, majority spins tunnel to the minority states and respectively minority spins to majority

states. Therefore, the conductance in this situation can be expressed as follows:

$$G_{AP} \propto \; D^1_{\uparrow}(E_F)D^2_{\downarrow}(E_F) + D^1_{\downarrow}(E_F)D^2_{\uparrow}(E_F) \tag{7}$$

Again, as for the "two-currents" model, the difference of conductance between the parallel and antiparallel configurations $G_{AP} \neq G_P$, arises from the the difference of the density of states at the Fermi level in the two ferromagnetic layers for majority and minority spins: $D_{\uparrow}(E_F) \neq D_{\downarrow}(E_F)$. Jullière defined a spin polarization variable $\mathcal{P}_i$ at each ferromagnet i (i =1, 2) which is used to evaluate the tunnel magnetoresistance ratio TMR:

$$\mathcal{P}_i = \frac{D^i_{\uparrow}(E_F) - D^i_{\downarrow}(E_F)}{D^i_{\uparrow}(E_F) + D^i_{\downarrow}(E_F)} \tag{8}$$

$$TMR = \frac{R_{ap} - R_p}{R_p} = \frac{2\mathcal{P}_1\mathcal{P}_2}{1 - \mathcal{P}_1\mathcal{P}_2} \tag{9}$$

This simple model was used too evaluate the TMR ratio of Fe/Ge/Co magnetic tunnel junction which was of the order of 10% [136].

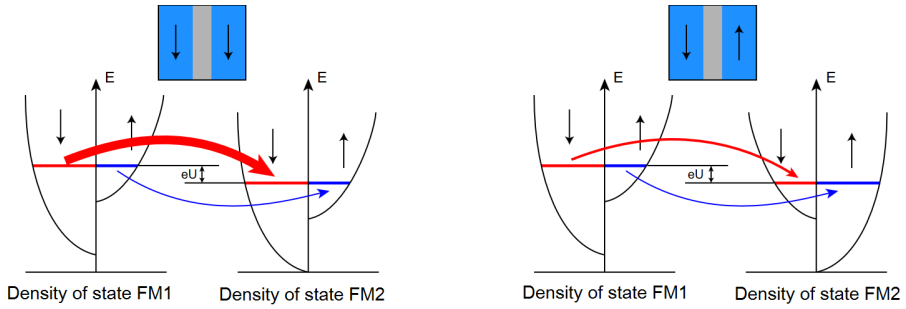

Figure 22: Figure extracted from [9]. Principle of the tunneling process in two different configurations: parallel and antiparallel. This schematic illustrates the Jullière model. Thicker arrows signifies a higher probability to tunnel.

A more precise model was proposed by Slonczewski in 1989 [137] assuming two identical ferromagnetic layers separated by an insulating barrier. This model was obtained by solving the Schrödinger equation considering a rectangular potential shape barrier with an energy height

higher that the Fermi level. In this approach, the spin polarization depends on the wave vectors of majority spins $k_\uparrow$ and minority spins $k_\downarrow$ and, interestingly, also on the exponential attenuation of evanescent states $\propto exp(-2\kappa d)$ in the barrier where κ depends on the energy height of the barrier and d is the spatial distance from the barrier. For this reason, the size of the barrier should be as small as possible to minimize the attenuation κ. According to this model the spin polarization is defined as follows:

$$P_i = \frac{k_\uparrow^i - k_\downarrow^i}{k_\uparrow^i + k_\downarrow^i} \frac{\kappa^2 - k_\uparrow^i k_\downarrow^i}{\kappa^2 + k_\uparrow^i k_\downarrow^i} \tag{10}$$

Considering this definition for the polarization, similarly to Eq. 5, the conductance of the MTJ can be expressed as a function of the relative angle between the magnetization of the two ferromagnetic layers θ and the mean conduction of the MTJ called G_0:

$$G = G_0[1 + P_1 P_2(1 + cos\theta)] \tag{11}$$

For the TMR ratio, the same definition than the one for the Jullière model Eq. 9 holds, if the spin polarizations are replaced by their new expressions.

Experimentally, in first magnetic tunnel junctions based on amorphous aluminum oxide insulating layer, the highest TMR value found at room temperature was around 70% [138][139][140]. In 2004, the first MTJs with epitaxial MgO insulating barriers(Fe/MgO/CoFe) were fabricated by Yuasa[141] and Parkin[142]. Besides the height and width of the insulating barrier, the TMR ratio of these MTJs was improved due to the nature of the barrier, which became crystalline, and also due to crystalline orientation considerations at the interface [143]. Indeed in this crystalline MgO barriers, a filtering mechanism due to the coupling between the ferromagnetic Bloch states and evanescent states, occurs at the interface. This causes a faster decay of tunneled minority spins due to this coupling and as a consequence, a higher spin polarization and TMR of the MTJ. The magnetoresistance ratio can be relatively large compared to first generation of MTJs and also compared to metallic spin-valves having a GMR ratio ranging between 1% and 10% [144][145][146]. As an example in 2008, for CoFeB/MgO/CoFeB MTJs, TMR reached 600% at room temperature [147].

3.1.3 *Spin-transfer torques: Slonczewski and field-like torques*

The magnetoresistance effect presented in the previous subsection shows that the orientation of magnetization modifies the amount of electric current flow. Inversely, a spin polarized current can modify the orientation of the magnetization. Detailed reviews on spin transfer torques by Stiles, Miltat and Ralph can be found in [10][148].

In 1978, the spin-transfer torque was first predicted by Berger [149] and was experimentally investigated later to move magnetic domain walls [150][151] in large magnetic devices, which required high applied currents (45 A). The interest in spin-transfer torque was relaunched in 1996, in the case of CPP metallic spin-valve multi-layers, where Slonczewski [152] and Berger [153] independently predicted that by applying a sufficiently high current, a high enough spin-transfer torque can modify the direction of magnetization of one of the layers.

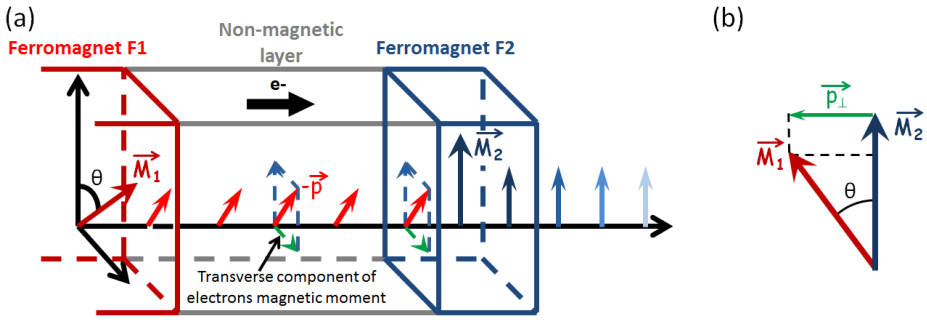

Figure 23: a) Principle of spin-transfer torque in a spin-valve multi-layer structure. b) The transverse component of the magnetic current is transfered to the local magnetization of the second ferromagnet. Figure extracted from [8].

Fig. 23-a shows the principle of spin-transfer torque in thin FM1/NM/FM2 spin-valve multi-layer in a CPP configuration, where the applied dc current is injected perpendicularly to the layers. As represented in this figure, the first ferromagnetic layer F1 is thick while the second ferromagnetic layer F2 is thin. Thus, F1 plays the role a fixed spin polarizing layer and F2 has a free magnetization which is sensitive

to the injection of external spin current. As presented previously, the non magnetic layer can be metallic or an insulating barrier. The non collinear magnetizations of the two ferromagnetic layers $\overrightarrow{M_1}$ and $\overrightarrow{M_2}$ form an angle θ. The initial injected dc current becomes spin-polarized by passing through the first ferromagnetic layer F1 (see 3.1.1 for more details). The electrons of this spin-current carry a magnetic moment aligned with $\overrightarrow{M_1}$. Then, this spin polarized current passes through the nonmagnetic layer (through metallic transport or tunneling) and eventually is injected in the second ferromagnetic layer F2.

Since the magnetizations $\overrightarrow{M_1}$ and $\overrightarrow{M_2}$ are non colinear, the magnetic moment carried by the spin polarized current in the non-magnetic layer has a transverse component to $\overrightarrow{M_2}$. This transverse component is referred to as $\overrightarrow{p_\perp}$ in Fig. 23-b. By passing through F2, the electrons of the spin polarized current modify the direction of the magnetic moment they carry and align it along $\overrightarrow{M_2}$. As a consequence, they lose their initial transverse component $\overrightarrow{p_\perp}$. Due to the conservation of angular momentum, this lost $\overrightarrow{p_\perp}$ is transferred to the local magnetization of the ferromagnet F2 which can be seen as a torque acting on the magnetization $\overrightarrow{M_2}$. This torque is referred to as the spin-transfer torque $\overrightarrow{T} \propto \overrightarrow{p_\perp} = \overrightarrow{M_2} \times (\overrightarrow{M_2} \times \overrightarrow{M_1})$.

This simple description of the spin-transfer phenomenon gives an intuitive insight, however is not fully satisfactory for experimental spin-torque observations, in particular it can not predict an additional torque called field-like torque observed in experiments (as will be discussed in the following). In reality, there are strong evidences that spin-transfer torque is an interfacial effect [154][155]. Thus, at the NM/FM2 interface, for an incident spin polarized current I_{inc}, one should consider both spin polarized currents which are transmitted I_{trans}, and reflected I_{refl} (See Fig. 24).

In a case where there is no action of the spin polarized current on the local magnetization, the transmitted component is exactly equal to the sum of the incident and reflected ones ($\overrightarrow{I_{refl}} + \overrightarrow{I_{inc}} = \overrightarrow{I_{trans}}$). In a case where the spin polarized current acts on the local magnetization, this equality is not valid. Due to the conservation of angular momentum, a spin-transfer torque is transferred to the local magnetization. Thus, the spin-transfer torque is expressed as $\overrightarrow{T} = \overrightarrow{I_{refl}} + \overrightarrow{I_{inc}} - \overrightarrow{I_{trans}}$[10].

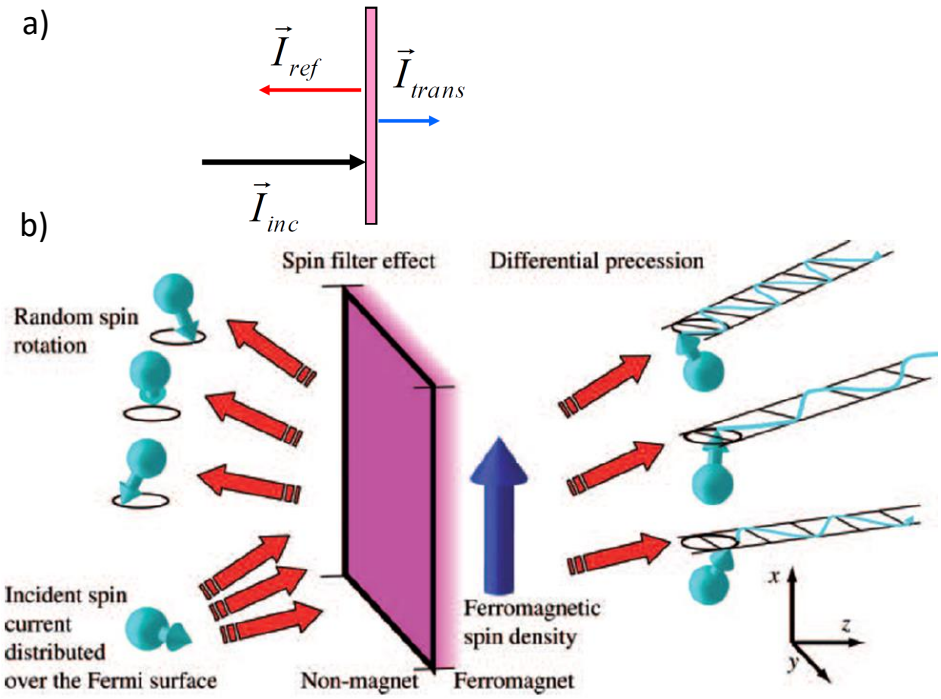

Figure 24: a) Principle of reflection and transmission phenomena of an incident spin-polarized current at an NM/M interface. b) Schematic of mechanisms occurring at the interface. In the lower left corner, the incident spin polarized current is represented with electrons having the same spin state which is transverse to the direction of the magnetization of the ferromagnetic layer. These electrons come with different random incident direction (here represented as having three different incident directions). In the top left corner, the reflected spins are distributed over many directions. In the right corner, the transmitted electron spins are precessing as a function of their distance from the interface. Figure extracted from [10].

In order to have a spin-polarized current exerting a torque on the magnetization $\overrightarrow{M_2}$ of the free-layer, this one should not be collinear to the magnetization $\overrightarrow{M_1}$. Therefore only the perpendicular components of the spin polarized current will contribute to the spin-transfer torque, $\overrightarrow{T} = \overrightarrow{I^{\perp}_{inc}} + \overrightarrow{I^{\perp}_{refl}} - \overrightarrow{I^{\perp}_{trans}}$.

Due to different mechanisms affecting the spin polarized currents at the interface, the spin-transfer torque quantity does not cancel out. A first mechanism called "spin precession" allows the complete absorption of the perpendicular transmitted component $< \overrightarrow{I^{\perp}_{trans}} > \approx 0$ if FM2 is thick enough. Indeed, when the transmitted electron enter in the ferromagnetic material, they precess spatially around the effective field caused by the energy splitting between majority and minority spins ($k_{\uparrow} \neq k_{\downarrow}$). Due to this precession, over all transmitted electrons, which travel various distances in the material, the total transmitted spin current average out after few lattice parameter penetration $< \overrightarrow{I^{\perp}_{trans}} > \approx 0$.

Through a second mechanism refereed as "spin rotation" which is here a quantum mechanical phenomenon, the perpendicular reflected component $< \overrightarrow{I^{\perp}_{refl}} >$ is affected. Depending on the spin propagation direction of the incident electron spin, the reflected electron rotates its spin. In metallic junctions, due to this spin rotation, over all reflected electrons, the total reflected spin current average out $< \overrightarrow{I^{\perp}_{refl}} > \approx 0$. However, in magnetic tunnel junctions this quantity is not negligible $< \overrightarrow{I^{\perp}_{refl}} > \neq 0$, mainly because the transport is realized through tunneling electrons which are mostly propagating perpendicularly to the barrier. This imposes a smaller propagation dispersion and therefore a reduced spin dephasing for reflected electrons. Finally the net spin-torque in magnetic tunnel junctions is expressed as follows:

$$< \overrightarrow{I} > \approx < \overrightarrow{I^{\perp}_{inc}} > + < \overrightarrow{I^{\perp}_{refl}} > \tag{12}$$

The incident component contributes to a spin-torque acting in the $(\overrightarrow{m}, \overrightarrow{p})$ plane, where $\overrightarrow{m}$ and $\overrightarrow{p}$ are respectively the unit vectors defining the direction of the local magnetization $\overrightarrow{M}$ and the transverse component $\overrightarrow{p_{\perp}}$. This spin-torque is referred to as the in-plane torque or more commonly as the Slonczewski torque $\overrightarrow{\Gamma_{Slonc}}$, which is similar to the intuitive vision initially presented at the beginning of this section.

$$\overrightarrow{I}_{Slonc} = \gamma_{Slonc} \overrightarrow{m} \times (\overrightarrow{m} \times \overrightarrow{p}) \tag{13}$$

The reflected component gives rise to a torque which is perpendicular to the $(\overrightarrow{m}, \overrightarrow{p})$ plane, referred to as the out-of-plane torque or field-like torque $\overrightarrow{\Gamma_{fl}}$:

$$\overrightarrow{\Gamma}_{fl} = \gamma_{fl}(\overrightarrow{m} \times \overrightarrow{p}) \tag{14}$$

The efficiency of spin-transfer torque depends on the applied voltage [156][157] and asymmetry of electrodes [158] of the magnetic tunnel junction. In order to take into account the action of the two aforementioned spin-transfer torques in spin-torque nano-oscillators studied in this thesis, we assume the following expressions at low applied bias voltages [159][160]:

$$\gamma_{Slonc} = a_j J M_s \qquad \gamma_{fl} = b_j J M_s \tag{15}$$

Where J is the applied charge current density, M_s is the saturation magnetization of the free-layer of the tunnel junction, a_j and b_j are respectively the Slonczewski and field-like torque efficiencies. Those efficiencies are expressed as following [159][160]:

$$a_j = \frac{|g|\mu_B}{2|e|}\frac{\mathcal{P}}{LM_s} \qquad b_j = r_{fl}a_j \tag{16}$$

Here $|g|$ is the Lande factor, μ_B is the Bohr magneton, $|e|$ is the elementary charge, $\mathcal{P}$ is the spin polarization of the junction (see previous section), L is the thickness of the free-layer and r_{fl} is a fixed constant that varies between 0.1 and 0.4 in magnetic tunnel junctions [154][161][162].

3.2 Magnetization dynamics and spin-torque nano-oscillators

3.2.1 *Landau-Lifshitz-Gilbert equation*

The spin-transfer torque phenomena introduced in previous subsection modifies the magnetization dynamics. Here we introduce the differential equation which describes the magnetization dynamics. In the absence of spin-transfer effect, in a case where the magnetic configuration is away from equilibrium, the magnetization precesses around the local field $\overrightarrow{H}_{eff}$ of the magnetic material. In order to describe this

magnetization precession, Landau and Lifshitz proposed an equation of motion in 1935 [163], which includes a phenomenological damping term. Later in 1955, Gilbert introduced a different variant [164] that gave rise to the Landau-Lifshitz-Gilbert (LLG) equation:

$$\frac{d\overrightarrow{m}}{dt} = -\gamma_0 \overrightarrow{m} \times \overrightarrow{H}_{eff} + \alpha \overrightarrow{m} \times \frac{d\overrightarrow{m}}{dt} \tag{17}$$

Here γ_0 is defined as $\gamma_0 = \mu_0 \gamma$ where μ_0 is the magnetic constant or the permeability of free space, and γ is the gyromagnetic ratio of the free-electron. α is the phenomenological Gilbert damping coefficient which corresponds to the energy dissipation of the magnetic system. This coefficient can be assimilated to a frictional coefficient and varies from one magnetic material to another (α_{NiFe} ≈0.007-0.008, α_{FeB} ≈0.01 [165]). More details about the origin of this damping can be found in [166][167]. In order to take into account the effect of spin-transfer on the magnetization dynamics, the spin-transfer torque is simply added to the right hand side of the LLG equation 17:

$$\frac{d\overrightarrow{m}}{dt} = -\gamma_0 \overrightarrow{m} \times \overrightarrow{H}_{eff} + \alpha \overrightarrow{m} \times \frac{d\overrightarrow{m}}{dt} - \gamma_{Slonc} \overrightarrow{m} \times (\overrightarrow{m} \times \overrightarrow{p}) - \gamma_{fl} (\overrightarrow{m} \times \overrightarrow{p}) \tag{18}$$

The field-like torque can be seen as a local field $\overrightarrow{H_{fl}} = \frac{\gamma_{fl}}{\gamma_0} \overrightarrow{p}$ that can be contained in the expression of a modified effective field [8]. Thus, the equation 18 can be simplified as following:

$$\frac{d\overrightarrow{m}}{dt} = -\gamma_0 \overrightarrow{m} \times (\overrightarrow{H}_{eff} + \overrightarrow{H_{fl}}) + \alpha \overrightarrow{m} \times \frac{d\overrightarrow{m}}{dt} - \gamma_{Slonc} \overrightarrow{m} \times (\overrightarrow{m} \times \overrightarrow{p}) \tag{19}$$

In order to emphasize the role of the Slonczewski torque on the magnetization dynamics, one can assume that the spin polarization vector $\overrightarrow{p} = \frac{1}{||\overrightarrow{H_{eff}}||} \overrightarrow{H_{eff}}$ is collinear with the effective field and that the field-like torque do not contribute to the magnetization dynamics $\gamma_{fl} = 0$. Thus, as α is small [168], by neglecting terms in α^2, one can rewrite the LLG equation as the following:

$$-\frac{1}{\gamma_0} \frac{d\overrightarrow{m}}{dt} = \overrightarrow{m} \times \overrightarrow{H}_{eff} + \widetilde{\alpha} \overrightarrow{m} \times (\overrightarrow{m} \times \overrightarrow{H}_{eff}) \tag{20}$$

Where, we define the effective damping (using Eq. 15):

$$\widetilde{\alpha} = \alpha + \frac{\gamma_{Slonc}}{\gamma_0 ||\overrightarrow{H}_{eff}||} = \alpha + \frac{a_j M_s}{\gamma_0 ||\overrightarrow{H}_{eff}||} J \tag{21}$$

From this effective damping term definition, we see that the spin-transfer torque due to the Slonczewski torque can be seen as an extra-term added to the damping. Depending on the sign of the applied charge current J this term is an extra-damping ($J > 0$) or an anti-damping ($J < 0$) term. In particular, for a sufficiently large applied current, the spin-torque compensates the damping term and therefore the effective damping can be zero ($\widetilde{\alpha} = 0$). In Fig. 25 the

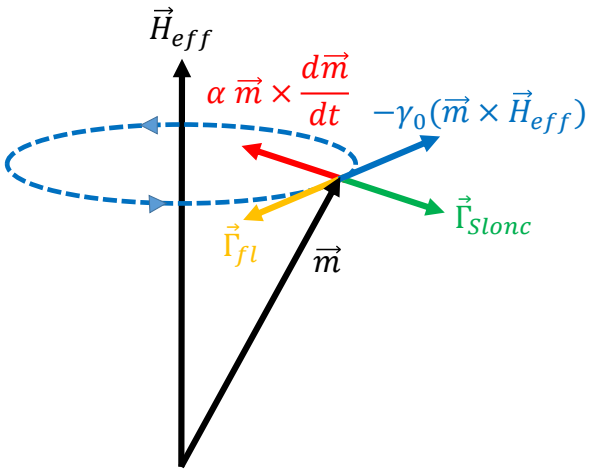

Figure 25: Schematic showing the torques acting on the local magnetization in presence of an effective magnetic field. The red arrow represents the damping which tries to bring back the magnetization along the effective field. The blue arrow corresponds to the magnetization precession around the effective field. The green and orange arrows correspond respectively to the Slonczewski and field-like torques.

action of the Slonczewski torque exerting on the magnetization $\overrightarrow{m}$ for $J < 0$ is presented. In this situation, the Slonczewski torque is against the natural damping. For sufficiently high applied current, the initial stable equilibrium determined by the effective field becomes unstable. Depending on the shape of the potential energy, two situations can occur: either it leads to a new stable static equilibrium or to steady

initial magnetization oscillations around the equilibrium. The first case is refereed to as magnetization switching and the second case as sustained magnetization oscillations which plays a key role in spin-torque nano-oscillators (see next section).

3.2.2 *Principle of spin-torque nano-oscillators and brief history*

The spin-torque nano-oscillator concept was born from the combination of spin-transfer and magnetoresistance phenomena. This spintronic device generates electrical oscillations when a dc current is applied to it. Spin-torque nano-oscillators can be seen as spin valve FM1/NM/FM2 magnetic structures (metallic spin valve or a magnetic tunnel junction). As seen in the previous sections, the two magnetic layers do not play the same role, one is required to obtain a spin-polarized current and is refereed to as a fixed or pinned layer because its magnetization is fixed in one direction, while the other one refereed to as the free-layer can easily modify its magnetization direction. By choosing adequate thicknesses and magnetic materials, one can control the magnetization of both these layers. As an example, often at the begining of the development of spin-torque oscillators, the thickness of the fixed layer was larger than the one of the free-layer. Indeed, the larger is the volume of the magnetic layer, the higher is the current density needed to modify its magnetization through the spin-torque. On the contrary, for low thicknesses of the free-layer, smaller current density can easily modify the magnetization of the free-layer and destabilizes it. Beyond this thickness consideration, strong developments were also focused on the choice of magnetic stack materials allowing a control of the magnetization of the layers. A very common approach is to use a synthetic antiferromagnet structure (SAF). This approach which was used in the structure of samples measured in this thesis, corresponds to an AF/F1/M/F2 stack structure where AF is an antiferromagnetic layer (PtMn), F1 and F2 are two ferromagnetic layers separated by a thin metallic layer(Ru). Due to a bias exchange interaction between AF and F1, the magnetization of F1 is pinned in one direction. One second interaction called RKKY (Ruderman-Kittel-Kasuya-Yosida [169]) is established between the two F1 and F2 ferromagnetic layers. By accurately choosing the thickness of the metallic layer, this RKKY interaction leads to a situation where the

magnetization of the ferromagnetic layers (F1 and F2) are coupled in opposite directions. Here, the upper ferromagnetic layer F2 corresponds to the fixed layer. Due to the strong interactions with the magnetization of lower magnetic layers, the magnetization of F2 can not be easily modified, meaning that strong applied magnetic field will be required for this modification. The (F1/M/F2) structure which can be seen as a bilayer antiferromagnet and is referred as the synthetic antiferromagnet structure (SAF), it allows to mutually cancel the dipolar field radiated by F1 and F2. Thus, the free-layer will not be strongly affected by the very small stray field generated by the lower magnetic layers.

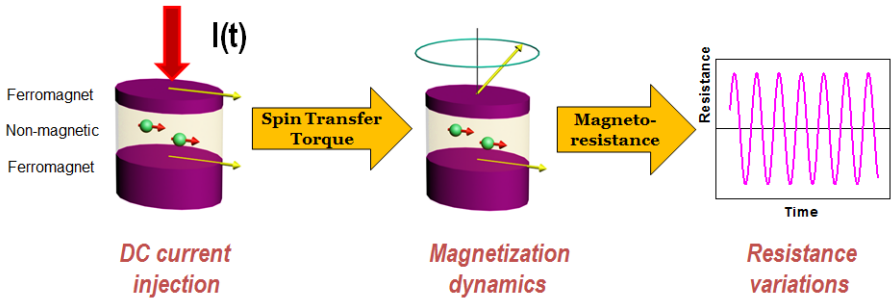

Figure 26: Principle of a spin-torque nano-oscillator. An applied dc current is injected through the magnetic structure. The electrons of this current become spin-polarized following the direction of the polarizing layer (the thick one). This spin-polarized current applies a spin-transfer torque on the magnetization of the free layer (the thin one) which can lead to sustained precession. Due to the magnetoresistance effect (GMR or TMR), those oscillations are converted into oscillations of electrical resistance.

Fig. 26 shows the working principle of spin-torque nano-oscillators. When an applied dc current is injected to this structure, its electrons becomes spin polarized following the magnetization of the polarizer (FM1). Then, this spin-polarized current interacts with the free-layer (FM2) and exerts a spin-transfer torque (see section 3.1.3) on its magnetization. As shown in the previous section, for particular conditions of applied dc current and applied magnetic field, this spin-transfer torque leads to sustained oscillation of the free-layer magnetization. During these oscillations, the relative angle between the magnetization of the free-layer and the fixed layer varies. Due to the magnetoresis-

tance effect (GMR or TMR, see section 3.1.2.2), this variation of the relative angle induces a modification of the electrical resistance of the magnetic structure. In this way, one can measure an oscillating voltage across the two terminals of the device. Therefore, a spin-torque nano-oscillator converts an applied dc current into an electrical ac signal. As we will see later, the frequency of these oscillations depends on the applied dc current and on the applied magnetic field.

The development of spin-torque nano-oscillators occurred with several distinct geometries: nano-pillar, nano-contact and hybrid geometries. Those geometries presented in Fig. 27 allow to induce a sufficiently high current density necessary to reach local magnetization precession. In the nano-pillar geometry the entire structure is etched during fabrication. Different techniques are used to fabricate nano-pillars such as electron beam lithography and ion-milling [170] or electrodeposition [171] or other techniques [172]. The typical size of nano-pillars is between 100 and 500 nm. In a nano-contact geometry, the applied current is injected in spatially expanded multilayers. The contact can be realized using a sharp mechanical contact, where the dimension of the nano-contact can reach 10 nm [173]. Nano-contacts can be also fabricated using lithography techniques, in this case the size of the nano-contact is of the order 100 nm [174][175]. For more details, one can read [176]. In addition, in the hybrid geometry, one magnetic layer is spatially extended (as for nano-contact geometry) while the other one is etched (as for nano-pillar geometry).

First experimental indirect observations of magnetization dynamics due to spin-torque were realized in 1998 by Tsoi et al. [173]. However, first direct experimental observation of magnetic oscillations were done in 2003 by Kiselev et al. [177] for nano-pillar geometry and in 2004 by Rippard et al [178][179] in point contact geometry. The electrical power of the observed oscillations were very small, of the order 100 pW, mainly because those first implementations were metallic spin valve structures (respectively Cu/Co, CoFe/NiFe) with a low GMR$\approx$ 1%. Later, due to the higher TMR (10% to 100%) ratio obtained by replacing the non-magnetic metallic layer by an insulting one (MgO), the power of oscillations increased reaching up to 10 nW [180] and 40 nW [181]. Since the early days of spin-torque oscillators,

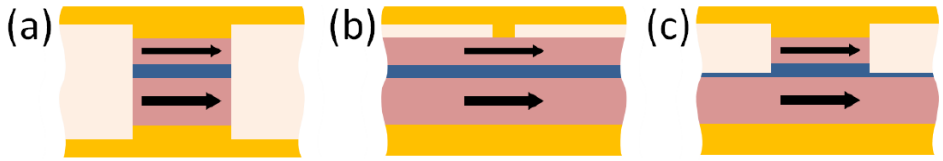

Figure 27: Different geometries of spin-torque nano-oscillators. Thick and thin arrows correspond respectively to the magnetization of the reference and free layers. Figure extracted from [11]. The yellow regions correspond to the metallic electrodes bringing the electrical current. The burgundy regions correspond to the magnetic layers. The dark blue region corresponds to the spacer (metallic or insulating). The white regions correspond to insulating materials surrounding the spin-torque nano-oscillator. a) nano-pillar geometry. b) nano-contact geometry. c) hybrid geometry.

in order to reach the performances of standard oscillators (for instance out-put power of the order of 1 mW for VCOs [182]) and also to improve the signal to noise ratio for their detection, the development of spin-torque oscillators were pushed to increase their out-put power.

In 2014, the power of oscillations of spin-torque nano-oscillators based on MgO magnetic tunnel junction structures continued to increase and reached $3.6\mu W$ with a high quality factor (a maximum of Q=6400 for an oscillation power of 1.4 μW) [183]. Recently an oscillation power higher than 10 μW was reported in 2016 [184]. Fig. 28 shows the evolution of the output power of spin-torque oscillators since 2003. As a general view, for highest output power devices, one can see an exponential increase of the output power as a function of recent decades (+3 dBm/year).

One other important direction for spin-torque oscillators was the improvement of their spectral coherence. For this reason, spin-torque oscillators with a vortex magnetization distribution in their free-layer were extensively studied. First spin-torque vortex oscillator was proposed in 2007 by Pufall et al.[185] in point-contacts. After the concept was extended to MgO based magnetic tunnel junctions [186][183]. Using these vortex based oscillators, in 2016, a frequency linewidth of 116 kHz was reported [184] which is much smaller than the ones

Table 1: Comparison between different spin-torque nano-oscillators. NP, NC, and V correspond respectively to nano-pillar geometry, nano-contact geometry and nano-pillar with a vortex configuration. GMR and MTJ indicate if the the spin-torque oscillator has a metallic spin-valve or a magnetic tunnel junction structure. P, f, Δf, Q, MR, and R correspond respectively to the output power, oscillation frequency range, minimal frequency linewidth, maximum quality factor, magnetoresistance ratio and static resistance which were reported.

Ref	Type	Size(nm^2)	P	f(GHz)	Δf	Q	MR/R
[177]	NP(GMR)	9100	89pW	5-10	-	-	1%,8Ω
[190]	NP(GMR)	1300	20pW	11-12	3.2MHz	-	0.4%,13Ω
[191]	NP(GMR)	5000	0.1nW	11-12	3.8MHz	3150	1%,3Ω
[192]	NP(GMR)	11700	5nW	10-11	10MHz	1124	3%,9Ω
[193]	NP(GMR)	6600	1nW	3.5-4	-	266	12%,8Ω
[178]	NC(GMR)	1250	87pW	5-40	58	800	2%,4Ω
[179]	NC(GMR)	1250	87pW	9.7-34.4	1.89	18000	1%,15Ω
[189]	NC(GMR)	1250	70pW	10-46	4.5	7300	0.4%,6Ω
[194]	NC(GMR)	15000	25nW	0.8-2	3	-	10%,10Ω
[195]	V(GMR)	9500	0.8pW	0.9-2.2	0.3	4000	1%,19Ω
[196]	NP(MTJ)	49000	20nW	4-7	21	238	48%,16Ω
[197]	NP(MTJ)	5000	25nW	4-10	26	1000	100%,3kΩ
[198]	NP(MTJ)	45000	142nW	3-12	20	-	70%,43Ω
[199]	NP(MTJ)	13000	550nW	4-7	47	-	66%,143Ω
[200]	NP(MTJ)	31000	200nW	2.6-2.8	80	35	88%,4kΩ
[187]	NP(MTJ)	11000	500nW	2-6.3	46.6	135	66%,2kΩ
[188]	NC(MTJ)	7500	2.4μW	2-5	12	350	46%,38Ω
[201]	NC(MTJ)	7500	63nW	2.5-15	3.4	3200	38%,55Ω
[186]	V(MTJ)	23000	5μW	0.4-0.9	1.1	718	14%,57Ω
[183]	V(MTJ)	70000	1.4μW	0.5-0.5	0.07	6400	128%,35Ω
[184]	V(MTJ)	82000	10.1μW	0.15-0.3	0.16	2000	190%,57Ω

obtained with spin-torque oscillators having a uniform magnetization distribution [187][188]. However, it should be noticed that the reachable frequency of spin-torque vortex oscillators is generally comprised between hundreds of MHz and 2.2 GHz, which is much smaller than the ones of oscillators presenting uniform magnetization distributions which can reach frequencies up to 65 GHz [189]. The size of spin-torque vortex oscillators is also of the order of hundreds of nm and remains relativelly large compared to some uniform spin-torque oscillators which can be scaled-down to tens of nm [178]. A more detailed comparison of the state of the art of spin-torque nano-oscillators is given in Tab. 1.

Nevertheless, the fact that spin-torque vortex oscillators present high signal to noise ratio and low frequency linewidth [184], and also that their magnetization dynamics is well understood and match quantitatively with experimental results [160], make them very attractive for demonstration purposes. For this reason, in the experimental part of this thesis, the spin-torque oscillators used for bio-inspired operations will be exclusively vortex-based spin-torque nano-oscillators. These kind of oscillators will be presented in more details in the next chapter.

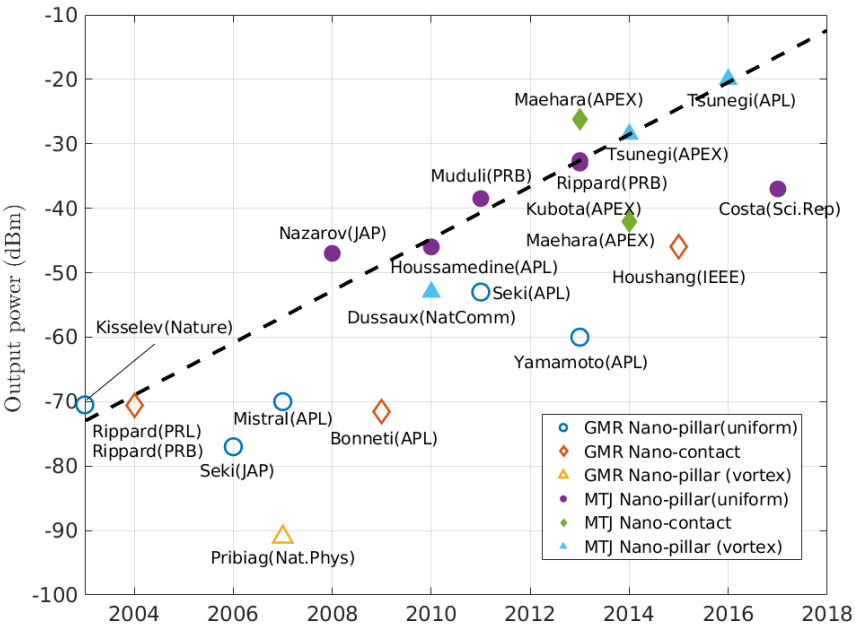

Figure 28: Evolution of the output power of spin-torque nano-oscillators in dBm as a function of the publication year. The black dash line corresponds to the trend line evolution of highest output powers reported in last decades.

In order to observe experimentally oscillations in first spin-torque nano-oscillators, often an external applied magnetic field was required [177][178]. Different strategies were developed to avoid the use of an external applied field. By designing the angular shape of the spin-torque ("wavy shape")[202] or by controlling the direction of the remanent field of the ferromagnetic layers [203][204][205], different

groups were able to observe in absence of external magnetic field microwave oscillations in spin-torque oscillators presenting uniform magnetization. In the case of nano-pillar oscillators presenting vortex magnetization distribution in their free-layer, other kinds of strategies were used: either by choosing a perpendicular magnetization [206][160] or by choosing a vortex configuration [207][208] for the polarizing layer. Here, these approaches are not presented individually, however the main goal of all of them is to reach a configuration where the spin-torque acting on the magnetization remains opposite to the damping torque acting on it and this for all the precession trajectory [10].

3.2.3 *Nonlinear auto-oscillator theory*

In order to describe the dynamics of spin-torque oscillators, a general formalism called "auto-oscillator model" was proposed by Slavin et al. [168]. Importantly, this nonlinear auto-oscillator is not only dedicated to spin-torque nano-oscillators, and can be generalized to a more vast class of nonlinear oscillators such as Van der Pol oscillators [209]. This model allows to describe conditions required to obtain self-sustained oscillations and is also particularly used to estimate the effect of thermal noise on oscillations. Importantly, this model allows to describe conditions for the synchronization of nonlinear oscillators to external signals, and for this reason it will be used in the experimental and simulation results of this thesis.

This model describes the dynamics of a single excited mode in a two dimensional plane space defined using its power amplitude $\sqrt{p(t)}$, and its phase $\phi(t)$. Its dynamics can be written using a complex variable $c(t) = \sqrt{p(t)}e^{i\phi(t)}$ and is described by the following equation ($i^2 = -1$):

$$\frac{dc}{dt} + i\omega(p)c(t) + [\Gamma_+(p) - \Gamma_-(p)]c(t) = f(t) \tag{22}$$

Here, ω is the oscillator resonance frequency, Γ_+ is the intrinsic damping for energy dissipation, Γ_- is the negative damping for energy dissipation, and f is the driving force which models the interaction with external signal. In the case of a spin-torque oscillator, Γ_+ corresponds to the intrinsic damping due to the Gilbert damping, Γ_-

corresponds to the effect of spin-torque. This model is qualified as nonlinear, because it can be seen from this equation that most of its parameters depends on the auto-oscillation power p (for instance damping terms and the resonance frequency).

In the case of self-sustained oscillations not interacting with an external force ($f = 0$), the auto-oscillation dynamics can be described through its power amplitude p, and its phase ϕ ($p = |c|^2$, and $\phi = \arg(c)$):

$$\frac{dp}{dt} + 2[\Gamma_+(p) - \Gamma_-(p)]p = 0 \tag{23}$$

$$\frac{d\phi}{dt} + \omega(p) = 0 \tag{24}$$

One can find stationary condition $c_0(t) = \sqrt{p_0}e^{i\phi(t)}$ for which the power amplitude is constant in time $\frac{dp}{dt} = 0$. Thus, from Eq. 23, the stable solution p_0 is given where there is compensation between positive and negative damping terms $\Gamma_+(p_0) = \Gamma_-(p_0)$. Those two damping terms increase and decreases as a function of the oscillation power p in general, thus a unique stable condition p_0 can be found. The particular case $\Gamma_+(p = 0) = \Gamma_-(p = 0)$ corresponds to the threshold for self-sustained oscillations.

In the case of spin-torque oscillators the following expressions for damping terms and frequencies can be found in the case of a magnetic vortex configuration [160]:

$$\begin{aligned} \omega(p) &\approx \omega_0 + Np \\ \Gamma_+(p) &\approx \alpha\omega_0(1 + Qp) \\ \Gamma_-(p) &\approx \alpha\omega_0 \frac{I}{I_{th}} \end{aligned} \tag{25}$$

Here, ω_0 is the resonant frequency of the auto-oscillator, N is the coefficient of the nonlinear frequency shift, α is the damping parameter, Q is nonlinear damping parameter, I is the applied current contributing to the negative damping term corresponding to the spin-torque, and I_{th} is the current corresponding to the threshold for self-sustained

oscillations. The presented expressions Eq. 25 which only slightly differ from the one of spin-torque oscillators having a uniform magnetization distribution [168] will be used in chapter 5 to realize simulations of the dynamics of spin-torque vortex oscillators in the nonlinear auto-oscillator formalism presented here.

3.3 DYNAMICS IN PRESENCE OF EXTERNAL FORCE STIMULI

When an external oscillating signal with a certain frequency f_{ext} is sent to a spin-torque nano-oscillator its dynamics is modified leading to different non-autonomous regimes: injection-locking corresponding a regime were the oscillator synchronizes to the frequency of an external source, mutual synchronization corresponding to a situation where two or more oscillators mutually synchronize with each other to a common frequency. Other regimes such as parametric excitation [210][211], resonant excitation [212], or frequency modulation [213][214] can occur but those last ones will not be described in this thesis. Here, a particular focus will be given to synchronization phenomena occurring with oscillators, and in particular with spin-torque nano-oscillators.

3.3.1 *Coupling and mutual synchronization of spin-torque nano-oscillators*

Huygens was the first to introduce the notion of synchronization in 17th century. He observed than two oscillating clocks were able to synchronize to each other: they ended up oscillating at a common frequency (in anti-phase). By analyzing this phenomenon, Huygens discovered that synchronization was due to the coupling provided by the common vibration of the stand to which clocks were suspended. Since this discovery, this mutual synchronization phenomena was widely observed in different domains such as in Josephson junctions [120], neural activity of the brain [21], millennium bridge [215], clapping audiences [216] circadian rhythms [217], assemblies of metronomes [217], financial stock markets [217], ecosystems [218], and crickets

[219]. For more details, a review on synchronization is proposed by Pikovsky et al. [217].

In the case of spin-torque nano-oscillators mutual synchronization can be categorized following the coupling mechanisms leading to this phenomenon. Three mechanisms should be distinguished: those mediated by spin-waves, mediated by dipolar magnetic fields, and mediated by self-generated microwave currents. Here we briefly introduce some of the experimental synchronization measurements realized recently with spin-torque oscillators. In these experimental observations, in terms of frequency spectrum, synchronization occurs when the individual frequency peaks of the oscillator merge to one common frequency peak. As predicted by theory, this leads to a reduction of the frequency linewidth and a high output power which is higher than the sum of the individual out power emissions [217].

Mutual synchronization between spin-torque nano-oscillators was first demonstrated by Kaka et al. [220], and Mancoff et al. [221] in nano-contact spin-torque oscillators having uniform magnetization configuration. The two nano-contacts separated by few hundreds of nanometers interact with each other through propagating spin-waves. Those nano-contacts are fed by independent or common applied currents and they share the same free-layer. One can find more details and explanation on this interaction in [222][223][224]. Using the same approach, Ruotolo et al. [225] demonstrate the synchronization of four nano-contacts having a magnetic vortex configuration. Recently Houshang et al. [226], demonstrated the synchronization of up to 5 nano-contacts mediated by spin-waves. The same coupling mechanism was used beyond the class of spin-torque nano-oscillators in assemblies of spin-Hall nano-oscillators [227] allowing the synchronization of up to 9 of such oscillators. In these class of oscillators the spin-torque exerted on the magnetization is due to a spin-polarized current generated by the spin-Hall effect appearing for instance in heavy metal materials such an Platinum. These oscillators will not be evoked in this thesis, but they are an active research area and interestingly recently their potential for neuromorphic applications was highlighted by the group of Akerman et al. [228]. It should be noticed, that in these implementations mediated by spin-waves, spin-torque oscillators

can also be coupled through dipolar magnetic fields. However, several theoretical and experimental works show that spin-wave mechanism was the dominant interaction leading to synchronization [229][223]. Due to the attenuation length of spin waves (which is for instance around 1.5 μm in Permalloy NiFe), this coupling remains mainly local and efficient between neighboring oscillators. This can be an issue if a large array of spin-torque oscillators is required to be synchronized.

Another local mechanism leading to synchronization between spin-torque nano-oscillators is the coupling due to their emitted dipolar magnetic fields [230]. In the case of oscillators having a uniform magnetization, this interaction is weaker than the one due to spin-waves. However, according to micromagnetic simulations done by Belanovsky et al. [231] in the case of vortex based spin-torque nano-oscillators this interaction can be sufficiently efficient. A first demonstration of mutual synchronization of spin-torque nano-oscillators through dipolar fields was demonstrated by Locatelli et al. [232] for two metallic spin-valves nano-pillars separated by 100 nm distance. According to simulations realized by Abreu Araujo et al. [233], even in optimal magnetic configuration the dipolar magnetic field interaction is not efficient for distances higher than 600 nm. Nevertheless, this coupling is interesting because it emerges naturally in densely packed arrays of oscillators, and recently an original approach in order to control the synchronization between two dipolarly coupled vortex spin-torque nano-oscillators were proposed using a third one in between [234].

In order to escape from the distance constraint imposed by spin-waves and magnetic dipolar interactions, one alternative approach is to leverage the electrical coupling due to the common microwave currents generated by spin-torque oscillators. Indeed, in their self-sustained regime, each oscillator generates a microwave electrical currents having the frequency of its oscillator. When this alternating current is sent to a different oscillator using electrical connections, it exerts an alternating spin-torque on the dynamics of this oscillator. Therefore, through this additional spin-torque, the electrical microwave emission of one oscillator acts on the dynamics of the other oscillator and vice versa. This approach was first proposed by Grollier et al. [235] in 2006 and was adapted to different electrical circuit

symmetries [236]. A first demonstration of mutual synchronization of two electrically coupled vortex spin-torque nano-oscillators was established by Lebrun et al. [237]. Recently, up to eight oscillators were synchronized through electrical coupling mechanism [238]. The main advantage of this coupling is the fact it is global, meaning that instead of being restricted to neighbors, all oscillators of an assembly will interact through the common microwave signal. This is an important point for building large array of interacting spin-torque nano-oscillators. For this reason, in this thesis the electrical coupling approach will be used to couple spin-torque nano-oscillators together.

3.3.2 *Injection-locking of spin-torque nano-oscillators*

In this subsection, we focus on a particular synchronization effect called injection-locking which occurs between an oscillator in its self-sustained regime and an external source signal forcing the oscillator dynamics. Contrary to mutual synchronization, the interaction in this case is unidirectional meaning that the external source is not affected by the oscillator dynamics. This particular synchronization case has a large importance in this thesis and it will be leveraged in both experiments and simulations in order to achieve neuromorphic operations using spin-torque nano-oscillators (Chapter 4 to 6).

Injection-locking can be described analytically in the nonlinear auto-oscillator formalism presented in the previous subsection. In this case, Slavin et al. [168] consider an external oscillating forcing $f(t) = f_e e^{-i\omega_e t}$ having a frequency ω_e in the right hand-side of the Eq. 22. The insertion of this external source term leads to the following amplitude and phase equations:

$$\frac{dp}{dt} + 2[\Gamma_+(p) - \Gamma_-(p)]p(t) = 2\sqrt{p}F_e cos(\omega_e t + \phi - \psi_e) \tag{26}$$

$$\frac{d\phi}{dt} + \omega(p) = -\frac{F_e}{\sqrt{p}} sin(\omega_e t + \phi - \psi_e) \tag{27}$$

Here $F_e$is the real amplitude of the external source ($F_e = |f_e|$) ,

and ψ_e is its initial phase ($\psi_e = \arg(f_e)$).

In order to see the influence of the external source on the oscillator dynamics, it is convenient to do a change of variable where a slow auto-oscillator phase Φ is introduced: $\Phi = \omega_e t + \phi - \psi_e$. In the case of a linear oscillator, meaning that its frequency can be considered as a constant ω_g and not depending on the oscillation power, these considerations applied to a stationary state ($\frac{dp}{dt} = 0$) lead to the following equation often called Adler equation [239]:

$$\frac{d\Phi}{dt} = (\omega_e - \omega_g) - \frac{F_e}{\sqrt{p_0}} sin(\Phi) \tag{28}$$

Injection-locking in this equation corresponds to a situation where the oscillator and the external source have a constant relative phase $\frac{d\Phi}{dt} = 0$ which leads to the expression (coming from $|sin\Phi| < 1$) defining the injection locking range Δ_0:

$$|\omega_e - \omega_g| < \frac{F_e}{\sqrt{p_0}} = \Delta_0 \tag{29}$$

This injection-locking range Δ_0 corresponds to the frequency bandwidth on which the oscillator shares the same frequency as the external source ($\frac{d\phi}{dt} = \omega_e$). It should be noticed that this description is valid for the first harmonic of the oscillating signal and can be extended to higher order harmonics by adapting the Eq. [239] with a new definition of the phase difference $\Phi = n\omega_e t + m\phi - \psi_e$ where n and m are integers.

In the case of nonlinear oscillators, which frequency depends on the oscillation power through a relation such as the one presented in the previous subsection: $\omega = \omega_0 + Np$, the same calculation presented for the linear case can be adapted leading to a larger injection locking Δ range than in the linear case:

$$|\omega_e - \omega_g| < \frac{F_e}{\sqrt{p_0}} \sqrt{1 + \nu^2} = \sqrt{1 + \nu^2} \Delta_0 = \Delta \tag{30}$$

Here ν is the normalized nonlinear frequency shift defined as follows:

$$\nu = \frac{N}{\frac{d\Gamma_+(p)}{dp} - \frac{d\Gamma_-(p)}{dp}} \tag{31}$$

The presented definition of injection locking-range Δ will be used in chapter 6 in order to simulate large arrays of spin-torque nano-oscillators synchronizing with external sources. In addition, the definition of Δ highlights three factors which influence the injection-locking range: the real amplitude of the external force, the nonlinearity of the oscillator, and its oscillation power.

In order to evaluate the synchronization frequency bandwidth, the injection-locking experience consists in observing the evolution of the oscillator frequency as a function of the frequency of the external source ω_e which is swept around the natural frequency of the oscillator $\omega \approx \omega_g$. A typical frequency evolution is represented in Fig. 29. It should be noticed that injection-locking can also occur for external frequencies close to integer numbers of natural frequencies of oscillator $\omega \approx n\omega_g$. In particular, in chapter 2, injection-locking experiments will be presented for the case $n = 2$.

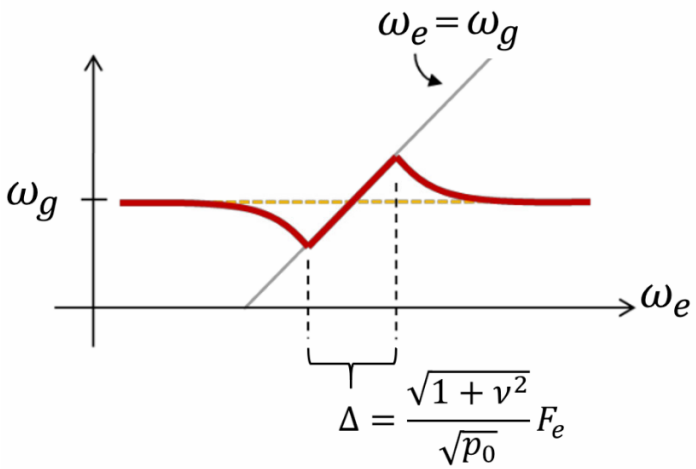

Figure 29: Schematic of the evolution of the frequency of an oscillator in presence of an external frequency ω_e having a natural frequency ω_g. Figure adapted from [12].

First experimental observation of injection-locking with spin-torque nano-oscillators was reported by Rippard et al. in 2005 [240] for metallic spin-valves having uniform magnetic configurations. Such kind of synchronization experiments were used to evaluate the cou-

pling electrical coupling strength leading to synchronization [241] and were extended to the case of oscillators having a magnetic tunnel junction structure [242]. In 2011, first injection-locking experiments for magnetic tunnel junctions spin-torque oscillators having a vortex configuration were achieved by Dussaux et al. [243] demonstrating the large synchronization ability of these oscillator both at f and $2f$ and even at fractional frequencies such as $\frac{3}{2}f$. In all of these injection-locking experiments, the microwave electrical coupling was the mechanism for the synchronization. Injection-locking experiments presented in the chapter 3 of this thesis, will be achieved through this electrical mechanism.

Another important mechanism leading to injection-locking of spin-torque oscillators is due to dipolar magnetic fields that can be provided by a micro-strip antenna fabricated in the vicinity of the oscillator. The external microwave electrical signal is sent into this antenna which generates the microwave fields acting on the dynamics of the spin-torque oscillators. This approach was used in the case of magnetic oscillators having a uniform magnetization by Urazhdin et al. [212] and was extended to the case of vortex based nano-oscillators by Hamadeh et al. [244]. This approach using the antenna will be used experimentally in chapter 4 in order to achieve individual injection-locking of an assembly of four oscillators for neuromorphic applications.

3.4 APPLICATIONS POTENTIAL OF SPIN-TORQUE NANO- OSCILLATORS

Spin-torque nano-oscillators are good candidates for several different application fields. Indeed these spintronic devices have numerous advantages such as their nanometric size, compatibility with CMOS technology, large frequency tunability [189], tolerance to radiations [245]. In this section few applications of spin-torque nano-oscillators will be briefly presented in this section. Importantly, it should be mentioned, that magnetic-tunnel-junction structure involved in spin-torque oscillators is starting to be a part of the manufacturing process of microelectronics foundries. Indeed, a large effort for building magnetic access memory MRAM devices was achieved in the recent decade, and

first commercialized devices appeared recently [246]. These memories will not be described here, however they are an important illustration of the fact that magnetic-tunnel-junction structures are technology-ready for large on-chip integration. Therefore, implementations with large numbers of nano-oscillators are quite promising with spin-torque nano-oscillators compared to the other nano-oscillator technologies presented in the first chapter.

3.4.1 *Microwave emission*

A straightforward field of applications for spin-torque nano-oscillators is the one of microwave emitters. Today, a wide range of emitted frequencies need to be covered, for instance from 100 MHz to 5 GHz for mobile, and from 5 to 25 GHz for spatial or radar applications. Therefore, the large frequency bandwidth (100 MHz to 65 GHz) covered by oscillators is good advantage. In addition, their small size (order of 100 nm) compared to voltage control oscillators (VCO) having often a size larger than the micrometer, make spin-torque oscillators very suitable for miniaturized on-board systems. However, an important issue remains the phase noise of these oscillators (-90 dBc/Hz) which is still larger than the one of VCOs (-110 dBc/Hz)[247]. In order to solve this problem several strategies were proposed, namely implementing a phase-locked-loop circuit for the spin-torque nano-oscillators [248][249] or by synchronizing an assembly of spin-torque nano-oscillators which improves both the output power and the coherence [238].

Interestingly, spin-torque nano-oscillators can also be used in order to transmit information for wireless applications through the discrete changes of the amplitude of their carrier signal as a function of the modulation current. This approach called "amplitude-shift-keying" was demonstrated experimentally allowing a transmission of information with a rate of 200 kbit/s, which can be improved to 1.5Gbit/s [250]. Using a different approach leveraging frequency changes of the oscillator called "frequency-shift-keying" higher information transmission rate was demonstrated experimentally up to 400 Mbit/s [251][252].

Another application field of spin-torque oscillators concerns the read-heads of hard-disk drives. Read-heads are often made of magnetic-

tunnel-junctions which through magnetoresistance effects modify their resistance in presence of the stray field of magnetic bits. In order to accelerate the reading rate, an alternative approach is to use spin-torque nano-oscillators [253] as a read-head. By interacting with the magnetic stray-field of stored bits, spin-torque nano-oscillators can modify their frequency and therefore read the bit which should improve the data transmission rate.

3.4.2 *Microwave detection and frequency mixing*

When spin-torque nano-oscillators are excited by a microwave signal with a certain frequency they can rectify their dc voltage [247]. When the frequency of this microwave signal is close to an eigenfrequency of the magnetic free-layer, the magnetization starts to oscillate. This oscillation is converted to a microwave oscillation of the resistance of the oscillator. Therefore, the voltage of the device will corresponds to the product of two oscillating microwave variables: the injected microwave current and the resulting microwave resistance. The time average of this product leads to a non-zero rectified dc voltage. This effect is called spin-diode effect and was proposed for the detection of microwave currents. Contrary to Schottky diodes used for rf detection, spin-torque oscillators have smaller size and can have higher detection sensitivity [254] (of the order of 12000 mV/mW while for Shottky diodes it is close to 3800 mV/mW). In the last decade, different strategies as vortex expulsion or injection-locking were leveraged to obtain a sufficient spin-diode effect respectively for building rf detectors [255] and agile frequency spectrum analyzers [256].

Another application of this effect is to use spin-diode effect in order to build energy harvesters [257]. Indeed by capturing neighboring microwaves, spin-torque nano-oscillators through the spin-diode effect can generate a sufficient rectified dc voltage that can be used to feed other electric devices such as photo-sensors autonomously. Spin-diode results reported by Fang et al. [258] for broadband input microwave frequencies are encouraging approach towards building such kind of nanometric energy harvesters.

3.4.3 *Neuromorphic application potential*

As it was mentioned in the first chapter, spin-torque nano-oscillators are promising building blocks to emulate neuron-like units and different computation models involving spin-torque oscillators are achieved numerically. By studying the impact of different transformations used at this numerical step, the critical role of the spin-torque nano-oscillator and, in particular, its nonlinear amplitude response in order to solve the problem was highlighted. The approach used to train to recognize digits corresponds to reservoir computing. Beyond the application context of spin-torque nano-oscillator today, this work is an important demonstration proof of using nano-oscillators in order to achieve neuromorphic computing at the nano-scale. In the same line of thinking, next chapters of this thesis will present neuromorphic computing results using a different approach leveraging synchronization with this time four coupled spin-torque nano-oscillators.

3.5 CONCLUSION

We have seen in this chapter fundamental spintronic physical phenomena underlying the features of spin-torque nano-oscillators. Through the state-of-the art of these nano-oscillators the important properties required to building a hardware oscillator-based assembly than can emulate biological neural network were presented. Through their small size, nonlinear response, compatibly with CMOS technology, well-known magnetization dynamics, high frequency tunability, low frequency linewidth and high output power at the nano-scale and other working properties, they are very promising for neuromorphic applications. In particular, their ability to synchronize was highlighted which will be leveraged in next chapters to realize first neuromorphic operations. The large application field of spin-torque oscillators was also briefly presented which emphasizes the fact that beyond fundamental studies, these spintronic oscillators and technology-ready for implementations.

4

OSCILLATIONS AND SYNCHRONIZATION OF SPIN-TORQUE VORTEX OSCILLATORS

In this chapter, I will present the theoretical and experimental properties of a particular class of spin-torque nano-oscillators that were mainly studied in this thesis called spin-torque vortex nano-oscillator. The dynamics leading to oscillations and synchronization phenomena that were observed experimentally will be emphasized. In particular, the synchronization of two coupled spin-torque vortex oscillators in presence of an electrical mutual coupling will be studied both experimentally and by simulations. This will give rise to a preliminary understanding of synchronization of those oscillators in presence of coupling which will be an important feature in order to demonstrate an array of coupled spin-torque nano-oscillators able to realize neuromorphic operations in chapter 5.

4.1 VORTEX SPIN-TORQUE NANO-OSCILLATORS

As mentioned in the previous chapter, the first spin-torque nano-oscillators had uniform magnetization distributions for their free-layer. Since then, spin-torque nano-oscillators with a vortex magnetization configuration in their free layer have been investigated, and have generated a high interest in the community due to their low frequency linewidth and higher signal to noise ratio [195][186][184]. In this section, the static properties of magnetic vortices will be described, as well as their dynamics under spin-transfer torque.

4.1.1 *The magnetic vortex*

The magnetization distribution depends on both the size and shape of the ferromagnetic studied system. In a static case, any magnetization distribution (uniform or non-uniform) is resulting from a competition between different categories of energy in the ferromag-

netic system: exchange, dipolar and Zeeman energy. In particular, at remanence, the magnetization distribution which minimizes these two energies in ferromagnetic disks can be a magnetic vortex distribution. Depending on the height, radius of the ferromagnetic cylinder, and the exchange length of the material $L_E = \sqrt{\frac{2A}{\mu_0 M_s^2}}$, three distinct ground states can be distinguished: uniform in-plane, uniform out-of-plane and non-uniform vortex configurations. Here A is the stiffness exchange constant and M_s is the saturation magnetization of the material. (For typical ferromagnetic materials used in the free-layer of the sample of this thesis, this length can be evaluated to L_E(NiFe)$\approx$ 5.7 nm and L_E(FeB)$\approx$ 11.8 nm.) Fig. 30 presents regions for which the radius of the cylinder and its height lead to one of these three configurations.

For radius and height values leading to vortex configuration ground state, the majority of the magnetization curls in-plane except in a small region called vortex-core where it becomes out-of-plane. A magnetic vortex is characterized by its polarity and chirality. The polarity corresponds to the direction of the magnetization component which is out-of-plane $P = m_z(0) = \pm 1$. The chirality corresponds to the curling direction of the in-plane magnetization, $C = 1$ if it is anti-clockwise and $C = -1$ if it is clock-wise. At the end, four different (C,P) configuration can occur and are shown in Fig. 31.

Different analytical approaches were proposed to describe the magnetization distribution [259] [259] [260] namely by reducing the problem by finding an analytical function for the out-of-plane magnetization distribution giving rise to different models. For more details, a comparison between these models (Usov is the most commonly studied) are proposed by Gaidedei [261]. Here we mainly present the magnetic vortex state appearing in a circular section, however it can be also found in elliptical [262] or square ferromagnetic sections [263].

For a circular ferromagnetic cylinder, at the remanence, the magnetic vortex is located in the center of the section of the ferromagnetic cylinder. However, when a applied magnetic field is applied in the plane of the section, the vortex core is displaced and leaves the cen-

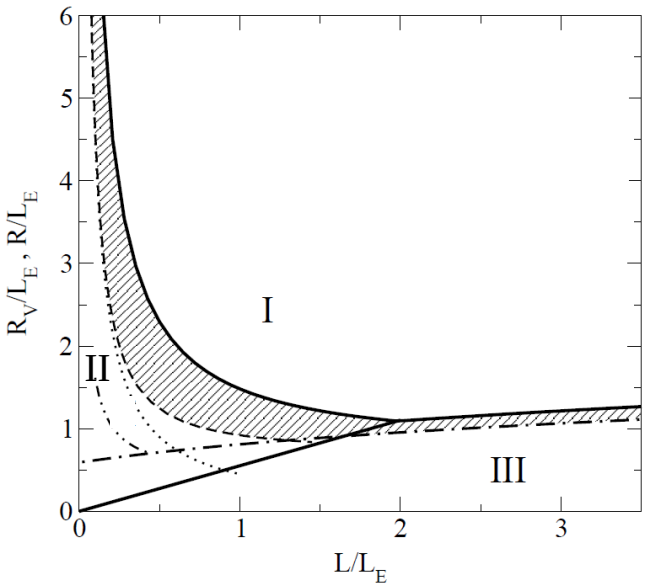

Figure 30: Stability diagram of the three different configurations of the magnetization distribution in a ferromagnetic cylinder having a section radius $\mathcal{R}$ and height L. This diagram was originally taken from Metlov et.al.[13]. The diagram presents three distinct regions. I: magnetic vortex state, II: magnetized uniformly in-plane, III: magnetized uniformly out-of-plane. The dashed region corresponds to a metastable configuration between the three different ground states.

ter of the disk. Through this vortex core position displacement, the magnetization distribution tries to align its mean planar magnetization with the direction of the applied magnetic field. This allows to minimize the total magnetic energy which includes the dipolar, exchange and also the Zeemann energy (due to the applied magnetic field). The stability of the vortex state was studied in presence of an in-plane applied magnetic field both in simulations [264][265] and experimentally [266][267][268]. For high in-plane applied magnetic field, the magnetization is uniform and is aligned with the direction of the applied magnetic field. By decreasing this field, the transition between the uniform configuration and the vortex one occurs at the nucleation field H_n. Close to this field value, during this transition

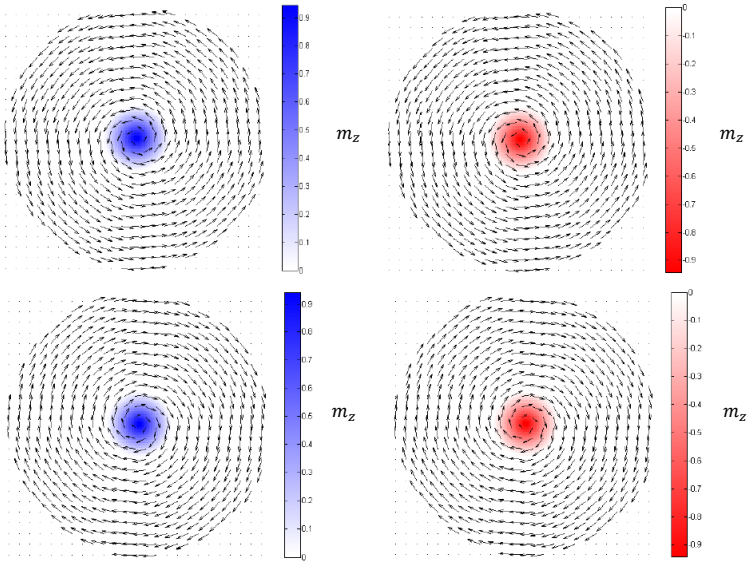

Figure 31: Four different (C, P) configurations for the magnetization distribution: (1,1), (1,-1), (-1,1), (-1,-1), figure extracted from [11]. Blue and red colors correspond respectively to positive and negative out-of-plane magnetization m_z.

an intermediate metastable state can appear which corresponds to a magnetization that is curly in the plane while the vortex core is absent from the disk. This intermediate state is often called to "C-state".

For a case where the magnetic vortex is inside the ferromagnetic disk, several analytical description for the spatial magnetization distribution of the vortex were proposed [259][261].

4.1.2 *Dynamics of vortex spin-torque oscillators*

The magnetic vortex presents several different dynamical modes. These modes were observed experimentally [269][270][271] and confirmed by simulations and analytical studies [272][273], and their frequency depends on the aspect ratio of the ferromagnetic disk. The fundamental mode is called the gyrotropic mode and corresponds to the spatial oscillation of the vortex core around the magnetic equilibrium center of the disk. Higher modes corresponding to radial and azimuthal modes can be observed but those will not be considered

in the following. In the rest of this thesis, an exclusive focus will be given to the dynamics of the magnetic vortex in the gyrotropic mode.

In order to describe the dynamics of the gyrotropic mode, one should consider the Thiele equation approach proposed in 70's to describe the dynamics of vortex in semi-infinite wires [274]. Importantly, the magnetization dynamics in this case can be seen as a translation of the magnetization distribution and therefore can be reduced to the description of magnetization of one particular point. In the case of a magnetic vortex in a ferromagnetic disk, the description of the dynamics can be reduced to the center of the vortex core $\mathbf{X_c}$ corresponding to cylindrical coordinates (s_c, θ_c) in the 2D plane of the ferromagnetic disk. Here s_c corresponds to the normalized radius position in a feromagnetic disk of radius $\mathcal{R}$. When the vortex leaves its equilibrium state corresponding to the center of the disk, several hypothesis should be considered in this formalism to simplify the calculations, namely the translation of the vortex core, the absence of magnetization deformation or the introduction of an image vortex outside of the ferromagnetic disk to cancel the apparition of magnetic charges at the border of the disk ($\vec{m}.\vec{dr} = 0$ where $\vec{dr}$ is the elementary radial vector defined at the border of the disk) called the Two-vortex Ansatz (TVA). Here, those hypothesis will not be detailed but detailed descriptions are given in [275][12].

In order to establish the Thiele equation of motion for the vortex core, the Landau-Lifschiz-Gilbert equation Eq. 18 is projected in a spherical basis defined in the ferromagnetic disk. Then by integrating the energy variations overall the disk a new dynamical equation can be derived:

$$\mathbf{G} \times \frac{d\mathbf{X_c}}{dt} - \mathbf{D}(\mathbf{X_c})\frac{d\mathbf{X_c}}{dt} - \frac{\partial W}{\partial \mathbf{X_c}} + \mathbf{F^{STT}} = 0 \tag{32}$$

The details of the calculation to establish this equation from Eq. 18 can be found in [12]. The different terms of this equation will be described in the following. The different terms of Eq. 32 can be seen as four different forces acting on the center of the vortex core having a position $\mathbf{X_c}$. The first term $\mathbf{G} \times \frac{d\mathbf{X_c}}{dt}$ corresponds to the Gyroforce. This

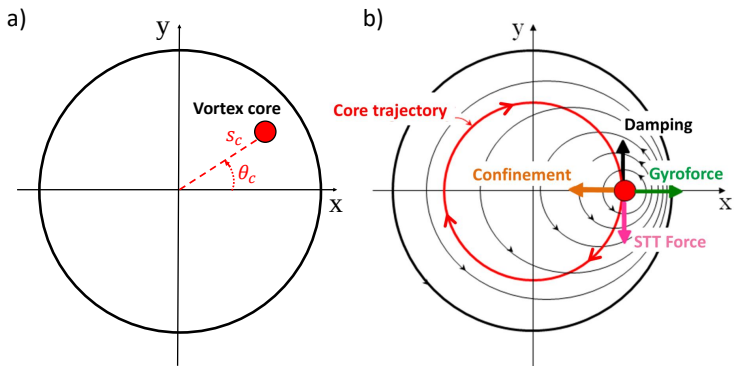

Figure 32: a) Schematic representation of the vortex core position coordinate used in the 2D plane of the ferromagnetic disk. b) Schematic representation of the different forces acting on the vortex core in the Thiele formalism. Figure extracted from Lebrun et al. [8]

.

force is responsible for the rotational motion of the vortex core around the center of the dot. The gyrovector **G** is associated to the cross product of magnetization gradients and is pointing perpendicularly to ferromagnetic disk surface. In the case of an applied perpendicular field $H_\perp$, the gyrovector magnitude can be defined as follows:

$$G = (2\pi L \frac{M_s}{\gamma_0} P)(1 - P\cos\theta_0) \tag{33}$$

Here, $\theta_0 = cos^{-1}\frac{H_\perp}{\mu_0 M_s}$ is the free layer magnetization angle which allows to take into account the influence of the perpendicular applied magnetic field $H_\perp$ on the magnetization of the free-layer, P is the vortex polarity, M_s is the saturation magnetization of the free-layer, L is the free-layer thickness.

The second term of Eq.32 represents the damping force pointing in the opposite direction of the motion of the vortex core. The amplitude of this damping term is defined as follows and depends nonlinearly on the amplitude position of the vortex core:

$$D = D_0(1 + \xi(\frac{s_c}{\mathcal{R}})^2) \tag{34}$$

Where D_0 corresponds to the following expression:

$$D_0 = \alpha(2\pi L\frac{M_s}{\gamma_0})(\frac{1}{2}\ln\left(\frac{R}{2b}\right) - \frac{1}{8})\sin^2\theta_0 \tag{35}$$

Here, $\xi = 0.6$, α is the Gilbert damping coefficient defined previously, $\mathcal{R}$ is the radius of the ferromagnetic disk, and b corresponds to the size of the vortex core radius $b = 2L_{ex} = 2\sqrt{\frac{2A}{\mu_0 M_s^2}}$ (here A is the exchange stiffness constant introduced previously). The calculation giving this term can be found in [11]

The third term of Eq.32 corresponds to the confinement forces which are applied in the 2d plane of the vortex core trajectory. It tends to return the vortex core to the dot center in order to reduce the total energy. This planar confinement force regroups two different types of terms deriving from the integration of two energies present in the effective field of Eq.18, W_{ms} and W_{Oe}. Those terms are due to the Zeeman interaction with respectively the magneto-static field and the Oersted field appearing when an electrical current is applied:

$$W = W_{ms} + W_{Oe} \tag{36}$$

The magnetostatic energy can be expressed as follows:

$$W_{ms} = \frac{1}{2}\kappa_{ms}s_c^2 + \frac{1}{4}\kappa_{ms}^{'}\frac{s_c^4}{\mathcal{R}^2} + O(s_c^6) \tag{37}$$

And the energy due to the Oersted field confinement can be expressed as follows:

$$W_{Oe} = \frac{1}{2}\kappa_{Oe}CJs_c^2 + \frac{1}{4}\kappa_{Oe}^{'}CJ\frac{s_c^4}{\mathcal{R}^2} + O(s_c^6) \tag{38}$$

Here, C corresponds to the chirality of the vortex, and J is the electrical current density injected in the nanopillar. The different coefficients involved in these two expressions were calculated through the evaluation of the energy integrals by Guslienko et al. [276], Gaididei et al. [261] and Khvalkovskiy et al. [206]. Concerning the magnetostatic term those coefficients are defined as follows:

$$\kappa_{ms} = (\frac{10}{9})\mu_0 M_s^2\frac{L^2}{\mathcal{R}}\sin^2\theta_0 \tag{39}$$

$$\kappa_{ms}^{'} = 0.25\kappa_{ms} \tag{40}$$

Concerning the term due to the Oersted field confinement they are defined as follows:

$$\kappa_{Oe} = 0.85\mu_0 M_s L\mathcal{R}\sin\theta_0 \tag{41}$$

$$\kappa_{Oe}^{'} = -0.5\kappa_{Oe} \tag{42}$$

The last term of Eq.32, corresponds to the force due to spin-torque due to the Slonczewski and field-like torque introduced in the previous chapter(see Eq. 18). The force due to the Slonczewski torque can be decomposed in two components: $\mathbf{F}_{\perp}^{\mathbf{Slonc}}$ and $\mathbf{F}_{\parallel}^{\mathbf{Slonc}}$ due respectively to the perpendicular p_z and in-plane p_x components of the magnetization of the polarizer $\mathbf{p} = p_z\mathbf{z} + p_x\mathbf{x}$. Thus, the force due to spin-torque can be defined as follows:

$$\mathbf{F}^{\mathbf{STT}} = \mathbf{F}_{\perp}^{\mathbf{Slonc}} + \mathbf{F}_{\parallel}^{\mathbf{Slonc}} + \mathbf{F}^{\mathbf{field-like}} \tag{43}$$

The first force term $\mathbf{F}_{\perp}^{\mathbf{Slonc}}$ will act as an anti-damping force. Depending on the sign of the applied current J, it will acts in the same direction than the damping force ($J > 0$) or in the opposite direction ($J < 0$). This force can be expressed as follows:

$$\mathbf{F}_{\perp}^{\mathbf{Slonc}} = a_j J(\mathbf{z} \times \mathbf{X_c}) \tag{44}$$

Where a_j corresponds to the following expression:

$$a_j = \pi\frac{\hbar\mathcal{P}}{2e}p_z sin^2\theta_0 \tag{45}$$

Here, $\mathcal{P}$ is the spin polarization of the magnetic junction, $\hbar = 1.054 \times 10^{-34} J.s^{-1}$, and $e = 1.602 \times 10^{-19} C$. It should be noticed that perpendicular component of the magnetization of the polarizer p_z depends on saturation magnetization M_s^{pol} of the polarizer and also on the applied perpendicular magnetic field $H_\perp$ [160]:

$$p_z = \frac{H_\perp}{\mu_0 M_s^{pol}} \tag{46}$$

The second force term $\mathbf{F}_{\parallel}^{\mathbf{Slonc}}$ will act as an in-plane magnetic field. This force can be expressed as follows:

$$\mathbf{F}_{\parallel}^{\mathbf{Slonc}} = a_j^x J \mathbf{x} \tag{47}$$

Where a_j^x corresponds to the following expression:

$$a_j^x = \pi \frac{\hbar \mathcal{P}}{2e} bC \tag{48}$$

Here, p is the polarity of the vortex, b is the radius of the vortex core which in the first approximation is related to the exchange length of the free-layer $b \approx 2L_E$. However the applied perpendicular magnetic field H_{perp} affects this radius and one can also take into account this contribution using simulations (see [275]).

The third force term $\mathbf{F}^{\mathbf{field-like}}$ will also act as an in-plane magnetic field. This force can express as follows:

$$\mathbf{F}^{\mathbf{field-like}} = b_j J(\mathbf{z} \times \mathbf{p}) \tag{49}$$

Where b_j corresponds to the following expression:

$$b_j = C\pi \frac{\hbar \mathcal{P}}{2e} \frac{2}{3} \mathcal{R} r_{fl} \tag{50}$$

Here C is the chirality of the vortex, $\mathcal{R}$ is the the radius of the free-layer disk and r_{fl} is the amplitude ratio of the field-like torque over the Slonczewski torque defined in the previous chapter (varies. between 0.1 and 0.4). In the case of a uniform polarizer, the in-plane contribution of the Slonczewski torque $\mathbf{F}_{\parallel}^{\mathbf{Slonc}}$ and the field-like torque $\mathbf{F}^{\mathbf{field-like}}$ average out for one gyration of the vortex core. Therefore, in this case their impact on the gyration dynamics can be neglected.

By including all of the other terms in the expression of the four forces acting on the vortex core in the Thiele equation Eq. 32 and projecting this equation in the 2D plane of the ferromagnetic disk following the procedure described by Dussaux et al., one can find a differential system where phase θ_c and amplitude s_c are coupled to each other [159].

$$\frac{d\theta_c}{dt} = \frac{\kappa}{G}(1 + \eta(\frac{s_c}{\mathcal{R}})^2) \tag{51}$$

$$\frac{ds_c}{dt} = \frac{D_0\kappa}{G^2}(J_{oc} - (\eta + \xi)(\frac{s_c}{\mathcal{R}})^2) \tag{52}$$

Where, $\kappa = \kappa_{ms} + \kappa_{Oe}J$, $\eta = \frac{\kappa'_{ms} + \kappa'_{Oe}J}{\kappa_{ms} + \kappa_{Oe}J}$, and $J_{oc} = \frac{a_j JG}{D_0\kappa}$. This system of differential equations is used to simulate the magnetization dynamics of spin-torque vortex oscillators studied in this thesis. It should be noticed that the expression of these equations and those defined in the Slavin et al. formalism (Eq. 23 and 24) are quite similar and illustrates the nonlinearity of spin-torque vortex oscillators in their gyrotropic mode. One can also see that the frequency of the oscillator can be obtained by evaluating $\frac{d\theta_c}{dt}$.

4.2 ELECTRICALLY COUPLED VORTEX SPIN-TORQUE NANO-OSCILLATORS

In this section, I present both experimental results and simulations concerning the synchronization of a spin-torque vortex nano-oscillator to an external microwave signal when it is electrically coupled to another oscillator. More precisely an enhancement of the synchronization bandwidth to the external signal also called injection-locking range was observed compared to a situation not including mutual coupling. This evolution of the injection-locking range was studied for different coupling strengths. This work is mainly described in [14].

4.2.1 *Samples*

The experimental results presented in this chapter are obtained for magnetic tunnel junctions fabricated by with the following composition: Ta/CuN/Ta/ PtMn(20)/CoFe(2)/Ru(0.85)/CoFeB(2.2)/CoFe(0.5)/MgO(1)/ CoFeB(1.5)/Ta(0.2)/NiFe(7)/Ta. Here PtMn(20)/CoFe(2)/ Ru(0.85)/CoFeB(2.2) is a synthetic ferrimagnet (SyF) uniformly magnetized in-plane, that is used as a polarizer, CoFeB(1.5)/Ta(0.2)/NiFe(7) is the free layer. Thicknesses are given in brackets in nm. Samples were grown by sputter-deposition and patterned down to the bottom electrode into circular nanopillars with a diameter of 200 nm. The nano-pillars exhibit a TMR of 64% at room temperature. These samples (RFHR008)

were fabricated by collaborators working in International Iberian Laboratory (INL) together with CEA LETI and Spintec in the context of the MOSAIC project.

4.2.2 *Experimental injection locking in a system of electrically coupled spin-torque vortex oscillators*

The samples used for this experimental study are the same ones presented in the previous section 4.2.1. Two of such kind of spin-torque nano-oscillators are connected in series, and electrically coupled through their own electrical microwave emissions. In order to obtain an efficient spin-transfer torque acting on the magnetic vortex core of the free-layer, a magnetic field $\mu_0 H_\perp = 0.240$ T perpendicular to the magnetic layers is maintained constant during the measurement. Fig. 33 shows the corresponding electrical circuit measurement. In each nano-oscillator, the applied dc current is injected perpendicularly to the layers and as it was described in the previous section, it leads to vortex core dynamics and induces through magneto-resistive effects a microwave oscillating resistance variation that can be read-out. It should be noticed that the circuit allows an individual control on the dc current flowing through each nano-oscillator independently. For this reason, the dc current is supplied by two different dc current sources. Therefore, this individual control on the two injected dc currents, allows to tune the frequency of the two nano-oscillators independently. As in the circuit described in the previous section, an external microwave current is injected in the circuit using a microwave source. The power amplitude of the signal injected to circuit is -15 dBm and its frequency is around twice the frequency of the carrier frequency of the two oscillators. Finally, a spectrum analyzer is used to record the total microwave signal of the coupled nano-oscillators 1 and 2 (called STO1 and STO2 in Fig. 33)

Using this approach, the injection-locking range of oscillator 1 to the external microwave signal can be studied while it is also coupled to the oscillator 2. The dc current flowing in oscillator 1 is kept constant $I_{STO1} = 6.3$ mA and the injection-locking range experiments (presented in the previous sections) are performed. These experiments are done for different values of flowing dc current through oscillator 2 I_{STO2}. The injection locking experiments were focused on oscillator

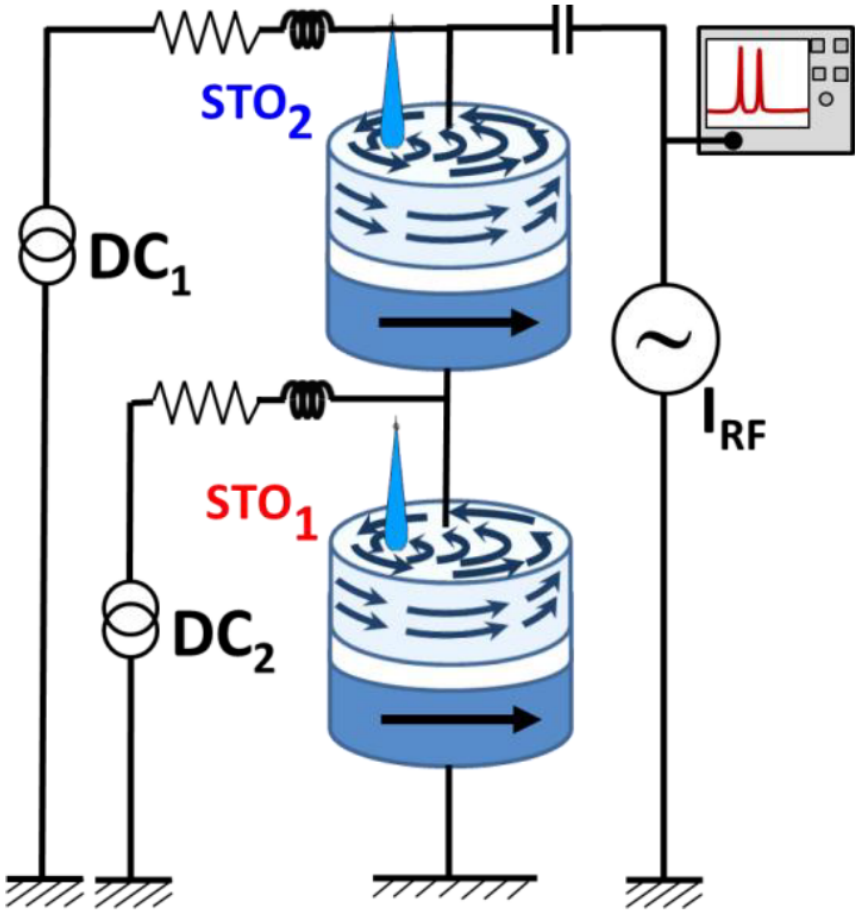

Figure 33: Schematic of the electrical circuit of the experimental system of two electrically coupled nano-oscillators.

1, because experimentally it exhibits a larger ability to adapt its frequency in presence of external stimuli.

Fig. 34 summarizes an injection-locking experiment obtained in the studied two coupled nano-oscillator system. The red filled square curve corresponds to the frequency of oscillator 1 in a situation where it is not electrically coupled the oscillator 2. Here, this situation is

obtained when the flowing current in oscillator 2 is zero $I_{STO2} = 0$ mA, which corresponds to an absence of oscillation and therefore microwave emission from this oscillator. In this situation, one can see that for frequencies of the external source between $F_{ext} = 762.8$ MHz and $F_{ext} = 766.18$ MHz, the frequency of oscillator 1 is locked to the half of the frequency of the external source. Thus, one can deduce an injection-locking range of $\Delta^{STO1}_{uncoupled} = 1.69$ MHz.

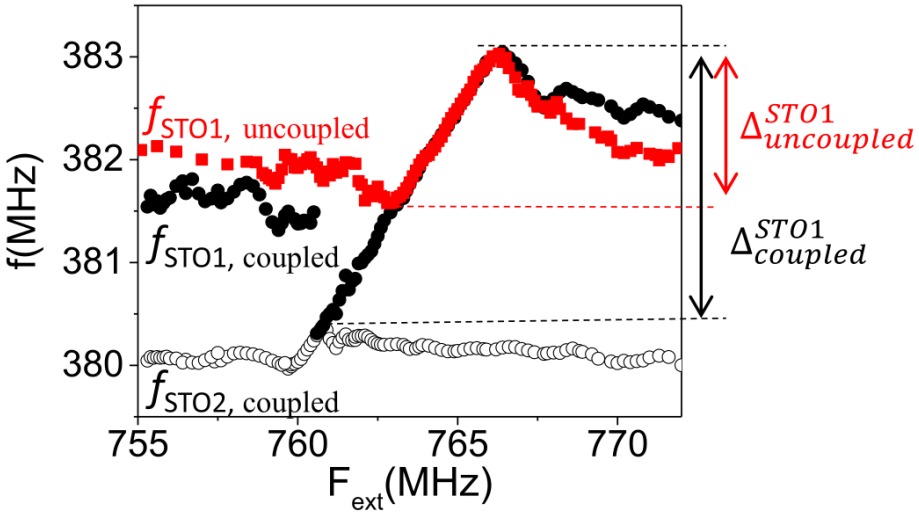

Figure 34: Injection locking experiments with oscillator 1 uncoupled ($I_{STO2} = 0$ mA, red squares) and with oscillator 1 coupled to oscillator 2 ($I_{STO2} = 3.25$ mA, black dots, solid dots represent the frequency of oscillator 1 and open dots the one of oscillator 2). The current applied to oscillator 1 is kept fixed ($I_{STO1} = 6.3$ mA). Vertical arrows highlight the injection locking range of oscillator 1, delimited by horizontal dashed lines.

Then, by injecting a sufficient dc current through oscillator 2 in order to induce its oscillation, the two oscillators couple together electrically. It should be noticed that the strength of coupling between oscillators is inversely proportional to their frequency difference [217]. In particular, for a small frequency difference this can lead to mutual synchronization [237]. For the studied experimental system, this occurs for a frequency difference lower than 2 MHz. Here, the mutual synchronization of oscillators is avoided by tuning the frequency of

the oscillators to obtain a frequency difference slightly larger than 2 MHz.

The black filled dots in Fig. 34 represent the frequency of oscillator 1 in a situation where this oscillator is coupled to oscillator 2 obtained for a current of $I_{STO2} = 3.25$ mA. Black open dots correspond to the frequency of oscillator 2 for this particular flowing current. One can see on the frequency evolution of oscillator 1, that its injection-locking range is expanded in a one side compared to a case where it is not coupled to the oscillator 2 ($I_{STO2} = 0$ mA). As a result, the injection-locking range grows from $\Delta^{STO1}_{uncoupled} = 1.69$ MHz in the uncoupled case to $\Delta^{STO1}_{coupled} = 2.77$ MHz in the case it is coupled.

When the frequency of the external source is increased (from left to right in Fig. 34), at some point the oscillator 1 starts to get attracted by the external source, thus its frequency is pulled down towards half of the frequency of the external source. Therefore, the frequency of oscillator of 1 becomes closer to the one of the oscillator 2. This causes an increase of their mutual interaction in such a way that the oscillator 2 starts to assist the external source in pulling down the frequency of oscillator 1. Due to this additional force, the frequency of oscillator 1 decreases further and gets locked to the common frequency shared by the oscillator 2 and the external source. This observed phenomena occurs at an external frequency $F_{ext} = 760.6$ MHz. As can be seen in Fig. 34, this frequency value is well lower than the value at which oscillator 1 gets locked to the external source in the uncoupled case corresponding to $F_{ext} = 762.8$ MHz. To summarize, the injection-locking range increases by 64 % in the coupled case compared to the uncoupled case.

In order to confirm the injection locking enhancement mechanism, numerical simulations were performed in both uncoupled and coupled cases. The frequency evolution of the two oscillators 1 and 2 obtained in these simulations are shown in Fig. 35. As for the experimental injection-locking results, the red square curves represent the frequency of the oscillator 1 in the uncoupled case, the black filled curve represent this frequency in the coupled case, and open black curve represent the frequency of the oscillator 2.

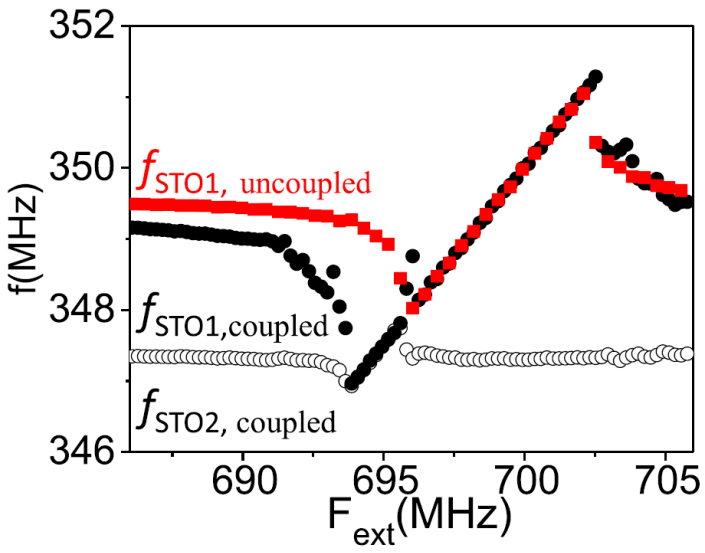

Figure 35: Numerical simulations of injection locking with oscillator 1 uncoupled ($I_{STO2} = 0$ mA, red squares) and coupled to oscillator 2 ($I_{STO2} = 3.57$ mA, black dots, solid dots represent the frequency of oscillator 1 and open dots the one of oscillator 2). The current applied to oscillator 1 is kept fixed ($I_{STO1} = 2.6$ mA).

In these simulations, the magnetization dynamics of two electrically coupled vortex oscillators is obtained by solving numerically the differential Thiele equation (presented in the previous sections) simultaneously for the two vortex $i = 1, 2$:

$$\mathbf{G_i} \times \frac{d\mathbf{X_i}}{dt} - \mathbf{D_i}(\mathbf{X_i})\frac{d\mathbf{X_i}}{dt} - \frac{\partial W_i(I_{rf}^{com})}{\partial \mathbf{X_i}} + \mathbf{F_i^{STT}}(I_{rf}^{com}) = 0 \quad (53)$$

Here, $\mathbf{X_i} = (x_i, y_i)$ is the vortex core position, $\mathbf{G_i}$ is the gyrovector, $\mathbf{D_i}$ is the damping, W_i is the potential energy of the vortex, $\mathbf{F_i^{STT}}$ is the spin-transfer force. The total microwave current I_{rf}^{com} flowing through the oscillators consists of the external microwave current provided by the source, as well as the microwave currents emitted by the oscillators themselves. This current is described as an additional common alternating current that goes through all N nano-oscillators [277] $I_{rf}^{com} = \frac{1}{Z_0 + \sum_{i=1}^{N} R_i} \sum_{i=1}^{N} \lambda \Delta R_i I_{dc}^i y_i$. Here ΔR_i is the mean resistance variation due to the vortex core gyrotropic motion through

tunnel magnetoresistance, Z_0 is the load impedance which is equal to 50 Ω, R_i is the resistance of the junctions and $\lambda = 2/3$[278]. The material parameters considered are extracted from the analytical fitting of the experimental response of each oscillator and are summarized in Tab. 2. As in the injection locking experiments presented previously in

Parameters	STO1	STO2
TMR	32%	8.6%
D $(kg.rad^{-1}.s^{-1})$	5.5×10^{-15}	1.14×10^{-15}
G $(kg.rad^{-1}.s^{-1})$	1.65×10^{-13}	1.09×10^{-13}
a_J $(kg.m^2.A^{-1}.s^{-2})$	20×10^{-17}	9.43×10^{-17}
b_j $(kg.m^2.A^{-1}.s^{-2})$	5.0×10^{-17}	1.14×10^{-17}
κ_{ms} $(kg.s^{-2})$	3×10^{-4}	1.43×10^{-4}
κ'_{ms} $(kg.s^{-2})$	7.5×10^{-4}	7.18×10^{-15}
κ_{Oe} $(kg.m^2.A^{-1}.s^{-2})$	5×10^{-16}	8.25×10^{-16}
κ'_{Oe} $(kg.m^2.A^{-1}.s^{-2})$	-4.2×10^{-15}	-6.2×10^{-15}
ξ	0.5	8.0

Table 2: Individual parameters of the two nano-oscillators used to simulate the experimental network of coupled spin-torque vortex oscillators. Here the TMR parameter corresponds to an effective value used in order to take into consideration the reduction induced by the applied dc current.

this section, the dc current flowing through oscillator 1 is kept constant $I_{STO1} = 2.6$ mA. The value of the applied dc current in this simulation is chosen is such a way to obtain oscillation frequencies comparable to the experimental one. The frequency obtained in simulations for the two vortex oscillators, are extracted from 5 μs time traces of the angular evolutions of the vortex core trajectories of the two oscillators. These simulations point out the fact that the observed synchronization ability at half of the frequency of the external signal is mainly due to the field-like torque (introduced in the previous sections).

As shown in Fig. 35, the injection-locking range presented in Fig. 34 increases due to the electrical coupling. Indeed, due to the electrical coupling between oscillator 1 and 2 in simulations, the injection-locking

range of oscillator 1 is increased from 3 MHz to 4.32 MHz. This corresponds to an enhancement of 42 % of its injection-locking range. These numerical results are in good agreement with the general behavior observed in injection-locking experiments in presence of coupling. In particular, it allows to reproduce the unidirectional injection-locking range enhancement. In fact, only the left frequency boundary of the locking range is modified in the presence of electrical coupling, while the upper bound of the locking range remains constant.

4.2.3 *Influence of the the coupling strength on the injection locking-range*

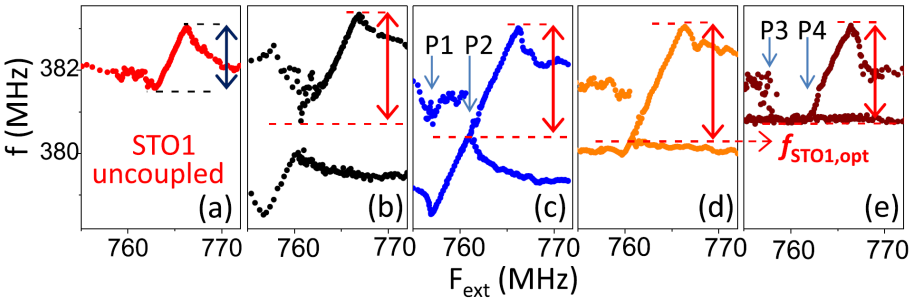

Figure 36: Experimental injection locking experiments at 2f and P=-15 dBm of oscillator 1 uncoupled (red curve) or coupled to oscillator 2 (black, blue, orange, and brown curves) for different I_{STO2} values of the dc current flowing through oscillator 2: respectively from left to right: $I_{STO2} = 0$ mA (red), $I_{STO2} = 2.95$mA (black), $I_{STO2} = 3.05$ mA (blue), $I_{STO2} = 3.25$ mA (orange), $I_{STO2} = 3.35$ mA (brown). Arrows highlight the injection locking range of oscillator 1, delimited by horizontal dashed lines. Figure extracted from [14]

In order to evaluate experimentally the influence of the coupling strength on the injection-locking range, the flowing dc current in oscillator 2 I_{STO2} is varied while the flowing dc current in oscillator 1 is maintained constant ($I_{STO1} = 6.3$ mA). Using this procedure, the frequency difference between the two oscillators is modified, which corresponds to the tuning of the electrical coupling strength between the two oscillator. More precisely, in the conditions of the experiment,

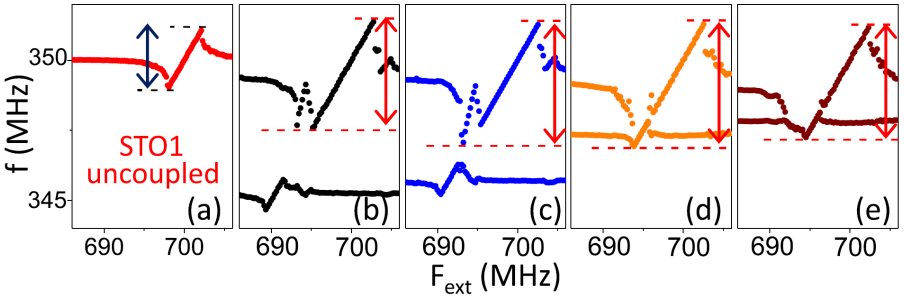

Figure 37: Simulations of injection locking experiments at 2f and P=-15 dBm of oscillator 1 uncoupled (red curve) or coupled to oscillator 2 (black, blue, orange, and brown curves) for different I_{STO2} values of the dc current flowing through oscillator 2: respectively from left to right: $I_{STO2} = 0$ mA (red), $I_{STO2} = 3.3$ mA (black), $I_{STO2} = 3.35$ mA (blue), $I_{STO2} = 3.57$ mA (orange), $I_{STO2} = 3.65$ mA (brown). Arrows highlight the injection locking range of oscillator 1, delimited by horizontal dashed lines. Figure extracted from [14]

an increase of the dc current flowing in oscillator 2 I_{STO2} is translated into a decrease of the frequency detuning between the two oscillators, and as a consequence to an increase of the coupling strength. In this line of thinking, the injection-locking range is performed at different values of I_{STO2}. Fig.36 and Fig.37 show injection-locking range results obtained at few different chosen I_{STO2} values, respectively in experiments and simulations. The first red graph of both of these two experimental and simulation figures (Fig.36 and Fig.37) correspond to the frequency evolution of the oscillator 1 where it is uncoupled to the other oscillator ($I_{STO2} = 0$ mA). The rest of the injection-locking graphs, represents injection locking situations where the oscillators are coupled: From left to right (black, blue, orange, and brown), these graphs are obtained for values of I_{STO2} increasing from 2.95 mA to 3.35 mA. In each of such graphs, the value of the injection-locking range of the oscillator 1 was extracted and its enhancement compared to a reference injection-locking range obtained in the uncoupled case is displayed in Fig. 38 and Fig. 39 respectively for experiments and simulations. In the case where the two oscillators are coupled, these two figures show how the injection-locking of oscillator 1 is enhanced

as a function of the flowing dc current in oscillator 2 I_{STO2}. In par-

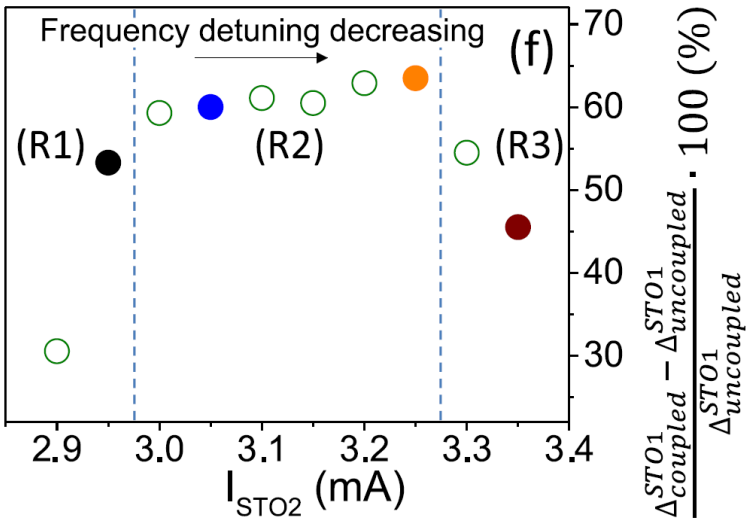

Figure 38: Experiments: Enhancement of the injection locking range of oscillator 1 due to its coupling to oscillator 2 as a function of the dc current applied on oscillator 2 I_{STO2}. The frequency difference between oscillators decreases as I_{STO2} increases. Filled dots are from the injection-locking data shown in Fig. 36 and are plotted with the same color than the corresponding injection-locking curves. Figure extracted from [14]

ticular, these figures show that by taking advantage of the coupling to oscillator 2, the experimental injection-locking range can be enhanced up to a value of 65% larger than the injection-locking range obtained in the uncoupled case. From the observation of these figures, one can also deduce 3 different trends in the evolution of the locking range as a function of I_{STO2} (see Fig. 38). In good agreement with experiments, the same qualitative bell shape evolution dependence as a function of I_{STO2} with the corresponding 3 trends is found. In both Fig. 38, the following regions can be distinguished:

- Region 1 (R1 in Fig. 38) corresponds to I_{STO2} lower than 3mA. In this region, the influence of the coupling is weak namely because the frequency detuning between oscillator 1 and 2 is still relatively large. In this region, the mechanism of enhancement of the injection-locking range of oscillator is due to the frequency pulling of oscillator's 1

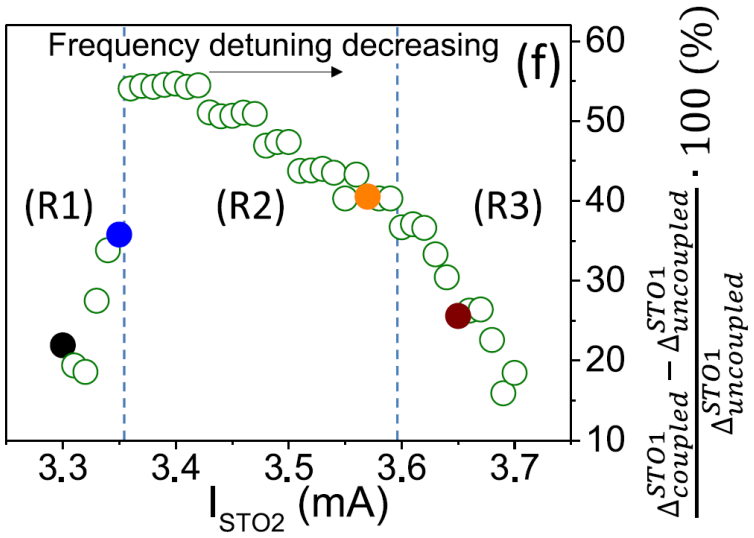

Figure 39: Simulations: enhancement of the injection locking range of oscillator 1 due to its coupling to oscillator 2 as a function of the dc current applied on oscillator 2 I_{STO2}. Filled dots are from the simulated injection-locking data shown in Fig. 37 and are plotted with the same color than the corresponding injection-locking curves. Figure extracted from [14]

frequency caused by the coupling to the oscillator 2, see Fig. 38-black curve. Due to injection-locking of oscillator 2 to the external signal, its frequency becomes close to the frequency of oscillator 1. Due to this effect, the frequency of oscillator 1 is strongly pulled down. As a consequence of this pulling mechanism, the injection-locking of oscillator 1 is enhanced up to 2.56 MHz which corresponds to an enhancement of 53% compared to the reference uncoupled situation. This behavior is also captured by numerical simulations and similar frequency evolutions can be seen in Fig. 39-black and blue curves. It should be noticed that an additional feature was identified in those figures, before the oscillator 1 is synchronized to the external source. In fact, the frequency of oscillator 1 evolves with a different slopes than the one given by the frequency of the external source. This effect was easier to highlight in simulations, however it is also present in experimental graphs and was identified as the locking of the oscillator 1 to a modulation signal defined as $F_{ext} - f_{STO2}$. In addition, concerning the region 1, Fig. 38 also shows that the injection locking range

of oscillator 1 sharply increases as a function of I_{STO2}. This observed phenomena can be explained by two factors:

First, the increase of I_{STO2} causes a reduction of the frequency detuning and oscillator 2 locks better and better to the external source. As a consequence, the frequency of oscillator 2 is more and more increased through injection locking. This increase of the frequency of oscillator 2 increases the interactions with oscillator 1 and allows a more efficient pulling of the frequency of oscillator 1.

The second factor corresponds to the increase of the power emitted by oscillator 2 when its applied dc current is increased. This increase of the emitted power is translated into an increase of the electrical coupling between the two oscillators and thus into an increase of the ability of oscillator 2 to attract the the oscillator 1.

- Region 2 (R2 in Fig. 38) corresponds to I_{STO2} between 3 and 3.25 mA. Due to the higher current applied in oscillator 2, the frequency detuning in this region is smaller than in region 1. Therefore the coupling between the two oscillators is also stronger. In this region R2, the injection locking range of oscillator 1 occurs through the simultaneous locking of oscillator 1 to oscillator 2 and to the external source. The blue curve of Fig. 38 shows how this injection locking occurs in this region R2. As in the region R1, a frequency pulling effect occurs towards the frequency of oscillator 1 (point P1 in Fig. 38-blue curve). It should be noticed that the frequency of oscillator 1 here is well below the minimum frequency of oscillator 1 in the reference uncoupled case corresponding to the red curves of Fig. 38. Upon increasing F_{ext}, oscillator 1 gets eventually locked to both the external source and oscillator 2. This effect can be seen when the frequency of oscillator 2 is increased due to frequency locking to the external source (point P2 in Fig. 38-blue curve). In this configuration, the injection locking range of oscillator 1 was estimated to 2.74 MHz which corresponds to an enhancement of 62% compared to the uncoupled case. When the frequency detuning between two oscillators is reduced further (see Fig. 38-orange curve) oscillator 1 gets locked to the external source at external frequency values F_{ext} around the upper boundary of the injection-locking range of the oscillator 2. As

it is shown in Fig. 39-orange curve, simulations reproduced the experimental observed behavior.

By observing the injection-locking evolution shown in region 2 of Fig. 38, one can see that the injection-locking range of oscillator 1 increases as a function of I_{STO2} but in a slower manner than in region 1, meaning that the reduction of the frequency detuning in this region does affect injection-locking range of oscillator 1. This can be explained by the fact that oscillator 1 does not only experience frequency pulling, but is also locked to the common frequency shared by the external source and the oscillator 2. In this situation, it should be noticed that there is a range of F_{ext} external frequency values for which the oscillator 2 has the same frequency than the external source $f_{STO2} = \frac{F_{ext}}{2}$ and is therefore independent from its applied dc current I_{STO2}. In this context, oscillator 1 gets lock to the external source, for a external frequency value (defining the lower boundary of the injection-locking range for the oscillator 1) which is independent of the frequency detuning. Therefore, the injection-locking range of oscillator 1 is independent can be seen as independent of the frequency detuning.

However, it should be noticed that upon increasing I_{STO2}, the power emitted by oscillator 2 continues to increase which increases the electrical coupling strength between the two oscillators. For this reason, the injection-locking range of oscillator 1 continue to increase slightly in region R2 while its evolution is independent of the frequency detuning. Highest injection-locking range enhancements were obtained in this region for $I_{STO2} = 3.25$ mA, which corresponds to an enhancement of 64% of the injection-locking range compared to the reference uncoupled situation.

- Region 3 (R3 in Fig. 38) corresponds to I_{STO2} higher than 3.25 mA. In this region the frequency detuning is smaller and the coupling strength is stronger compared to regions R2 and R1. Here, it should be noticed that for similar applied dc currents I_{STO2}, in a case where oscillator 2 is uncoupled, this oscillator shows a high emitted power and lower nonlinearity (see previous chapter). Due to these properties, the injection-locking range of oscillator 2 is small while it

attracts more strongly oscillator 1. As it is shown in Fig. 38-brown curve, oscillator 1 experiences a frequency pulling effect towards the external source which leads to the frequency locking between the two oscillators 1 and 2. It should be noticed that in this frequency locking configuration the oscillator 2 is not yet locked to the external source (point P3 in Fig. 38-brown curve). For higher external source frequency values F_{ext}, oscillator 1 gets eventually locked to the external source. However, this occurs only in a situation where $\frac{F_{ext}}{2} > f_{STO2}$ (point P4 in Fig. 38-brown curve).

This observed behavior was also captured by numerical simulations, see Fig. 39-brown curve. It should be noticed that in these simulation results, the minimum frequency reached by oscillator 1 is considered to be the lower boundary of its injection-locking range. In experimental results, this boundary corresponds to the frequency of oscillator 2. Using this definition for the injection-locking range of oscillator 1 decreases in region 3 upon increasing I_{STO2}. This observed decrease is due to the fact that in this region, the frequency of oscillator 2 which imposes the lower boundary of the injection-locking range of oscillator 1, is above the optimal frequency for which a maximum injection-locking range can be obtained (reached for $I_{STO2} = 3.25$ mA, in the region 2), see Fig. 38-brown curve. Therefore, by increasing I_{STO2}, the frequency of the oscillator 2 continue to increase which is translated as a reduction of the injection locking range of oscillator 1.

4.2.4 *Conclusion*

As a conclusion, the electrical coupling between spin-torque nano-oscillators allows to increase their ability to synchronize to external signal. More precisely, it allows to enhance the injection-locking range of one spin-torque oscillator to external sources. By modifying the coupling strength between the oscillators, this locking range can be tuned. As it was presented in this section, experimentally this was achieved by controlling the dc current flowing in the other oscillator. Two different mechanisms explain the enhancement of the injection-

locking: frequency pulling and frequency locking between oscillators. Due to these two different mechanisms, different trends in the dependencies of the injection-locking range on the frequency detuning were observed.

4.3 CONCLUSION

Experimental and simulation results concerning the enhancement and control of the synchronization ability of coupled spin-torque nano-oscillators to external signals was demonstrated. This is an important preliminary understanding on how synchronization of such oscillators in presence of electrical coupling can be controlled in assemblies of coupled oscillators. Indeed, the synchronization of such electrically coupled assemblies will be leveraged to realize neuromorphic computing operations.

The main results of this chapter are:

- Experimental demonstration of the control of the coupling between spin-torque oscillators thourgh their frequency detuning.
- Enhancement of the injection locking-range by a factor of 1.64, due to the electrical coupling
- Control of the synchronization ability of coupled spin-torque nano-oscilaltors.
- Identification of mechanisms explaining the evolution of the injection locking enhancement as a function of the frequency detuning.

5

FIRST DEMONSTRATION OF PATTERN RECOGNITION WITH COUPLED SPIN-TORQUE NANO-OSCILLATORS

In this chapter, I will present an experimental neuromorphic implementation of an array of four coupled oscillators based on spin-torque nano-oscillators. The pattern recognition of spoken vowels with a high success rate and the experimental demonstration of real-time learning based on the synchronization of nano-oscillators are the main results of this chapter. (This work is mainly described in [24]).

5.1 COMPUTATION PARADIGM LEVERAGING SYNCHRONIZATION PATTERN

5.1.1 *Oscillator-based network architecture for pattern recognition*

In this section the general architecture of the oscillator-based neural network that will be implemented experimentally is presented. The major point here is to highlight how synchronization phenomena occurring in such a network is leveraged in our experimental implementation. At the end, this network will be used to achieve pattern recognition (see last sections of this chapter). Importantly, in the same line of thinking presented at the end of chapter 1 [104] [33] [85], the neurons of the neural network, presented in the following, will be emulated by oscillators which possess their own natural frequency.

Fig. 40 presents the oscillatory neural network used for pattern recognition in this chapter. It consists of a network of oscillators illustrated in gray color which communicate with each other using bidirectional connections represented by blue arrows. We define those oscillators as "processing" ones. Each of them is connected to all the other ones. This connection layout correspond to an all-to-all coupling.

The input of this network is provided by a set of input oscillators which

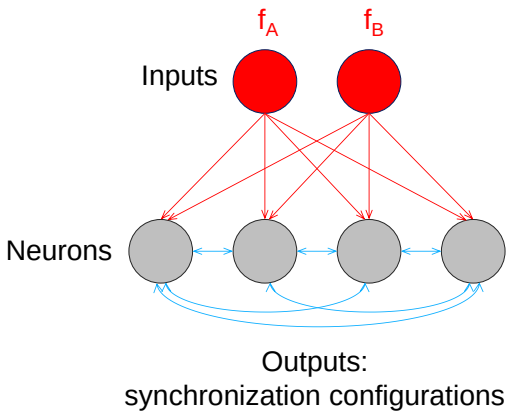

Figure 40: Schematic of the oscillatory-based neural network.

are represented in red color. Those oscillators possess unidirectional couplings to the processing oscillators. This means that on the one hand the input oscillators perturb the oscillation of the processing oscillators and on the other hand their oscillation frequency is not influenced by input oscillators. The inputs of the network are encoded in the natural frequency of these input oscillators that we call f_A and f_B.

In this present architecture, the output of the network corresponds to the synchronization state that can occur in the network. Depending on the inputs sent (f_A, f_B), distinct synchronization states can emerge from the network. It can be a synchronization between some of the processing oscillators or it can be a synchronization between input oscillators and the processing oscillators.

As seen in chapter 1, the pattern recognition potential of this oscillator-based neural architecture was already studied theoretically. In these studies, a slightly different variant of the presented network was proposed to realize pattern recognition tasks [3] [279] (see Fig. 15 of Chapter 1). In this variant, instead of having unidirectional connections as in Fig. 40, input oscillators have bidirectional ones. This means that the input oscillator itself is influenced by the other oscillators. The reason for the choice of unidirectional connections made for the experimental implementation, is that it simplifies the way the

inputs are presented to the network.

5.1.2 *Learning ability*

In order to realize complex cognitive tasks as image or spoken recognition, it is important to be able to perform learning which is ubiquitous in current artificial neural networks. The network presented in the previous subsection has the ability to perform learning to classify inputs properly. For this purpose, it is necessary to adjust the coupling strength between pairs of oscillators, similarly to the adjustment of synaptic connections between biological neurons (see chapter 1) in these networks. This led to approaches where each individual coupling between pairs of oscillators is manipulated during the learning process [33][85].

To achieve this goal, one way is to implement a strong coupling between oscillators leading to perfect synchronization. Beyond the fact that strong coupling is far from what is observed biologically in the brain where coupling between neurons is weak [280], this approach is difficult to implement physically in hardware. The difficulty of this approach comes from the fact that implementing hard-wired all-to-all connections between oscillators is required which can occupy large space in large network implementations. In addition, having a physical control on the coupling between oscillators in hardware, in particular at the nano-scale, still remains difficult to realize.

For all of these reasons, in order to achieve learning with spintronic nano-oscillators, we choose a different approach where we take inspiration from the learning scheme proposed by Vassieleva et al. [3]. In this approach, strong coupling and perfect synchronization between oscillators are not required. Instead, weak coupling and quasi-synchronization (see chapter 1) of the oscillator network are leveraged. In addition, this approach proposes a learning method where the natural frequencies of oscillators are adjusted. Indeed, a modification of natural frequency of two coupled oscillators can be translated as a modification of the coupling strength between them. As an example, for close natural

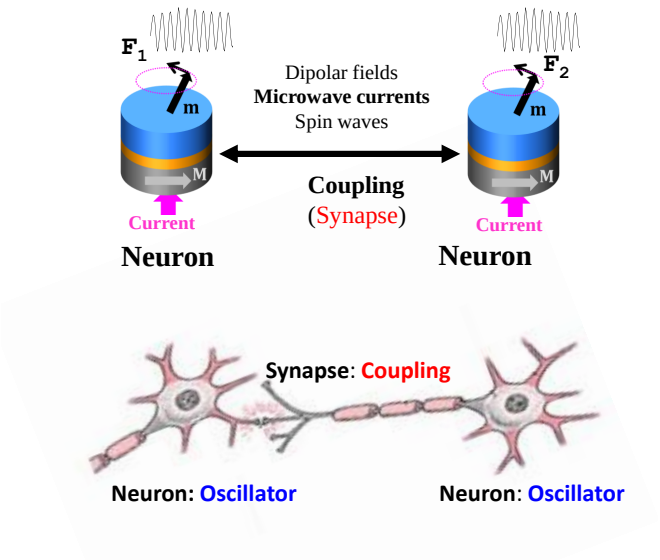

Figure 41: Bottom: Illustration of the synaptic connection between two biological neurons. Top: its spintronic oscillatory based equivalent composed of two coupled spin-torque nano-oscillators with a control on their oscillation frequency F_1 and F_2 using individual injected dc currents.

frequencies the coupling between oscillators will be stronger than for far natural frequencies.

A general view of the presented approach is shown in Fig. 41 where by analogy, the coupling phenomenon can be seen as a synaptic connection. In this schematic, the two interacting spin-torque nano-oscillators, with distinct natural frequencies F_1 and F_2, can be seen as two connected biological neurons. Different types of coupling between spin-torque nano-oscillators can occur. For instance it can be due to spin waves, dipolar fields or electrical microwave currents. As in the previous chapter, in order to manipulate those couplings, a modification of the natural frequency detuning $F_1 - F_2$ can be achieved by modifying the dc currents injected in each nano-oscillators. In the previous chapter, the synchronization properties of oscillators to external microwave signals was modified by changing their frequency detuning [14]. Following this approach, in the next sections, experimental learning will be achieved through the modification of

the natural frequency of each spin-torque nano-oscillator using the adjustment of the individual applied dc currents.

5.2 EXPERIMENTAL IMPLEMENTATION

5.2.1 *Samples*

The samples used for the demonstration of neuromorphic operations in this chapter are magnetic tunnel junctions with a MgO tunnel barrier. Contrary to the samples studied in the previous chapter, these samples have a FeB free-layer instead of a permalloy (NiFe) one. Those samples were fabricated in the group of S. Yuasa in the National Institute of Advanced Science and Technology (Tsukuba, Japan). They have a stacking structure of buffer/ PtMn(15)/ $Co_{71}Fe_{29}$(2.5)/ Ru(0.9)/ $CoFe_{20}B_{20}$(1.6)/ $Co_{70}Fe_{30}$(0.8)/ MgO(1)/ $Fe_{80}B_{20}$(4)/ MgO(1) / Ta(8)/ Ru(7) (thicknesses are given in brackets in nm)(Fig. 42). One should notice that the FeB layer is sandwiched in a stack of MgO/FeB/MgO/Ta. An additional MgO layer between FeB and Ta allows to reduce spin-pumping effects and as a consequence reduces the effective damping for which a smaller spin-torque is needed to destabilize the magnetization of the free-layer [165]. The resistance-area product (RA) is 3.6 $\Omega\mu m^2$. Samples were patterned with a diameter of 375 nm using Ar ion etching and e-beam lithography. The resistance of the samples is close to 40 Ω and the magneto-resistance ratio is about 100 % at room temperature. For the considered FeB free-layer dimensions (2R=375 nm, L=4 nm), as for the samples of the previous chapter the ground state is a magnetic vortex. Once again, we choose to use spin-torque nano-oscillators with a vortex magnetic texture because they have a high signal to noise ratio and the analytical description of their dynamics is well understood and matches experimental results quantitatively.

5.2.2 *Experimental set-up*

We transpose to hardware the neural network described in the previous section and illustrated in (Fig. 40) in the set-up illustrated in (Fig. 43). The symmetric neural interconnections between two neurons

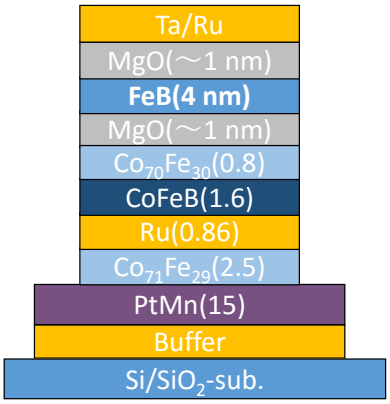

Figure 42: Schematic of the sample stack structure used for the neuromorphic task.

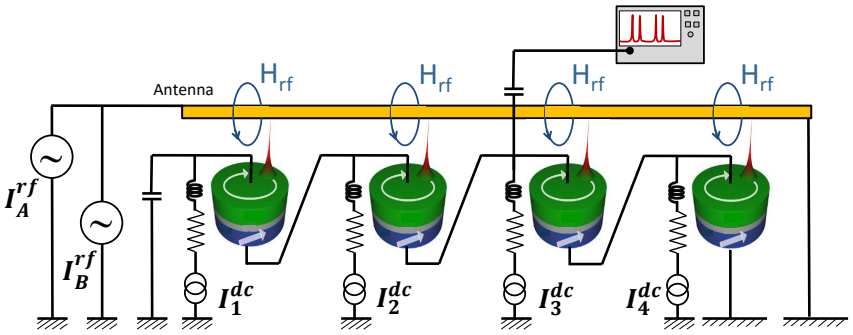

Figure 43: Schematic of the electrical circuit of the experimental nano-oscillator network used for bio-inspired operations.

illustrated in (Fig. 40) are implemented experimentally by connecting electrically the four nano-oscillators using millimeter-long aluminum wires. In this way, an electrical microwave loop is obtained where all microwave currents generated by every nano-oscillator propagate and in turn influence the common network dynamics. This mutual influence occurs because those emitted microwaves currents generate a microwave spin-torque in each nano-oscillator. This additional torque modifies the individual dynamics of every nano-oscillator, and in particular their frequency. Therefore, the four nano-oscillators are

electrically coupled. In this configuration, nano-oscillators are not coupled by the magnetic dipolar fields they radiate because they are too far away from each other (they are millimeters away). As in the previous chapter, a magnetic field is applied perpendicularly to all the four coupled spin-torque nano-oscillators. During all the experimental measurements presented in this chapter, this applied magnetic field is maintained constant: $\mu_0 H_\perp = 0.530$ T. To obtain self-sustained oscillations of the magnetization of each nano-oscillator, an applied dc current needs to be injected in each of them.

An important feature of the presented circuit is to have a control on the oscillation frequency of every nano-oscillator. To achieve this goal, we exploit the tunability property of oscillators. For this purpose, an individual control on the dc current flowing through each nano-oscillator was realized. Four dc currents ($I_1^{dc}, I_2^{dc}, I_3^{dc}, I_4^{dc}$) are supplied to the circuit by four different sources. The current flowing through each nano-oscillator ($I_1^{STNO}, I_2^{STNO}, I_3^{STNO}, I_4^{STNO}$) can be deduced by applying the Kirchhoff's current law:

$$\begin{aligned} I_1^{STNO} &= I_1^{dc} \\ I_2^{STNO} &= I_1^{dc} + I_2^{dc} \\ I_3^{STNO} &= I_1^{dc} + I_2^{dc} + I_3^{dc} \\ I_4^{STNO} &= I_1^{dc} + I_2^{dc} + I_3^{dc} + I_4^{dc} \end{aligned} \tag{54}$$

In order to inject two external microwave signals to the circuit, two different electrical microwave sources are used. Each of those sources A and B provide alternating monochromatic microwave currents with frequencies f_A and f_B with the same power amplitude $P_{ext} = 9$ dBm. These microwave currents are injected into a stripline fabricated on the top of the four nanopillars, therefore creating two alternating microwave magnetic fields in the vicinity of all of the four spin-torque nano-oscillators. The amplitude of these rf magnetic fields B_{rf}^{ind} seen by the active magnetic layer of the oscillators can be estimated by applying the Maxwell-Ampere's law. This amplitude depends only on two spatial parameters: the strip-line cross section and the distance between the strip-line and the nano-oscillator free-layer. The length of the strip-line antenna is set by the number of oscillators it should cover. In our case, the strip line has a width of 2.5 μm and

is fabricated 370 nm above the four nano-pillars. In order to moderate the injection of microwave eddy-currents due to the rf magnetic field, an insulating layer separates the strip-line and the nano-pillars. The resulting microwave fields seen by every nano-oscillator have an amplitude of B_{rf}^{ind}=0.1 mT. The magnetization dynamics of the four nano-oscillators is strongly affected by those microwave fields and as a result, the microwave emissions of the network is modified.

To detect microwave emissions of the four coupled nano-oscillator network, the alternating electrical current components are measured using a spectrum analyzer as shown in Fig. 43. A typical experimental frequency spectrum is shown in Fig. 44.

5.3 Experimental results on learning and pattern recognition

5.3.1 *Experimental synchronization states of the network*

In this section, we present the experimental synchronization states measured in the nano-oscillator network. The light blue curve of Fig. 44 show the frequency spectrum without inputs. In this case, we observe four different frequency peaks corresponding to the emitted microwave oscillations of the four spin-torque nano-oscillators. This spectrum also shows that the oscillator network is in a regime of moderate coupling where the oscillators dynamically influence each other but do not mutually synchronize.

The inputs of our experimental neural network are encoded in the frequencies f_A and f_B of the two fixed-amplitude microwave signals. When we send the inputs to the neural network, in other words when we inject the two microwave signals with frequencies f_A and f_B into the strip-line antenna, the frequency landscape of the network is modified. This output modification is shown in Fig. 44 by the frequency spectrum illustrated in dark blue. In this spectrum, we observe the apparition of two new narrow peaks represented in red in Fig. 44 with frequencies f_A and f_B. Therefore, the input signals from the strip-line can be detected in addition to the oscillator emissions. The presence of these input signatures in the frequency spectrum is due to capacitive

coupling between the strip line antenna and the metallic electrodes connecting the nano-oscillator. Therefore, an electrical microwave current is induced in the circuit.

The other microwave output change observed is that the peaks of oscillators 1 and 2 are shifted to lower frequencies. We interpret this shift as a frequency pulling effect where the frequency of those oscillators are attracted by the frequency f_A. An important observation on this dark blue spectrum is that the peak of oscillator 4 disappeared. This is because oscillator 4 is synchronized to the microwave input with frequency f_B. Therefore, for the illustrated frequency spectrum obtained with the set of microwave inputs ($f_A = 325$ MHz, $f_B = 370$ MHz), we are in presence of one particular synchronization state that we label (4B). In order to distinguish the different synchronization states of the network, we adopt the following notations:

- if oscillator (i) is synchronized to input X then the synchronization state is labelled as (iX).

- if oscillator (i) is synchronized to input X and at the same time oscillator (j) is synchronized to input Y then the synchronization state is labeled as (iX,jY).

By changing the set of microwave inputs (f_A,f_B), we have access to distinct synchronization states. As shown in (Fig. 45-left), by sweeping only one input frequency f_A and fixing the other one f_B, we were able to observe four different synchronizations states. When the frequency of the external source f^{ext} becomes close to the frequency of one of the oscillators $f^{(i)}_{STNO}$, the strong signal of the source pulls the adaptable frequency of the oscillator towards its own frequency value. One after the other, the four oscillators phase-lock to the external input illustrated by the red line. This synchronization occurs when the frequency of the external signal approaches the individual natural frequency of the oscillators shown by the blue dashed lines. In the locking range, the oscillator (i) shares the same frequency than the external signal. More generally, if the oscillator frequency $f^{(i)}_{STNO}$ coincides with the frequency of one of the external signals f^{ext}, we consider that the oscillator is synchronized to it. Practically, in our

analysis, we consider that the oscillator (i) is synchronized to an external signal if the following criteria is verified:

$$\mid f_{STNO}^{(i)} - f^{ext} \mid < \epsilon^{exp} \tag{55}$$

In our analysis we chose a threshold value $\epsilon^{exp} = 0.5$ MHz.

Keeping the dc currents through the oscillators fixed, the possible outputs of the neural network, represented in different colors in (Fig. 45-right), are the different synchronization configurations that appear for different frequencies of the two input signals. For every set of inputs (f_A,f_B), we measure the output frequency spectrum and deduce the corresponding synchronization states. Depending on the frequencies of the inputs (f_A, f_B), zero (grey regions), one or two oscillators are phase-locked. For example, in the petrol blue region labelled (2A), oscillator 2 is synchronized to input A. In the white region labelled (1A, 3B), oscillators 1 and 3 are synchronized to inputs A and B respectively. The synchronization state (4B) observed in the frequency spectrum of Fig. 44 is depicted in white-yellow color and can be seen as a rectangular frequency region.

To summarize, we experimentally identified 20 distinct synchronization states. All of these synchronization states measured here correspond to configurations where one or two oscillators are synchronized to one of the two external microwave inputs A or B.

5.3.2 *Spoken vowel classification task*

In this subsection, we present the classification task that we choose to implement using our experimental nano-oscillator network. We choose the spoken vowel classification task because, as the input of our neural network, this problem is already encoded in the frequency domain. This kind of frequency inputs is a particular example of what can be processed. Other kind of inputs could be sent and classified by our oscillator-based network.

In the case of spoken vowel classification task, vowels can be naturally described by a set of characteristic frequencies called formants.

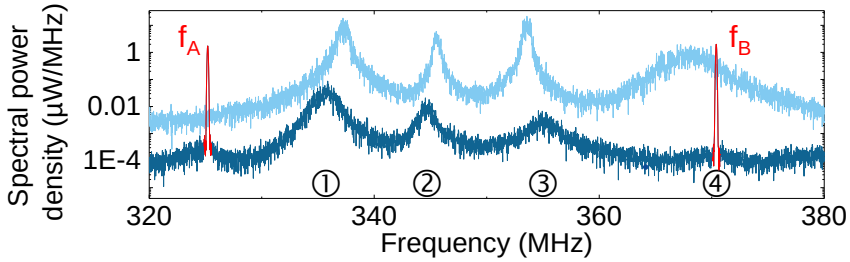

Figure 44: Microwave output emitted by the network of four oscillators without (light blue) and with (dark blue) the two microwave signals applied to the system. The two curves have been shifted vertically for clarity. The four peaks in the light blue curve correspond to the emissions of the four oscillators. The two red narrow peaks in the dark blue curve correspond to the external microwave signals with frequencies f_A and f_B. These frequency spectrum were obtained for an applied dc current set of $I_1 = 4.7$ mA, $I_2 = 6.2$ mA, $I_3 = 6.1$ mA and $I_4 = 5.5$ mA.

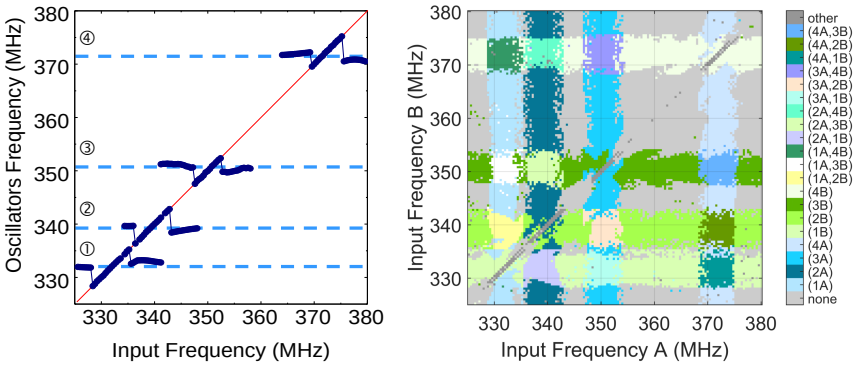

Figure 45: Left: Evolution of the four oscillator frequencies when the frequency of external source A is swept. Right: Experimental synchronization map of the nano-oscillator network in presence of two microwave stimuli having distinct frequencies. The x and y axis represent respectively the two frequencies f_A and f_B. Every color in this map illustrates one particular measured synchronization state appearing in the network, as described in the colorbar.

As shown in Fig. 46, by analyzing the Fourier transform of the temporal waveform of the pronounced vowel, the formant frequencies labeled as F_1, F_2, F_3, F_4 and F_5 can be identified on frequency spectra

as distinct frequency peaks. Fig. 47 shows the frequency distribution of the first and second formants F_1 and F_2 of 10 different spoken vowels represented by the 10 different elliptical curves containing cloud of points. Every point results from the pronunciation of a different speaker. It should be noticed that in the following we didn't choose this (F_1, F_2) representation of vowels to classify them because as shown in Fig. 47 the different clusters of vowels overlaps with each other. This means that distinct classes of vowels will have very similar F_1 and F_2 frequencies. For this reason, we also take into account in the inputs the additional formant frequencies to be able to distinguish classes of vowels between each other.

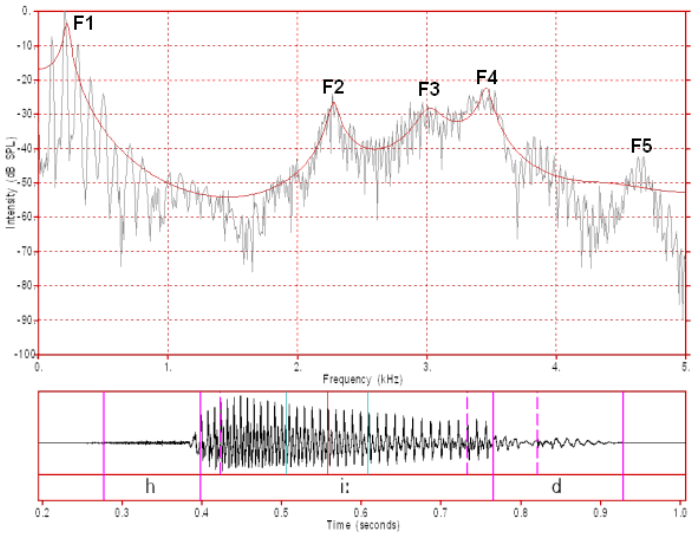

Figure 46: Top: Frequency spectrum of a vowel pronounced by a speaker. Bottom: Temporal waveform of a vowel pronounced by a speaker. This figure was extracted from Robert Mannell, http://clas.mq.edu.au/speech/acoustics/speech_spectra/fft_lpc_settings.html

We use as input data a subset of the Hillenbrand database comprising the following seven vowels pronounced by 37 different female speakers: "ae", "ah", "aw", "er", "ih", "iy" and "uw". Each vowel is characterized by 12 different frequencies. Those 12 frequencies correspond to 3 formants F_1, F_2 and F_3 evaluated in 4 different steps from the temporal waveforms. The first step is to evaluate those frequencies considering the temporal trace of the pronounced vowel in its steady

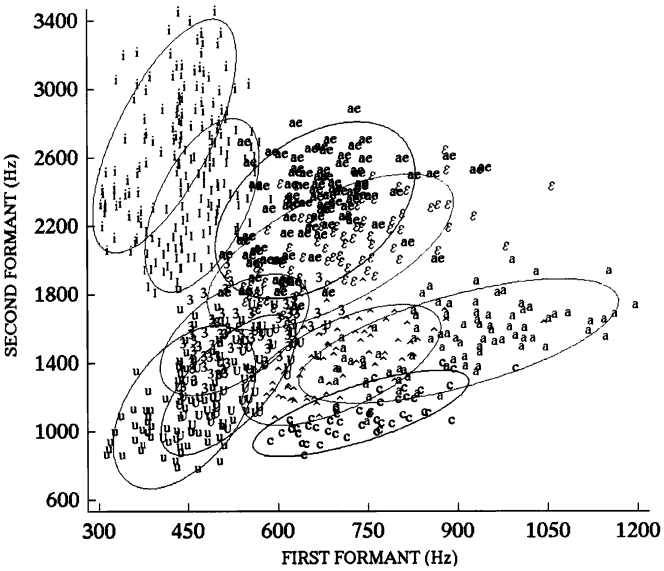

Figure 47: First two formant frequency distribution of different phonetic vowels extracted from Hillenbrand.[15]

state. The second, third and fourth steps are to evaluate formant frequencies respectively from the last 20%, 50% and 80% of the vowel waveform. To refer to these frequencies obtained using these four methods, we choose the following notation: $f_i^{steady-state}$, $f_i^{20\%}$, $f_i^{50\%}$ and $f_i^{80\%}$.

As illustrated in Fig. 46, the three first formant frequencies are typically in the range between 500 and 3500 Hz, therefore a transformation is needed to obtain input frequencies (f_A, f_B) in the range of operation of our oscillators between 325 and 380 MHz and that fit the grid-like geometry of the oscillator synchronization maps. For this purpose,

we perform two different linear combinations of these 12 formants in order to obtained two new characteristic frequencies (f_A, f_B):

$$\begin{aligned} f_A = A_1.f_1^{steady-state} + B_1.f_2^{steady-state} + C_1.f_3^{steady-state} \\ + D_1.f_1^{20\%} + E_1.f_2^{20\%} + G_1.f_3^{20\%} \\ + H_1.f_1^{50\%} + I_1.f_2^{50\%} + J_1.f_3^{50\%} \\ + K_1.f_1^{80\%} + L_1.f_2^{80\%} + M_1.f_3^{80\%} \\ + N_1 \end{aligned} \tag{56}$$

$$\begin{aligned} f_B = A_2.f_1^{steady-state} + B_2.f_2^{steady-state} + C_2.f_3^{steady-state} \\ + D_2.f_1^{20\%} + E_2.f_2^{20\%} + G_2.f_3^{20\%} \\ + H_2.f_1^{50\%} + I_2.f_2^{50\%} + J_2.f_3^{50\%} \\ + K_2.f_1^{80\%} + L_2.f_2^{80\%} + M_2.f_3^{80\%} \\ + N_2 \end{aligned} \tag{57}$$

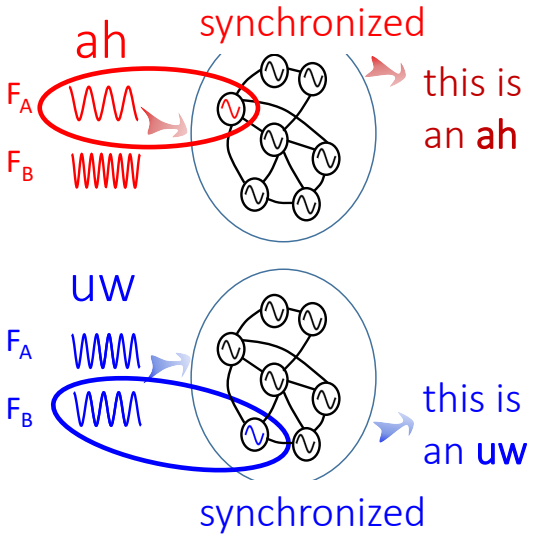

Figure 48: Principe of the vowel recognition procedure using synchronization.

The value of the coefficients of the two linear combinations are given in Appendix A.2. In order to choose these coefficients, we first record an experimental synchronization map, which is used as a calibration of the network. This synchronization map corresponds to

Spoken vowel	Synchronization pattern	Associated frequency difference vector
"ae"	(1A,3B)	$\mathbf{d_{ae}} = \begin{pmatrix} f_A^i - f_1 \\ 0 \\ f_B^i - f_3 \\ 0 \end{pmatrix}$
"ah"	(3A,1B)	$\mathbf{d_{ae}} = \begin{pmatrix} f_B^i - f_1 \\ 0 \\ f_A^i - f_3 \\ 0 \end{pmatrix}$
"aw"	(2A,1B)	$\mathbf{d_{ae}} = \begin{pmatrix} f_B^i - f_1 \\ f_A^i - f_2 \\ 0 \\ 0 \end{pmatrix}$
"er"	(1A,2B)	$\mathbf{d_{ae}} = \begin{pmatrix} f_A^i - f_1 \\ f_B^i - f_2 \\ 0 \\ 0 \end{pmatrix}$
"ih"	(3B)	$\mathbf{d_{ae}} = \begin{pmatrix} 0 \\ 0 \\ f_B^i - f_3 \\ 0 \end{pmatrix}$
"iy"	(4B)	$\mathbf{d_{ae}} = \begin{pmatrix} 0 \\ 0 \\ 0 \\ f_B^i - f_4 \end{pmatrix}$
"uw"	(1B)	$\mathbf{d_{ae}} = \begin{pmatrix} f_B^i - f_1 \\ 0 \\ 0 \\ 0 \end{pmatrix}$

Table 3: Table illustrating the synchronization states that we choose to assign to the seven vowels that we want to classify. The third column corresponds to a vector that will be evaluated during the learning procedure (see section 5.3.4).

a situation where all the synchronization states of the network are equally spaced in frequency from each other. In the next chapter, we will discuss the reason why we choose this specific synchonization map configuration to obtain high classification performances. Then, we assign a synchronization pattern to each vowel that we want to classify. Those assigned synchronization states are presented in Tab. 3. Then, the linear transformation of the formants that best matches the data points of each vowel with its associated synchronization pattern is determined through fitting by least square regression. The coefficients used in the two linear combinations and the two frequencies f_A and f_B corresponding to each vowel are given.

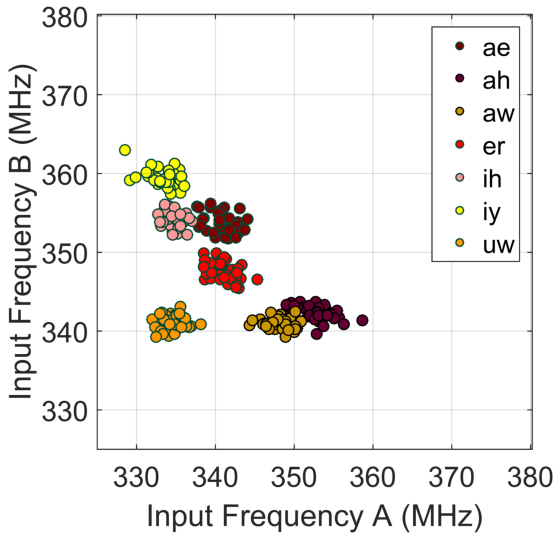

Figure 49: Inputs applied to the system, represented in the (f_A, f_B) plane. Each color corresponds to a different spoken vowel and each data point corresponds to a different speaker.

As a result, a new frequency representation of the spoken vowels is obtained in the plane (f_A, f_B). Fig. 49 illustrates the new vowel frequency distribution of the spoken vowels. Each point corresponds to one speaker. The spread in frequency for each vowel indicates that each speaker has a different pronunciation. Our goal is to recognize the vowel presented as input to the oscillator network independently of the speaker. Ideally, when different speakers pronounce the same vowel, we should expect the same output response of the neural network, which will be unique for the considered class of vowels. This principle is illustrated in Fig. 48. As shown in this figure, depending on the class of vowel presented to the network ("ae" or "aw"), the oscillator network will be in one unique synchronization state. Practically, one synchronization state corresponds to a situation where some oscillators of the network will be synchronized to one of the input stimuli. The important point is that vowels pronounced by different speakers but belonging to the same class of vowel should lead to the same synchronization state. And as a consequence, vowels belonging to different class of vowels should lead to different synchronization states.

This recognition principle can be translated graphically in our experimental synchronization state maps. Indeed, the scattered points corresponding to each vowel pronounced by different speakers should all be contained inside a different region of the oscillator synchronization map (Fig. 45-right). When we project those scattered points graphically in a configuration where the frequency of the oscillators are randomly chosen, as shown in (Fig. 53-a), the points corresponding to the same vowel class are spread through different synchronization states and the majority of them are not contained in a unique one. In order to approach a situation where most of the points corresponding to one vowel class are well contained in one unique synchronization state, it is necessary to modify the frequency position of the synchronization states. This modification of the frequencies is achieved through a learning procedure. The learning that was developed in this implementation is a supervised one.

5.3.3 *Cross validation procedure*

As the majority of supervised systems, our learning procedure is divided in two distinct stages: training and testing. Training was achieved using 80% of the total number of vowels in the database. The testing procedure was done using the remaining 20% data points. This allows estimating how a system is able to generalize what it learned in presence of unknown data points. To have a more precise estimation of this generalization performance, we apply a cross-validation technique. This technique allows estimating accurately the recognition performances of our network by repeating the training/testing procedure 5 times over distinct data point samples. Each time the selected data points used for testing are different: in the first (respectively second, third, fourth and fifth) cross-validation period, we use the first (respectively second, third, fourth and fifth) quintile (20%) of the data points for testing. This repartition of data points is illustrated in Fig. 50. The final recognition rate was obtained by averaging the testing recognition rates of the 5 cross-validation experiments. The same cross-validation procedure is used for all the neural networks (experimental and simulated).

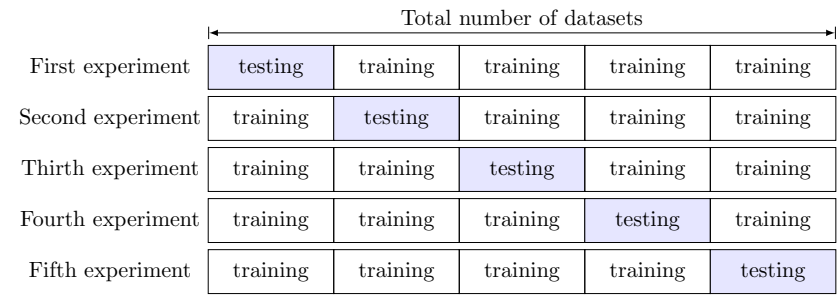

Figure 50: Schematic of the cross validation procedure. The total dataset is divided in five distinct subcategories (20%) where one of them corresponds to testing points illustrated in blue here. In our cross-validation procedure, we consider five different experiments where each time the testing dataset is chosen to be one of these five subcategories.

5.3.4 *Learning algorithm*

During the training stage, the internal parameters of the network need to be finely tuned until each synchronization region encompasses the cloud of points corresponding to the vowel it has been assigned. For this purpose, we take advantage of the high frequency tunability of spin-torque nano-oscillators to modify the synchronization map by tuning the dc current through each oscillator. This was achieved by adapting a training algorithm proposed by Vassieleva et al. [3] and described in the first section of this chapter.

The analysis of the output, which depends on the frequencies of the microwave inputs, can therefore easily be used to classify the spoken vowels. Using automatic LabView-Matlab program routines, we optimized our frequency spectrum analysis technique in order to be able to detect the synchronization states of the network in real-time during the experimental measurement.

Each spectrum recorded with the spectrum analyzer is sent to the computer, where a program analyzes it. The information we use as input to this program is: (i) the value of the two frequencies of the external microwave signals (f_A, f_B) and (ii) the oscillator frequencies at each dc current values in the absence of external microwave signals ($f_{1,0}$, $f_{2,0}$, $f_{3,0}$, $f_{4,0}$). The output data that we extract from each

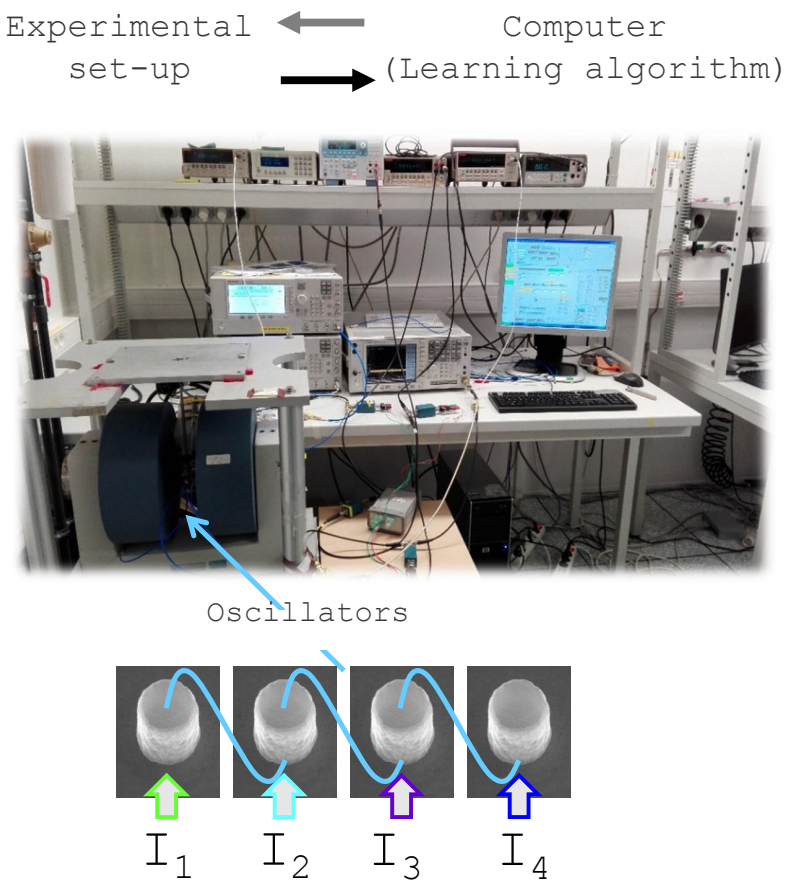

Figure 51: Experimental set-up used to achieve real-time training of the nano-oscillator network for vowel recognition task. The set-up can be seen as a feed-back loop between the experimental network and a computer.

spectrum analysis are the four values of the oscillator frequencies in the presence of microwave inputs. Then, another program takes these oscillator frequencies to extract the synchronization states and check if the applied vowel was properly recognized.

From this analysis, the synchronization pattern that corresponds to the input vowel is determined. This is compared to the synchronization pattern initially assigned to that specific vowel to check if it was successfully classified or not. If we are in the training proce-

dure and the vowel is not properly classified, the on-line learning algorithm calculates how the four dc currents should be modified to reduce the recognition error. This information is then sent back to the experimental set-up, where the dc currents are automatically modified accordingly.

Now, we present the training procedure that was applied to our spin-torque nano-oscillator network to learn to recognize different classes of input stimuli. We focus on synchronization states that were assigned to each class of vowel (Tab. 3). It should be noticed that possible mutual synchronization states due to the synchronization of pairs of oscillators are not considered. Only synchronization occurring between oscillators and external inputs are considered.

Graphically, to have a perfect recognition of one class of vowel, all data points in the frequency input map that correspond to this vowel (Fig. 49) must be contained in their assigned synchronization pattern in the experimental map (Fig. 45-right). If this is not the case, for each association spoken vowel-synchronization state we define a frequency difference vector with four components that will be used in the learning procedure. This vector is described in the third colomn of Tab. 3. Starting from a random map configuration Fig. 45-right, the automatic learning rule that I developed allows us to converge to a configuration where most data points for each vowel class are contained in their respective assigned synchronization pattern. This learning rule can be seen as a sign-stochastic gradient descent (sign-SGD) [281] which works in the following way:

a) We present to the network a randomly chosen input data point i belonging to one vowel class. This is equivalent to sending two microwave input stimuli with frequencies f_A^i and f_B^i.

b) From the resulting spectra, we extract the frequencies of the four spin-torque oscillators (f_1, f_2, f_3, f_4) in presence of the microwave input stimulus.

c) We determine the resulting synchronization configurations by comparing the oscillator frequencies to the input frequencies f_A^i and

f_B^i. Then, we compare the obtained synchronization configuration with the one assigned to this vowel.

d) For each vowel presented to the network, we define an associated frequency difference vector, which describes the frequency distance between the applied input and the assigned synchronization region. For instance, if the presented data point belongs to the vowel class «ae», we compute $\mathbf{d_{ae}} = \begin{pmatrix} f_A^i - f_1 \\ 0 \\ f_B^i - f_3 \\ 0 \end{pmatrix}$

If one of the two synchronization events assigned to «ae» has occurred, we only compute the frequency difference which corresponds to the other event. For instance, if oscillator 1 is correctly synchronized to external source f_A^i , then we compute only

$$\mathbf{d_{ae}} = \begin{pmatrix} 0 \\ 0 \\ f_B^i - f_3 \\ 0 \end{pmatrix}$$

e) We repeat steps a) to d) for all seven vowel classes.

f) We compute the sign of the vector sum of all seven associated frequency difference vectors $\mathbf{D}$:

$$\mathbf{D} = sgn(\mathbf{d_{ae}} + \mathbf{d_{ah}} + \mathbf{d_{aw}} + \mathbf{d_{er}} + \mathbf{d_{ih}} + \mathbf{d_{iy}} + \mathbf{d_{uw}}) = \begin{pmatrix} D_1 \\ D_2 \\ D_3 \\ D_4 \end{pmatrix}$$

g) Then, we compute a new dc current set $\begin{pmatrix} I_1' \\ I_2' \\ I_3' \\ I_4' \end{pmatrix}$, which will be applied to the four oscillators. This new dc current set is deduced from the following equation where the present injected dc current is updated:

$$\begin{pmatrix} I_1^{'} \\ I_2^{'} \\ I_3^{'} \\ I_4^{'} \end{pmatrix} = \begin{pmatrix} I_1 \\ I_2 \\ I_3 \\ I_4 \end{pmatrix} + \mu. \begin{pmatrix} D_1.sgn[(\frac{\partial f_1}{\partial I})_{I=I_1}] \\ D_2.sgn[(\frac{\partial f_2}{\partial I})_{I=I_2}] \\ D_3.sgn[(\frac{\partial f_3}{\partial I})_{I=I_3}] \\ D_4.sgn[(\frac{\partial f_4}{\partial I})_{I=I_4}] \end{pmatrix}$$

In this equation, $\mu = 0.1$ mA is the learning rate of our algorithm. At each step, the applied dc current through each oscillator can be modified only by $\pm\mu$. Here $sgn[(\frac{\partial f_k}{\partial I})_{I=I_k}]$ represents the sign of the frequency evolution versus injected dc current of the k-th-oscillator at the value of current I_k. For this, the frequency versus current dependence of each independent oscillator has been previously characterized. Upon modifying the dc currents following this learning procedure, the oscillator frequencies change. This translates into a displacement of the synchronization patterns in the experimental synchronization map.

We repeat all previous stages (stage a) to g)) N times where N is the total number of training steps. At each iteration (step i), the synchronization map evolves towards an optimal configuration where the global frequency difference vector $\mathbf{d_{tot}} = \mathbf{d_{ae}} + \mathbf{d_{ah}} + \mathbf{d_{aw}} + \mathbf{d_{er}} + \mathbf{d_{ih}} + \mathbf{d_{iy}} + \mathbf{d_{uw}}$ is minimized.

In the next section, we will see that by increasing the number of training steps N, we experimentally observe an increase of the recognition rate of all the vowels until it saturates.

5.3.5 *Demonstration of real-time learning for vowel recognition*

In Fig. 53, the synchronization maps obtained at different stages of the training process are illustrated: (a) step 0 (b) step 7 (c) step 15 and (d) step 86. Graphically, we see that step after step, cloud of vowels are less spread through different synchronization regions. In particular, in the synchronization map corresponding to step 86 (d), the majority of input points of the same class of vowels are well contained in one synchronization state. This situation corresponds to the case where the oscillator network learned to classify vowels correctly.

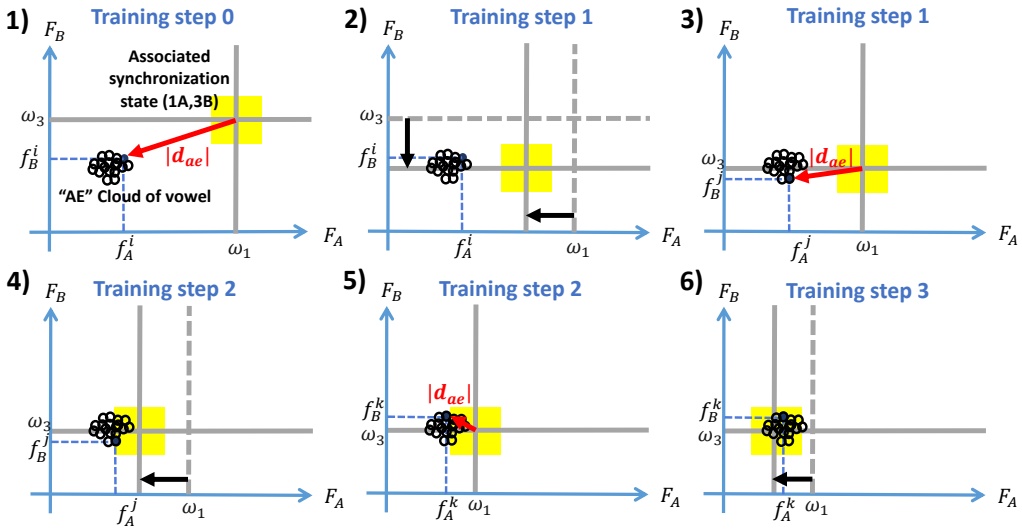

Figure 52: Principe of vowel recognition algorithm. Step after step, the synchronization state that was assigned to vowel "ae" is modifying its frequency position. This occurs in a such a way that the distance between the center of the synchronization state and one random chosen vowel at each step is reduced. The red arrow illustrates the distance vector at every step. An the end, the majority of the vowel cloud is contained in the synchronization state.

In Fig. 54, the dc current applied through each oscillator and the individual natural frequency of each of them are plotted during the learning process as a function of the training steps. The most important modification of applied dc current and frequency are observed at the beginning stages of the training process. After 48 training steps, dc currents and frequencies stop evolving, indicating that an optimum was found by the system. In order to know if at this final stage the oscillator network learned to classify vowels properly we need to evaluate the vowel recognition rate.

The average recognition rate for the seven vowels is represented as a function of the number of training steps in Fig. 55. Recognition rates obtained with the set of data points used for training and for

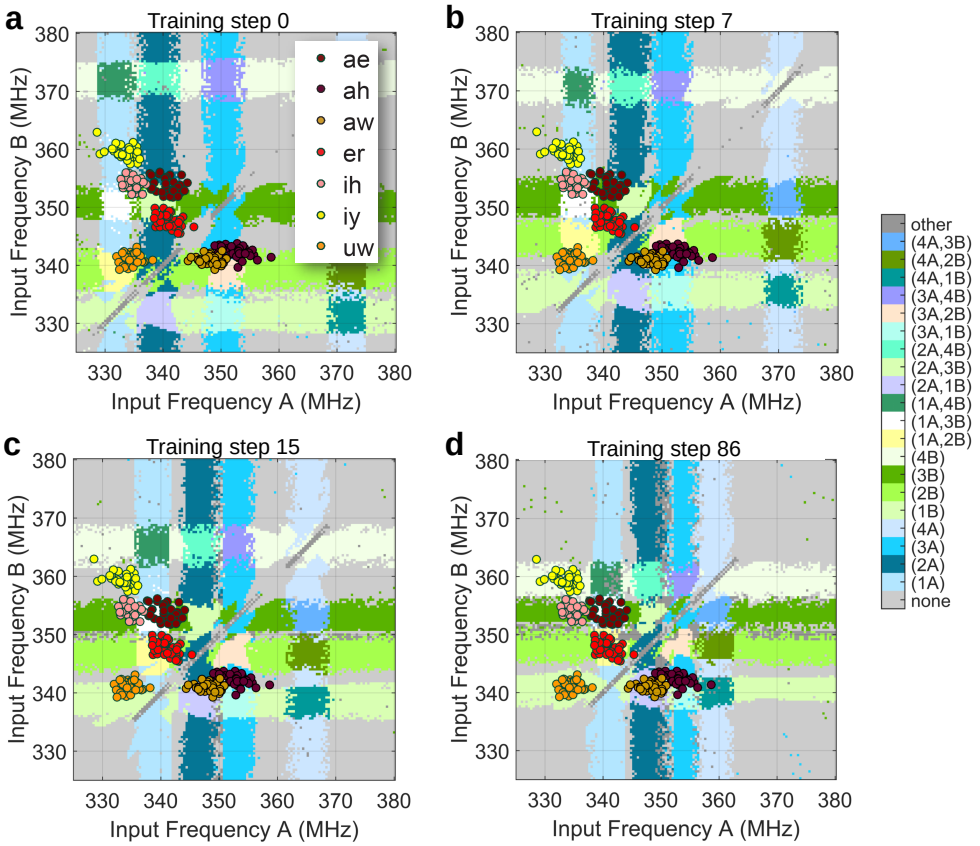

Figure 53: Experimental synchronization states maps measured at four different learning steps: step 0 (map a), step 7 (map b), step 15 (map c) and step 86 (map d). The circular colored points plotted on the top of every synchronization map correspond to the frequency distribution of the vowel input that should be recognized by the network.

testing are illustrated respectively by the red and orange curve. At step 0, the recognition rate is almost zero, signifying that vowels are not recognized at all. After step 48, this recognition rate saturates and stop increasing, signifying that the training process can be stopped. For the illustrated synchronization maps showing the learning process, the final recognition rates on the training and testing data sets reach values up to 89% and 88% respectively.

Using the cross validation technique presented in subsection 5.3.3,

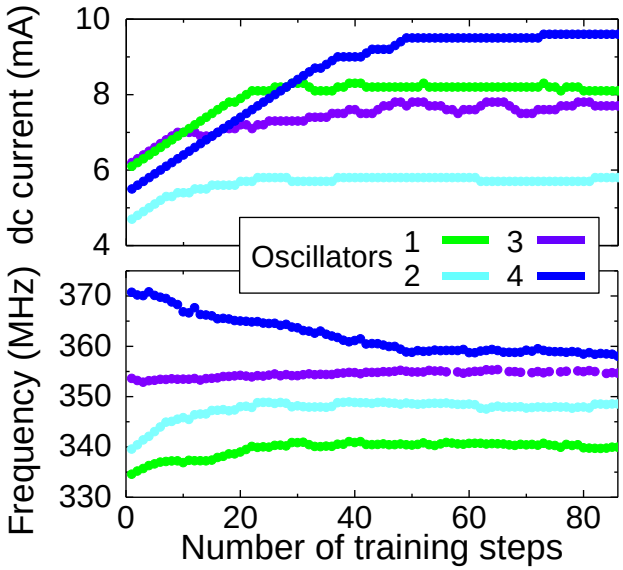

Figure 54: Top: experimental evolution of the individual applied dc currents I_1, I_2, I_3 and I_4 received by the four nano-oscillators as a function of the training steps of the learning process. Bottom: corresponding individual frequency evolution of the four nano-oscillators as a function of the training steps of the learning process.

we extract a reference value for the experimental recognition rate by repeating the training procedure experimentally several times with different combinations of training and testing sets. This cross-validation technique yields an average value of 84.3% for the experimental recognition rate on the testing set.

This performance of our oscillator network will be discussed and compared to the ones obtained with other forms of neural networks used in machine learning in section 5.3.7 of this chapter. A numerical study of this oscillatory-based network will be presented in the next chapter to understand and identify oscillator properties that will impact the obtained recognition performances.

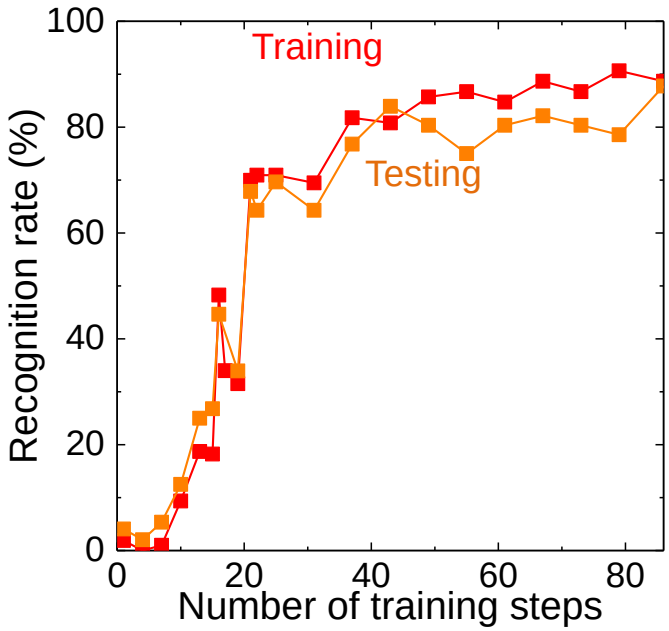

Figure 55: The experimental vowel recognition rate evolution as a function of the number of training steps during the learning process for both training examples (in red) and testing examples (in orange).

5.3.6 *Learning and recognition of higher number of vowel classes*

To go further, we show here that the scheme that we used to learn to classify 7 vowels can be extended to classify all twelve vowels of the Hillenbrand database. For this, we use a larger number of the twenty experimentally observed synchronization states and combine several of them to recognize the same class of vowel.

The initial and final map of synchronization states with the corresponding vowels is shown in Fig. 57. Similarly to the previous section, the currents injected in the oscillators, their frequency and the recognition rate during training are plotted in Fig. 57. We reach a recognition rate of 68.4% on train and test datasets.

This recognition rate is lower than the one obtained to classify 7 vowels. However, it can be increased in the future by increasing the number of oscillators in the system. Indeed, the number of synchronization regions that can be used and combined for recognition scales as N^2 where N is the number of oscillators [279].

5.3.7 *Comparison with static neural networks*

In order to have a deeper insight on the experimental recognition rates obtained with our oscillatory-based network, we compare it to more conventional forms of neural networks. The software simulation of these networks was realized with the help of our collaborators in C2N (Damir Vodenicarevic, Maxence Ernoult, Nicolas Locatelli and Damien Querlioz). In this comparison, the recognition performances that we consider are those obtained to classify the 7 class of vowels (see section 5.3.5). For this comparison study, we first consider a conventional, static, multi-layer neural network. This kind of network can achieve better-than-human recognition rates at complex tasks, such as image classification. This performance however, comes at the expense of the large number of parameters that need to be trained, a major hurdle for hardware implementation.

Fig. 58-b shows the recognition rate of a multilayer perceptron, trained in software through backpropagation on the same database as the experimental neural network, with 30,000 vowel presentations. As illustrated in Fig. 58-a, this network, composed of static neurons, takes as inputs the 12 formant frequencies characterizing each pronounced vowel. The first layer of this network corresponds to the linear combination that was applied to formants for our experiments. The hidden layer neurons, with *tanh* activation functions, receive a weighted sum of these inputs (plus a bias term). The output layer, with softmax activation functions, has seven neurons, one for each vowel class.

As can be seen in Fig. 58-b, the recognition rate is excellent, reaching 97% when the number of trained parameters is large (synaptic weights illustrated in red in Fig. 58-a). However, the performance rapidly degrades for small numbers of trained parameters, diving below 65%

for 27 trained parameters. This result is quite general: state-of-the-art networks with feedback such as standard Recurrent Neural Network (RNNs) or Long Term Short Term Memory networks (LSTMs) have limited performance when the number of trained parameters is small. In contrast, the recognition rate of our experimental oscillatory neural network is over 84% for only 30 trained parameters: as illustrated in red in Fig. 58-c, the 26 weights converting formants to inputs, and the currents through the oscillators. For an ideal, noiseless, oscillatory network, the success rate reaches 89% after cross validation (see next Chapter). The networks also learn rapidly (350 vowel presentations are used).

This high performance with a small number of trained parameters comes from the combination of two phenomena: as shown in Fig. 58-c the oscillatory network can do better than the sum of its individual components due to its complex, coupled, dynamical features and in addition, the oscillators collectively contribute to pattern recognition by synchronizing to the inputs. This result shows that the performance of hardware neural networks can be boosted by enhancing neuron functionalities beyond simple non-linear activation functions, through oscillations and synchronization.

5.4 CONCLUSION

We have seen in this chapter the first experimental demonstration of brain-inspired computing operation with a network of coupled nano-oscillators. We focused on the spoken vowel recognition task and were able to demonstrate the recognition of 7 of them with a success rate of 88%. To reach this performances, we were able to realize the experimental demonstration of learning capabilities with coupled oscillators. This learning capability was possible through the tunability property of the studied oscillators.

The main results of this chapter are:

- Design of the experimental oscillatory based neural network implementing electrical microwave connections coupling four spin-torque nano-oscillators.
- Experimental demonstration of the recognition of seven vowels using nano-oscillators with the performances close to the state of the art: 88%.
- Experimental demonstration of learning ability of the nano-oscillator network through the adjustments of natural oscillator frequencies using the modification of the individual applied dc currents.
- Experimental demonstration of the recognition of twelve vowels using nano-oscillators with a success rate of 68.4%.

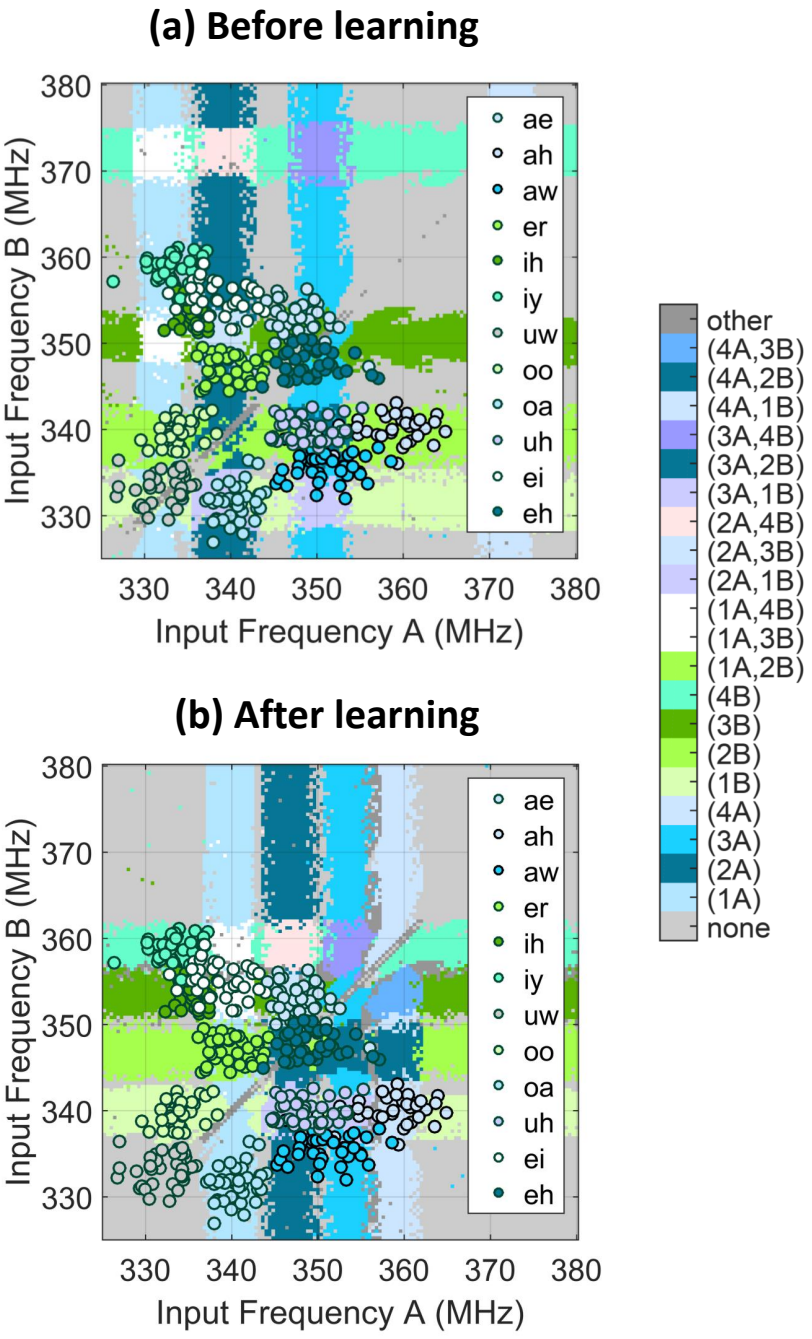

Figure 56: Recognition of twelve vowels using experimental synchronization states maps measured at two different learning steps: before learning (map a) and after learning (map b). The circular colored points plotted on the top of every synchronization map correspond to the frequency distribution of the vowel inputs that should be recognized by the network.

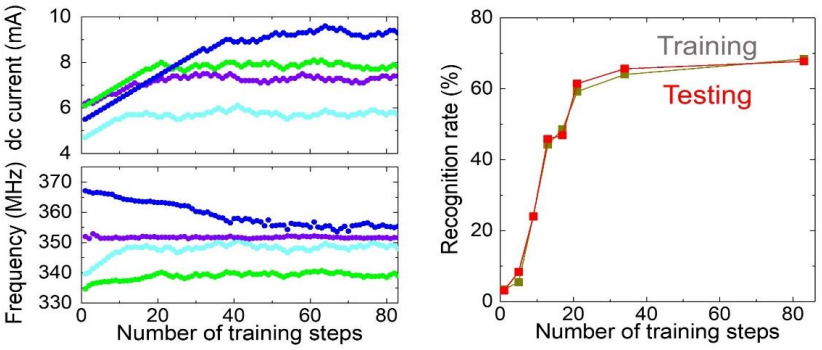

Figure 57: Left: Experimental evolution of the individual applied dc currents received by the four nano-oscillators as a function of the training steps (top). Corresponding individual frequency evolution of the four nano-oscillators as a function of the training steps of the learning process (bottom). Right: Experimental recognition of twelve vowels as a function of the number of training steps during the learning process for both training examples (in red) and testing examples (in orange).

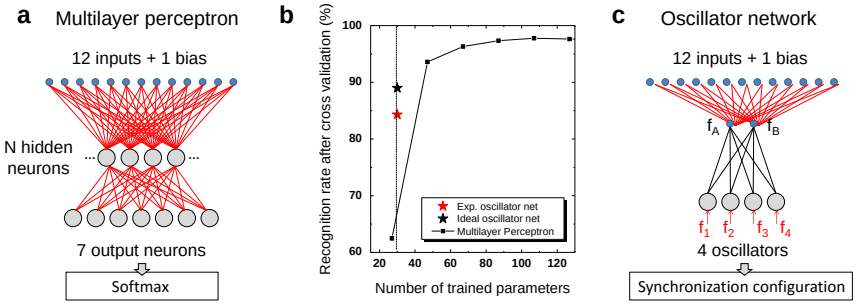

Figure 58: a) Schematic diagram of the multilayer perceptron artificial neural network simulated in order to perform spoken vowel recognition. b) Evolution of the vowel recognition rate as a function of the number of trained parameters for the simulated multilayer perceptron and its comparison to the experimental results of the oscillator network for the same task. c) Schematic diagram of the equivalent artificial neural network corresponding to our experimental oscillator network.

6

OPTIMIZING THE RECOGNITION PERFORMANCES OF COUPLED NANO-OSCILLATORS

In this chapter, in order to understand and optimize the recognition performances of coupled nano-oscillator networks, I simulate numerically arrays of coupled nano-oscillators. I present the numerical simulations that were performed to investigate the important features that oscillators should possess to classify accurately. I mainly evaluate the impact of different oscillator characteristics as tunability and mutual coupling on the classification performance of the network. Two type of simulations were realized: one where I focus numerically on the behavior of the experimental spintronic neuromorphic implementation including natural nano-device variabilities presented in the previous chapter, and the other one where I consider the case of general nonlinear oscillators. (This work is partly described in [24]).

6.1 NUMERICAL IMPLEMENTATION

6.1.1 *Numerical study of spin-torque vortex oscillator array: results reproducing experiments*

The model of coupled Thiele equations was used to reproduce the recognition performances observed in the experiment presented in the previous chapter. This requires to reproduce quantitatively the frequency position of synchronization states of the network. For this purpose, we first calibrate the individual model describing each nano-oscillator. Therefore, before considering the case of coupled nano-oscillators, we simulate analytically the behavior of every nano-oscillator of the experimental network which are different from each other. These differences are due to nano-oscillator variabilities which can appear because of the manufacturing process.

The black curves shown in Fig. 59 are the experimental frequency versus applied dc current response of the four oscillators used in the

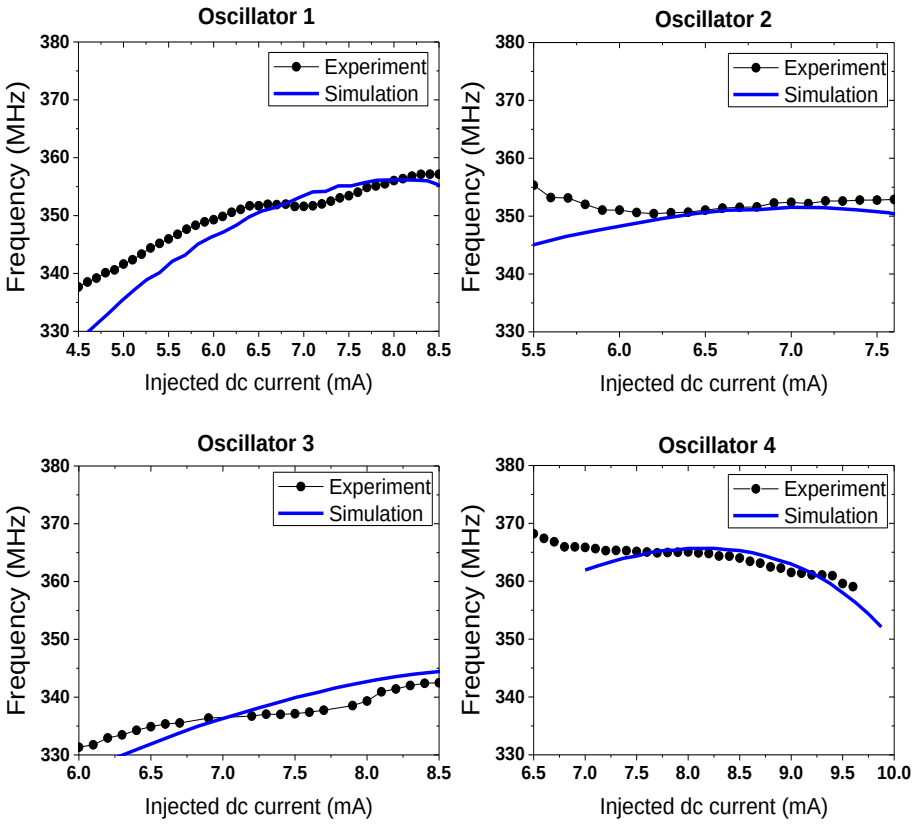

Figure 59: Experimental (black) and numerical (blue) frequency versus applied dc current evolution of the four spin-torque vortex nano-oscillators used for neuromorphic computation.

experimental network presented in the previous chapter. These measurements were performed before the demonstration of neuromorphic operations under a perpendicular applied magnetic field $\mu_0 H_\perp = 0.530$ T. The blue line drawn on top of those experimental curves of the Fig. 59 are the simulated frequency versus applied dc current responses obtained by solving the individual Thiele equations. As it is shown we find a relatively good agreement between the experiment and the simulation. The simulation parameters defined in chapter 2 (vortex dynamics section) used to obtain this good agreement are presented in Tab. 4. Those parameters slightly differ from the theoretical ones but still remain in the same expected order of magnitude.

Parameters	Oscillator1	Oscillator2	Oscillator3	Oscillator4	Theoretical
TMR	74.35%	91.67%	80.58%	74.35%	100%
b_j	1.05×10^{-17}	1.13×10^{-17}	7.44×10^{-18}	2.73×10^{-17}	-
D $(kg.rad^{-1}.s^{-1})$	5.5×10^{-15}	1.14×10^{-15}	5.5×10^{-15}	1.14×10^{-15}	4.05×10^{-15}
G $(kg.rad^{-1}.s^{-1})$	2.43×10^{-13}	2.47×10^{-13}	2.73×10^{-13}	2.37×10^{-13}	1.53×10^{-13}
a_j $(kg.m^2.A^{-1}.s^{-2})$	1.76×10^{-16}	1.62×10^{-16}	1.24×10^{-16}	1.63×10^{-16}	5.55×10^{-16}
κ_{ms} $(kg.s^{-2})$	4×10^{-4}	4×10^{-4}	4×10^{-4}	4×10^{-4}	1.23×10^{-4}
κ'_{ms} $(kg.s^{-2})$	9.6×10^{-5}	9.6×10^{-5}	1×10^{-3}	1×10^{-3}	3.08×10^{-5}
κ_{Oe} $(kg.m^2.A^{-1}.s^{-2})$	2.93×10^{-15}	2.93×10^{-15}	2.93×10^{-15}	2.93×10^{-15}	2.30×10^{-15}
κ'_{Oe} $(kg.m^2.A^{-1}.s^{-2})$	-6.75×10^{-15}	-6.75×10^{-15}	-4.25×10^{-15}	-2.93×10^{-15}	1.15×10^{-15}
ξ	3.5	2.1	4.0	1.1	0.6

Table 4: Individual parameters of the four nano-oscillators used to simulate the experimental network of coupled spin-torque vortex oscillators. The last column corresponds to the theoretical values expected for the oscillators used in the experiment.

6.1.2 *Simulation of the synchronization states of the experimental network*

Once the individual frequency versus applied dc current responses are well described by the simulation, we go a step further to reproduce the synchronization states observed experimentally. For this purpose, we numerically solve the differential system of the four coupled Thiele equations in presence of two distinct external forces A and B. This differential system of coupled Thiele equations is simply an extension of the model used in chapter 3 from two to four coupled nano-oscillators (see Eq. 53). The magnetization dynamics of the four nano-oscillators is obtained by solving numerically the coupled differential Thiele equation 58 simultaneously for the four vortex $i = 1, 2, 3, 4$.

$$\mathbf{G_i} \times \frac{d\mathbf{X_i}}{dt} - \mathbf{D_i}(\mathbf{X_i})\frac{d\mathbf{X_i}}{dt} - \frac{\partial W_i(I_{rf}^{com})}{\partial \mathbf{X_i}} + \mathbf{F_i^{STT}}(I_{rf}^{com}) = 0 \quad (58)$$

Here, $\mathbf{X_i} = (X_i, Y_i)$ is the vortex core position, $\mathbf{G_i}$ is the gyrovector, $\mathbf{D_i}$ is the damping, W_i is the potential energy of the vortex, $\mathbf{F_i^{STT}}$ is the spin-transfer force.

As in chapter 3, the electrical coupling between nano-oscillators due to their microwave emissions is described as an additional common

alternating current that goes through all nano-oscillators [277] $I_{rf}^{com} = \frac{1}{Z_0 + \sum_{i=1}^{4} R_i} \sum_{i=1}^{4} \lambda \Delta R_i I_i^{STNO} y_i$. Here ΔR_i is the mean resistance variation due to the vortex core gyrotropic motion through tunnel magnetoresistance, Z_0 is the load impedance which is equal to 50 Ω, R_i is the resistance of the junctions and $\lambda = 2/3$ [278]. Here $y_i = \frac{Y_i}{r_i}$ is the Y position of the vortex core in the nano-dot plane (X, Y) normalized by the radius of the free-layer r_i. This description of the resistance variation is obtained for a magnetization of the reference layer which is aligned with the x axis.

As in the experiment described in the previous chapter, the two forces A and B are introduced to our simulation model as two distinct microwave magnetic fields acting on the vortex core trajectory. They have the same amplitude with two distinct frequencies that we call f_A and f_B (as previously).

With a frequency step of $df = 0.2$ MHz, we sweep the frequency f_A and f_B of the two external forces in the same frequency range than in the experiment between 320 and 380 MHz. Thus each simulated synchronization map (see Fig. 60) is constituted of 300x300=90 000 simulated points. These simulated points are independent from each other. This allows us to run simulations in parallel on GPUs (Graphics Processing Unit). Every simulated pixel in the map is calculated by numerically solving the system of coupled differential equation 58 using a fourth order Runge-Kutta scheme in absence of thermal fluctuations (T=0 K). By evaluating the Cartesian position and velocity of each vortex core in the dot-plane (x, y), we extract the instantaneous frequency of each oscillator through the angular evolution $f(t) = \frac{1}{2\pi}\frac{d\phi}{dt}$. The steady state frequency of each oscillator is obtained by computing the temporal average of the instantaneous frequency over the last 20% of the simulated time trace. The duration of every complete time trace was 5 μs. As in the experiment, the synchronization between oscillators and external microwave signals is detected by analyzing the frequency difference between oscillators and external sources (see criteria of chapter 4, Eq. 55) with the same frequency threshold $\epsilon^{exp} = 0.5$ MHz. It should be noticed that these

simulations do not capture the noisy response of oscillators at the nano-scale.

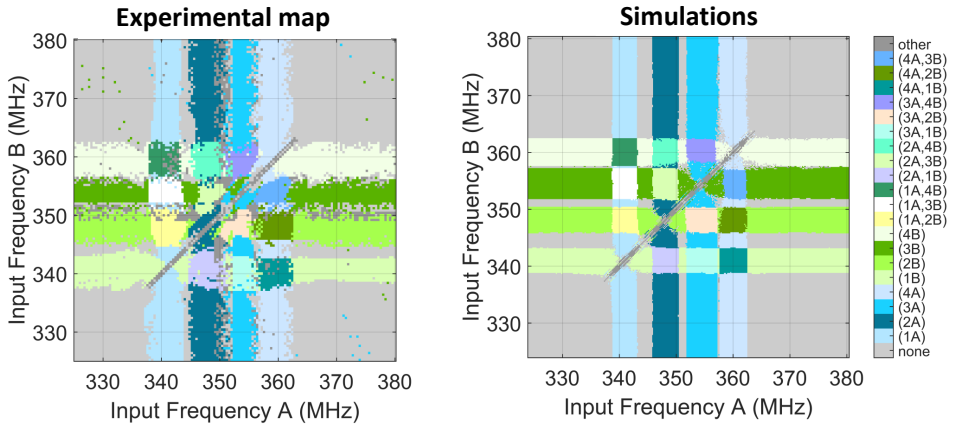

Figure 60: Left: Experimental synchronization state map obtained at the step 86 of the training process presented in the previous chapter. Right: Simulated synchronization state map obtained using the parameters presented in Tab. 4.

As it is shown in Fig. 60, we find a good agreement in terms of frequency between the synchronization state obtained at step 86 of the training process presented in the previous chapter and the synchronization state map obtained from the simulation of coupled Thiele equation in presence of external microwave stimuli. The set of applied dc currents in the simulated model differs quantitatively from the ones used in the experiment. This is mainly due to the fact that frequency versus applied dc current characteristics slightly differs between the experimental measurement and the analytical description (see Fig. 59). This good agreement between experiment and simulation is also confirmed for other sets of applied dc current corresponding to distinct training steps in the experiment. As an example, the measured synchronization states illustrated in Fig. 61 corresponding respectively to steps 7, 15, 35 and 44 of the training process, are similar in frequency positions to the simulated synchronization states obtained for the dc current sets applied in the experiments. The observed good agreement between the presented simulations and our experiments, validates the

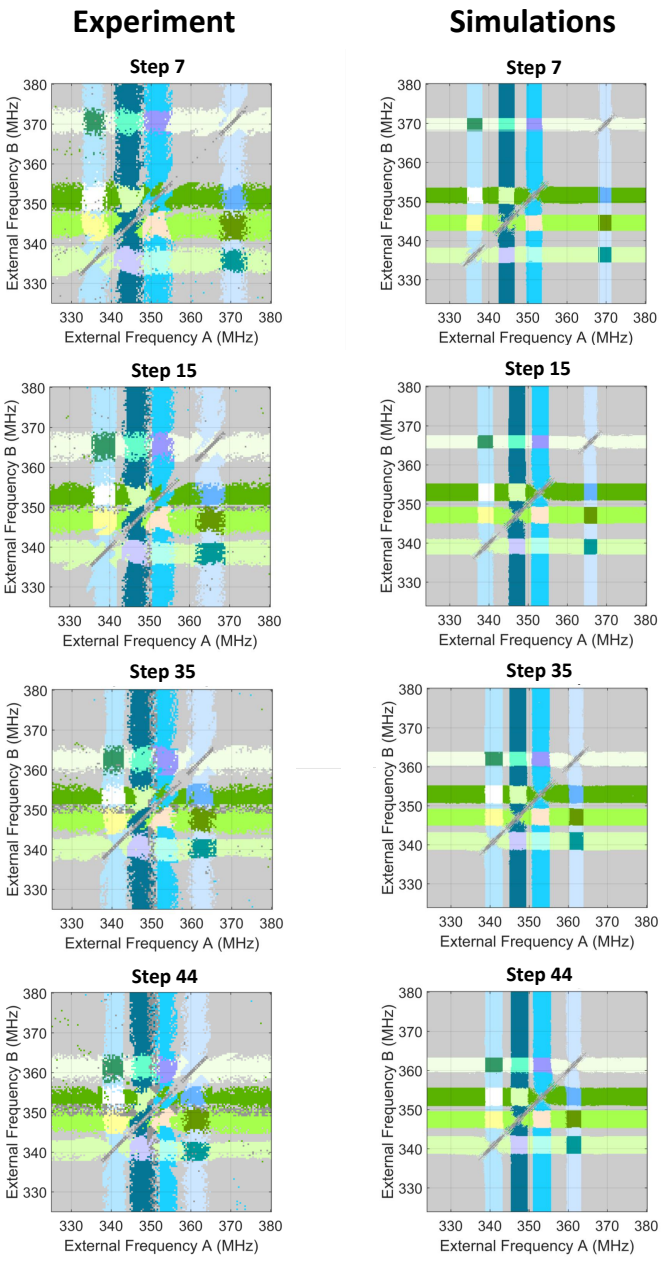

Figure 61: Left colomn: Experimental synchronization states obtained at steps 7, 15, 35 and 44 of the training process. Right column: Simulated synchronization state maps corresponding to training steps of the experiment.

choice of our model which will be used in the sections 6.2 and 6.3 to evaluate the recognition performances of our implementation.

6.1.3 *Numerical study of general ideal nonlinear oscillators*

Besides the particular case of spin-torque nano-oscillators, the interest of a more general model should be emphasized. Indeed, using a more general model will allow to not only use spintronic nano-oscillators but also open the perspective of taking advantage of other categories of nonlinear oscillators. For this reason, we simulate arrays of ideal nonlinear oscillators. By ideal, we mean that the oscillators are noiseless and can have an arbitrary large ability to modify their dynamics. To simulate those oscillators, we consider the van der Pol model of nonlinear dynamics that captures the main qualitative features of spin-torque nano-oscillators and can be generalized to other nonlinear oscillators (see examples in chapter 1). Another important feature of this numerical study is the absence of variability from an oscillator to another which was not the case in the model presented in the previous section. Indeed, we consider four identical nonlinear oscillators which only differ by their natural frequencies $\omega_{0,i}$. More precisely, their natural frequency differ by a relative mismatch of 2%. ($\omega_{0,i+1} = 1.02 \times \omega_{0,i}$) which is analogous to the mismatch observed experimentally. The dynamics of oscillators are modified by two microwave signals A and B with a force amplitude F_e and distinct frequencies $\omega_{e,A}$ and $\omega_{e,B}$. This leads to the following differential equations Eq. 59-60 in polar coordinates (s_i, ϕ_i), where the index i ($i = 1, 2, 3, 4$) represents the i-th oscillator:

$$\begin{aligned} \frac{ds_i}{dt} &= -\alpha\omega_{0,i}(1 - \frac{I}{I_{th}} + Qs_i^2)s_i \\ &+F_e cos\phi_i(cos(\psi_{e,A} - \omega_{e,A}t) + cos(\psi_{e,B} - \omega_{e,B}t)) \\ &+\epsilon F_e cos\phi_i \sum_{j=1}^{N} s_j cos\phi_j \end{aligned} \tag{59}$$

$$\frac{d\phi_i}{dt} = \omega_{0,i}(1 + N_0 s_i) + \frac{F_e}{s_i} sin\phi_i (cos(\psi_{e,A} - \omega_{e,A}t) + cos(\psi_{e,B} - \omega_{e,B}t)) + \epsilon \frac{F_e}{s_i} sin\phi_i \sum_{j=1}^{N} s_j cos\phi_j \quad (60)$$

In these equations, $\omega_{0,i}$ is the natural angular frequency of the oscillator, $\alpha = 0.013$ is the damping coefficient, $Q = 3.0207$ is the nonlinear damping parameter, I is the dc current injected in the oscillator, I_{th}=1 mA is the threshold dc current of self-sustained oscillations of the magnetization, N_0 is the nonlinear frequency shift normalized by the natural angular frequency. Concerning the external microwave forces injected into the model, $\omega_{e,A}$ and $\omega_{e,B}$ are the respective angular frequencies of the two external microwave inputs A and B, $\psi_{e,A}$ and $\psi_{e,B}$ are their relative phase shifts (Here $\psi_{e,A} = \psi_{e,B} = 0$). $F_e = 1.3 \times 10^{-3}$ is the coupling strength to each external microwave input signal A and B, and ϵ is the mutual coupling strength between oscillators, normalized by the coupling to the inputs.

6.1.4 *Evaluation of recognition performances in simulations*

Beyond the agreement level that can be expected from the two presented oscillator models with our experiments, an important goal of these simulations is to evaluate the classification performances of such network as a function of the oscillator parameters namely tunability N_0 and mutual coupling strength ϵ. The modification of these two parameters is not an easy task to realize experimentally. Indeed, the modification of these properties would require to modify the size or the material of the nano-oscillator. Therefore, a numerical evaluation of recognition performances as a function of the oscillator parameters can give insights about the key properties required to maximize recognition performances.

Following this line of thinking, tunability and mutual coupling strength are modified and a new optimized classification rate is calculated for each new set of tunability or mutual coupling strength parameters.

Each set of parameters corresponds to different oscillator behaviors and thus give rise to different synchronization state maps. In particular the range of operation of the oscillators is modified and, in consequence, the linear combination previously applied to the formants (See Eq 56 and 57) to obtain two characteristic frequencies f_A and f_B in the range of operation of the oscillators is no longer optimal. Due to this, the linear combination of the formants should be adapted for each oscillator parameter. Therefore, for each set of oscillator parameters that we modify it is important to calibrate the linear combination that will be applied to formants frequency inputs. This calibration is done for a synchronization map where a maximum recognition rate is expected. In our implementation, the best recognition rate with the newly considered oscillator parameters is optimized when:

The natural frequency $\omega_{0,i}$ difference between oscillators $\delta_{ij} = |\omega_{0,i} - \omega_{0,j}|$ is similar, meaning that only 5% deviation is possible:

$$\delta_{12} \approx \delta_{23} \approx \delta_{34} \tag{61}$$

, in a such way that the following is verified:

$$\begin{aligned} |\delta_{12} - \delta_{23}| &< 0.05 \times \delta_{12} \\ |\delta_{23} - \delta_{34}| &< 0.05 \times \delta_{12} \end{aligned} \tag{62}$$

The width of the injection locking range $\Delta_{(i)}$ of all 4 oscillators is similar:

$$\Delta_{(1)} \approx \Delta_{(2)} \approx \Delta_{(3)} \approx \Delta_{(4)} \tag{63}$$

in a such way that the following is verified:

$$\begin{aligned} |\Delta_{12} - \Delta_{23}| &< 0.05 \times \Delta_{12} \\ |\Delta_{23} - \Delta_{34}| &< 0.05 \times \Delta_{12} \end{aligned} \tag{64}$$

Thus, we first estimate which values of ω_i and $\Delta_{(i)}$ fulfill these requirements and we calculate the linear transformation of the formants whose final frequencies (inputs to the network) better fit the synchronization map expected from these ω_i and $\Delta_{(i)}$.

Finally, for each oscillator parameters and associated linear combination of the formants, we simulate numerically the learning process and find the optimum recognition rate. Following this procedure, we study the influence of oscillator tunability (section 6.2) and mutual coupling (section 6.3) on the classification ability of our network for both ideal and non-ideal oscillator models.

6.2 IMPACT OF FREQUENCY TUNABILITY

In this section, we present the simulated recognition performances obtained for oscillator networks where we vary their ability to synchronize by modifying their frequency tunability. This study was first realized considering identical ideal oscillator model for simulation. Then it was extended to the case of spin-torque nano-oscillators reproducing experimental results including variabilities between oscillators. In order to study only the impact of the frequency tunability, we realize those simulations in absence of mutual coupling between oscillators.

6.2.1 *Impact of frequency tunability in the case of identical ideal van der Pol oscillators*

By modifying the nonlinear frequency shift parameter N_0, we directly vary the frequency tunability of van der Pol oscillators presented in the model of ideal identical oscillators (see Eq. 59 and 60). For every tunability value N_0 we realize the same learning procedure described previously to classify the seven vowels. As in the experimental procedure, once the linear combination of formant frequency inputs is determined it is kept constant during all the simulated training. At the end, the maximum recognition rate to classify properly the seven vowels is evaluated for each tunability value.

In Fig. 62, in black squares, the obtained recognition rate is shown as a function of the nonlinear frequency shift N_0 of the simulated network of identical ideal oscillators. As it is shown, in absence of frequency tunability corresponding to $N_0 = 0$ the recognition performances are very poor and are smaller than 50%. The recognition rate increases with tunability reaching values higher than 90% for $N_0 = 0.18$. For

higher tunability values, the recognition rate appears to saturate above 90%. In Fig. 63, we illustrate the final synchronization state maps obtained at the end of the learning process for three tunability values: $N_0 = 0$, $N_0 = 0.14$, $N_0 = 0.2$.

For the $N_0 = 0$ case, shown in Fig. 63-(1), clouds of vowels are not well classified mainly because the majority of frequency input vowels fall in states where oscillators are not synchronized. In the absence of frequency tunability $N_0 = 0$, the free-running frequency of oscillators is constant and cannot be modified by varying the applied dc current. For this reason, synchronization region remains at the same frequency position, and it is not possible to modify their position in order to adapt to the input vowel frequency. As a consequence, the oscillator network is not able to learn. In addition, the size of the synchronization region is too small. This is due to the fact that the frequency of the oscillator is not depending on the evolution of amplitude and, in consequence the oscillator is less able to modify its own frequency to be synchronized to external signal. In the formalism of the non-linear auto-oscillator theory, this corresponds to a case where the injection locking range of the oscillator defined as $\Delta = \frac{\sqrt{1+\nu^2}}{\sqrt{p_0}} F_e$ is reduced to $\Delta = \frac{1}{\sqrt{p_0}} F_e$ (see Chapter 2 for more details about notations and theory).

On the contrary, for the $N_0 = 0.2$ case, shown in Fig. 63-(3), the majority of the frequency input vowels fall in one unique synchronization states. This can be explained by two facts. First, the frequency width of synchronization regions are larger due to the increase of the tunability. Second, the frequency position of the synchronization region can be modified in a sufficient frequency range because, by modifying the applied current, the free-running frequency of oscillators covers a large frequency range. This allows to adapt the synchronization map as a function of the vowel inputs and achieve learning.

More systematically, for all the observed synchronization state maps that were obtained, we observe that the recognition rate is closely related to the way the synchronization regions are positioned with respect to each other. As an example in a case where synchronization

regions are separated by an intermediate region where synchronization is not occurring, the classification performances are low. On the contrary, in a case where synchronization regions are not separated by an intermediate non synchronized area, meaning that synchronization regions are bordering each other (see Fig. 63-(3)), the classification performances are higher.

In order to highlight this effect on recognition performances, we evalu-

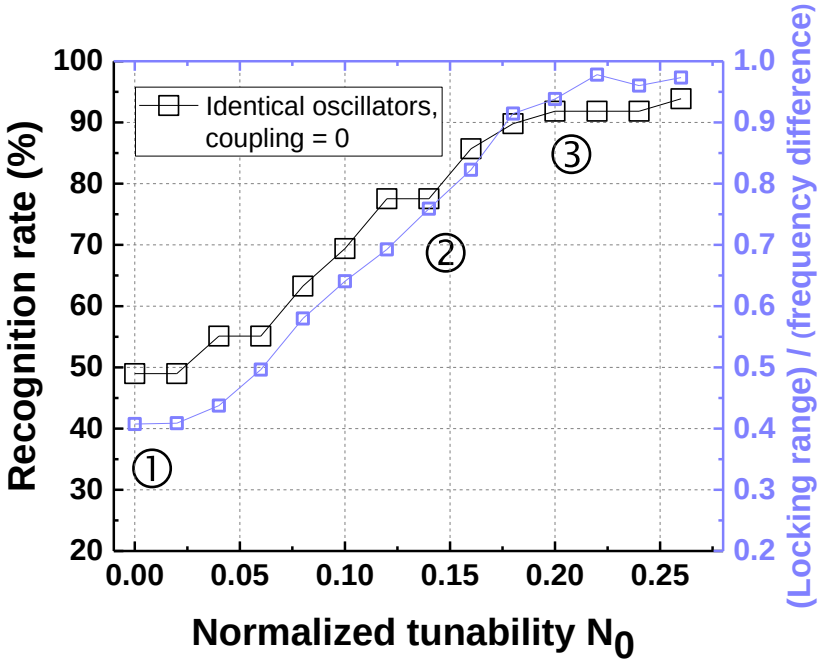

Figure 62: Evolution of the maximum vowel recognition rate of a network of four identical van der Pol oscillator obtained as a function of the normalized tunability of the oscillators (black). Evolution of the ratio of the mean injection locking range normalized by the mean frequency difference between oscillators as a function of the normalized tunability (violet).

ate the mean injection locking range $\bar{\Delta} = \frac{1}{4}(\Delta_{(1)} + \Delta_{(2)} + \Delta_{(3)} + \Delta_{(4)})$ normalized by the mean frequency (free-running) difference between oscillators $\bar{\delta} = \frac{1}{3}(\delta_{12} + \delta_{23} + \delta_{34})$ where $\delta_{12} = |\omega_1 - \omega_2|$, $\delta_{23} = |\omega_2 - \omega_3|$ and $\delta_{34} = |\omega_3 - \omega_4|$. This ratio denoted as $\rho = \frac{\bar{\Delta}}{\bar{\delta}}$, is shown in purple

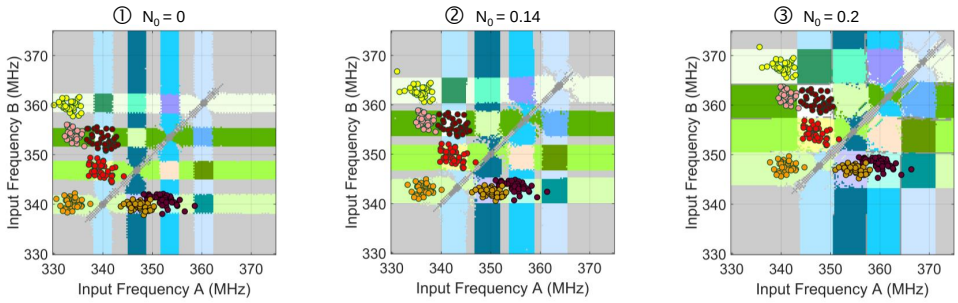

Figure 63: Simulated synchronization state maps obtained at the end of the training process corresponding to recognition rates illustrated in Fig. 62 for respectively (from left to right) $N_0 = 0$, $N_0 = 0.14$ and $N_0 = 0.2$

on the top of the recognition rate versus tunability graph of Fig. 62. In this graph, we observe that the recognition rate and ρ follow the same trend as a function of the normalized tunability N_0. Therefore, the maximum recognition rate should be expected in the case where $\rho = 1$, corresponding to a situation where all the synchronization regions are perfectly bordering each other in terms of frequency position. For sufficient normalized tunability $N_0 > 0.18$, this situation tends to be realized using identical ideal oscillators. In the next subsection, we study the case of non-identical oscillators including variabilities and reproducing the behavior of spin-torque nano-oscillators used in our experiments.

6.2.2 *Impact of frequency tunability in the case of spin-torque nano-oscillators with experimental variability*

In this subsection, we see how the frequency tunability impacts the recognition performances of a network of four nano-oscillators with variabilities corresponding to the experimental implementation. For this purpose, the simulated Thiele model of spin-torque nano-oscillators that was used to reproduce our experimental results (See

subsections 6.1.1 and 6.1.2) is exploited. As in the previous case, the mutual coupling is not taking into account in the simulation.

In order to change the tunability in the description given by the Thiele formalism, we choose to modify the nonlinear magnetostatic and Oersted $\kappa_{Oe}^{'}$ and $\kappa_{ms}^{'}$ confinement in equations. Therefore, we introduce a hyperparameter η that we vary in order to modify those parameters as following: $\tilde{\kappa_{ms}^{'}} = \eta\kappa_{ms}^{'}$ and $\tilde{\kappa_{Oe}^{'}} = \eta\kappa_{Oe}^{'}$. This modification of the nonlinear confinement is equivalent to a modification of the nonlinear frequency shift expressed as follows (see the theory introduced in Chapter 2): $\tilde{N_{Thiele}} = \frac{\tilde{\kappa_{ms}^{'}} + \tilde{\kappa_{Oe}^{'}}J}{G} = \eta\frac{\kappa_{ms}^{'} + \kappa_{Oe}^{'}J}{G} = \eta N_{Thiele}$. Here η goes from 0 to 1.5 with a step of 0.1. To be able to compare the tunability variations realized in this study with those realized in the model of identical ideal oscillation (previous subsection), we extract for every η the corresponding normalized tunability N_0 for every oscillator. These extracted values are not identical from one oscillator to the other one and thus we focus on their mean average over the four oscillators of the network.

Therefore, as for the identical van der Pol model, for each normalized tunability N_0, we repeat the vowel recognition evaluation and report the maximum recognition rate. Black circles in Fig. 64 show the evolution of this maximum recognition rate as a function of the normalized tunability N_0. As for the identical van der Pol model, in the absence of tunability, $N_0 = 0$, the oscillator network is not able to classify properly vowels, then the recognition rate is close to 30%. By increasing the tunability of the oscillators the recognition rate increases, reaching almost 90% for $N_0 > 0.20$. By taking into account variabilities in the behavior of the four oscillators of this simulated network, for the same normalized tunability N_0, we obtain as expected a smaller recognition rate that the one that can be obtained in the case of identical ideal van der Pol oscillators (previous subsection). Indeed, as it is shown in Fig. 64 and Fig. 62, for the same tunabilty $N_0 = 0.18$, in the case of identical ideal oscillators the recognition rate was of the order of 91% while in the case of a network including variabilities the recognition rate was at 74%. As in the case of ideal van der Pol oscillators, this last recognition rate is related to the relative

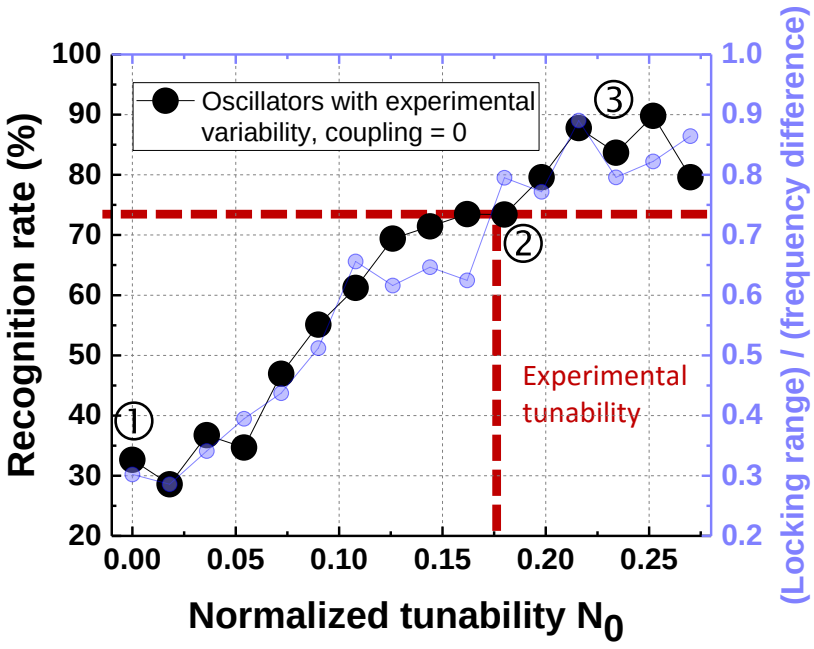

Figure 64: Evolution of the maximum vowel recognition rate of a simulated network of four spin-torque nano-oscillators with experimental variabilities as a function of the normalized tunability of the oscillators (black circles). Evolution of the ratio of the mean injection locking range normalized by the mean frequency difference between oscillators as a function of the normalized tunability (violet).

positioning of synchronization regions. This effect is captured by the mean injection locking range normalized by the frequency difference of the oscillators ρ. As for the recognition rate, for the same normalized tunability N_0, the coefficient ρ is smaller than the one obtained in the case of ideal van der Pol oscillators. We interpret this effect as the fact that variability causes an asymmetry in both the size of the synchronization regions and the operating frequency ranges from one oscillator to another one. As an example, in Fig. 65, the corresponding synchronization maps can have different widths for the synchronization region.

To summarize, the oscillator variability degrades the vowel classification performances with regards to Fig. 62. It should be noticed that for a normalized tunability corresponding to the experimental

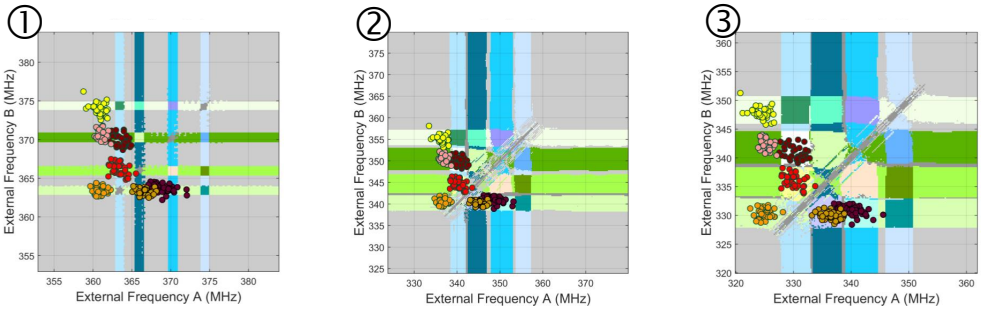

Figure 65: Simulated synchronization state maps obtained at the end of the training process corresponding to recognition rates illustrated in Fig. 64 for respectively (from left to right) $N_0 = 0$, $N_0 = 0.18$ and $N_0 = 0.23$

conditions $N_0^{exp} = 0.18$, the recognition rate is only 74%, below the case of identical oscillators (90% in Fig. 62), but also well below the recognition rates that we obtained experimentally with mutually coupled oscillators (89%). This result highlights the importance of coupling for successful classification, which we study in more detail in the next subsection for $N_0 = 0.18$.

6.3 IMPACT OF COUPLING

6.3.1 *Impact of electrical mutual coupling on recognition performances*

In this section, we see how mutual coupling impacts the classification performance of the spin-torque nano-oscillator network. For this purpose, the influence of coupling between oscillators on the recognition performances has been studied through the differential equations (see Eq. 32), following the formalism of Thiele. The coupling between oscillators is modified by introducing a hyperparameter k in

the simulation model. It tunes the impact of the microwave signal I_{rf} emitted by all the four oscillators on the dynamics of each of them.

$$I_{rf} = \frac{1}{Z_0 + \sum_{i=1}^{N=4} R_{(i)}} \left(\sum_{i=1}^{N=4} k\lambda \Delta R_{(i)} I_{(i)}^{dc} y_{(i)} \right) \tag{65}$$

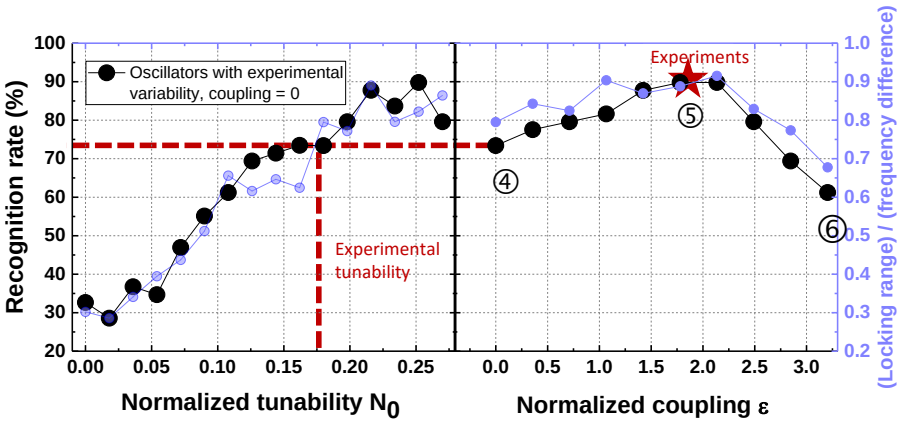

Figure 66: (Left): Evolution of the vowel recognition rate of a simulated network of four spin-torque nano-oscillators with experimental variabilities as a function of the normalized tunability of the oscillators (black circles) and its corresponding mean injection locking range normalized by the mean frequency difference between oscillators as a function of the normalized tunability (violet). (Right): Evolution of the vowel recognition rate of the same simulated network as a function of the normalized coupling of the oscillators (black circles). Evolution of the corresponding ratio of the mean injection locking range normalized by the mean frequency difference between oscillators as a function of the noramlized coupling (violet). The red star illustrates the recognition rate obtained experimentally.

The case where $k = 0$ signifies that oscillators are not coupled to each other. The case where $k = 1$ corresponds to a configuration where oscillators are expected to be coupled as in the conditions of our experiments. The coupling strength is modified gradually by tuning k from 0.0 to 1.8 with a step of 0.2. In order to be able to compare the coupling variations realized in this study with the strength of external sources, we extract for each k the corresponding normalized

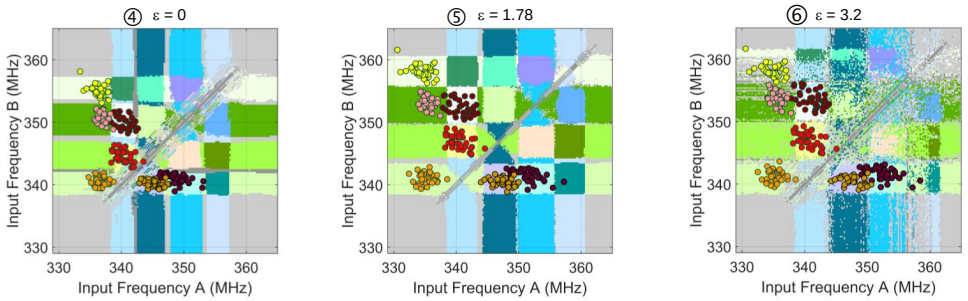

Figure 67: Simulated synchronization maps obtained at the end of the training process corresponding to recognition rates illustrated in Fig. 66 for respectively (from left to right) $\epsilon = 0$, $\epsilon = 1.78$ and $\epsilon = 3.2$.

coupling ϵ. This quantity can be interpreted as the effective force applied between oscillators due to mutual coupling normalized by the external force F_e: $\epsilon = \dfrac{F_{coupling}}{F_e}$.

In our case, the coupling between oscillators is due to the electrical connections in series and arises mainly from the field-like torque [282], while the external force is applied through microwave fields. Therefore $\epsilon = \dfrac{\beta_j J_{rf}}{\mu_0 H_r f}$ with $J_{rf} = \dfrac{I_{rf}}{\pi R^2}$ the total current density emitted by the four oscillators [283], H_{rf} the amplitude of the applied microwave field, β_j the field-like torque efficiency. Finally, as for the simulations concerning the impact of the tunability (previous section), we repeat the vowel recognition evaluation for distinct coupling strength ϵ and evaluate the maximum recognition rate. We use basic microwave characterizations and injection locking measurements to quantify β_j, J_{rf} and H_{rf} ($\mu_0 H_{rf} = 0.27$ mT), from which the experimental value of the coupling coefficient is estimated to be $\epsilon^{exp} = 1.79$.

Fig. 66 shows the dependence of the recognition rate with the normalized coupling strength ϵ. As can be seen in Fig. 66 there is a range of intermediate coupling for which the recognition rate is optimized. As for the tunability study of the previous section, this high recognition rate is also related to a higher mean injection locking range normalized by mean frequency difference noted as ρ. Indeed, for high recognition rate we observe a higher ρ ratio illustrated in violet in Fig. 66. This

observation shows that electrical mutual coupling causes an increase of the size of the injection locking ranges while the frequency difference between oscillators remains unchanged or decreased. It should be noticed that this behavior was already observed in the case of two coupled oscillators in presence of one external source signal in chapter 3. Those observations can give a qualitative understanding of this phenomenon of increasing injection locking range due to coupling. However, the presence of an additional external source and other oscillators with a high coupling ability can lead to complex and hardly predictable dynamics. In particular, for values of coupling above the optimum range $\epsilon > 2$, the recognition rate decreases upon increasing coupling. This coincides with the synchronization maps becoming noisier and noisier upon increasing the coupling (see Fig. 67), which explains the decrease in classification performance. In order to better understand the reasons behind these noisy maps, we focus in the next section on the stability of synchronization state in presence of high coupling regimes.

6.3.2 *Instabilities at high coupling regimes*

In order to see the impact of high coupling, we first studied the evolution of the frequency of two coupled oscillators when one of them is initially synchronized to an external source. For this simple case we varied the strength of the electrical coupling between oscillators. Fig. 68 shows the simulated frequencies of the two oscillators labeled oscillators 1 and 2 when oscillator 1 is initially locked to the external source. As can be seen, when the coupling strength becomes large enough, the attractive force between oscillators is so strong that oscillator 1 gets unlocked from the external microwave signal and eventually synchronizes to oscillator 2. This explains how an initially stable synchronization state (between one oscillator and one source) can be destroyed if mutual coupling between oscillators is large enough.

Therefore, for a value of the coupling coefficient $\epsilon > 2.24$ the mutual coupling destroys the injection locking of the oscillator to an external source given the conditions under consideration in Fig 66. The aforementioned behavior explains by itself a reduction of synchronization regions to the external source and thus of the recognition rate when

the ϵ is greater than 2. But it is not the reason behind the noisy maps obtained in this range of high coupling shown in Fig. 67-(3).

To elucidate this point, for each coupling condition ϵ, we have repeated in Fig 69 the simulated maps for several different sets of initial conditions. This corresponds to solve the coupled Thiele equation for distinct initial vortex core positions (X_0, Y_0). For 4 distinct coupling values ϵ (0, 1.78, 2.49 and 3.20), we choose 10 different initial vortex positions, simulate the oscillator network and observe the final synchronization states that can occur (See Fig 69).

While for low and intermediate coupling only the edges of synchronization regions are dependent on initial conditions, for large coupling we obtain different noisy maps where for the majority of frequency inputs (f_A, f_B) the final synchronization states are highly sensitive to initial conditions. In other words, given the same values of input frequencies f_A and f_B, a different synchronization state is obtained depending on the initial conditions. This suggests that for high couplings the dynamics of the oscillator network tends to become chaotic. These numerical results are still preliminary and would require further studies including the computation of Lyapounov exponents. It should be noticed that several theoretical studies already report presence of chaos in high coupling regimes in arrays of coupled Kuramoto oscillators [284][285].

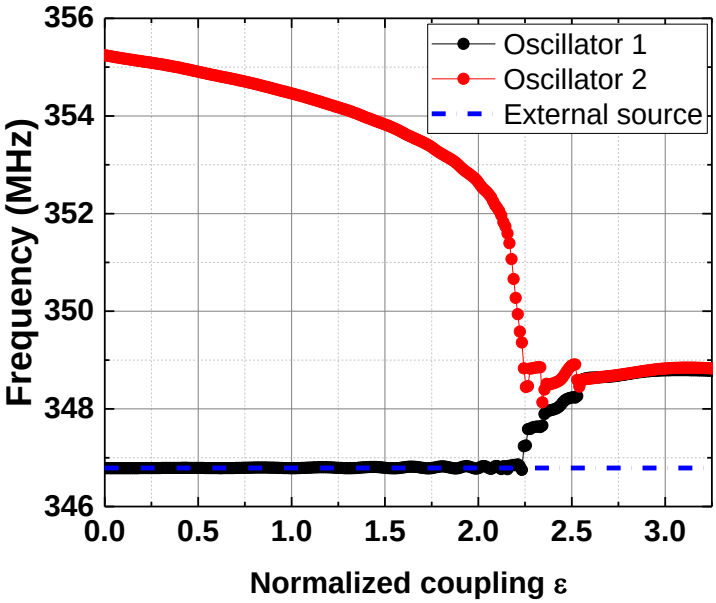

Figure 68: Frequency evolution of two simulated nano-oscillators (1) and (2) in the presence of an external source with frequency $f_{ext} = 346.8$ MHz (dashed blue line) as a function of the mutual electrical coupling. For low coupling regime, oscillator 1 is initially sycnhronized to the external source.

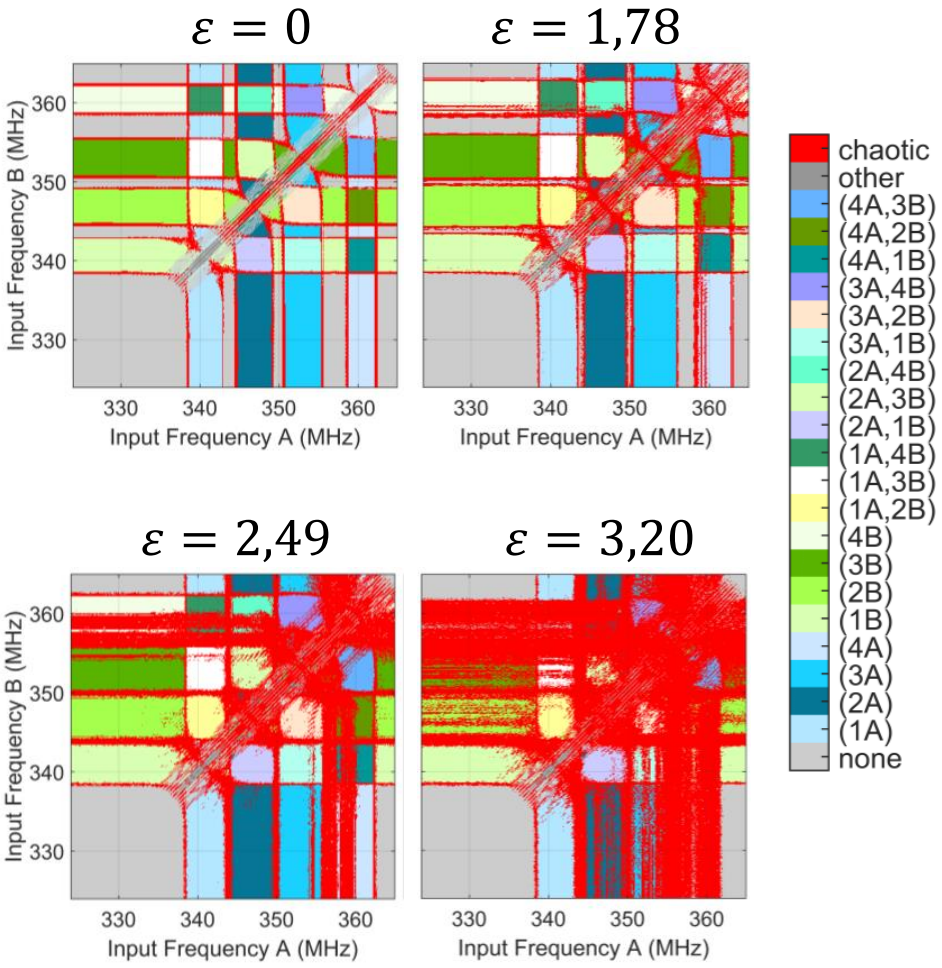

Figure 69: Sensitivity of synchronization states to initial conditions as a function of coupling ϵ. The maps have been simulated with 10 different initial conditions. The final state is indicated as red if at least one of the final states differs from the others.

6.4 CONCLUSION

We have seen in this chapter that both frequency tunability and intermediate mutual coupling are key ingredients to optimize the recognition performances of an array of four coupled nano-oscillators. In the case of ideal identical van der Pol oscillators, the recognition rate increases with the tunability of oscillators. A maximum recognition rate higher than 90% can be obtained for high tunability values. This behavior is also observed in the case of an array of spin-torque nano-oscillators having experimental variability, but the recognition rate remains lower than the one obtained with identical van der Pol oscillators. For a tunability value corresponding to the experimental conditions, the simulated recognition rate for uncoupled oscillators is lower than the maximum that can be reached and is also smaller that the one obtained experimentally. However, by including mutual coupling interaction between oscillators, we observe an improvement of the initial recognition performances. For coupling strength corresponding to experimental conditions, we were able to reproduce in simulations the recognition performances observed experimentally. For higher coupling regimes, we observe a decrease of the recognition rate. We relate this decrease to frequency instabilities due to the desynchronization of oscillators from external stimuli and to synchronization behaviors that tend to become chaotic.

The main results of this chapter are:

- Using the Thiele equation approach, we were able to reproduce in simulations the synchronization states observed in experiment at different steps of the learning process.
- The recognition performance of oscillator arrays increases with the frequency tunability of oscillators.
- For a given tunability, the recognition rate is improved by the presence of an intermediate mutual coupling between oscillators.
- For high coupling regimes, the recognition rate is deteriorated due to instabilities in the frequency and final synchronization state of oscillators.

7

LARGE ARRAYS OF SPIN-TORQUE NANO-OSCILLATORS

In order to compete with large neural networks used in machine learning, the number of training parameters in our oscillator-based network should be larger. A natural way to achieve this goal is to increase the number of nano-oscillators in the interacting array. Such arrays are promising for broadband microwave signal detection and processing as well as neuromorphic computing. For these applications, large arrays of spin-torque nano-oscillators able to process microwave inputs over a wide frequency range with high sensitivity are needed. Since individual oscillators respond to inputs in a narrow range around their frequency, the frequency of oscillators should be tuned to be equally spaced, while maintaining the range of frequency sensitivity equal in all the oscillators. Following this line of thinking, in this chapter, I show that large arrays of nano-oscillators able to respond to microwave inputs over a wide range of frequency can be designed. I calculate the optimal operating points (applied DC currents) and physical properties (size and aspect ratio) of the oscillators in the array, and we explore the limits of these arrays considering realistic nano-fabrication techniques. I first design an array of 100 oscillators. Then, for realistic manufacturing physical size and applied dc current parameters, we show using analytics that the maximum number of spin-torque nano-oscillators that can be assembled in an array with these characteristics exceeds several hundreds. Finally, I perform simulations including mutual electrical coupling between oscillators, and show that the analytical findings remain robust.

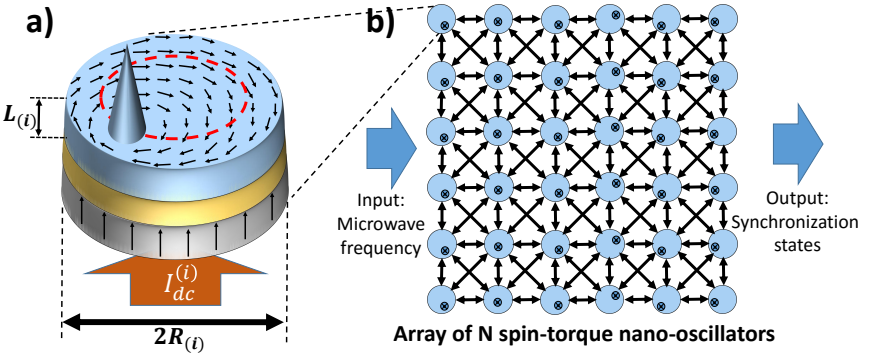

Figure 70: a) Schematic illustration of the spin-torque nano-oscillator having a magnetic vortex configuration for the free layer (blue). The yellow layer illustrates the non-magnetic layer and the gray layer corresponds to the pinned layer. The magnetization of the free layer is planar except in the vortex core area where it becomes out of plane. b) The schematic illustrates an array of N interacting spin-torque nano-oscillators receiving microwave frequency inputs. The different synchronization states of this array correspond to the output.

7.1 DESIGNING LARGE ARRAYS OF SPIN-TORQUE NANO-OSCILLATORS

7.1.1 *Models*

In order to design large arrays of spin-torque nano-oscillators, we first perform an analytical study of the oscillator geometry and applied direct current for every nano-oscillator. As illustrated in Fig. 70-a, we focus on spin-torque nano-oscillators with a vortex configuration in the free layer [13] because the analytical description of their dynamics matches quantitatively experimental results [276, 286, 160](or see 6.1.1). However, it should be noticed that the methods we use can be extended to all types of spin-torque nano-oscillators[168].

We consider the Thiele equation [274, 159] describing the trajectory of the vortex core. Now, in this section, we solve this equation in the steady-state. This give us analytical expressions for important variables which will affect the oscillations and the synchronization

ability of oscillators. In this line of thinking, the frequency of the vortex oscillations $f^{(i)}$ can be determined Eq. 66 [159].

$$f^{(i)} = \frac{1}{2\pi G^{(i)}}\{\kappa_{ms}^{(i)} + \kappa_{Oe}^{(i)} J^{(i)} + (\kappa_{ms}^{'(i)} + \kappa_{Oe}^{'(i)} J^{(i)}) p_0^{(i)}\} \tag{66}$$

As it was shown in the previous chapter, this oscillator is nonlinear and as a consequence, its frequency depends on the power amplitude of oscillations $p_0^{(i)}$ described by Eq. 67[159].

$$p_0^{(i)} = \frac{\frac{a_j^{(i)} G^{(i)}}{D^{(i)}} J^{(i)} - (\kappa_{ms}^{(i)} + \kappa_{Oe}^{(i)} J^{(i)})}{\kappa_{ms}^{'(i)} + \kappa_{Oe}^{'(i)} J^{(i)} + \xi(\kappa_{ms}^{(i)} + \kappa_{Oe}^{(i)} J^{(i)})} \tag{67}$$

The nonlinearity of such auto-oscillator is characterized by the nonlinear frequency shift parameter [168] $\nu^{(i)}$ Eq. 68.

$$\nu^{(i)} = \frac{G^{(i)}}{D^{(i)}} \frac{\kappa_{ms}^{'(i)} + \kappa_{Oe}^{'(i)} J^{(i)}}{\kappa_{ms}^{'(i)} + \kappa_{Oe}^{'(i)} J^{(i)} + \xi(\kappa_{ms}^{(i)} + \kappa_{Oe}^{(i)} J^{(i)})} \tag{68}$$

This ν parameter combined with the power amplitude $p_0^{(i)}$ affects the frequency injection-locking range $\Delta^{(i)}$ where the oscillator synchronizes its oscillations to an external microwave signal of amplitude F_e. Here, we remind the injection locking-range expression described by Eq. 69[168].

$$\Delta^{(i)} = \frac{\sqrt{1 + {\nu^{(i)}}^2}}{\sqrt{p_0^{(i)}}} F_e \tag{69}$$

All the terms of these equations are described in Tab. 5 and 6. These parameters correspond to FeB free-layers. Tab. 5 shows constant parameters that we didn't modify during the study presented in this chapter, while Tab. 6 shows parameters which were varied during the study from one oscillator to other. This was due to the choice of the free-layer radius $\mathcal{R}_{(i)}$, thickness $L_{(i)}$, and applied dc current $I_{dc}^{(i)}$. Indeed, as shown in Tab. 6, the presented coefficients corresponding to electrical current density $J^{(i)}$, the damping $D^{(i)}$, the confinement due to the Oersted field $\kappa_{Oe}^{(i)}$, the magnetostatic confinement $\kappa_{ms}^{(i)}$ and the gyroforce $G^{(i)}$, depend on the free-layer radius $\mathcal{R}_{(i)}$, thickness $L_{(i)}$, and applied dc current $I_{dc}^{(i)}$.

$H_\perp = 0.530$ T (fixed perpendicular applied magnetic field)
$M_s = 1.5 \times 10^{-7} A.m^{-1}$ (free-layer saturation magnetization)
$\alpha = 0.0054$ (Gilbert damping)
$A = 20 \times 10^{-11} A.m^{-1}$ (exchange constant)
$\mathcal{P} = 0.26$ (spin polarization of the magnetic junction)
$M_s^{pol} = 1.2 \times 10^{-6} A.m^{-1}$ (polarizer magnetization)
$\xi = 0.6$ (nonlinear damping coefficient)[160, 287]
$\theta_0 = cos^{-1} \dfrac{H_\perp}{\mu_0 M_s}$ (free layer magnetization angle)
$b = 2L_{ex} = 2\sqrt{\dfrac{2A}{\mu_0 M_s^2}}$ (vortex core radius)
$a_j = \pi \dfrac{\hbar P}{2e} \dfrac{H_\perp}{\mu_0 M_s^{pol}} sin^2\theta_0$ (spin-transfer torque efficiency)

Table 5: Constant parameters of the study for FeB free-layer. Here $\mu_0 = 4\pi \times 10^{-7} T.m.A^{-1}$, $\hbar = 1.054 \times 10^{-34} J.s^{-1}$, $\gamma_0 = 1.76 \times 10^{11} rad.s^{-1}.T^{-1}$ and $e = 1.602 \times 10^{-19} C$

$D^{(i)} = \alpha(2\pi L_{(i)} \dfrac{M_s}{\gamma_0})(\dfrac{1}{2} \ln\left(\dfrac{\mathcal{R}_{(i)}}{2b}\right) - \dfrac{1}{8}) \sin^2\theta_0$ (damping)[159]
$G^{(i)} = (2\pi L_{(i)} \dfrac{M_s}{\gamma_0})(1 - \cos\theta_0)$ (gyrovector magnitude)
$\kappa_{ms}^{(i)} = (\dfrac{10}{9})\mu_0 M_s^2 \dfrac{L(i)^2}{\mathcal{R}_{(i)}} \sin^2\theta_0$ (magnetostatic confinement)[276, 261]
$\kappa_{ms}^{'(i)} = 0.25\kappa_{ms}$ (nonlinear magnetostatic confinement)[261]
$\kappa_{Oe}^{(i)} = 0.85\mu_0 M_s L_{(i)} \mathcal{R}_{(i)} \sin\theta_0$ (Oersted field confinement)[287]
$\kappa_{Oe}^{'(i)} = -0.5\kappa_{Oe}$ (nonlinear Oersted field confinement)[287]

Table 6: Parameters depending on the applied dc current $I_{dc}^{(i)}$, the free-layer radius $\mathcal{R}_{(i)}$ and the free-layer thickness $L_{(i)}$.

7.1.2 *Design procedure*

We now use the analytical model presented in the previous subsection to design an array of spin-torque nano-oscillators that can process a wide range of input frequencies, without gaps, and with the same individual input bandwidth response to all frequencies. We

will tune the applied dc current $I_{dc}^{(i)}$, the free-layer radius $\mathcal{R}_{(i)}$ and the free-layer thickness $L_{(i)}$ in the model to design this array. In this design, the individual frequency of oscillators are regularly spaced, and each oscillator has a synchronization range equal to this spacing. To do this, the frequency $f^{(i)}$ and the injection locking range $\Delta_{(i)}$ of every spin-torque nano-oscillator of the array need to be tuned to fulfill the following two conditions:

$$(i) \mid f^{(i+1)} - f^{(i)} \mid = \delta_f \pm \epsilon. \tag{70}$$

$$(ii) \Delta_{(i)} = \delta_f \pm \epsilon^{'}. \tag{71}$$

ϵ and $\epsilon^{'}$ are respectively the maximal frequency and injection-locking range deviations that we tolerate in the choice of our individual parameters, here chosen as 5% of the frequency spacing value ($\epsilon^{'} = \epsilon = 0.05\delta_f$). In the neuromorphic computing design of [24], conditions (i) and (ii) gave the highest performances at pattern classification both in experiments and in simulations for a small array of 4 spin-torque nano-oscillators. Eq. 69 and 66 show that the frequency $f^{(i)}$ and the injection locking range $\Delta_{(i)}$ of each oscillator (i) can be tuned by three parameters: the free-layer radius, thickness and applied dc current $\{\mathcal{R}_{(i)}, L_{(i)}, I_{dc}^{(i)}\}$.

We chose to separate the individual frequencies with a frequency step δ_f of 5 MHz, which corresponds to easily achievable locking ranges for this type of oscillators [24]. In order to take into account the reachable size accuracy during the nano-dot manufacturing processes, we also impose a minimal dot radius variation between nano-oscillators of $\delta\mathcal{R} = 2.0$ nm and a minimal free layer thickness variation of $\delta L = 0.1$ nm from one nano-dot to another one $\mid \mathcal{R}_{(i)} - \mathcal{R}_{(j)} \mid > \delta\mathcal{R}$, $\mid L_{(i)} - L_{(j)} \mid > \delta L$.

It should be noticed that for large free-layers, the amount of applied current required to reach the current density needed to obtain auto-oscillations will increase. This increase of applied dc current

causes large Joule heating that can be detrimental. To avoid this, we consider a maximum nano-dot radius size of 300 nm. Furthermore, the maximum and minimum nano-pillar radius (300 and 150 nm) and thickness (8.1 and 3.0 nm) are chosen in such a way that the magnetic ground state of the FeB layer is always a vortex state. Considering FeB exchange length $L_{ex} \approx 11.8nm$, we verified the magnetic state configurations expected for cylindrical nanopillars. According to the magnetic stability diagram calculated by Metlov et al. [13] presented in Fig. 71, for FeB free layer thicknesses $L_{(i)}$ comprised between 3.0 and 8.1 nm and radi $\mathcal{R}_(i)$ larger than 47.5 nm, the magnetic configuration is a stable vortex ground state.

Finally, the applied dc currents $I_{dc}^{(i)}$ are chosen according to the accuracy of the electric circuit supplying them. Therefore, we impose a minimal current variation of $\delta I = 0.1$ mA from one oscillator to the other: $\mid I_{dc}^{(i)} - I_{dc}^{(j)} \mid > \delta I$.

7.1.3 *Numerical results*

Fig. 72-a and b show the calculated values of free-layer radius, thickness and applied dc current that fill these constraints as well as conditions (i) and (ii). In the different panels, each colored dot corresponds to one of the 100 oscillators of the array. The bottom panel of Fig. 72-a shows the auto-oscillation frequencies of the oscillators as a function of their radius $\mathcal{R}_{(i)}$. The corresponding thicknesses $L_{(i)}$ are represented in different colors. The resulting frequencies cover a microwave range of 510 MHz starting from 145 MHz and ending at 655 MHz. The top panel of Fig. 72-a shows the corresponding injection-locking ranges of each nano-oscillator. The distribution of this injection locking range is narrow around 5 MHz with a dispersion of the order of 0.5 MHz. This means that, as desired, every nano-oscillator of the array has a similar sensitivity to the external inputs that it receives. In Fig. 72-b, the dc currents applied to each individual oscillator are shown. As can be seen, those applied dc currents have been chosen higher than the critical dc current $I_c^{(i)}$ (dashed lines) required to obtain auto-oscillations. In addition, the applied dc current is always set smaller than the breakdown current (red straight line) which

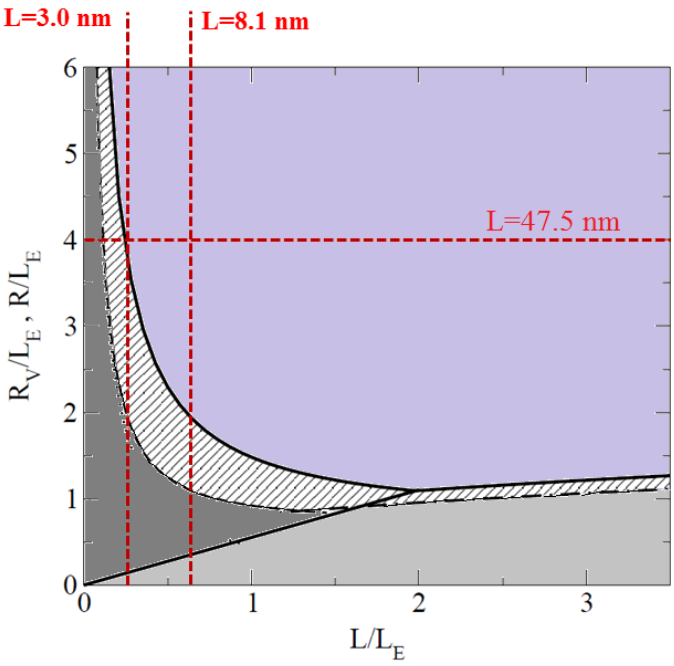

Figure 71: Stability diagram of the magnetic configuration in cylindrical nano-pillars. This diagram is taken from Metlov et al.[13]. The diagram presents three distinct regions. Purple region: magnetic vortex state, dark gray: magnetized uniformly in-plane, light gray: magnetized uniformly out-of-plane. The vertical red dashed line correspond to FeB free-layer thicknesses $L = 3$ nm and $L = 8.1$ nm. The horizontal red dashed line corresponds to a corresponding free-layer FeB radius of $\mathcal{R} = 47.5$ nm.

should not be reached, otherwise the magnetic junction would be damaged.

To summarize this section, we were able to design a large array of spin-torque nano-oscillators for which the aforementioned conditions 70 and 71 were verified. This design highlights the numerous constraints on both the free-layer size and applied dc current and shows that the choice of parameters depends strongly on those constraints.

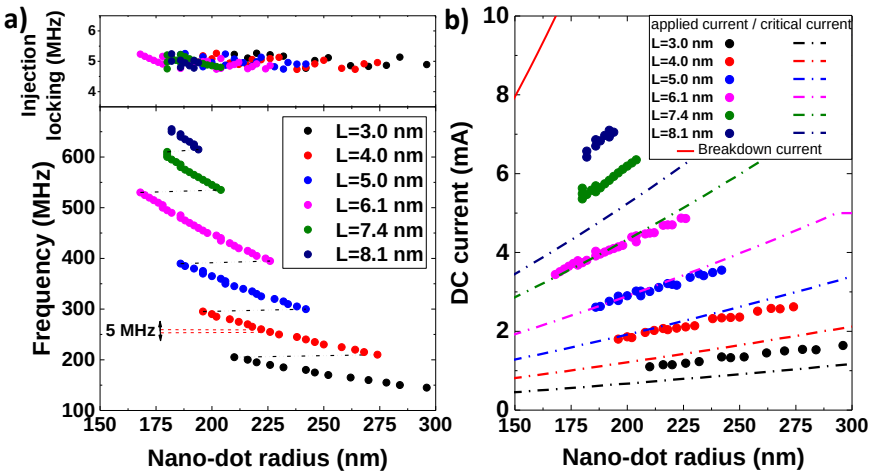

Figure 72: a) Lower graph: analytical auto-oscillation frequency of each nano-oscillator resulting from the application of the selected individual dc current as a function of the chosen nano-dot radius. The color code indicates the corresponding free layer thickness. Upper graph: distribution of the analytical injection locking range for an external microwave signal amplitude $P_{ext} = -3$ dBm, as a function of the chosen nano-dot radius for different thicknesses. The analytical injection locking range remains contained around 5 MHz. b) Chosen applied dc current versus nano-dot radius for the different chosen free-layer thicknesses, dashed lines correspond to the critical current to obtain auto-oscillations. The red line evaluates the dc current corresponding to the breakdown voltage. All of these results were obtained for a fixed applied perpendicular field $H_\perp = 0.530$ T and other constant parameters presented in Tab. 5.

7.2 MAXIMUM SIZE OF THE ARRAYS

7.2.1 *Impact of frequency separation δ_f*

Maximizing frequency sensitivity and frequency bandwidth on which the array of oscillators would respond requires increasing the number of oscillators in the array. In this part we explore the condition that are required to build such larger arrays, while insuring frequency and synchronization requirements (i) and (ii). Based on individual Thiele equation solutions Eq. 66-67-69 given by the minimal variations of the free-layer size $(\delta\mathcal{R}, \delta L)$ and applied dc current δI, we determine the

maximum number of nano-oscillators in the array for the constraints.

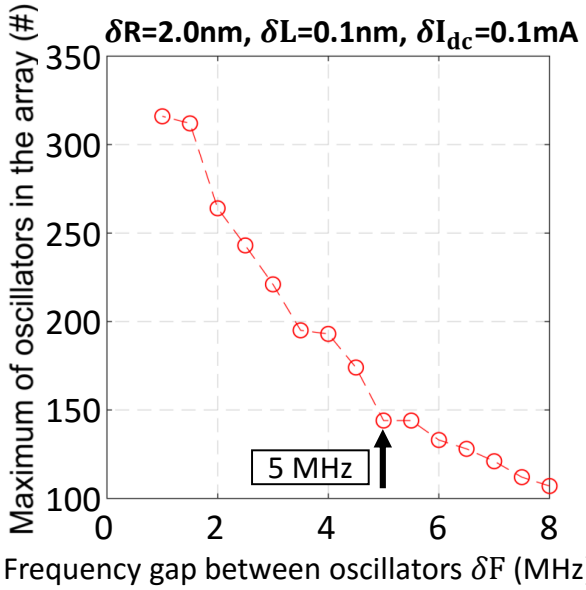

Figure 73: Variation of the maximum number of nano-oscillators in array depending on the frequency gap between their auto-oscillation frequencies. For small frequency gaps $\delta_f = 1.5$ MHz, arrays of more than 300 nano-oscillators with suitable frequency and synchronization features can be designed.

Initially, for fixed minimal variations on free-layer radius $\delta\mathcal{R} = 2.0$ nm, thickness $\delta L = 0.1$ nm and dc current $\delta I = 0.1$ mA, we varied the frequency separation allowed between auto-oscillation frequencies δ_f from 1.0 to 8.0 MHz (Fig. 73). Decreasing this frequency separation means that every nano-oscillator will be sensitive to a smaller portion of the input frequency bandwidth. As shown in Fig. 73 with the frequency spacing decrease, the maximum size of the nano-oscillator arrays increases in such a way that it reaches more than 300 nano-oscillators size for a frequency spacing of $\delta_f \approx 1.5$ MHz.

7.2.2 *Impact of miminimum size variations ($\delta\mathcal{R}, \delta L$) and applied dc current variations δI*

The minimum size variation ($\delta\mathcal{R}, \delta L$) for the free-layer of nano-oscillators also influences the maximum working-size of large arrays. Fig.74-a shows the calculated maximum number of nano-oscillators in the array with the following dc current and frequency constraints: $\delta I = 0.05$ mA and $\delta_f = 5.0$ MHz. The red region corresponding to arrays larger than one hundred nano-oscillators are obtained for conditions where the allowed minimal variation on radius and thickness are the smallest ones ($\delta\mathcal{R} < 2$ nm and $\delta L < 2$ nm).

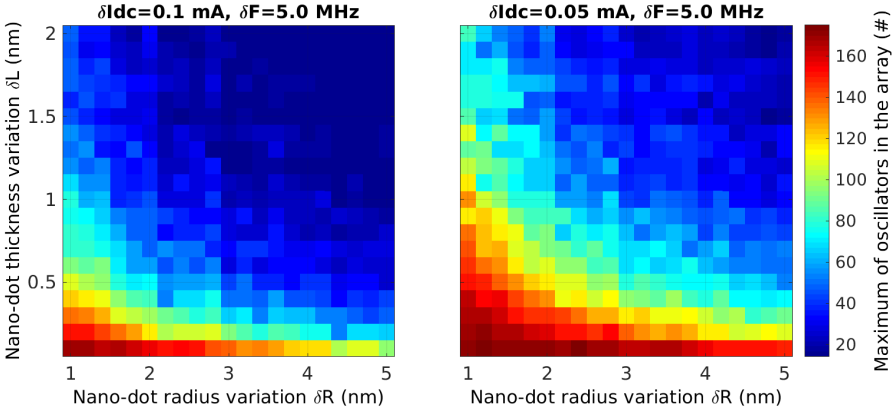

Figure 74: Maximum number of nano-oscillators in array illustrated as color representation which depends on the minimal radius and thickness variation allowed for the nano-pillars for a minimal dc current variation of a) $\delta I = 0.10$ mA and b) $\delta I = 0.05$

Nevertheless, if we allow a smaller minimal dc current variation ($\delta I = 0.05$ mA, in Fig.74-b), we observe that the red region expands, meaning that arrays of more than 100 nano-oscillators can be designed for less limited nano-pillar dimension constraints ($\delta\mathcal{R} < 2$ nm and $\delta L < 2$ nm). These analytical results highlight the concurrent impact of both nano-pillar size constraints ($\delta\mathcal{R}, \delta L$) and dc current and frequency constraints ($\delta I, \delta_f$) on the maximum working size of nano-oscillator arrays.

To summarize, the maximum number of nano-oscillators strongly

depends on minimal dc current variation δI and minimal free-layer size variations $(\delta\mathcal{R}, \delta L)$. However, this study also shows that even if $\mathcal{R}$ and L cannot be precisely designed in order to reach a a certain number of nano-oscillators in the array, an improvement of the precision on I helps to reach a similar number of nano-oscillators.

7.3 BEHAVIOR OF LARGE ARRAYS IN PRESENCE OF ELECTRICAL COUPLING AND EXTERNAL MICROWAVE INPUTS

7.3.1 *Model*

As shown in Fig. 72, the largest arrays are obtained for the smallest frequency spacing, for which spin-torque nano-oscillators are highly coupled and can be mutually synchronized which can affect their ability to be synchronized to an external signal. This collective coupling effect is not captured by the individual analytical description of each nano-oscillator presented in sections 7.1 and 7.2. In this section, we examine the impact of oscillator mutual couplings on the array behavior through numerical simulations. For this purpose, we first study the collective behavior of an array of 100 electrically coupled spin-torque nano-oscillators receiving the sum of two distinct external microwave magnetic fields. The parameter set of all nano-oscillators in the array are the ones determined and depicted in Fig. 72.

As in the previous chapter, the electrical coupling between nano-oscillators resulting from their microwave emissions is described as an additional common alternative current that goes through all nano-oscillators[277] $I_{rf}^{com} = \frac{1}{Z_0 + \sum_{i=1}^{N} R_i} \sum_{i=1}^{N} \lambda \Delta R_i I_{dc}^{i} y_i$. Here ΔR_i is the mean resistance variation due to the vortex core gyrotropic motion through tunnel magnetoresistance, Z_0 is the load impedance which is equal to 50 Ω, R_i is the resistance of the junctions, I_{dc}^{i} is the individual applied dc current, and $\lambda = 2/3$[278]. Here $y_i = \frac{Y_i}{\mathcal{R}_i}$ is the Y position of the vortex core in the nano-dot plane (X, Y) normalized by the radius of the free-layer $\mathcal{R}_i$. We used the same simulation framework used previously to reproduce numerically the synchronization state features observed experimentally for an array of two [14] and four[24] coupled nano-oscillators in presence of external

microwave stimuli.

As in the previous chapter, the magnetization dynamics of the nano-oscillators is obtained by solving numerically the coupled differential Thiele equation 72 simultaneously for the N vortex $i = 1, 2, ..N$.

$$\mathbf{G_i} \times \frac{d\mathbf{X_i}}{dt} - \mathbf{D_i}(\mathbf{X_i})\frac{d\mathbf{X_i}}{dt} - \frac{\partial W_i(I_{rf}^{com})}{\partial \mathbf{X_i}} + \mathbf{F_i^{STT}}(I_{rf}^{com}) = 0 \quad (72)$$

Here, $\mathbf{X_i} = (x_i, y_i)$ is the vortex core position, $\mathbf{G_i}$ is the gyrovector, $\mathbf{D_i}$ is the damping, W_i is the potential energy of the vortex, $\mathbf{F_i^{STT}}$ is the spin-transfer force.

7.3.2 *Simulation of large arrays in presence of external microwave inputs and with electrical coupling*

Fig. 4a shows the large variety of synchronization states obtained when two distinct external microwave stimuli with frequencies (f_A, f_B) are injected to the array of one hundred spin-torque nano-oscillators. By sweeping the frequency of these external stimuli in the frequency range covered by the nano-oscillator array from 145 MHz to 655 MHz, each nano-oscillator is regularly synchronized and desynchronized from the external signal around its free-running auto-oscillation frequency. Every colored square corresponds to one unique synchronization state.

In this configuration, 9900 different synchronization states can be achieved (by comparison, previous experimental work with four coupled nano-oscillators showed only 12 synchronization states[24]). As shown on the synchronization map of Fig. 4a and its corresponding frequency zoom area Fig. 4b, the individual injection-locking ranges and the frequency gap between closest nano-oscillator frequencies are very similar and, as designed, have a frequency size deviation smaller than 5%. This deviation from the desired frequency features ((i) and (ii)) varies with the collective electrical coupling conditions.

7.3.3 *Impact of higher electrical coupling in large arrays*

To highlight the aforementioned deviation, we study a smaller array of 10 coupled spin-torque nano-oscillators in presence of two injected

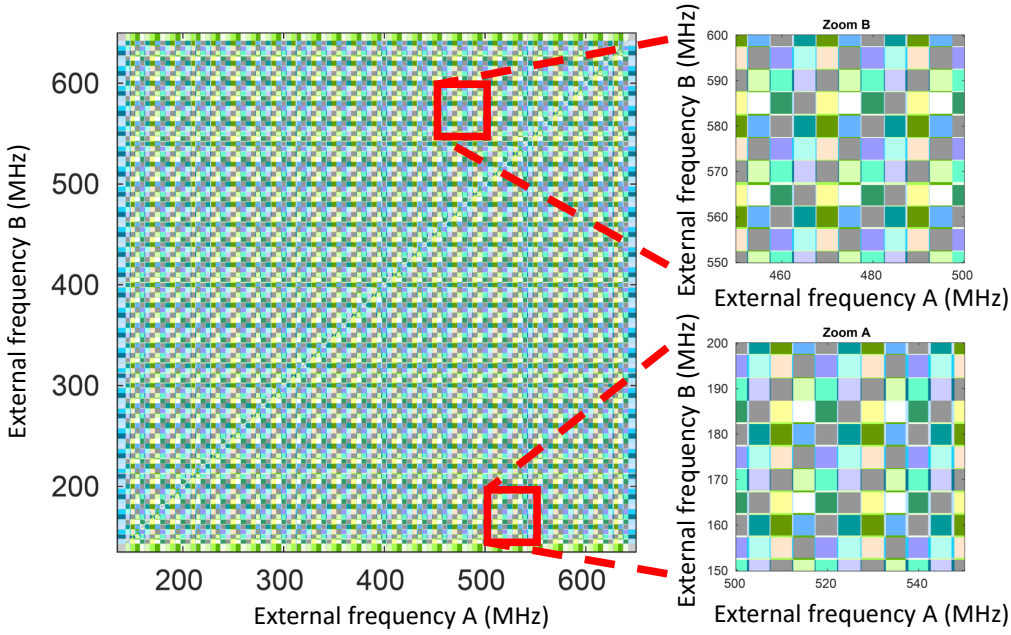

Figure 75: Simulated synchronization state map of the 100 nano-oscillators with chosen free-layer dimensions and applied dc currents. The x and y axis correspond to the two frequency microwave inputs injected electrically to the array. Depending on the frequency of these frequency inputs, regularly one spin-torque nano-oscillator synchronize to one of the two microwave inputs. Each small square represent one particular synchronization state. (Different synchronization states can have the same color). Small zoom on the square area of the main synchronization map.

microwave signals and simulate the system as it was done for the array of 100 nano-oscillators but varying the electrical coupling. To simulate distinct electrical coupling environments, we multiply the common emitted microwave current generated by all spin-torque nano-oscillators I_{rf}^{com} by an arbitrary factor k and consider the following new common microwave current $I_{rf}^{com} = k.I_{rf}^{com}$. As shown in Fig. 4c, the increase of coupling modifies the mean injection-locking range size of the 10 spin-torque nano-oscillators of the array in such a way that in the high coupling regimes corresponding to $k > 1.5$, the synchronization response of the array diverges from the initially designed one. For such electrical coupling conditions, the spin-torque nano-oscillator

array will not be sensitive to input microwave frequencies. It should be noticed that the observed injection locking range decrease is not occurring for standard experimental coupling condition corresponding to $k = 1$. This numerical result shows that the analytical approach to designing large size arrays that we propose is robust to electrical coupling effects.

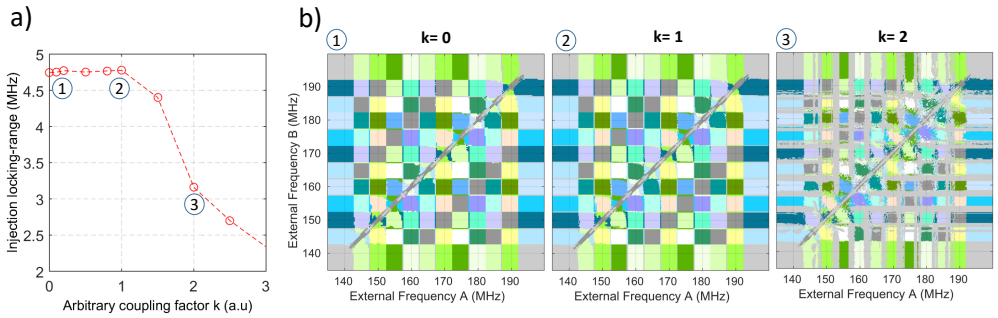

Figure 76: a) Mean injection locking-range of 10 simulated coupled spin-torque nano-oscillators versus the arbitrary coupling factor k, k=1 corresponds to standard experimental conditions. b) Corresponding synchronization state maps obtained respectively from left to right k=0, k=1, k=2.

Fig. 76-b illustrates the corresponding synchronization state maps from which the mean injection locking range was evaluated. As it can be seen on these maps, for intermediate coupling conditions corresponding to k=1 the synchronization states are regularly spaced and are well defined while for higher coupling conditions corresponding to k=2, the synchronization states are no more well defined and other undesired synchronization states represented by gray color appear in those regions. This explains why the mean injection-locking range corresponding to this high coupling condition is smaller.

7.4 CONCLUSION

According to the analytical study presented in this chapter, the individual dimensions of the free layer and the applied direct current are sufficient parameters to obtain suitable frequency and synchronization bandwidth to design large spin-torque nano-oscillator arrays sensi-

tive to wide input frequency bandwidths. The precision that can be achieved on this parameters, due to nano-processing and electrical circuit design, imposes the maximum size of spin-torque nano-oscillator arrays. We have shown that the maximum size of such array is 300 spin-torque nano-oscillators for realistic manufacturing parameters. Finally, we have shown numerically that mutual couplings in the array modifies the effective injection locking range of the oscillators. However, for low and intermediate electrical couplings corresponding to typical experimental conditions, the spin-torque nano-oscillator arrays show the same sensitivity to the whole input frequency bandwidth as designed. In summary, we have shown through simulations the possibility to build a device made of a large array of electrically coupled spin-torque nano-oscillator able to respond to a wide range of microwave input frequency with a constant sensitivity in the whole operating bandwidth.

The main results of this chapter are:

- By choosing analytically appropriate individual applied dc current and free-layer size of spin-torque nano-oscillators, we were able to design an array of 100 spin-torque nano-oscillators, for which the expected analytical frequencies are regularly spaced and the individual synchronization bandwidth are similar.
- The maximum number of nano-oscillators in such arrays was determined, giving the minimum applied dc current and free-layer size variations. For most optimal constraints, we estimate that we can design arrays of more than 300 nano-oscillators.
- For low and intermediate electrical couplings corresponding to typical experimental conditions, the spin-torque nano-oscillator arrays show the same sensitivity to the whole input frequency bandwidth as initially designed for the uncoupled case.

8

SUMMARY AND CONCLUSIONS

This thesis shows the first experimental demonstration of brain-inspired computing with an array of coupled nano-oscillators. This demonstration was possible through the exceptional properties of spin-torque nano-oscillators. In order to realize this demonstration the synchronization ability of these nano-oscillators was leveraged to achieve a pattern recognition task corresponding to vowel recognition. The other important aspect of this demonstration was the achievement of experimental learning with coupled nano-oscillators which would not be possible without the high frequency tunability of the studied coupled nano-oscillators. The recognition performance obtained through this small implemented neural network is of the order of 88% which is high considering that the network comprises only four oscillator-like neurons. The recognition performance comparison with artificial neural network algorithms highlighted the fact that this high recognition performance is due to the rich physics of the hardware neurons implemented here by nonlinear oscillators.

Simulations of studied experimental nano-oscillators reveal the crucial role of both high tunability and intermediate coupling between oscillators to optimize the recognition response of nano-oscillator networks leveraging synchronization for pattern classification tasks. It should be noticed that the network used for the demonstration of brain-inspired operations was very small and in order to achieve more difficult tasks, larger hardware neural network need to be implemented. Thus, the perspective of building arrays of hundreds of spin-torque nano-oscillators with the constraints of nanotechnology was studied numerically. These results could help to open new paths towards scaling-up arrays of coupled spin-torque nano-oscillators for brain-inspired computing.

A possible perspective to this thesis could be the physical implementation of large arrays of spin-torque nano-oscillators in order to realize complex cognitive tasks. This kind of future implementation

can require to tune and control large number of physical parameters such as the applied dc current. This feature can be achieved through dedicated peripheral electronic circuits specially designed to modify the behavior of the oscillator array.

An important issue that should be taken into account in the future realization of computing systems based of spin-torque oscillators is their energy consumption. Beyond the energy contribution due to the read-out and control circuits surrounding nano-oscillators, it is important to reduce their individual energy consumption. Indeed, as the number of the spin-torque oscillators becomes larger, the energy contribution to make them operate should become more and more predominant. In order to reduce the energy consumption due to oscillators, an important challenge is to reduce the value of the individual applied dc current. To achieve this goal, one approach is to reduce the spin-torque oscillator lateral size to 10-20 nm [288], allowing high current densities with small applied dc currents. Interestingly, such dimensions are already achieved for magnetic tunnel junctions used in STT-MRAM magnetic memories. The fact that such memories are included in the industrial fabrication process of biggest microelectronic foundries [289], is a positive signal towards optimization and integration of such magnetic tunnel junctions that can be adapted to play the role of the next generation of down-scaled spin-torque oscillators.

Interconnection with other multi-functional spintronic devices that can emulate synaptic weights in arrays of coupled spin-torque oscillators is also an important future challenge to overcome. Indeed, pioneer spintronic devices based on magnetic domain wall propagation in magnetic tunnel junctions are already proposed and demonstrated to play the role of synapses [290]. This interconnection may allow to implement a fully spintronic nano-scale system emulating physically in hardware the two main components of neural networks which are neurons and synapses.

Beyond the physical implementation of basic properties of neural networks at the nano-scale allowing for instance inference, one should also consider to embed the powerful artificial neural network algorithms

developed for deep learning which are crucial to achieve interesting and complex tasks nowadays. As an example, a major issue is the physical implementation of back-propagation algorithms in deep neural networks. In order to avoid additional complexity to the physical hardware, interesting approaches leveraging the dynamics of physical systems can be proposed [291]. Once again the nonlinear dynamics of spin-torque oscillators can play a crucial role in these interesting approaches.

These perspectives associated to this thesis should contribute to open the path to energy efficient on-chip brain-inspired computing devices.

A

APPENDICES

A.1 GLOSSARY

A.1.1 *Fundamental physical constants*

Symbols	Names	Values	Units
e	elementary charge	1.602×10^{-19}	C
$\hbar$	reduced Planck constant	1.054×10^{-34}	$J.s$
μ_0	magnetic constant	$4\pi \times 10^{-7}$	$T.mA^{-1}$
γ	gyromagnetic ratio (free electron)	1.761×10^{11}	$rad.s^{-1}.T^{-1}$
g	Landé g-factor	2	-
μ_B	Bohr magneton	9.274×10^{-24}	$J.T^{-1}$

A.1.2 *Material properties*

Symbols	Names	Units
$D_{(\uparrow\downarrow)}(E_F)$	density of states at the Fermi level (spin dependent)	m^{-3}
$r_{(\uparrow\downarrow)}$	resistivity (spin dependent)	$\Omega^{-1}.m$
$j_{(\uparrow\downarrow)}$	current density (spin dependent)	$A.m^{-2}$
J	charge current density	$A.m^{-2}$
$k_{(\uparrow\downarrow)}$	wave vector amplitude (spin dependent)	m^{-1}
$R_{(ap,p)}$	resististance (in antiparallel or parallel configuration)	Ω
$G_{(ap,p)}$	conductance (in antiparallel or parallel configuration)	S
$\mathcal{P}_i$	spin polarization (of the ferromagnetic layer i)	-

A.1.3 *Magnetic properties*

Symbols	Names	Units
$\overrightarrow{M_i}$	local magnetization of the ferromagnetic layer i	$A.m^{-1}$
$\overrightarrow{p}$	unit vector of local magnetization of the polarizer	-
$\overrightarrow{m}$	unit vector of local magnetization of the free-layer	-
$\overrightarrow{H}_{eff}$	effective magnetic field	$A.m^{-1}$
M_s	saturation magnetization of	$A.m^{-1}$
M_s^{pol}	saturation magnetization of the polarizer	$A.m^{-1}$
$H_\perp$	fixed perpendicular applied magnetic field	$A.m^{-1}$
α	Gilbert damping coefficient	$A.m^{-1}$
θ	angle between $\overrightarrow{m}$ and $\overrightarrow{p}$	rad
A	exchange constant	$A.m^{-1}$
$L_{ex} = \sqrt{\frac{2A}{\mu_0 M_s^2}}$	exchange length	m

A.1.4 *Geometric parameters*

Symbols	Names	Units
L	free-layer thickness	m
$\mathcal{R}$	radius of the free-layer	m
$(x, y) = (\frac{X}{\mathcal{R}}, \frac{Y}{\mathcal{R}})$	normalized Cartesian position coordinates	-
$s = \sqrt{x^2 + y^2}$	normalized amplitude of the oscillator	-

A.1.5 *Parameters used in the dynamics of the magnetic vortex*

Symbols	Names	Units
(s_c, θ_c)	polar vortex core position	m,rad
b	vortex core radius	m
P	vortex polarity	-
C	vortex chirality	-
θ_0	free layer magnetization angle	rad
D_0	damping magnitude[159]	$kg.rad^{-1}.s^{-1}$
ξ	nonlinear damping coeficient[160, 287]	-
G	gyrovector magnitude	$kg.rad^{-1}.s^{-1}$
a_j	efficiency of the Slonczewski torque	$kg.m^2.A^{-1}.s^{-2}$
b_j	efficiency of the field-like torque	$kg.m^2.A^{-1}.s^{-2}$
κ_{ms}	magnetostatic confinement[261]	$kg.s^{-2}$
$\kappa_{ms}^{'}$	nonlinear magnetostatic confinement[261]	$kg.s^{-2}$
κ_{Oe}	Oersted field confinement[287]	$kg.m^2.A^{-1}.s^{-2}$
$\kappa_{Oe}^{'}$	nonlinear Oersted field confinement[287]	$kg.m^2.A^{-1}.s^{-2}$

A.2 COEFFICIENTS USED FOR THE TWO LINEAR COMBINATIONS APPLIED TO VOWEL FORMANTS

Coefficients	Values	Coefficients	Values
A_1	434.12796	A_2	-2132.59467
B_1	3876.66394	B_2	3471.05641
C_1	-2720.95643	C_2	1761.05172
D_1	23736.72522	D_2	-14515.22882
E_1	-8692.08149	E_2	3704.32823
G_1	1978.73518	G_2	-117.44496
H_1	4297.31026	H_2	3038.31175
I_1	-149.58903	I_2	1409.6298
J_1	-23.0464	J_2	-80.14666
K_1	6447.12594	K_2	5676.35479
L_1	5821.65047	L_2	2441.92994
M_1	-2904.5703	M_2	-3344.9537
N_1	3.27684×10^8	N_2	3.38139×10^8

A.3 SUMMARY IN FRENCH, RÉSUMÉ EN FRANÇAIS

A.3.1 *Introduction et contexte*

Ces dernières décennies, le domaine de l'intelligence artificiel a montré un impressionnant progrès permettant d'accomplir des tâches cognitives considérées initialement comme trop complexes pour être effectuées par des ordinateurs (reconnaissance vocal ou d'images). Désormais, au-delà de l'exécution d'instructions précises, le calcul devient de plus en plus synonyme de systèmes intelligents qui sont capables d'apprendre à partir des données et qui peuvent adapter leurs réponses en fonction de leurs environnements. Cette percée a été rendu possible par le développement d'algorithmes innovants inspirées du cerveau mené depuis les années 50. Les premières observations du cerveau en neurosciences ont donné lieu au développement à une catégorie importante d'algorithmes, qui est celle des réseaux de neurones artificiels. En dépit du manque de compréhension sur le fonctionnement complet du cerveau, ces algorithmes ont pu surpasser les humains pour réaliser plusieurs taches particulières. Un exemple frappant de la puissance de

ces algorithmes inspirés du cerveau peut être illustré par les récentes défaites des meilleurs champions au jeu de Go[16][17]. Même s'il s'agit là d'un exploit majeur dans le domaine de l'intelligence artificielle, cela ne doit pas masquer une lacune importante dans la faËœcon dont ces succès ont été achevés. En effet, la consommation énergétique des ordinateurs pour exécuter des algorithmes d'intelligence artificielle est beaucoup plus grande que celle du cerveau. Cette consommation devrait continuer à augmenter avec l'augmentation du nombre de paramètres nécessaires pour réaliser des taches de plus en plus complexes.

Une des raisons pour lesquelles ces algorithmes inspirés du cerveau consomment plus d'énergie que le cerveau provient de la différences d'architecture fondamentale qu'il y a entre le cerveau et les ordinateurs actuels. Sur ces derniers, la mémoire et l'unité de calcul sont séparés spatialement, ce qui entraîne un transport de données important sous forme de va et vient entre ces unités causant une forte consommation énergétique. A l'inverse, le cerveau est une architecture massivement parallèle où les neurones et les synapses qui jouent le rôle respectivement d'unité de calcul et de mémoire sont enchevêtrés et sont très proches spatialement les uns des autres ce qui réduit le transport de l'information. Pour cette raison, les ordinateurs conventionnels ne sont pas optimisés pour l'exécution d'algorithmes inspirés du cerveau. Ces observations motivent le développement d'approches de calcul alternatives qui prennent inspiration de la biologie, appelées approches de calcul bio-inspiré. Ces observations motivent également le développement de systèmes physiques alternatifs qui vont pouvoir combiner des fortes performances en terme de calcul pour réaliser des taches cognitives et des faibles consommations en terme d'énergie. Afin de développer des systèmes de calcul inspiré du cerveau, il est important de pouvoir émuler le comportement des neurones biologiques [18][19][20]. Ces unités de calcul du cerveau peuvent être vu comme des petits oscillateurs non-linéaire connectés les uns avec les autres via des connexion réglable portés par les synapses. Différents modèles pour faire du calcul avec des assemblées d'oscillateurs non-linéaires ont pu voir le jour en Physique et en Neurosciences [22][21]. A titre d'exemple, pour faire du calcul ces modèles exploitent différents phénomènes dynamiques telles que la synchronisation qui se produit dans le cerveau. Dès lors que le nombre d'oscillateurs est élevés (de l'ordre de 10^{11} neu-

rones et 10^{15} synapses dans le cerveau humain), ces modèles sont très puissants pour des taches de reconnaissance de motifs. Implémenter ces modèles physiquement en hardware nécessitent donc d'assembler un très grand nombre d'oscillateurs non-linéaires. Pour éviter de concevoir des circuit de grandes tailles, les dispositifs physiques qui vont donc émuler individuellement les neurones et les synapses doivent être suffisamment petits. Au vu du grand nombre de neurones et de synapses dans le cerveau, ces dispositifs physiques doivent être idéalement nanométriques. C'est pour cette raison que les dispositifs nanométriques capables d'émuler les fonctionnalités des neurones et des synapses sont nécessaires pour implémenter physiquement des systèmes de calcul inspiré du cerveau. En particulier, les nano-oscillateurs sont très prometteurs pour émuler les neurones. En dépit de plusieurs propositions pour faire du calcul inspiré du cerveau en utilisant les nano-oscillateurs, il n'y a pas eu de démonstration physique de ce type d'approche. Cela est dû aux fortes sensibilités au bruit et à la difficulté de contrôler les propriétés des nano-oscillateurs à l'échelle nanométriques. Néanmoins, en tirant parti des propriétés exceptionnelles des nano-oscillateurs magnétiques, récemment, une première démonstration de calcul inspiré du cerveau a pu être établi et cela en utilisant un seul nano-oscillateurs à transfert de spin [23]. Dans cette approche, la dynamique transitoire de l'amplitude des oscillations a été exploité pour reconnaitre des empreintes vocales prononcés par différents locuteurs et cela avec des performances à l'état de l'art. Cependant, pour réaliser des taches cognitives de plus en plus complexes, il est nécessaire de démontrer une propriété importante des réseaux de neurones qui est l'apprentissage. Cette étape consiste en une procédure itérative au cours de laquelle un réseau de neurones est entrainé avec une fraction des données d'entrées et où il ajuste ses paramètres internes (ses connexions entre neurones) afin d'améliorer ses performances de reconnaissance ou de classification. Une difficulté majeure dans l'apprentissage des réseaux de nano-oscillateurs couplés est qu'il faut ajuster le couplage entre eux. Cette thèse présente une première démonstration expérimentale de calcul inspiré du cerveau avec une assemblée physique de nano-oscillateurs couplés [24]. Cette démonstration tire parti du phénomène de synchronisation des nano-oscillateurs à transfert de spin pour réaliser une tache de reconnaissance de motifs illustré par la reconnaissance de voyelles. Grace aux

larges accordabilités en fréquence des nano-oscillateurs à transfert de spin, la capacité d'apprentissage des nano-oscillateurs couplés a été également démontré pour la première fois [6].

A.3.2 *Résultats*

A.3.2.1 *Chapitre 1*

Le premier chapitre de cette thèse présente la principale motivation du calcul inspiré du cerveau et montre comment les oscillations observées dans les neurones biologiques peuvent être utilisés pour concevoir un modèle d'assemblée d'oscillateurs non-linéaire pour faire du calcul. Les différents types de nano-oscillateurs prometteur pour mener ce but y sont présentés.

A.3.2.2 *Chapitre 2*

Le second chapitre de cette thèse introduit les nano-oscillateurs à transfert de spin. Les phénomènes physiques ainsi que les principes qui mènent aux oscillations y sont décrit. Un accent particulier y est porté à la dynamique non-linéaire et la capacité de synchronisation des nano-oscillateurs à transfert de spin. Ces propriétés sont surlignées dans l'objectif de faire du calcul inspiré du cerveau.

A.3.2.3 *Chapitre 3*

Le troisième chapitre introduit brièvement une catégorie particulière de nano-oscillateurs à transfert de spin que sont les oscillateurs à base de vortex magnétiques. La dynamique et la synchronisation de ces oscillateurs sont présentés à la fois théoriquement et expérimentalement. En particulier, j'y ai montré les propriétés de synchronisation à un signal alternative extérieur des oscillateurs. Cette synchronisation peut être modifié par l'intermédiaire du couplage électrique avec un second oscillateur. Les principaux résultats de ce chapitre sont les suivants :

- Démonstration expérimental du contrôle du couplage électrique entre deux oscillateurs à transfert de spin via la modification des fréquences individuelles respectives des oscillateurs.

- Augmentation de la gamme de synchronisation à la source extérieur par un facteur de 1.64 en présence d'un couplage électrique avec un autre oscillateur.

- Contrôle de la synchronisation des nano-oscillateur à transfert de spin couplés.

- Identification des mécanismes expliquant l'évolution de l'augmentation de la gamme de synchronisation au signal extérieur en fonction de la différence de fréquence entre les oscillateurs.

A.3.2.4 *Chapitre 4*

Ce chapitre présente les principaux résultats expérimentaux de calcul inspiré du cerveau. Dans ce chapitre, j'ai montré qu'une assemblée de quatre nano-oscillateurs à transfert de spin peuvent classifier des voyelles prononcées par différents locuteurs. Cette démonstration a été possible en exploitant les états de synchronisation aux signaux extérieurs qui émergent sans le réseau d'oscillateur. En utilisant la large accordabilité en fréquence des nano-oscillateur à transfert de spin, nous avons également démontré expérimentalement la capacité d'apprentissage des nano-oscillateurs couplés pour classifier. Les principaux résultats de ce chapitre sont les suivants :

-Implémentation expérimental d'un réseau d'oscillateurs sur la base d'un réseau de quatre nano-oscillateurs à transfert de spin connectés les uns avec les autres via des connexions électriques micro-ondes.

-Démonstration expérimental de la reconnaissance de sept voyelles prononcés par différents locuteurs avec un taux de reconnaissance proche de l'état de l'art : 88%.

-Démonstration expérimental de la capacité d'apprentissage du réseau de nano-oscillateurs couplés rendu possible à travers l'ajustement des fréquences individuelles des nano-oscillateurs. Cette ajustement a pu être réalisé grâce au contrôle individuel sur le courant dc appliqué dans chaque nano-oscillateur.

-Démonstration expérimental de reconnaissances de 12 voyelles prononcés par différents locuteurs avec le réseau de nano-oscillateurs couplés avec un taux de reconnaissance de l'ordre de 68.4%.

A.3.2.5 *Chapitre 5*

Ce chapitre présente les simulations de réseaux d'oscillateurs réalisé dans l'objectif de comprendre l'origine des performances en taux reconnaissance observées expérimentalement. A travers ces simulations j'ai pu montrer de l'accordable en fréquences ainsi que l'existence d'un couplage intermédiaire entre sont des propriétés cruciales pour obtenir de forts taux de reconnaissances. Les principaux résultats de ce chapitre sont les suivants :

-En utilisant l'approche de l'équation de Thiele, j'ai pu reproduire en simulation les états de synchronisations observés expérimentalement à différents étape du processus d'apprentissage.

-Le taux de reconnaissance des réseaux d'oscillateurs étudiés augmente en fonction de l'accordabilité en fréquence des oscillateurs.

-Pour une valeur d'accordabilité donnée, le taux de reconnaissance peut être amélioré en présence d'un couplage intermédiaire entre les oscillateurs à transfert de spin.

-Pour de fortes valeurs de couplage, le taux de reconnaissance décroit. Cette diminution est due à l'instabilité de la fréquence et des états de synchronisations dans le temps.

A.3.2.6 *Chapitre 6*

Dans ce chapitre, afin de réaliser des taches cognitives plus difficiles nécessitant de large réseaux de neurones, nous avons démontré numériquement qu'un réseau d'une centaine de nano-oscillateurs à transfert de spin peut être conçu avec les contraintes standards de nano-fabrication.

Les principaux résultats de ce chapitre sont les suivants :

-En choisissant analytiquement le courant dc appliqué ainsi que la taille de la couche libre des nano-oscillateurs à transfert de spin, j'ai pu concevoir une assemblée d'une centaine de nano-oscillateurs pour lesquelles les fréquences individuelles sont régulièrement espacé et les gammes de synchronisation sont similaires.

-Pour des variations de taille de couche libre données ainsi que pour un maximum de courant dc appliqué, le nombre maximum de nano-oscillateurs à transfert de spin a été déterminé pour lesquelles on peut obtenir des fréquences régulièrement espacé et des gammes de synchronisation similaires. Sous ces contraintes, d'après mes estimations, des réseaux de plus de 300 nano-oscillateurs peuvent être conçus.

-Pour des couplages électriques intermédiaires correspondant aux conditions expérimentales, les réseaux d'oscillateurs de grandes tailles (typiquement de l'ordre de 100 nano-oscillateurs) présentent les mêmes caractéristiques en termes de synchronisation et séparation en fréquences que celles pour lesquelles le réseau avait été conçu initialement en l'absence de couplage.

A.3.2.7 *Conclusion and perspectives*

Ces résultats ouvrent de nouvelles voies au calcul bio-inspiré de haute efficacité énergétique intégrable sur puce grâce à des dispositifs nanométriques non-linéaires qui peuvent s'adapter et apprendre. En terme de perspectives de nouveaux défis sont posé, tel que l'implémentation physique de réseaux d'oscillateurs de grande taille ainsi que le réglage de leurs paramètres. Aussi, se pose le défi de l'interconnexion des nano-oscillateur avec d'autre dispositifs spintronique jouant le rôle de synapse ainsi que l'implémentation en hardware de réseaux de neurones exploitant les algorithme d'apprentissage profond.

BIBLIOGRAPHY

[1] M. Hopkins, G. Pineda-García, P. A. Bogdan, and S. B. Furber, "Spiking neural networks for computer vision," *Interface Focus*, vol. 8, no. 4, p. 20180007, 2018. (Cited on pages xvi and 26.)

[2] P. A. Merolla, J. V. Arthur, R. Alvarez-Icaza, A. S. Cassidy, J. Sawada, F. Akopyan, B. L. Jackson, N. Imam, C. Guo, Y. Nakamura, *et al.*, "A million spiking-neuron integrated circuit with a scalable communication network and interface," *Science*, vol. 345, no. 6197, pp. 668–673, 2014. (Cited on pages xvi, 26, and 27.)

[3] E. Vassilieva, G. Pinto, J. A. De Barros, and P. Suppes, "Learning pattern recognition through quasi-synchronization of phase oscillators," *IEEE Transactions on Neural Networks*, vol. 22, no. 1, pp. 84–95, 2011. (Cited on pages xvi, 31, 32, 104, 105, and 120.)

[4] D. Vodenicarevic, N. Locatelli, F. A. Araujo, J. Grollier, and D. Querlioz, "A nanotechnology-ready computing scheme based on a weakly coupled oscillator network," *Scientific reports*, vol. 7, p. 44772, 2017. (Cited on pages xvi and 32.)

[5] N. Retdian, S. Takagi, and N. Fujii, "Voltage controlled ring oscillator with wide tuning range and fast voltage swing," in *ASIC, 2002. Proceedings. 2002 IEEE Asia-Pacific Conference on*, pp. 201–204, IEEE, 2002. (Cited on pages xvii, 36, and 37.)

[6] J. Philippe, G. Arndt, E. Colinet, M. Savoye, T. Ernst, E. Ollier, and J. Arcamone, "Fully monolithic and ultra-compact nems-cmos self-oscillator based-on single-crystal silicon resonators and low-cost cmos circuitry," in *Micro Electro Mechanical Systems (MEMS), 2014 IEEE 27th International Conference on*, pp. 1071–1074, IEEE, 2014. (Cited on pages xvii, 38, and 39.)

[7] X. Feng, C. White, A. Hajimiri, and M. L. Roukes, "A self-sustaining ultrahigh-frequency nanoelectromechanical oscillator,"

Nature nanotechnology, vol. 3, no. 6, p. 342, 2008. (Cited on pages xvii, 38, and 39.)

[8] R. Lebrun, *Coupled vortex dynamics in spin-torque oscillators : from resonant excitation to mutual synchronization*. Paris Saclay, Dec. 2015. (Cited on pages xvii, xx, 45, 46, 51, 56, and 82.)

[9] W. Commons. (Cited on pages xvii and 49.)

[10] M. D. Stiles and J. Miltat, "Spin-transfer torque and dynamics," in *Spin dynamics in confined magnetic structures III*, pp. 225–308, Springer, 2006. (Cited on pages xviii, 51, 52, 53, and 64.)

[11] N. Locatelli, *Dynamique par transfert de spin et synchronisation d'oscillateurs couples a base de vortex magnetiques*. phdthesis, Universite Paris Sud - Paris XI, Dec. 2012. (Cited on pages xix, 61, 80, and 83.)

[12] E. Grimaldi, *Etude des proprietes non-lineaires et de l'origine du bruit d'oscillateurs a transfert de spin a base de vortex : vers le developpement de nano-dispositifs radiofrequences spintroniques*. phdthesis, Universite Paris Sud-Paris XI, June 2015. (Cited on pages xix, 71, and 81.)

[13] K. L. Metlov and K. Y. Guslienko, "Stability of magnetic vortex in soft magnetic nano-sized circular cylinder," *Journal of magnetism and magnetic materials*, vol. 242, pp. 1015–1017, 2002. (Cited on pages xix, xxvii, 79, 160, 164, and 165.)

[14] M. Romera, P. Talatchian, R. Lebrun, K. J. Merazzo, P. Bortolotti, L. Vila, J. D. Costa, R. Ferreira, P. P. Freitas, M.-C. Cyrille, U. Ebels, V. Cros, and J. Grollier, "Enhancing the injection locking range of spin torque oscillators through mutual coupling," *Applied Physics Letters*, vol. 109, no. 25, p. 252404, 2016. (Cited on pages xx, xxi, 86, 93, 94, 95, 96, 106, and 169.)

[15] J. Hillenbrand, L. A. Getty, M. J. Clark, and K. Wheeler, "Acoustic characteristics of american english vowels," *The Journal of the Acoustical society of America*, vol. 97, no. 5, pp. 3099–3111, 1995. (Cited on pages xxii and 115.)

[16] D. Silver, A. Huang, C. J. Maddison, A. Guez, L. Sifre, G. Van Den Driessche, J. Schrittwieser, I. Antonoglou, V. Panneershelvam, and M. Lanctot, "Mastering the game of Go with deep neural networks and tree search," *Nature*, vol. 529, no. 7587, pp. 484–489, 2016. (Cited on pages 3, 23, and 183.)

[17] D. Silver, J. Schrittwieser, K. Simonyan, I. Antonoglou, A. Huang, A. Guez, T. Hubert, L. Baker, M. Lai, and A. Bolton, "Mastering the game of go without human knowledge," *Nature*, vol. 550, no. 7676, pp. 354–359, 2017. (Cited on pages 3, 23, and 183.)

[18] G. Indiveri, F. Corradi, and N. Qiao, "Neuromorphic architectures for spiking deep neural networks," in *2015 IEEE International Electron Devices Meeting (IEDM)*, pp. 4.2.1–4.2.4, Dec. 2015. (Cited on pages 4 and 183.)

[19] "Dynap-se." https://www.ini.uzh.ch/en/research/groups/ncs/chips/Dynap-se.html. Accessed: 2010-09-30. (Cited on pages 4, 25, and 183.)

[20] M. D. Pickett, G. Medeiros-Ribeiro, and R. S. Williams, "A scalable neuristor built with mott memristors," *Nature materials*, vol. 12, no. 2, p. 114, 2013. (Cited on pages 4, 24, 34, 35, and 183.)

[21] J. Fell and N. Axmacher, "The role of phase synchronization in memory processes," *Nature reviews neuroscience*, vol. 12, no. 2, p. 105, 2011. (Cited on pages 4, 15, 66, and 183.)

[22] D. R. Chialvo, "Emergent complex neural dynamics," *Nature physics*, vol. 6, no. 10, p. 744, 2010. (Cited on pages 4, 15, and 183.)

[23] J. Torrejon, M. Riou, F. A. Araujo, S. Tsunegi, G. Khalsa, D. Querlioz, P. Bortolotti, V. Cros, K. Yakushiji, A. Fukushima, H. Kubota, S. Yuasa, M. D. Stiles, and J. Grollier, "Neuromorphic computing with nanoscale spintronic oscillators," *Nature*, vol. 547, no. 7664, pp. 428–431, 2017. (Cited on pages 4, 21, and 184.)

[24] M. Romera, P. Talatchian, S. Tsunegi, F. Abreu Araujo, V. Cros, P. Bortolotti, J. Trastoy, K. Yakushiji, A. Fukushima, H. Kubota,

S. Yuasa, M. Ernoult, D. Vodenicarevic, T. Hirtzlin, N. Locatelli, D. Querlioz, and J. Grollier, "Vowel recognition with four coupled spin-torque nano-oscillators," *Nature*, vol. 563, no. 7730, pp. 230–234, 2018. (Cited on pages 5, 103, 135, 163, 169, 170, and 184.)

[25] E. R. Kandel, J. H. Schwartz, T. M. Jessell, D. of Biochemistry, M. B. T. Jessell, S. Siegelbaum, and A. Hudspeth, *Principles of neural science*, vol. 4. McGraw-hill New York, 2000. (Cited on pages 10 and 23.)

[26] L. Lapicque, "Recherches quantitatives sur l'excitation electrique des nerfs traitee comme une polarization," *Journal de Physiologie et de Pathologie Generalej*, vol. 9, pp. 620–635, 1907. (Cited on pages 10 and 13.)

[27] A. L. Hodgkin and A. F. Huxley, "A quantitative description of membrane current and its application to conduction and excitation in nerve," *The Journal of physiology*, vol. 117, no. 4, pp. 500–544, 1952. (Cited on page 10.)

[28] L. Caruso, T. Wunderle, C. M. Lewis, J. Valadeiro, V. Trauchessec, J. T. Rosillo, J. P. Amaral, J. Ni, P. Jendritza, C. Fermon, S. Cardoso, P. Peixeiro Freitas, P. Fries, and M. Pannetier-Lecoeur, "In vivo magnetic recording of neuronal activity," *Neuron*, vol. 95, no. 6, pp. 1283–1291, 2017. (Cited on page 10.)

[29] E. M. Izhikevich, "Which model to use for cortical spiking neurons?," *IEEE transactions on neural networks*, vol. 15, no. 5, pp. 1063–1070, 2004. (Cited on page 15.)

[30] M. Rabinovich, R. Huerta, and G. Laurent, "Transient dynamics for neural processing," *Science*, pp. 48–50, 2008. (Cited on page 15.)

[31] O. Marre, P. Yger, A. P. Davison, and Y. Frégnac, "Reliable recall of spontaneous activity patterns in cortical networks," *Journal of neuroscience*, vol. 29, no. 46, pp. 14596–14606, 2009. (Cited on page 15.)

[32] F. C. Hoppensteadt and E. M. Izhikevich, "Associative memory of weakly connected oscillators," in *Neural Networks, 1997., International Conference on*, vol. 2, pp. 1135–1138, IEEE, 1997. (Cited on pages 15 and 30.)

[33] F. C. Hoppensteadt and E. M. Izhikevich, "Oscillatory neurocomputers with dynamic connectivity," *Physical Review Letters*, vol. 82, no. 14, p. 2983, 1999. (Cited on pages 15, 36, 103, and 105.)

[34] Y. LeCun, Y. Bengio, and G. Hinton, "Deep learning," *nature*, vol. 521, no. 7553, p. 436, 2015. (Cited on page 16.)

[35] A. Likas, N. Vlassis, and J. J. Verbeek, "The global k-means clustering algorithm," *Pattern recognition*, vol. 36, no. 2, pp. 451–461, 2003. (Cited on page 17.)

[36] D. E. Rumelhart, G. E. Hinton, and R. J. Williams, "Learning internal representations by error propagation," tech. rep., California Univ San Diego La Jolla Inst for Cognitive Science, 1985. (Cited on page 19.)

[37] Y. LeCun, L. Bottou, Y. Bengio, and P. Haffner, "Gradient-based learning applied to document recognition," *Proceedings of the IEEE*, vol. 86, no. 11, pp. 2278–2324, 1998. (Cited on page 20.)

[38] C. Szegedy, S. Ioffe, V. Vanhoucke, and A. A. Alemi, "Inception-v4, inception-resnet and the impact of residual connections on learning.," in *AAAI*, vol. 4, p. 12, 2017. (Cited on page 20.)

[39] A. Canziani, A. Paszke, and E. Culurciello, "An analysis of deep neural network models for practical applications," *arXiv preprint arXiv:1605.07678*, 2016. (Cited on pages 20, 22, and 23.)

[40] A. Graves, A.-r. Mohamed, and G. Hinton, "Speech recognition with deep recurrent neural networks," in *Acoustics, speech and signal processing (icassp), 2013 ieee international conference on*, pp. 6645–6649, IEEE, 2013. (Cited on page 21.)

[41] Z. C. Lipton, J. Berkowitz, and C. Elkan, "A critical review of recurrent neural networks for sequence learning," *arXiv preprint arXiv:1506.00019*, 2015. (Cited on page 21.)

[42] M. Schuster and K. K. Paliwal, "Bidirectional recurrent neural networks," *IEEE Transactions on Signal Processing*, vol. 45, no. 11, pp. 2673–2681, 1997. (Cited on page 21.)

[43] S. Hochreiter and J. Schmidhuber, "Long short-term memory," *Neural computation*, vol. 9, no. 8, pp. 1735–1780, 1997. (Cited on page 21.)

[44] W. Xiong, J. Droppo, X. Huang, F. Seide, M. Seltzer, A. Stolcke, D. Yu, and G. Zweig, "Achieving human parity in conversational speech recognition," *arXiv preprint arXiv:1610.05256*, 2016. (Cited on page 21.)

[45] Y. Bengio, P. Simard, and P. Frasconi, "Learning long-term dependencies with gradient descent is difficult," *IEEE transactions on neural networks*, vol. 5, no. 2, pp. 157–166, 1994. (Cited on page 21.)

[46] R. Pascanu, T. Mikolov, and Y. Bengio, "On the difficulty of training recurrent neural networks," in *International Conference on Machine Learning*, pp. 1310–1318, 2013. (Cited on page 21.)

[47] P. J. Werbos, "Backpropagation through time: what it does and how to do it," *Proceedings of the IEEE*, vol. 78, no. 10, pp. 1550–1560, 1990. (Cited on page 21.)

[48] H. Jaeger, "The echo state approach to analysing and training recurrent neural networks-with an erratum note," *Bonn, Germany: German National Research Center for Information Technology GMD Technical Report*, vol. 148, no. 34, p. 13, 2001. (Cited on page 21.)

[49] W. Maass, T. Natschlager, and H. Markram, "Real-time computing without stable states: A new framework for neural computation based on perturbations," *Neural computation*, vol. 14, no. 11, pp. 2531–2560, 2002. (Cited on page 21.)

[50] J. Backus, *Can programming be liberated from the von Neumann style?: a functional style and its algebra of programs*. ACM, 2007. (Cited on page 22.)

[51] M. Horowitz, "1.1 computing's energy problem (and what we can do about it)," in *Solid-State Circuits Conference Digest of Technical Papers (ISSCC), 2014 IEEE International*, pp. 10–14, IEEE, 2014. (Cited on page 23.)

[52] A. Krizhevsky, I. Sutskever, and G. E. Hinton, "Imagenet classification with deep convolutional neural networks," in *Advances in neural information processing systems*, pp. 1097–1105, 2012. (Cited on page 23.)

[53] E. Nurvitadhi, G. Venkatesh, J. Sim, D. Marr, R. Huang, J. Ong Gee Hock, Y. T. Liew, K. Srivatsan, D. Moss, S. Subhaschandra, *et al.*, "Can fpgas beat gpus in accelerating next-generation deep neural networks?," in *Proceedings of the 2017 ACM/SIGDA International Symposium on Field-Programmable Gate Arrays*, pp. 5–14, ACM, 2017. (Cited on page 23.)

[54] A. Shacham, K. Bergman, and L. P. Carloni, "Photonic networks-on-chip for future generations of chip multiprocessors," *IEEE Transactions on Computers*, vol. 57, no. 9, pp. 1246–1260, 2008. (Cited on page 23.)

[55] I. O'Connor, "Optical solutions for system-level interconnect," in *Proceedings of the 2004 international workshop on System level interconnect prediction*, pp. 79–88, ACM, 2004. (Cited on page 23.)

[56] C. Mead, "Neuromorphic electronic systems," *Proceedings of the IEEE*, vol. 78, no. 10, pp. 1629–1636, 1990. (Cited on page 24.)

[57] M. Mahowald and R. Douglas, "A silicon neuron," *Nature*, vol. 354, no. 6354, p. 515, 1991. (Cited on page 24.)

[58] G. Indiveri, "A low-power adaptive integrate-and-fire neuron circuit," in *Circuits and Systems, 2003. ISCAS'03. Proceedings of the 2003 International Symposium on*, vol. 4, pp. IV–IV, IEEE, 2003. (Cited on page 24.)

[59] C. Mead and M. Ismail, *Analog VLSI implementation of neural systems*, vol. 80. Springer Science & Business Media, 2012. (Cited on page 24.)

[60] N. Qiao and G. Indiveri, "Scaling mixed-signal neuromorphic processors to 28 nm fd-soi technologies," in *Biomedical Circuits and Systems Conference (BioCAS), 2016 IEEE*, pp. 552–555, IEEE, 2016. (Cited on page 24.)

[61] M. D. Pickett and R. S. Williams, "Sub-100 fj and sub-nanosecond thermally driven threshold switching in niobium oxide crosspoint nanodevices," *Nanotechnology*, vol. 23, no. 21, p. 215202, 2012. (Cited on pages 24, 34, and 35.)

[62] J. J. Yang, D. B. Strukov, and D. R. Stewart, "Memristive devices for computing," *Nature nanotechnology*, vol. 8, no. 1, p. 13, 2013. (Cited on page 24.)

[63] J. Schemmel, D. Briiderle, A. Griibl, M. Hock, K. Meier, and S. Millner, "A wafer-scale neuromorphic hardware system for large-scale neural modeling," in *Circuits and systems (ISCAS), proceedings of 2010 IEEE international symposium on*, pp. 1947–1950, IEEE, 2010. (Cited on page 24.)

[64] J. Schemmel, A. Grübl, S. Hartmann, A. Kononov, C. Mayr, K. Meier, S. Millner, J. Partzsch, S. Schiefer, S. Scholze, *et al.*, "Live demonstration: A scaled-down version of the brainscales wafer-scale neuromorphic system," in *Circuits and systems (ISCAS), 2012 IEEE international symposium on*, pp. 702–702, IEEE, 2012. (Cited on page 24.)

[65] B. V. Benjamin, P. Gao, E. McQuinn, S. Choudhary, A. R. Chandrasekaran, J.-M. Bussat, R. Alvarez-Icaza, J. V. Arthur, P. A. Merolla, and K. Boahen, "Neurogrid: A mixed-analog-digital multichip system for large-scale neural simulations," *Proceedings of the IEEE*, vol. 102, no. 5, pp. 699–716, 2014. (Cited on page 25.)

[66] D. Demarchi, *ECG signals classification using Neuromorphic hardware*. PhD thesis, ETH Zurich, 2018. (Cited on page 25.)

[67] E. Stromatias, F. Galluppi, C. Patterson, and S. Furber, "Power analysis of large-scale, real-time neural networks on spinnaker," in *Neural Networks (IJCNN), The 2013 International Joint Conference on*, pp. 1–8, IEEE, 2013. (Cited on page 25.)

[68] M. Davies, N. Srinivasa, T.-H. Lin, G. Chinya, Y. Cao, S. H. Choday, G. Dimou, P. Joshi, N. Imam, S. Jain, *et al.*, "Loihi: A neuromorphic manycore processor with on-chip learning," *IEEE Micro*, vol. 38, no. 1, pp. 82–99, 2018. (Cited on page 27.)

[69] E. Goto, "The parametron, a digital computing element which utilizes parametric oscillation," *Proceedings of the IRE*, vol. 47, no. 8, pp. 1304–1316, 1959. (Cited on page 28.)

[70] N. Takeuchi, Y. Yamanashi, and N. Yoshikawa, "Reversible computing using adiabatic superconductor logic," in *International Conference on Reversible Computation*, pp. 15–25, Springer, 2014. (Cited on page 28.)

[71] Y. E. Kesim, D. Gala, J. A. Bain, and J. A. Weldon, "Phase based boolean computation using gete 6 oscillators," in *Nanotechnology (IEEE-NANO), 2017 IEEE 17th International Conference on*, pp. 850–854, IEEE, 2017. (Cited on page 28.)

[72] I. Mahboob and H. Yamaguchi, "Bit storage and bit flip operations in an electromechanical oscillator," *Nature nanotechnology*, vol. 3, no. 5, p. 275, 2008. (Cited on page 28.)

[73] S. A. Lee, "k-phase oscillator synchronization for graph coloring," *Mathematics in Computer Science*, vol. 3, no. 1, pp. 61–72, 2010. (Cited on page 28.)

[74] A. Parihar, N. Shukla, M. Jerry, S. Datta, and A. Raychowdhury, "Vertex coloring of graphs via phase dynamics of coupled oscillatory networks," *Scientific reports*, vol. 7, no. 1, p. 911, 2017. (Cited on page 28.)

[75] Y. Fang, M. J. Cotter, D. M. Chiarulli, and S. P. Levitan, "Image segmentation using frequency locking of coupled oscillators," in *Cellular Nanoscale Networks and their Applications (CNNA), 2014 14th International Workshop on*, pp. 1–2, IEEE, 2014. (Cited on page 28.)

[76] K. Yogendra, D. Fan, Y. Shim, M. Koo, and K. Roy, "Computing with coupled spin torque nano oscillators," in *Design Automation Conference (ASP-DAC), 2016 21st Asia and South Pacific*, pp. 312–317, IEEE, 2016. (Cited on pages 28, 29, and 30.)

[77] D. E. Nikonov, G. Csaba, W. Porod, T. Shibata, D. Voils, D. Hammerstrom, I. A. Young, and G. I. Bourianoff, "Coupled-oscillator associative memory array operation for pattern recognition," *IEEE Journal on Exploratory Solid-State Computational Devices and Circuits*, vol. 1, pp. 85–93, 2015. (Cited on page 29.)

[78] P. Maffezzoni, L. Daniel, N. Shukla, S. Datta, and A. Raychowdhury, "Modeling and simulation of vanadium dioxide relaxation oscillators," 2015. (Cited on page 29.)

[79] K. Kudo and T. Morie, "Self-feedback electrically coupled spin-hall oscillator array for pattern-matching operation," *Applied Physics Express*, vol. 10, no. 4, p. 043001, 2017. (Cited on page 29.)

[80] J. J. Hopfield, "Neural networks and physical systems with emergent collective computational abilities," *Proceedings of the national academy of sciences*, vol. 79, no. 8, pp. 2554–2558, 1982. (Cited on pages 29 and 30.)

[81] F. C. Hoppensteadt and E. M. Izhikevich, "Synchronization of mems resonators and mechanical neurocomputing," *IEEE Transactions on Circuits and Systems I: Fundamental Theory and Applications*, vol. 48, no. 2, pp. 133–138, 2001. (Cited on pages 30 and 31.)

[82] P. Maffezzoni, B. Bahr, Z. Zhang, and L. Daniel, "Analysis and design of boolean associative memories made of resonant oscillator arrays," *IEEE Transactions on Circuits and Systems I: Regular Papers*, vol. 63, no. 11, pp. 1964–1973, 2016. (Cited on page 30.)

[83] F. C. Hoppensteadt and E. M. Izhikevich, "Synchronization of laser oscillators, associative memory, and optical neurocomputing," *Physical Review E*, vol. 62, no. 3, p. 4010, 2000. (Cited on page 30.)

[84] R. W. Hölzel and K. Krischer, "Pattern recognition with simple oscillating circuits," *New Journal of Physics*, vol. 13, no. 7, p. 073031, 2011. (Cited on pages 30 and 31.)

[85] R. Holzel, *A Neural Network of Weakly Coupled Nonlinear Oscillators with a Global, Time-dependent Coupling: Theory and Experiment*. 2013. (Cited on pages 30, 36, 103, and 105.)

[86] T. Nishikawa, Y.-C. Lai, and F. C. Hoppensteadt, "Capacity of oscillatory associative-memory networks with error-free retrieval," *Physical review letters*, vol. 92, no. 10, p. 108101, 2004. (Cited on page 30.)

[87] F. Stella and A. Treves, "Associative memory storage and retrieval: involvement of theta oscillations in hippocampal information processing," *Neural plasticity*, vol. 2011, 2011. (Cited on page 31.)

[88] I. Kononenko, "Machine learning for medical diagnosis: history, state of the art and perspective," *Artificial Intelligence in medicine*, vol. 23, no. 1, pp. 89–109, 2001. (Cited on page 31.)

[89] A. Geiger, P. Lenz, and R. Urtasun, "Are we ready for autonomous driving? the kitti vision benchmark suite," in *Computer Vision and Pattern Recognition (CVPR), 2012 IEEE Conference on*, pp. 3354–3361, IEEE, 2012. (Cited on page 31.)

[90] G. Csaba and W. Porod, "Computational study of spin-torque oscillator interactions for non-boolean computing applications," *IEEE Transactions on Magnetics*, vol. 49, no. 7, pp. 4447–4451, 2013. (Cited on page 31.)

[91] Y. Fang, C. N. Gnegy, T. Shibata, D. Dash, D. M. Chiarulli, and S. P. Levitan, "Non-boolean associative processing: Circuits, system architecture, and algorithms," *IEEE Journal on Exploratory Solid-State Computational Devices and Circuits*, vol. 1, pp. 94–102, 2015. (Cited on pages 31 and 37.)

[92] D. Vodenicarevic, N. Locatelli, J. Grollier, and D. Querlioz, "Synchronization detection in networks of coupled oscillators for pattern recognition," in *Neural Networks (IJCNN), 2016 International Joint Conference on*, pp. 2015–2022, IEEE, 2016. (Cited on page 32.)

[93] D. Silver, A. Huang, C. J. Maddison, A. Guez, L. Sifre, G. Van Den Driessche, J. Schrittwieser, I. Antonoglou, V. Panneershelvam, M. Lanctot, *et al.*, "Mastering the game of go with deep neural networks and tree search," *nature*, vol. 529, no. 7587, p. 484, 2016. (Cited on page 33.)

[94] H.-T. Kim, B.-J. Kim, S. Choi, B.-G. Chae, Y. W. Lee, T. Driscoll, M. M. Qazilbash, and D. Basov, "Electrical oscillations induced by the metal-insulator transition in vo 2," *Journal of Applied Physics*, vol. 107, no. 2, p. 023702, 2010. (Cited on page 35.)

[95] A. Beaumont, J. Leroy, J.-C. Orlianges, and A. Crunteanu, "Current-induced electrical self-oscillations across out-of-plane threshold switches based on vo2 layers integrated in crossbars geometry," *Journal of Applied Physics*, vol. 115, no. 15, p. 154502, 2014. (Cited on page 35.)

[96] A. Crunteanu, J. Givernaud, J. Leroy, D. Mardivirin, C. Champeaux, J.-C. Orlianges, A. Catherinot, and P. Blondy, "Voltage- and current-activated metal–insulator transition in vo2-based electrical switches: a lifetime operation analysis," *Science and technology of advanced materials*, vol. 11, no. 6, p. 065002, 2010. (Cited on page 35.)

[97] N. Shukla, A. Parihar, E. Freeman, H. Paik, G. Stone, V. Narayanan, H. Wen, Z. Cai, V. Gopalan, R. Engel-Herbert, *et al.*, "Synchronized charge oscillations in correlated electron systems," *Scientific reports*, vol. 4, p. 4964, 2014. (Cited on page 35.)

[98] W.-Y. Tsai, X. Li, M. Jerry, B. Xie, N. Shukla, H. Liu, N. Chandramoorthy, M. Cotter, A. Raychowdhury, D. M. Chiarulli, *et al.*, "Enabling new computation paradigms with hyperfet-an emerging device," *IEEE Transactions on Multi-Scale Computing Systems*, vol. 2, no. 1, pp. 30–48, 2016. (Cited on page 35.)

[99] N. Shukla, A. Parihar, M. Cotter, M. Barth, X. Li, N. Chandramoorthy, H. Paik, D. G. Schlom, V. Narayanan, A. Raychowdhury, *et al.*, "Pairwise coupled hybrid vanadium dioxide-mosfet (hvfet) oscillators for non-boolean associative computing," in

Electron Devices Meeting (IEDM), 2014 IEEE International, pp. 28–7, IEEE, 2014. (Cited on page 35.)

[100] S. Datta, N. Shukla, M. Cotter, A. Parihar, and A. Raychowdhury, "Neuro inspired computing with coupled relaxation oscillators," in *Proceedings of the 51st Annual Design Automation Conference*, pp. 1–6, ACM, 2014. (Cited on page 35.)

[101] W. Yi, K. K. Tsang, S. K. Lam, X. Bai, J. A. Crowell, and E. A. Flores, "Biological plausibility and stochasticity in scalable vo 2 active memristor neurons," *Nature communications*, vol. 9, no. 1, p. 4661, 2018. (Cited on page 35.)

[102] A. A. Sharma, J. A. Bain, and J. A. Weldon, "Phase coupling and control of oxide-based oscillators for neuromorphic computing," *IEEE Journal on Exploratory Solid-State Computational Devices and Circuits*, vol. 1, pp. 58–66, 2015. (Cited on page 36.)

[103] T. C. Jackson, A. A. Sharma, J. A. Bain, J. A. Weldon, and L. Pileggi, "Oscillatory neural networks based on tmo nano-oscillators and multi-level rram cells," *IEEE journal on Emerging and Selected Topics in Circuits and Systems*, vol. 5, no. 2, pp. 230–241, 2015. (Cited on page 36.)

[104] T. Aonishi, K. Kurata, and M. Okada, "Statistical Mechanics of an Oscillator Associative Memory with Scattered Natural Frequencies," *Physical Review Letters*, vol. 82, pp. 2800–2803, Mar. 1999. (Cited on pages 36 and 103.)

[105] A. A. Sharma, I. V. Karpov, R. Kotlyar, J. Kwon, M. Skowronski, and J. A. Bain, "Dynamics of electroforming in binary metal oxide-based resistive switching memory," *Journal of Applied Physics*, vol. 118, no. 11, p. 114903, 2015. (Cited on page 36.)

[106] Y. Tomita, K. Suzuki, T. Matsumoto, T. Yamamoto, H. Yamaguchi, and H. Tamura, "An 8-to-16ghz 28nm cmos clock distribution circuit based on mutual-injection-locked ring oscillators," in *VLSI Circuits (VLSIC), 2013 Symposium on*, pp. C238–C239, IEEE, 2013. (Cited on page 37.)

[107] D. X. Tran and T. T. Dang, "An ultra-low power consumption and very compact 1.49 ghz cmos voltage controlled ring oscillator," in *Advanced Technologies for Communications (ATC), 2014 International Conference on*, pp. 239–244, IEEE, 2014. (Cited on page 37.)

[108] K. L. Ekinci, "Nems: All you need is feedback," *Nature nanotechnology*, vol. 3, no. 6, p. 319, 2008. (Cited on page 38.)

[109] C. Chen, D. Zanette, D. Czaplewski, J. Guest, and D. Lopez, "A self-saturating mechanical oscillator with linear feedback," in *APS Meeting Abstracts*, 2016. (Cited on page 38.)

[110] M. Zalalutdinov, K. L. Aubin, M. Pandey, A. T. Zehnder, R. H. Rand, H. G. Craighead, J. M. Parpia, and B. H. Houston, "Frequency entrainment for micromechanical oscillator," *Applied Physics Letters*, vol. 83, no. 16, pp. 3281–3283, 2003. (Cited on page 38.)

[111] S. N. Kazmi, M. A. Hafiz, K. N. Chappanda, S. Ilyas, J. Holguin, P. M. Costa, and M. I. Younis, "Tunable nanoelectromechanical resonator for logic computations," *Nanoscale*, vol. 9, no. 10, pp. 3449–3457, 2017. (Cited on page 38.)

[112] A. Peschot, C. Qian, and T.-J. Liu, "Nanoelectromechanical switches for low-power digital computing," *Micromachines*, vol. 6, no. 8, pp. 1046–1065, 2015. (Cited on page 38.)

[113] G. C. Adam, A. Solot, A. Dinescu, M. Fernandez-Bolaños, A. M. Ionescu, and A. Müller, "Exploring the use of a nems relay as an integrated selector device for reram," (Cited on page 38.)

[114] S. Moradi, S. A. Bhave, and R. Manohar, "Energy-efficient hybrid cmos-nems lif neuron circuit in 28 nm cmos process," *arXiv preprint arXiv:1712.07299*, 2017. (Cited on pages 38 and 39.)

[115] E. Colinet and C. Kharrat, "Modal control of mechanically coupled nems array for tunable oscillators," in *2010 First Workshop on Hardware and Software Implementation and Control of Distributed MEMS*, pp. 16–19, IEEE, 2010. (Cited on page 39.)

[116] M. Zhang, G. S. Wiederhecker, S. Manipatruni, A. Barnard, P. McEuen, and M. Lipson, "Synchronization of micromechanical oscillators using light," *Physical review letters*, vol. 109, no. 23, p. 233906, 2012. (Cited on page 39.)

[117] M. H. Matheny, M. Grau, L. G. Villanueva, R. B. Karabalin, M. Cross, and M. L. Roukes, "Phase synchronization of two anharmonic nanomechanical oscillators," *Physical review letters*, vol. 112, no. 1, p. 014101, 2014. (Cited on page 39.)

[118] S. P. Benz and C. J. Burroughs, "Coherent emission from two-dimensional josephson junction arrays," *Applied physics letters*, vol. 58, no. 19, pp. 2162–2164, 1991. (Cited on page 40.)

[119] S. P. Benz and C. J. Burroughs, "Two-dimensional arrays of josephson junctions as voltage-tunable oscillators," *Superconductor Science and Technology*, vol. 4, no. 11, p. 561, 1991. (Cited on page 40.)

[120] A. K. Jain, K. Likharev, J. Lukens, and J. Sauvageau, "Mutual phase-locking in josephson junction arrays," *Physics Reports*, vol. 109, no. 6, pp. 309–426, 1984. (Cited on pages 40 and 66.)

[121] S. P. Benz and P. Booi, "High-frequency oscillators using phase-locked arrays of josephson junctions," *IEEE transactions on ultrasonics, ferroelectrics, and frequency control*, vol. 42, no. 5, pp. 964–966, 1995. (Cited on page 40.)

[122] A. Cawthorne, P. Barbara, S. Shitov, C. Lobb, K. Wiesenfeld, and A. Zangwill, "Synchronized oscillations in josephson junction arrays: The role of distributed coupling," *Physical Review B*, vol. 60, no. 10, p. 7575, 1999. (Cited on page 40.)

[123] Y. N. Ovchinnikov and V. Z. Kresin, "Networks of josephson junctions and their synchronization," *Physical Review B*, vol. 88, no. 21, p. 214504, 2013. (Cited on page 40.)

[124] K. Wiesenfeld, P. Colet, and S. H. Strogatz, "Frequency locking in josephson arrays: Connection with the kuramoto model," *Physical Review E*, vol. 57, no. 2, p. 1563, 1998. (Cited on page 40.)

[125] S. A. Cybart, E. Cho, T. Wong, B. H. Wehlin, M. K. Ma, C. Huynh, and R. Dynes, "Nano josephson superconducting tunnel junctions in yba 2 cu 3 o 7–δ directly patterned with a focused helium ion beam," *Nature nanotechnology*, vol. 10, no. 7, p. 598, 2015. (Cited on page 40.)

[126] K. Segall, M. LeGro, S. Kaplan, O. Svitelskiy, S. Khadka, P. Crotty, and D. Schult, "Synchronization dynamics on the picosecond time scale in coupled josephson junction neurons," *Physical Review E*, vol. 95, no. 3, p. 032220, 2017. (Cited on page 40.)

[127] T. Kashiwagi, H. Kubo, K. Sakamoto, T. Yuasa, Y. Tanabe, C. Watanabe, T. Tanaka, Y. Komori, R. Ota, G. Kuwano, *et al.*, "The present status of high-t c superconducting terahertz emitters," *Superconductor Science and Technology*, vol. 30, no. 7, p. 074008, 2017. (Cited on page 40.)

[128] N. F. Mott, "The electrical conductivity of transition metals," *Proc. R. Soc. Lond. A*, vol. 153, no. 880, pp. 699–717, 1936. (Cited on page 43.)

[129] J. Coey, "Permanent magnets: Plugging the gap," *Scripta Materialia*, vol. 67, no. 6, pp. 524–529, 2012. (Cited on page 44.)

[130] A. Fert and I. Campbell, "Two-current conduction in nickel," *Physical Review Letters*, vol. 21, no. 16, p. 1190, 1968. (Cited on page 45.)

[131] M. N. Baibich, J. M. Broto, A. Fert, F. N. Van Dau, F. Petroff, P. Etienne, G. Creuzet, A. Friederich, and J. Chazelas, "Giant magnetoresistance of (001) fe/(001) cr magnetic superlattices," *Physical review letters*, vol. 61, no. 21, p. 2472, 1988. (Cited on page 46.)

[132] G. Binasch, P. Grünberg, F. Saurenbach, and W. Zinn, "Enhanced magnetoresistance in layered magnetic structures with antiferromagnetic interlayer exchange," *Physical review B*, vol. 39, no. 7, p. 4828, 1989. (Cited on page 46.)

[133] B. Dieny, C. Cowache, A. Nossov, P. Dauguet, J. Chaussy, and P. Gandit, "Anisotropy and angular variation of the giant

magnetoresistance in magnetic multilayers," *Journal of applied physics*, vol. 79, no. 8, pp. 6370–6375, 1996. (Cited on page 48.)

[134] P. M. Levy, S. Zhang, and A. Fert, "Electrical conductivity of magnetic multilayered structures," *Physical review letters*, vol. 65, no. 13, p. 1643, 1990. (Cited on page 48.)

[135] T. Valet and A. Fert, "Classical theory of perpendicular giant magnetoresistance in magnetic multilayers," *Journal of Magnetism and Magnetic Materials*, vol. 121, no. 1-3, pp. 378–382, 1993. (Cited on page 48.)

[136] M. Julliere, "Tunneling between ferromagnetic films," *Physics letters A*, vol. 54, no. 3, pp. 225–226, 1975. (Cited on pages 48 and 49.)

[137] J. C. Slonczewski, "Conductance and exchange coupling of two ferromagnets separated by a tunneling barrier," *Physical Review B*, vol. 39, no. 10, p. 6995, 1989. (Cited on page 49.)

[138] T. Miyazaki and N. Tezuka, "Giant magnetic tunneling effect in fe/al2o3/fe junction," *Journal of Magnetism and Magnetic Materials*, vol. 139, no. 3, pp. L231–L234, 1995. (Cited on page 50.)

[139] W. Gallagher, S. S. Parkin, Y. Lu, X. Bian, A. Marley, K. Roche, R. Altman, S. Rishton, C. Jahnes, T. Shaw, *et al.*, "Microstructured magnetic tunnel junctions," *Journal of Applied Physics*, vol. 81, no. 8, pp. 3741–3746, 1997. (Cited on page 50.)

[140] J. S. Moodera, L. R. Kinder, T. M. Wong, and R. Meservey, "Large magnetoresistance at room temperature in ferromagnetic thin film tunnel junctions," *Physical review letters*, vol. 74, no. 16, p. 3273, 1995. (Cited on page 50.)

[141] S. Yuasa, T. Nagahama, A. Fukushima, Y. Suzuki, and K. Ando, "Giant room-temperature magnetoresistance in single-crystal Fe/MgO/Fe magnetic tunnel junctions," *Nature materials*, vol. 3, no. 12, p. 868, 2004. (Cited on page 50.)

[142] S. S. Parkin, C. Kaiser, A. Panchula, P. M. Rice, B. Hughes, M. Samant, and S.-H. Yang, "Giant tunnelling magnetoresis-

tance at room temperature with MgO (100) tunnel barriers," *Nature materials*, vol. 3, no. 12, p. 862, 2004. (Cited on page 50.)

[143] W. Butler, X.-G. Zhang, T. Schulthess, and J. MacLaren, "Spin-dependent tunneling conductance of fe| MgO| Fe sandwiches," *Physical Review B*, vol. 63, no. 5, p. 054416, 2001. (Cited on page 50.)

[144] A. Berkowitz, J. Mitchell, M. Carey, A. Young, S. Zhang, F. Spada, F. Parker, A. Hutten, and G. Thomas, "Giant magnetoresistance in heterogeneous cu-co alloys," *Physical Review Letters*, vol. 68, no. 25, p. 3745, 1992. (Cited on page 50.)

[145] S. Mangin, D. Ravelosona, J. Katine, M. Carey, B. Terris, and E. E. Fullerton, "Current-induced magnetization reversal in nanopillars with perpendicular anisotropy," *Nature materials*, vol. 5, no. 3, p. 210, 2006. (Cited on page 50.)

[146] D. K. Pandya, P. Gupta, S. C. Kashyap, and S. Chaudhary, "GMR in excess of 10% at room temperature and low magnetic fields in electrodeposited Cu/Co nano-multilayer structures," *MRS Online Proceedings Library Archive*, vol. 961, 2006. (Cited on page 50.)

[147] S. Ikeda, J. Hayakawa, Y. Ashizawa, Y. Lee, K. Miura, H. Hasegawa, M. Tsunoda, F. Matsukura, and H. Ohno, "Tunnel magnetoresistance of 604% at 300 k by suppression of ta diffusion in CoFeB/MgO/CoFeB pseudo-spin-valves annealed at high temperature," *Applied Physics Letters*, vol. 93, no. 8, p. 082508, 2008. (Cited on page 50.)

[148] D. C. Ralph and M. D. Stiles, "Spin transfer torques," *Journal of Magnetism and Magnetic Materials*, vol. 320, no. 7, pp. 1190–1216, 2008. (Cited on page 51.)

[149] L. Berger, "Low-field magnetoresistance and domain drag in ferromagnets," *Journal of Applied Physics*, vol. 49, no. 3, pp. 2156–2161, 1978. (Cited on page 51.)

[150] P. Freitas and L. Berger, "Observation of s-d exchange force between domain walls and electric current in very thin permalloy

films," *Journal of Applied Physics*, vol. 57, no. 4, pp. 1266–1269, 1985. (Cited on page 51.)

[151] C.-Y. Hung and L. Berger, "Exchange forces between domain wall and electric current in permalloy films of variable thickness," *Journal of applied physics*, vol. 63, no. 8, pp. 4276–4278, 1988. (Cited on page 51.)

[152] J. C. Slonczewski, "Current-driven excitation of magnetic multilayers," *Journal of Magnetism and Magnetic Materials*, vol. 159, no. 1-2, pp. L1–L7, 1996. (Cited on page 51.)

[153] L. Berger, "Emission of spin waves by a magnetic multilayer traversed by a current," *Physical Review B*, vol. 54, no. 13, p. 9353, 1996. (Cited on page 51.)

[154] J. C. Sankey, Y.-T. Cui, J. Z. Sun, J. C. Slonczewski, R. A. Buhrman, and D. C. Ralph, "Measurement of the spin-transfer-torque vector in magnetic tunnel junctions," *Nature Physics*, vol. 4, no. 1, p. 67, 2008. (Cited on pages 52 and 55.)

[155] C. Wang, Y.-T. Cui, J. A. Katine, R. A. Buhrman, and D. C. Ralph, "Time-resolved measurement of spin-transfer-driven ferromagnetic resonance and spin torque in magnetic tunnel junctions," *Nature Physics*, vol. 7, no. 6, p. 496, 2011. (Cited on page 52.)

[156] I. Theodonis, N. Kioussis, A. Kalitsov, M. Chshiev, and W. Butler, "Anomalous bias dependence of spin torque in magnetic tunnel junctions," *Physical review letters*, vol. 97, no. 23, p. 237205, 2006. (Cited on page 55.)

[157] M. Chshiev, I. Theodonis, A. Kalitsov, N. Kioussis, and W. Butler, "Voltage dependence of spin transfer torque in magnetic tunnel junctions," *IEEE Transactions on Magnetics*, vol. 44, no. 11, pp. 2543–2546, 2008. (Cited on page 55.)

[158] S.-C. Oh, S.-Y. Park, A. Manchon, M. Chshiev, J.-H. Han, H.-W. Lee, J.-E. Lee, K.-T. Nam, Y. Jo, Y.-C. Kong, *et al.*, "Bias-voltage dependence of perpendicular spin-transfer torque in asymmetric MgO-based magnetic tunnel junctions," *Nature Physics*, vol. 5, no. 12, p. 898, 2009. (Cited on page 55.)

[159] A. Dussaux, A. V. Khvalkovskiy, P. Bortolotti, J. Grollier, V. Cros, and A. Fert, "Field dependence of spin-transfer-induced vortex dynamics in the nonlinear regime," *Physical Review B*, vol. 86, p. 014402, July 2012. (Cited on pages 55, 85, 160, 161, 162, and 181.)

[160] E. Grimaldi, A. Dussaux, P. Bortolotti, J. Grollier, G. Pillet, A. Fukushima, H. Kubota, K. Yakushiji, S. Yuasa, and V. Cros, "Response to noise of a vortex based spin transfer nano-oscillator," *Physical Review B*, vol. 89, no. 10, p. 104404, 2014. (Cited on pages 55, 63, 64, 65, 84, 160, 162, and 181.)

[161] H. Kubota, A. Fukushima, K. Yakushiji, T. Nagahama, S. Yuasa, K. Ando, H. Maehara, Y. Nagamine, K. Tsunekawa, D. D. Djayaprawira, *et al.*, "Quuantitative measurement of voltage dependence of spin-transfer torque in MgO-based magnetic tunnel junctions," *Nature Physics*, vol. 4, no. 1, p. 37, 2008. (Cited on page 55.)

[162] A. Chanthbouala, R. Matsumoto, J. Grollier, V. Cros, A. Anane, A. Fert, A. Khvalkovskiy, K. Zvezdin, K. Nishimura, Y. Nagamine, *et al.*, "Vertical-current-induced domain-wall motion in MgO-based magnetic tunnel junctions with low current densities," *Nature Physics*, vol. 7, no. 8, p. 626, 2011. (Cited on page 55.)

[163] L. Landau and E. Lifshitz, "On the theory of the dispersion of magnetic permeability in ferromagnetic bodies," *Phys. Z. Sowjetunion*, vol. 8, no. 153, pp. 101–114, 1935. (Cited on page 56.)

[164] T. L. Gilbert, "A phenomenological theory of damping in ferromagnetic materials," *IEEE Transactions on Magnetics*, vol. 40, no. 6, pp. 3443–3449, 2004. (Cited on page 56.)

[165] S. Tsunegi, H. Kubota, S. Tamaru, K. Yakushiji, M. Konoto, A. Fukushima, T. Taniguchi, H. Arai, H. Imamura, and S. Yuasa, "Damping parameter and interfacial perpendicular magnetic anisotropy of feb nanopillar sandwiched between MgO barrier and cap layers in magnetic tunnel junctions," *Applied Physics*

Express, vol. 7, no. 3, p. 033004, 2014. (Cited on pages 56 and 107.)

[166] Y. Tserkovnyak, H. J. Skadsem, A. Brataas, and G. E. Bauer, "Current-induced magnetization dynamics in disordered itinerant ferromagnets," *Physical Review B*, vol. 74, no. 14, p. 144405, 2006. (Cited on page 56.)

[167] M. C. Hickey and J. S. Moodera, "Origin of intrinsic gilbert damping," *Physical review letters*, vol. 102, no. 13, p. 137601, 2009. (Cited on page 56.)

[168] A. Slavin and V. Tiberkevich, "Nonlinear auto-oscillator theory of microwave generation by spin-polarized current," *IEEE Transactions on Magnetics*, vol. 45, no. 4, pp. 1875–1918, 2009. (Cited on pages 56, 64, 66, 69, 160, and 161.)

[169] S. Parkin and D. Mauri, "Spin engineering: Direct determination of the ruderman-kittel-kasuya-yosida far-field range function in ruthenium," *Physical Review B*, vol. 44, no. 13, p. 7131, 1991. (Cited on page 58.)

[170] J. Katine, F. Albert, R. Buhrman, E. Myers, and D. Ralph, "Current-driven magnetization reversal and spin-wave excitations in co/cu/co pillars," *Physical review letters*, vol. 84, no. 14, p. 3149, 2000. (Cited on page 60.)

[171] J.-E. Wegrowe, A. Fabian, P. Guittienne, X. Hoffer, D. Kelly, J.-P. Ansermet, and E. Olive, "Exchange torque and spin transfer between spin polarized current and ferromagnetic layers," *Applied physics letters*, vol. 80, no. 20, pp. 3775–3777, 2002. (Cited on page 60.)

[172] J. Sun, D. Monsma, D. Abraham, M. Rooks, and R. Koch, "Batch-fabricated spin-injection magnetic switches," *Applied Physics Letters*, vol. 81, no. 12, pp. 2202–2204, 2002. (Cited on page 60.)

[173] M. Tsoi, A. Jansen, J. Bass, W.-C. Chiang, M. Seck, V. Tsoi, and P. Wyder, "Excitation of a magnetic multilayer by an electric current," *Physical Review Letters*, vol. 80, no. 19, p. 4281, 1998. (Cited on page 60.)

[174] E. Myers, D. Ralph, J. Katine, R. Louie, and R. Buhrman, "Current-induced switching of domains in magnetic multilayer devices," *Science*, vol. 285, no. 5429, pp. 867–870, 1999. (Cited on page 60.)

[175] M. R. Pufall, W. H. Rippard, and T. J. Silva, "Materials dependence of the spin-momentum transfer efficiency and critical current in ferromagnetic metal/cu multilayers," *Applied physics letters*, vol. 83, no. 2, pp. 323–325, 2003. (Cited on page 60.)

[176] M. Stepanova and S. Dew, *Nanofabrication: techniques and principles*. Springer Science & Business Media, 2011. (Cited on page 60.)

[177] S. I. Kiselev, J. C. Sankey, I. N. Krivorotov, N. C. Emley, R. J. Schoelkopf, R. A. Buhrman, and D. C. Ralph, "Microwave oscillations of a nanomagnet driven by a spin-polarized current," *Nature*, vol. 425, no. 6956, pp. 380–383, 2003. (Cited on pages 60, 62, and 63.)

[178] W. H. Rippard, M. R. Pufall, S. Kaka, S. E. Russek, and T. J. Silva, "Direct-current induced dynamics in C o 90 F e 10/N i 80 F e 20 point contacts," *Physical Review Letters*, vol. 92, no. 2, p. 027201, 2004. (Cited on pages 60, 62, and 63.)

[179] W. H. Rippard, M. R. Pufall, S. Kaka, T. J. Silva, and S. E. Russek, "Current-driven microwave dynamics in magnetic point contacts as a function of applied field angle," *Physical Review B*, vol. 70, no. 10, p. 100406, 2004. (Cited on pages 60 and 62.)

[180] A. V. Nazarov, H. M. Olson, H. Cho, K. Nikolaev, Z. Gao, S. Stokes, and B. B. Pant, "Spin transfer stimulated microwave emission in MgO magnetic tunnel junctions," *Applied Physics Letters*, vol. 88, no. 16, p. 162504, 2006. (Cited on page 60.)

[181] D. Houssameddine, S. Florez, J. Katine, J.-P. Michel, U. Ebels, D. Mauri, O. Ozatay, B. Delaet, B. Viala, L. Folks, *et al.*, "Spin transfer induced coherent microwave emission with large power from nanoscale MgO tunnel junctions," *Applied Physics Letters*, vol. 93, no. 2, p. 022505, 2008. (Cited on page 60.)

[182] M. J. Deen, M. H. Kazemeini, and S. Naseh, "Performance characteristics of an ultra-low power vco," in *Circuits and Systems, 2003. ISCAS'03. Proceedings of the 2003 International Symposium on*, vol. 1, pp. I–I, IEEE, 2003. (Cited on page 61.)

[183] S. Tsunegi, H. Kubota, K. Yakushiji, M. Konoto, S. Tamaru, A. Fukushima, H. Arai, H. Imamura, E. Grimaldi, R. Lebrun, *et al.*, "High emission power and Q factor in spin torque vortex oscillator consisting of feb free layer," *Applied Physics Express*, vol. 7, no. 6, p. 063009, 2014. (Cited on pages 61 and 62.)

[184] S. Tsunegi, K. Yakushiji, A. Fukushima, S. Yuasa, and H. Kubota, "Microwave emission power exceeding 10 ÎŒ W in spin torque vortex oscillator," *Applied Physics Letters*, vol. 109, no. 25, p. 252402, 2016. (Cited on pages 61, 62, 63, and 77.)

[185] M. R. Pufall, W. H. Rippard, M. L. Schneider, and S. E. Russek, "Low-field current-hysteretic oscillations in spin-transfer nanocontacts," *Physical Review B*, vol. 75, no. 14, p. 140404, 2007. (Cited on page 61.)

[186] A. Dussaux, B. Georges, J. Grollier, V. Cros, A. V. Khvalkovskiy, A. Fukushima, M. Konoto, H. Kubota, K. Yakushiji, and S. Yuasa, "Large microwave generation from current-driven magnetic vortex oscillators in magnetic tunnel junctions," *Nature communications*, vol. 1, p. 8, 2010. (Cited on pages 61, 62, and 77.)

[187] H. Kubota, K. Yakushiji, A. Fukushima, S. Tamaru, M. Konoto, T. Nozaki, S. Ishibashi, T. Saruya, S. Yuasa, T. Taniguchi, *et al.*, "Spin-torque oscillator based on magnetic tunnel junction with a perpendicularly magnetized free layer and in-plane magnetized polarizer," *Applied Physics Express*, vol. 6, no. 10, p. 103003, 2013. (Cited on page 62.)

[188] H. Maehara, H. Kubota, Y. Suzuki, T. Seki, K. Nishimura, Y. Nagamine, K. Tsunekawa, A. Fukushima, A. M. Deac, K. Ando, *et al.*, "Large emission power over 2 μw with high Q factor obtained from nanocontact magnetic-tunnel-junction-based spin torque oscillator," *Applied Physics Express*, vol. 6, no. 11, p. 113005, 2013. (Cited on page 62.)

[189] S. Bonetti, P. Muduli, F. Mancoff, and J. \AAkerman, "Spin torque oscillator frequency versus magnetic field angle: The prospect of operation beyond 65 GHz," *Applied Physics Letters*, vol. 94, no. 10, p. 102507, 2009. (Cited on pages 62 and 72.)

[190] T. Seki, Y. Sakuraba, R. Okura, and K. Takanashi, "High power radio frequency oscillation by spin transfer torque in a co2mnsi layer: Experiment and macrospin simulation," *Journal of Applied Physics*, vol. 113, no. 3, p. 033907, 2013. (Cited on page 62.)

[191] Q. Mistral, J.-V. Kim, T. Devolder, P. Crozat, C. Chappert, J. Katine, M. Carey, and K. Ito, "Current-driven microwave oscillations in current perpendicular-to-plane spin-valve nanopillars," *Applied physics letters*, vol. 88, no. 19, p. 192507, 2006. (Cited on page 62.)

[192] T. Seki, Y. Sakuraba, H. Arai, M. Ueda, R. Okura, H. Imamura, and K. Takanashi, "High power all-metal spin torque oscillator using full heusler co2 (fe, mn) si," *Applied Physics Letters*, vol. 105, no. 9, p. 092406, 2014. (Cited on page 62.)

[193] T. Yamamoto, T. Seki, T. Kubota, H. Yako, and K. Takanashi, "Zero-field spin torque oscillation in co2 (fe, mn) si with a point contact geometry," *Applied Physics Letters*, vol. 106, no. 9, p. 092406, 2015. (Cited on page 62.)

[194] A. Houshang, M. Fazlali, S. Sani, P. Dürrenfeld, E. Iacocca, J. Åkerman, and R. Dumas, "Effect of excitation fatigue on the synchronization of multiple nanocontact spin-torque oscillators," *IEEE Magnetics Letters*, vol. 5, pp. 1–4, 2014. (Cited on page 62.)

[195] V. Pribiag, I. Krivorotov, G. Fuchs, P. Braganca, O. Ozatay, J. Sankey, D. Ralph, and R. Buhrman, "Magnetic vortex oscillator driven by dc spin-polarized current," *Nature Physics*, vol. 3, no. 7, p. 498, 2007. (Cited on pages 62 and 77.)

[196] A. V. Nazarov, K. Nikolaev, Z. Gao, H. Cho, and D. Song, "Microwave generation in MgO magnetic tunnel junctions due

to spin transfer effects," *Journal of Applied Physics*, vol. 103, no. 7, p. 07A503, 2008. (Cited on page 62.)

[197] D. Houssameddine, J. Sierra, D. Gusakova, B. Delaet, U. Ebels, L. Buda-Prejbeanu, M.-C. Cyrille, B. Dieny, B. Ocker, J. Langer, *et al.*, "Spin torque driven excitations in a synthetic antiferromagnet," *Applied Physics Letters*, vol. 96, no. 7, p. 072511, 2010. (Cited on page 62.)

[198] P. K. Muduli, Y. Pogoryelov, S. Bonetti, G. Consolo, F. Mancoff, and J. Åkerman, "Nonlinear frequency and amplitude modulation of a nanocontact-based spin-torque oscillator," *Physical Review B*, vol. 81, no. 14, p. 140408, 2010. (Cited on page 62.)

[199] W. Rippard, M. Pufall, and A. Kos, "Time required to injection-lock spin torque nanoscale oscillators," *Applied Physics Letters*, vol. 103, no. 18, p. 182403, 2013. (Cited on page 62.)

[200] J. Costa, S. Serrano-Guisan, B. Lacoste, A. Jenkins, T. Böhnert, M. Tarequzzaman, J. Borme, F. Deepak, E. Paz, J. Ventura, *et al.*, "High power and low critical current density spin transfer torque nano-oscillators using MgO barriers with intermediate thickness," *Scientific Reports*, vol. 7, no. 1, p. 7237, 2017. (Cited on page 62.)

[201] H. Maehara, H. Kubota, Y. Suzuki, T. Seki, K. Nishimura, Y. Nagamine, K. Tsunekawa, A. Fukushima, H. Arai, T. Taniguchi, *et al.*, "High Q factor over 3000 due to out-of-plane precession in nano-contact spin-torque oscillator based on magnetic tunnel junctions," *Applied Physics Express*, vol. 7, no. 2, p. 023003, 2014. (Cited on page 62.)

[202] O. Boulle, V. Cros, J. Grollier, L. Pereira, C. Deranlot, F. Petroff, G. Faini, J. Barnaś, and A. Fert, "Shaped angular dependence of the spin-transfer torque and microwave generation without magnetic field," *Nature Physics*, vol. 3, no. 7, p. 492, 2007. (Cited on page 63.)

[203] D. Houssameddine, U. Ebels, B. Delaët, B. Rodmacq, I. Firastrau, F. Ponthenier, M. Brunet, C. Thirion, J.-P. Michel,

L. Prejbeanu-Buda, *et al.*, "Spin-torque oscillator using a perpendicular polarizer and a planar free layer," *Nature materials*, vol. 6, no. 6, p. 447, 2007. (Cited on page 63.)

[204] Z. Zeng, G. Finocchio, B. Zhang, P. K. Amiri, J. A. Katine, I. N. Krivorotov, Y. Huai, J. Langer, B. Azzerboni, K. L. Wang, *et al.*, "Ultralow-current-density and bias-field-free spin-transfer nano-oscillator," *Scientific reports*, vol. 3, p. srep01426, 2013. (Cited on page 63.)

[205] T. Devolder, A. Meftah, K. Ito, J. Katine, P. Crozat, and C. Chappert, "Spin transfer oscillators emitting microwave in zero applied magnetic field," *Journal of applied physics*, vol. 101, no. 6, p. 063916, 2007. (Cited on page 63.)

[206] A. Khvalkovskiy, J. Grollier, A. Dussaux, K. A. Zvezdin, and V. Cros, "Vortex oscillations induced by spin-polarized current in a magnetic nanopillar: Analytical versus micromagnetic calculations," *Physical Review B*, vol. 80, no. 14, p. 140401, 2009. (Cited on pages 64 and 83.)

[207] N. Locatelli, V. Naletov, J. Grollier, G. De Loubens, V. Cros, C. Deranlot, C. Ulysse, G. Faini, O. Klein, and A. Fert, "Dynamics of two coupled vortices in a spin valve nanopillar excited by spin transfer torque," *Applied Physics Letters*, vol. 98, no. 6, p. 062501, 2011. (Cited on page 64.)

[208] R. Lebrun, N. Locatelli, S. Tsunegi, J. Grollier, V. Cros, F. A. Araujo, H. Kubota, K. Yakushiji, A. Fukushima, and S. Yuasa, "Nonlinear behavior and mode coupling in spin-transfer nano-oscillators," *Physical Review Applied*, vol. 2, no. 6, p. 061001, 2014. (Cited on page 64.)

[209] B. Van der Pol, "LXXXVIII. On relaxation-oscillations," *The London, Edinburgh, and Dublin Philosophical Magazine and Journal of Science*, vol. 2, no. 11, pp. 978–992, 1926. (Cited on page 64.)

[210] S. Urazhdin, V. Tiberkevich, and A. Slavin, "Parametric excitation of a magnetic nanocontact by a microwave field," *Physical*

review letters, vol. 105, no. 23, p. 237204, 2010. (Cited on page 66.)

[211] P. Bortolotti, E. Grimaldi, A. Dussaux, J. Grollier, V. Cros, C. Serpico, K. Yakushiji, A. Fukushima, H. Kubota, R. Matsumoto, *et al.*, "Parametric excitation of magnetic vortex gyrations in spin-torque nano-oscillators," *Physical Review B*, vol. 88, no. 17, p. 174417, 2013. (Cited on page 66.)

[212] S. Urazhdin, P. Tabor, V. Tiberkevich, and A. Slavin, "Fractional synchronization of spin-torque nano-oscillators," *Physical review letters*, vol. 105, no. 10, p. 104101, 2010. (Cited on pages 66 and 72.)

[213] S. Martin, C. Thirion, C. Hoarau, C. Baraduc, and B. Dieny, "Tunability versus deviation sensitivity in a nonlinear vortex oscillator," *Physical Review B*, vol. 88, no. 2, p. 024421, 2013. (Cited on page 66.)

[214] P. Muduli, O. Heinonen, and J. Åkerman, "Decoherence and mode hopping in a magnetic tunnel junction based spin torque oscillator," *Physical review letters*, vol. 108, no. 20, p. 207203, 2012. (Cited on page 66.)

[215] S. H. Strogatz, D. M. Abrams, A. McRobie, B. Eckhardt, and E. Ott, "Theoretical mechanics: Crowd synchrony on the millennium bridge," *Nature*, vol. 438, no. 7064, p. 43, 2005. (Cited on page 66.)

[216] Z. Néda, E. Ravasz, Y. Brechet, T. Vicsek, and A.-L. Barabási, "Self-organizing processes: The sound of many hands clapping," *Nature*, vol. 403, no. 6772, p. 849, 2000. (Cited on page 66.)

[217] A. Pikovsky, M. Rosenblum, and J. Kurths, *Synchronization: A Universal Concept in Nonlinear Sciences*. Cambridge University Press, Apr. 2003. Google-Books-ID: FuIv845q3QUC. (Cited on pages 66, 67, and 89.)

[218] B. Blasius, A. Huppert, and L. Stone, "Complex dynamics and phase synchronization in spatially extended ecological systems," *Nature*, vol. 399, no. 6734, p. 354, 1999. (Cited on page 66.)

[219] R. E. Mirollo and S. H. Strogatz, "Synchronization of pulse-coupled biological oscillators," *SIAM Journal on Applied Mathematics*, vol. 50, no. 6, pp. 1645–1662, 1990. (Cited on page 67.)

[220] S. Kaka, M. R. Pufall, W. H. Rippard, T. J. Silva, S. E. Russek, and J. A. Katine, "Mutual phase-locking of microwave spin torque nano-oscillators," *Nature*, vol. 437, no. 7057, pp. 389–392, 2005. (Cited on page 67.)

[221] F. Mancoff, N. Rizzo, B. Engel, and S. Tehrani, "Phase-locking in double-point-contact spin-transfer devices," *Nature*, vol. 437, no. 7057, p. 393, 2005. (Cited on page 67.)

[222] F. Macià, F. Hoppensteadt, and A. D. Kent, "Spin wave excitation patterns generated by spin torque oscillators," *Nanotechnology*, vol. 25, no. 4, p. 045303, 2014. (Cited on page 67.)

[223] M. Pufall, W. Rippard, S. Russek, S. Kaka, and J. Katine, "Electrical measurement of spin-wave interactions of proximate spin transfer nanooscillators," *Physical review letters*, vol. 97, no. 8, p. 087206, 2006. (Cited on pages 67 and 68.)

[224] M. Madami, S. Bonetti, G. Consolo, S. Tacchi, G. Carlotti, G. Gubbiotti, F. Mancoff, M. A. Yar, and J. Åkerman, "Direct observation of a propagating spin wave induced by spin-transfer torque," *Nature nanotechnology*, vol. 6, no. 10, p. 635, 2011. (Cited on page 67.)

[225] A. Ruotolo, V. Cros, B. Georges, A. Dussaux, J. Grollier, C. Deranlot, R. Guillemet, K. Bouzehouane, S. Fusil, and A. Fert, "Phase-locking of magnetic vortices mediated by antivortices," *Nature nanotechnology*, vol. 4, no. 8, p. 528, 2009. (Cited on page 67.)

[226] A. Houshang, E. Iacocca, P. Dürrenfeld, S. Sani, J. Åkerman, and R. Dumas, "Spin-wave-beam driven synchronization of nanocontact spin-torque oscillators," *Nature nanotechnology*, vol. 11, no. 3, p. 280, 2016. (Cited on page 67.)

[227] A. A. Awad, P. DÃŒrrenfeld, A. Houshang, M. Dvornik, E. Iacocca, R. K. Dumas, and J. Akerman, "Long-range mutual

synchronization of spin Hall nano-oscillators," *Nature Physics*, vol. 13, p. nphys3927, Nov. 2016. (Cited on page 67.)

[228] M. Dvornik, A. A. Awad, P. Dürrenfeld, A. Houshang, E. Iacocca, R. K. Dumas, and J. Åkerman, "Mutually synchronized spin hall nano-oscillators for neuromorphic computing (conference presentation)," in *Spintronics X*, vol. 10357, p. 103572J, International Society for Optics and Photonics, 2017. (Cited on page 67.)

[229] A. Slavin and V. Tiberkevich, "Theory of mutual phase locking of spin-torque nanosized oscillators," *Physical review B*, vol. 74, no. 10, p. 104401, 2006. (Cited on page 68.)

[230] A. Slavin and V. Tiberkevich, "Nonlinear self-phase-locking effect in an array of current-driven magnetic nanocontacts," *Physical Review B*, vol. 72, no. 9, p. 092407, 2005. (Cited on page 68.)

[231] A. Belanovsky, N. Locatelli, P. Skirdkov, F. A. Araujo, K. Zvezdin, J. Grollier, V. Cros, and A. Zvezdin, "Non-adlerian synchronization of dipolar coupled vortex spin-torque nano-oscillators," *arXiv preprint arXiv:1308.3811*, 2013. (Cited on page 68.)

[232] N. Locatelli, A. Hamadeh, F. A. Araujo, A. D. Belanovsky, P. N. Skirdkov, R. Lebrun, V. V. Naletov, K. A. Zvezdin, M. Muñoz, J. Grollier, *et al.*, "Efficient synchronization of dipolarly coupled vortex-based spin transfer nano-oscillators," *Scientific reports*, vol. 5, p. 17039, 2015. (Cited on page 68.)

[233] F. A. Araujo, A. Belanovsky, P. Skirdkov, K. Zvezdin, A. Zvezdin, N. Locatelli, R. Lebrun, J. Grollier, V. Cros, G. De Loubens, *et al.*, "Optimizing magnetodipolar interactions for synchronizing vortex based spin-torque nano-oscillators," *Physical Review B*, vol. 92, no. 4, p. 045419, 2015. (Cited on page 68.)

[234] F. Abreu Araujo and J. Grollier, "Controlling the synchronization properties of two dipolarly coupled vortex based spin-torque nano-oscillators by the intermediate of a third one," *Journal of*

Applied Physics, vol. 120, no. 10, p. 103903, 2016. (Cited on page 68.)

[235] J. Grollier, V. Cros, and A. Fert, "Synchronization of spin-transfer oscillators driven by stimulated microwave currents," *Physical Review B*, vol. 73, no. 6, p. 060409, 2006. (Cited on page 68.)

[236] B. Georges, J. Grollier, V. Cros, and A. Fert, "Impact of the electrical connection of spin transfer nano-oscillators on their synchronization: an analytical study," *Applied Physics Letters*, vol. 92, no. 23, p. 232504, 2008. (Cited on page 69.)

[237] R. Lebrun, S. Tsunegi, P. Bortolotti, H. Kubota, A. Jenkins, M. Romera, K. Yakushiji, A. Fukushima, J. Grollier, S. Yuasa, *et al.*, "Mutual synchronization of spin torque nano-oscillators through a long-range and tunable electrical coupling scheme," *Nature communications*, vol. 8, p. 15825, 2017. (Cited on pages 69 and 89.)

[238] S. Tsunegi, T. Taniguchi, R. Lebrun, K. Yakushiji, V. Cros, J. Grollier, A. Fukushima, S. Yuasa, and H. Kubota, "Scaling up electrically synchronized spin torque oscillator networks," *Scientific reports*, vol. 8, no. 1, p. 13475, 2018. (Cited on pages 69 and 73.)

[239] R. Adler, "A study of locking phenomena in oscillators," *Proceedings of the IRE*, vol. 34, no. 6, pp. 351–357, 1946. (Cited on page 70.)

[240] W. H. Rippard, M. R. Pufall, S. Kaka, T. J. Silva, S. E. Russek, and J. A. Katine, "Injection locking and phase control of spin transfer nano-oscillators," *Physical review letters*, vol. 95, no. 6, p. 067203, 2005. (Cited on page 71.)

[241] B. Georges, J. Grollier, M. Darques, V. Cros, C. Deranlot, B. Marcilhac, G. Faini, and A. Fert, "Coupling efficiency for phase locking of a spin transfer nano-oscillator to a microwave current," *Physical review letters*, vol. 101, no. 1, p. 017201, 2008. (Cited on page 72.)

[242] M. Quinsat, J. Sierra, I. Firastrau, V. Tiberkevich, A. Slavin, D. Gusakova, L. Buda-Prejbeanu, M. Zarudniev, J.-P. Michel, U. Ebels, *et al.*, "Injection locking of tunnel junction oscillators to a microwave current," *Applied Physics Letters*, vol. 98, no. 18, p. 182503, 2011. (Cited on page 72.)

[243] A. Dussaux, A. Khvalkovskiy, J. Grollier, V. Cros, A. Fukushima, M. Konoto, H. Kubota, K. Yakushiji, S. Yuasa, K. Ando, *et al.*, "Phase locking of vortex based spin transfer oscillators to a microwave current," *Applied Physics Letters*, vol. 98, no. 13, p. 132506, 2011. (Cited on page 72.)

[244] A. Hamadeh, N. Locatelli, V. Naletov, R. Lebrun, G. De Loubens, J. Grollier, O. Klein, and V. Cros, "Perfect and robust phase-locking of a spin transfer vortex nano-oscillator to an external microwave source," *Applied Physics Letters*, vol. 104, no. 2, p. 022408, 2014. (Cited on page 72.)

[245] H. Hughes, K. Bussmann, P. J. McMarr, S.-F. Cheng, R. Shull, A. P. Chen, S. Schafer, T. Mewes, A. Ong, E. Chen, *et al.*, "Radiation studies of spin-transfer torque materials and devices," *IEEE Transactions on Nuclear Science*, vol. 59, no. 6, pp. 3027–3033, 2012. (Cited on page 72.)

[246] S.-W. Chung, T. Kishi, J. Park, M. Yoshikawa, K. Park, T. Nagase, K. Sunouchi, H. Kanaya, G. Kim, K. Noma, *et al.*, "4gbit density stt-mram using perpendicular mtj realized with compact cell structure," in *Electron Devices Meeting (IEDM), 2016 IEEE International*, pp. 27–1, IEEE, 2016. (Cited on page 73.)

[247] A. Tulapurkar, Y. Suzuki, A. Fukushima, H. Kubota, H. Maehara, K. Tsunekawa, D. Djayaprawira, N. Watanabe, and S. Yuasa, "Spin-torque diode effect in magnetic tunnel junctions," *Nature*, vol. 438, no. 7066, p. 339, 2005. (Cited on pages 73 and 74.)

[248] S. Tamaru, H. Kubota, K. Yakushiji, S. Yuasa, and A. Fukushima, "Extremely coherent microwave emission from spin torque oscillator stabilized by phase locked loop," *Scientific reports*, vol. 5, p. 18134, 2015. (Cited on page 73.)

[249] M. Kreissig, R. Lebrun, F. Protze, K. Merazzo, J. Hem, L. Vila, R. Ferreira, M. Cyrille, F. Ellinger, V. Cros, *et al.*, "Vortex spin-torque oscillator stabilized by phase locked loop using integrated circuits," *AIP Advances*, vol. 7, no. 5, p. 056653, 2017. (Cited on page 73.)

[250] H. S. Choi, S. Y. Kang, S. J. Cho, I.-Y. Oh, M. Shin, H. Park, C. Jang, B.-C. Min, S.-I. Kim, S.-Y. Park, *et al.*, "Spin nano–oscillator–based wireless communication," *Scientific reports*, vol. 4, p. 5486, 2014. (Cited on page 73.)

[251] A. Ruiz-Calaforra, A. Purbawati, T. Brächer, J. Hem, C. Murapaka, E. Jiménez, D. Mauri, A. Zeltser, J. A. Katine, M.-C. Cyrille, L. D. Buda-Prejbeanu, and U. Ebels, "Frequency shift keying by current modulation in a MTJ-based STNO with high data rate," *Applied Physical Letters*, vol. 111, p. 082401, Aug. 2017. (Cited on page 73.)

[252] A. Purbawati, F. Garcia-Sanchez, L. D. Buda-Prejbeanu, and U. Ebels, "Enhanced modulation rates via field modulation in spin torque nano-oscillators," *Applied Physical Letters*, p. 122402, Mar. 2016. (Cited on page 73.)

[253] K. Mizushima, K. Kudo, T. Nagasawa, and R. Sato, "High-data-transfer-rate read heads composed of spin-torque oscillators," in *Journal of Physics: Conference Series*, vol. 266, p. 012060, IOP Publishing, 2011. (Cited on page 74.)

[254] S. Miwa, S. Ishibashi, H. Tomita, T. Nozaki, E. Tamura, K. Ando, N. Mizuochi, T. Saruya, H. Kubota, K. Yakushiji, *et al.*, "Highly sensitive nanoscale spin-torque diode," *Nature materials*, vol. 13, no. 1, p. 50, 2014. (Cited on page 74.)

[255] S. Menshawy, A. Jenkins, K. J. Merazzo, L. Vila, R. Ferreira, M.-C. Cyrille, U. Ebels, P. Bortolotti, J. Kermorvant, and V. Cros, "Spin transfer driven resonant expulsion of a magnetic vortex core for efficient rf detector," *AIP Advances*, vol. 7, no. 5, p. 056608, 2017. (Cited on page 74.)

[256] S. Louis, V. Tyberkevych, J. Li, I. Lisenkov, R. Khymyn, E. Bankowski, T. Meitzler, I. Krivorotov, and A. Slavin, "Low

power microwave signal detection with a spin-torque nano-oscillator in the active self-oscillating regime," *IEEE Transactions on Magnetics*, vol. 53, no. 11, pp. 1–4, 2017. (Cited on page 74.)

[257] S. Hemour, Y. Zhao, C. H. P. Lorenz, D. Houssameddine, Y. Gui, C.-M. Hu, and K. Wu, "Towards low-power high-efficiency rf and microwave energy harvesting," *IEEE transactions on microwave theory and techniques*, vol. 62, no. 4, pp. 965–976, 2014. (Cited on page 74.)

[258] B. Fang, M. Carpentieri, X. Hao, H. Jiang, J. A. Katine, I. N. Krivorotov, B. Ocker, J. Langer, K. L. Wang, and B. Zhang, "Giant spin-torque diode sensitivity in the absence of bias magnetic field," *Nature communications*, vol. 7, 2016. (Cited on page 74.)

[259] N. Usov and S. Peschany, "Modeling of equilibrium magnetization structures in fine ferromagnetic particles with uniaxial anisotropy," *Journal of magnetism and magnetic materials*, vol. 110, no. 1-2, pp. L1–L5, 1992. (Cited on pages 78 and 80.)

[260] A. Aharoni, "Upper bound to a single-domain behavior of a ferromagnetic cylinder," *Journal of applied physics*, vol. 68, no. 6, pp. 2892–2900, 1990. (Cited on page 78.)

[261] Y. Gaididei, V. P. Kravchuk, and D. D. Sheka, "Magnetic vortex dynamics induced by an electrical current," *International Journal of Quantum Chemistry*, vol. 110, pp. 83–97, Jan. 2010. (Cited on pages 78, 80, 83, 162, and 181.)

[262] K. Buchanan and P. Roy, "Ks buchanan, pe roy, m. grimsditch, fy fradin, ky guslienko, sd bader, and v. novosad, nat. phys. 1, 172 (2005).," *Nat. Phys.*, vol. 1, p. 172, 2005. (Cited on page 78.)

[263] S. Yakata, M. Miyata, S. Honda, H. Itoh, H. Wada, and T. Kimura, "Chirality control of magnetic vortex in a square py dot using current-induced oersted field," *Applied Physics Letters*, vol. 99, no. 24, p. 242507, 2011. (Cited on page 78.)

[264] K. Y. Guslienko and K. L. Metlov, "Evolution and stability of a magnetic vortex in a small cylindrical ferromagnetic particle

under applied field," *Physical Review B*, vol. 63, no. 10, p. 100403, 2001. (Cited on page 79.)

[265] W. Scholz, K. Y. Guslienko, V. Novosad, D. Suess, T. Schrefl, R. Chantrell, and J. Fidler, "Transition from single-domain to vortex state in soft magnetic cylindrical nanodots," *Journal of magnetism and magnetic materials*, vol. 266, no. 1-2, pp. 155–163, 2003. (Cited on page 79.)

[266] R. Cowburn, D. Koltsov, A. Adeyeye, M. Welland, and D. Tricker, "Single-domain circular nanomagnets," *Physical Review Letters*, vol. 83, no. 5, p. 1042, 1999. (Cited on page 79.)

[267] T. Hengstmann, D. Grundler, C. Heyn, and D. Heitmann, "Stray-field investigation on permalloy nanodisks," *Journal of Applied Physics*, vol. 90, no. 12, pp. 6542–6544, 2001. (Cited on page 79.)

[268] M. Schneider, H. Hoffmann, S. Otto, T. Haug, and J. Zweck, "Stability of magnetic vortices in flat submicron permalloy cylinders," *Journal of Applied Physics*, vol. 92, no. 3, pp. 1466–1472, 2002. (Cited on page 79.)

[269] V. Novosad, M. Grimsditch, K. Y. Guslienko, P. Vavassori, Y. Otani, and S. Bader, "Spin excitations of magnetic vortices in ferromagnetic nanodots," *Physical Review B*, vol. 66, no. 5, p. 052407, 2002. (Cited on page 80.)

[270] S.-B. Choe, Y. Acremann, A. Scholl, A. Bauer, A. Doran, J. Stöhr, and H. A. Padmore, "Vortex core-driven magnetization dynamics," *Science*, vol. 304, no. 5669, pp. 420–422, 2004. (Cited on page 80.)

[271] M. Buess, R. Höllinger, T. Haug, K. Perzlmaier, U. Krey, D. Pescia, M. Scheinfein, D. Weiss, and C. Back, "Fourier transform imaging of spin vortex eigenmodes," *Physical review letters*, vol. 93, no. 7, p. 077207, 2004. (Cited on page 80.)

[272] K. Y. Guslienko, W. Scholz, R. Chantrell, and V. Novosad, "Vortex-state oscillations in soft magnetic cylindrical dots," *Physical Review B*, vol. 71, no. 14, p. 144407, 2005. (Cited on page 80.)

[273] B. Ivanov and C. Zaspel, "High frequency modes in vortex-state nanomagnets," *Physical review letters*, vol. 94, no. 2, p. 027205, 2005. (Cited on page 80.)

[274] A. A. Thiele, "Steady-state motion of magnetic domains," *Physical Review Letters*, vol. 30, no. 6, p. 230, 1973. (Cited on pages 81 and 160.)

[275] A. Dussaux, *Etude des oscillations de vortex magnÃ©tiques induites par transfert de spin*. Paris 6, Jan. 2011. (Cited on pages 81 and 85.)

[276] K. Y. Guslienko, X. F. Han, D. J. Keavney, R. Divan, and S. D. Bader, "Magnetic Vortex Core Dynamics in Cylindrical Ferromagnetic Dots," *Physical Review Letters*, vol. 96, p. 067205, Feb. 2006. (Cited on pages 83, 160, and 162.)

[277] B. Georges, J. Grollier, V. Cros, and A. Fert, "Impact of the electrical connection of spin transfer nano-oscillators on their synchronization: an analytical study," *Applied Physics Letters*, vol. 92, no. 23, p. 232504, 2008. (Cited on pages 91, 138, and 169.)

[278] K. Y. Guslienko, B. Ivanov, V. Novosad, Y. Otani, H. Shima, and K. Fukamichi, "Eigenfrequencies of vortex state excitations in magnetic submicron-size disks," *Journal of Applied Physics*, vol. 91, no. 10, pp. 8037–8039, 2002. (Cited on pages 92, 138, and 169.)

[279] D. Vodenicarevic, N. Locatelli, F. A. Araujo, J. Grollier, and D. Querlioz, "A Nanotechnology-Ready Computing Scheme based on a Weakly Coupled Oscillator Network," *Scientific Reports*, vol. 7, 2017. (Cited on pages 104 and 129.)

[280] A. Sherman and J. Rinzel, "Rhythmogenic effects of weak electrotonic coupling in neuronal models," *Proceedings of the National Academy of Sciences*, vol. 89, no. 6, pp. 2471–2474, 1992. (Cited on page 105.)

[281] J. Bernstein, Y.-X. Wang, K. Azizzadenesheli, and A. Anandkumar, "signsgd: compressed optimisation for non-convex problems," *arXiv preprint arXiv:1802.04434*, 2018. (Cited on page 122.)

[282] R. Lebrun, S. Tsunegi, P. Bortolotti, H. Kubota, A. S. Jenkins, M. Romera, K. Yakushiji, A. Fukushima, J. Grollier, S. Yuasa, and V. Cros, "Mutual synchronization of spin torque nano-oscillators through a long-range and tunable electrical coupling scheme," *Nature Communications*, vol. 8, p. ncomms15825, June 2017. (Cited on page 152.)

[283] J. Grollier, V. Cros, and A. Fert, "Synchronization of spin-transfer oscillators driven by stimulated microwave currents," *Physical Review B*, vol. 73, no. 6, p. 060409, 2006. (Cited on page 152.)

[284] L. M. Childs and S. H. Strogatz, "Stability diagram for the forced kuramoto model," *Chaos: An Interdisciplinary Journal of Nonlinear Science*, vol. 18, no. 4, p. 043128, 2008. (Cited on page 154.)

[285] Y. L. Maistrenko, O. Popovych, and P. Tass, "Desynchronization and chaos in the kuramoto model," in *Dynamics of coupled map lattices and of related spatially extended systems*, pp. 285–306, Springer, 2005. (Cited on page 154.)

[286] P. Bortolotti, A. Dussaux, J. Grollier, V. Cros, A. Fukushima, H. Kubota, K. Yakushiji, S. Yuasa, K. Ando, and A. Fert, "Temperature dependence of microwave voltage emission associated to spin-transfer induced vortex oscillation in magnetic tunnel junction," *Applied Physics Letters*, vol. 100, no. 4, p. 042408, 2012. (Cited on page 160.)

[287] A. V. Khvalkovskiy, J. Grollier, N. Locatelli, Y. V. Gorbunov, K. A. Zvezdin, and V. Cros, "Nonuniformity of a planar polarizer for spin-transfer-induced vortex oscillations at zero field," *Applied Physics Letters*, vol. 96, p. 212507, May 2010. (Cited on pages 162 and 181.)

[288] M. Gajek, J. Nowak, J. Sun, P. Trouilloud, E. O'sullivan, D. Abraham, M. Gaidis, G. Hu, S. Brown, Y. Zhu, *et al.*, "Spin torque switching of 20 nm magnetic tunnel junctions with perpendicular anisotropy," *Applied Physics Letters*, vol. 100, no. 13, p. 132408, 2012. (Cited on page 176.)

[289] "Four Foundries Back MRAM." https://semiengineering.com/four-foundries-back-mram/. Accessed: 2017-09-30. (Cited on page 176.)

[290] S. Lequeux, J. Sampaio, V. Cros, K. Yakushiji, A. Fukushima, R. Matsumoto, H. Kubota, S. Yuasa, and J. Grollier, "A magnetic synapse: multilevel spin-torque memristor with perpendicular anisotropy," *Scientific reports*, vol. 6, p. 31510, 2016. (Cited on page 176.)

[291] B. Scellier and Y. Bengio, "Equilibrium propagation: Bridging the gap between energy-based models and backpropagation," *Frontiers in computational neuroscience*, vol. 11, p. 24, 2017. (Cited on page 177.)

université PARIS-SACLAY
ÉCOLE DOCTORALE
Physique en île-de-France (EDPIF)

Titre : Calcul bio-inspiré basé sur la synchronisation de nano-oscillateurs magnétiques

Mots clés : Calcul bio-inspiré, Spintronique, Nano-oscillateurs magnétiques, Synchronisation.

Résumé : Les nano-oscillateurs à transfert de spin sont des composants radiofréquences magnétiques non-linéaires, nanométrique, de faible consommation en énergie et accordables en fréquence. Ce sont aussi potentiellement des candidats prometteurs pour l'élaboration de larges réseaux d'oscillateurs couplés. Ces derniers peuvent être utilisés dans les architectures neuromorphiques qui nécessitent des assemblées très denses d'unités de calcul complexes imitant les neurones biologiques et comportant des connexions ajustables entre elles. L'approche neuromorphique permet de pallier aux limitations des ordinateurs actuels et de diminuer leur consommation en énergie. En effet pour résoudre des tâches cognitives telles que la reconnaissance vocale, le cerveau fonctionne bien plus efficacement en terme d'énergie qu'un ordinateur classique. Au vu du grand nombre de neurone dans le cerveau (100 milliards) une puce neuro-inspirée requière des oscillateurs de très petite taille tel que les nano-oscillateurs à transfert de spin. Récemment, une première démonstration de calcul neuromorphique avec un unique nano-oscillateur magnétique a été établie. Cependant, pour aller au-delà, il faut démontrer le calcul neuromorphique avec plusieurs nano-oscillateurs et pouvoir réaliser l'apprentissage. Une difficulté majeure dans l'apprentissage des réseaux de nano-oscillateurs est qu'il faut ajuster le couplage entre eux. Dans cette thèse, en exploitant l'accordabilité en fréquence des nano-oscillateurs magnétiques, nous avons démontré expérimentalement l'apprentissage des nano-oscillateurs couplés pour classifier des voyelles prononcées avec un taux de reconnaissance de 88%. Afin de réaliser cette tache de classification, nous nous sommes inspirés de la synchronisation des taux d'activation des neurones biologiques et nous avons exploité la synchronisation des nano-oscillateurs magnétiques à des stimuli micro-ondes extérieurs. Les taux de reconnaissances observés sont dus aux fortes accordabilités et couplage intermédiaire des nano-oscillateurs utilisés. Enfin, afin de réaliser des taches plus difficiles nécessitant de larges réseaux de neurones, nous avons démontré numériquement qu'un réseau d'une centaine de nano-oscillateurs magnétiques peut être conçu avec les contraintes standards de nano-fabrication.

Title : Bio-inspired computing leveraging the synchronization of magnetic nano-oscillators

Keywords : Bio-inspired computing, Spintronics, Spin-torque nano-oscillators, Synchronization.

Abstract : Spin-torque nano-oscillators are nonlinear, nano-scale, low power consumption, tunable magnetic microwave oscillators which are promising candidates for building large networks of coupled oscillators. Those can be used as building blocks for neuromorphic hardware which requires high density networks of neuron-like complex processing units coupled by tunable connections. The neuromorphic approach allows to overcome the limitation of nowadays computers and to reduce their energy consumption. Indeed, in order to perform cognitive tasks as voice recognition or image recognition, the brain is much more efficient in terms of energy consumption. Due to the large number of required neurons (100 billions), a neuromorphic chip requires very small oscillators such as spin-torque nano-oscillators to emulate neurons. Recently a first demonstration of neuromorphic computing with a single spin-torque nano-oscillator was established, allowing spoken digit recognition with state of the art performance. However, to realize more complex cognitive tasks, it is still necessary to demonstrate a very important property of a neural networks: learning an iterative process through which a neural network can be trained using an initial fraction of the inputs and then adjusting internal parameters to improve its recognition or classification performance. One difficulty is that training networks of coupled nano-oscillators requires tuning the coupling between them. Here, through the high frequency tunability of spin-torque nano-oscillators, we demonstrate experimentally the learning ability of coupled nano-oscillators to classify spoken vowels with a recognition rate of 88%. To realize this classification task, we took inspiration from the synchronization of rhythmic activity of biological neurons and we leveraged the synchronization of spin-torque nano-oscillators to external microwave stimuli. The high experimental recognition rates stem from the weak-coupling regime and the high tunability of spin-torque nano-oscillators. Finally, in order to realize more difficult cognitive tasks requiring large neural networks, we show numerically that arrays of hundreds of spin-torque nano-oscillators can be designed with the constraints of standard nano-fabrication techniques.

Université Paris-Saclay
Espace Technologique / Immeuble Discovery
Route de l'Orme aux Merisiers RD 128 / 91190 Saint-Aubin, France